



HAL
open science

Scale and Aggregate Size Effects on Concrete Fracture : Experimental Investigation and Discrete Element Modelling

Ran Zhu

► **To cite this version:**

Ran Zhu. Scale and Aggregate Size Effects on Concrete Fracture: Experimental Investigation and Discrete Element Modelling. Civil Engineering. École centrale de Nantes, 2018. English. NNT : 2018ECDN0063 . tel-02096918

HAL Id: tel-02096918

<https://theses.hal.science/tel-02096918>

Submitted on 11 Apr 2019

HAL is a multi-disciplinary open access archive for the deposit and dissemination of scientific research documents, whether they are published or not. The documents may come from teaching and research institutions in France or abroad, or from public or private research centers.

L'archive ouverte pluridisciplinaire **HAL**, est destinée au dépôt et à la diffusion de documents scientifiques de niveau recherche, publiés ou non, émanant des établissements d'enseignement et de recherche français ou étrangers, des laboratoires publics ou privés.

THESE DE DOCTORAT DE

L'ÉCOLE CENTRALE DE NANTES

COMUE UNIVERSITE BRETAGNE LOIRE

ECOLE DOCTORALE N° 602

Sciences pour l'Ingénieur

Spécialité : Génie Civil

Par

Ran ZHU

Scale and Aggregate Size Effects on Concrete Fracture : Experimental Investigation and Discrete Element Modelling

Thèse présentée et soutenue à l'Ecole Centrale de Nantes, le 20 décembre 2018

Unité de recherche : Institut de Recherche en Génie Civil et Mécanique (GeM)-UMR CNRS 6183

Rapporteurs avant soutenance :

Mohammed MATALLAH
Professeur, Université Aboubekr Belkaid Tlemcen

Stéphane MOREL
Professeur, Université de Bordeaux 1

Composition du Jury :

David GRÉGOIRE (**président du jury**)
Professeur, Université de Pau et des Pays de l'Adour

Mohammed MATALLAH
Professeur, Université Aboubekr Belkaid Tlemcen

Stéphane MOREL
Professeur, Université de Bordeaux 1

Cécile OLIVER-LEBLOND
Maître de conférences, Ecole Normale Supérieure Paris-Saclay

François BIGNONNET
Maître de conférences, Université de Nantes

Directeur de thèse

Ahmed LOUKILI
Professeur, Ecole Centrale de Nantes

Co-encadrant de thèse

Syed Yasir ALAM
Maître de conférences, Ecole Centrale de Nantes

Acknowledgments

First of all, I would like to thank my supervisor professor Ahmed Loukili, for giving me the chance to study in France, and for his availability, his advice and his supervision throughout this work. Then, a big thank you to my co-advisor of thesis Syed-yasir Alam, lecturer at the ECN, for having accompanied me during about three years, for the many discussions and reflections, and for his patience and the time he has created, especially at the end of this work. Thanks to them, these three years of research have been extremely enriching for me.

My gratitude goes also to the technicians of laboratory: Vincent Wysnieski, Mathias Marcel and Eric Manceau for their professionalism and their daily help. Thanks to Katia Cushion for her patience and kindness.

Thank you to Abderrahmane Rhardane for guiding me, helping and encouraging me during these past three years!

I appreciate the colleagues of MEO group for their support and especially for their patience in teaching me the French language.

I would also like to thank my Chinese friends who supported and encouraged me during these three years at the ECN.

Finally, a big thank you in my heart to my family for their understanding and unconditional support!

Abstract

It is now commonly understood that in the design of civil engineering structures, size effect must be taken into consideration. For concrete, this problem is complex because it does not exhibit plastic softening. The failure of concrete is generally preceded by propagation of cracks, characterized by a large microcracking zone (fracture process zone or FPZ) which is proportional to the maximum aggregate size (d_{\max}). This fracture process is accompanied by strain-softening in the form of microcracking and fractional slip.

Experimentally, size effect in concrete is commonly studied by using geometrically similar notched beams where the nominal strength (σ_N) obtained from the bending failure load is related to the characteristic dimension (D). This leads to a decrease in the ratio of d_{\max}/D with an increase in the size of the structure. One of the objective of this thesis is to study experimentally the effect of heterogeneity (d_{\max}/D) size. This ratio is recognized as a fundamental factor causing the size effect. Three aggregate grading segments were tested on three different sizes of beams and the cracking process was investigated by acoustic emission and the image correlation technique. These methods make it possible to trace the crack openings and identify distinctively the FPZ.

The results demonstrate a significant influence of the aggregate size on the fracture behaviour of concrete. There is a direct relationship between the size effect parameters obtained by Bazant's law and maximum aggregate size (d_{\max}). The results obtained from the specimen having the same size but made of concretes with different aggregate sizes produced the same classical size effect with identical transitional between LEFM and strength based laws.

The mechanical behaviour is modelled by the Discrete Element Method (DEM). However, the linear contact model inserted in DEM is not suitable to satisfy the materials like mortar and concrete with high unconfined compressive strength to tensile strength ratio. As a result, the model is modified to take into account the contribution of interparticle moments. The micromechanical parameters are determined by conventional tests with inverse analysis using the Levenberg-Marquardt algorithm. The results showed that this approach is able to reproduce the local cracking behaviour of concrete as well as classical size effect and aggregate size effect. Then, a softening model is developed to better reproduce the post-peak response and the cracking process.

Keywords : concrete, size effect, aggregate size, cracking, acoustic emission, digital image correlation, discrete elements, contact model.

Résumé

Il est de plus en plus admis que l'effet d'échelle doit être pris en compte dans la conception des structures de Génie Civil. Pour le béton, ce problème est complexe car celui-ci ne possède pas d'adoucissement plastique, et sa rupture est due à la fissuration caractérisée par une grande zone de microfissuration (fracture process zone) qui dépend de la taille du granulat d_{\max} . Cette fissuration passe par un adoucissement sous la forme de microfissures et de glissement interparticules.

Expérimentalement, l'effet d'échelle sur le béton est très souvent étudié à l'aide des corps d'épreuves homothétiques entaillés où l'on cherche à relier la résistance nominale (σ_N) estimée à partir de la charge de rupture en flexion à une dimension caractéristique D . Ceci conduit à une diminution du ratio d_{\max}/D avec l'augmentation de la taille de la structure. Parmi les objectifs de cette thèse est d'étudier expérimentalement l'impact de l'hétérogénéité (d_{\max}/D) supposé comme facteur fondamental de l'effet d'échelle. Trois coupures granulaires ont été testées sur trois tailles de poutres différentes en suivant le processus de fissuration par émission acoustique et la technique de corrélation d'images. Celles-ci permettent de suivre l'ouverture des fissures et identifient assez clairement la FPZ.

Les résultats mettent en évidence une grande influence de la taille du granulat sur le comportement à la rupture du béton. Il existe une relation directe entre les paramètres de l'effet d'échelle obtenus par la loi de Bazant et la taille du granulat (d_{\max}). Le traitement des résultats d'une même taille avec différentes granulométries dans le même diagramme conduit à la même loi d'effet d'échelle structurelle classique avec une valeur de transition identique.

La modélisation du comportement mécanique est effectuée par la méthode d'éléments discrets (DEM). Le modèle de contact linéaire ne s'avère pas adéquat pour le mortier et le béton où le rapport compression / traction est très élevé. De ce fait, il a été modifié pour prendre en compte la contribution des moments inter-granulaires. Les paramètres micromécaniques sont déterminés par des essais classiques avec une analyse inverse en utilisant l'algorithme de Levenberg-Marquardt. Les résultats montrent que cette approche est capable de reproduire le comportement à la fissuration locale du béton et de reproduire l'effet d'échelle et celui des granulats. Ensuite, un modèle d'adoucissement est développé afin de mieux reproduire la réponse post pic et le processus de fissuration.

Mots-clés : béton, effet d'échelle, taille de granulat, fissuration, émission acoustique, corrélation d'images, éléments discrets, modèle de contact.

Table of Contents

General Introduction	1
The scope of the thesis	2
Outline of the thesis	3
Chapter 1. Literature Review of Theoretical Models and Numerical Modelling of Concrete	5
1.1 <i>Introduction to the fracture process in concrete</i>	6
1.1.1 Fracture process zone: observation and characterization	7
1.1.2 Impact of ITZ on fracture behaviour	9
1.2 <i>Theoretical models for quasi-brittle fracture in concrete</i>	10
1.2.1 Cohesive Zone Model	10
1.2.2 Crack Band Model	11
1.2.3 Equivalent Elastic Crack Model	13
1.2.4 Damage Models	14
1.3 <i>Numerical modelling methods for concrete</i>	14
1.3.1 Continuum Approach	15
1.3.2 Discontinuum Approach	16
1.4 <i>Numerical method used in the thesis</i>	17
1.5 <i>Summary</i>	18
Chapter 2. A Comprehensive Approach for Numerical Modelling of Concrete by Discrete Element Method	19
2.1 <i>Brief history of the development of Discrete Element Method</i>	20
2.2 <i>State of the art on Discrete Element Method</i>	20
2.3 <i>Theory of Discrete Element Method</i>	24
2.4 <i>Contact model in the Discrete Element Method</i>	28
2.4.1 Stiffness Model	28
2.4.2 Slip Model	29
2.4.3 Bond Model	30
2.5 <i>Stress measurement</i>	32
2.6 <i>Strain rate measurement</i>	33
2.7 <i>Parallel bond model for the behaviour of the cementitious material</i>	34
2.8 <i>Modified Parallel Bond Model</i>	38
2.8.1 Description of contact model	38
2.8.2 Validation of new contact model	39
2.8.3 Application to concrete: microstructure description and mechanical behaviour	40
2.9 <i>Summary</i>	45
Chapter 3. Experimental Investigation and Discrete Element Modelling of Concrete Fracture through Size Effect	47
3.1 <i>Size effect in concrete</i>	48
3.1.1 Review of size effect theories	48
3.1.2 Literature review of size effect in concrete	49
3.2 <i>Experimental approach to characterize size effect</i>	52

3.2.1 Material	52
3.2.2 Specimen preparation and testing procedure.....	53
3.3 <i>Methods to analyse the fracture of concrete</i>	55
3.3.1 Acoustic emission	55
3.3.2 Digital image correlation.....	62
3.3.3 AE and DIC investigation	65
3.4 <i>Discussion and experimental exhibition of size effect</i>	70
3.5 <i>Numerical modelling for size effect using Discrete Element Method</i>	75
3.5.1 Calibration of microparameters for mortar phase.....	75
3.5.2 Effect of 2D and 3D	77
3.5.3 Microparameters for concrete: ITZ and aggregate phases	79
3.5.4 Numerical modelling of size effect.....	83
3.6 <i>Summary</i>	85
Chapter 4. A New Approach to Size Effect by Scaling Microstructure	87
4.1 <i>Introduction</i>	88
4.2 <i>Review of the aggregate size effect on the hardened concrete properties</i>	88
4.2.1 Effect on tensile strength.....	88
4.2.2 Effect on flexural strength.....	90
4.2.3 Effect on fracture characteristics.....	91
4.2.4 The role of aggregate size in classical size effect analysis.....	93
4.3 <i>A new approach to study aggregate size effect on the mechanical behaviour of concrete: An experimental study</i>	94
4.3.1 Effect of aggregate scaling on Brazilian strength.....	95
4.3.2 Aggregate size effect on flexural behaviour: transition from strength-based laws to LEFM.....	96
4.3.3 The relationship between aggregate size effect and classical size effect	98
4.3.4 AE and DIC investigation	100
4.4 <i>Modelling for aggregate effect</i>	102
4.5 <i>Local behaviours of concrete</i>	103
4.6 <i>Summary</i>	106
Chapter 5. A Displacement Softening Model for DEM and its Application	109
5.1 <i>Development of local softening bond model</i>	110
5.1.1 Yield surface.....	110
5.1.2 Model formulation.....	113
5.1.3 Model behaviour	115
5.2 <i>Parametric study</i>	117
5.2.1 Effect of friction coefficient	118
5.2.2 Effect of normal and shear strength.....	119
5.2.3 Effect of normal and shear stiffness	119
5.2.4 Effect of softening parameters	120
5.3 <i>Model validation at local and macroscopic scale</i>	121
5.4 <i>Application to concrete: study of aggregate grain size effect</i>	124
5.5 <i>Summary</i>	127
Conclusions and Perspectives.....	129
<i>Conclusions</i>	129
<i>Perspectives</i>	131

Appendixes.....	133
A. The grading curves for sand and aggregates.....	133
B. The regression curves.....	135
Bibliographic References	137

General Introduction

Due to the wide range of sources of concrete materials, low prices, a simple construction process, pourability and adaptability to various environments, the concrete structure has occupied an increasingly important position in civil engineering and hydraulic structural engineering. With the development of materials science, the increase in structural span and height, and the diversification of structural forms, the size of concrete structures is increasing (such as large-span bridges, super high-rise buildings, water conservancy dams, seaport projects, etc.). Additional requirements have been put forward in the design and construction of today's projects.

Strength as an important performance indicator of concrete, it is very important to reflect the actual strength of concrete. However, due to the heterogeneous and quasi-brittleness of concrete, its strength is not constant, but it will change regularly with the change of size. This represents an intrinsic property of quasi-brittle materials and this phenomenon is called size effect. Size effect can be traced to the 15th century. Researchers in diverse fields have done a lot of research on it. Since the mechanical properties of concrete are linked to the size of the specimen, the difference in the mechanical properties of different concrete specimens cannot be accurately described without studying the size effect phenomenon. In the civil engineering, hydraulic engineering, and other subjects, the actual structural size is relatively large, it is difficult to carry out systematic experiments on the actual structure, only small-scale specimen simulation can be carried out in the laboratory. Therefore, whether the experimental results obtained from the laboratory have to guide significance and practicality of the actual structure has become one of the problems faced by researchers. The research on size effect is mainly to study the scale effect phenomenon of concrete mechanical parameters and the relationship between various parameters. This study is helpful to establish the relationship between concrete mechanical behaviour and concrete mechanical properties and explain the intrinsic link between concrete composition and structural properties. In addition, the study of the size effect of concrete contributes to the development of the discipline of concrete fracture mechanics.

However, concrete is a composite of aggregate, mortar matrix and the interface between aggregate and mortar, and its fracture problem is much more complicated than ideal brittle materials. Before loading, micro-cavities and micro-cracks existed inside the concrete material. During the loading process, the micro-cracks are continuously generated, expanded and penetrated, and developed into macro-micro-cracks, which eventually resulted in the fracture of the concrete members. In addition, the development of cracks in concrete is not the development of a single crack, it has many cracks developing at the same time, and the crack propagation path is extremely tortuous and the crack surface is also rough. The fracture of the concrete structure may be the fracture of the mortar matrix or the fracture of the aggregate, or the failure of the bond interface between the mortar and the aggregate, and possibly the overall fracture caused by the combination of these fractures. According to the microstructure analysis of concrete, the failure of concrete is actually a complex structural change process. Therefore, the research on the performance of concrete structure should start from its mesostructure, focus on the characteristics of the non-uniformity of concrete materials, and explore deeply the failure mechanism of concrete damage and fracture according to its mesostructure and meso-mechanical properties.

The scope of the thesis

Size effect has been rigorously analysed by previous researchers. When a concrete structure is loaded, the strain energy is absorbed in the FPZ due to toughening mechanisms. As the structure size increases, FPZ becomes negligible, whereas, for small size structures, the FPZ can be of the same magnitude as the structure size. Thus, the presence of FPZ is considered the main cause of the size effect. Bažant [1] considered the size of FPZ as a material property and multiple of maximum aggregate size (d_{\max}). Generally, as an inert filler, aggregate accounts for 60 % - 80 % of the volume and 70 % - 85 % of the weight of concrete [1], of which, coarse aggregate occupies about 45 % of the volume of concrete [2]. Thus, the properties of coarse aggregate seem to have a significant effect on the performance of concrete. Coarse aggregate properties, such as grading, surface area, particle size and shape, angularity, surface texture, mineralogy, water absorption, and strength have been investigated [3-7].

Thus, it can be deduced that ratio between the structure size and the aggregate size is a fundamental factor which is causing the size effect. When the structure size increases, D/d_{\max} , the ratio between the characteristic structural dimension D and the maximum aggregate size d_{\max} increases and approaches D , the material behaviour approaches linear elastic fracture mechanics (LEFM). However, when the structure size is small i.e. at laboratory scale where D and d_{\max} are of the same magnitude, LEFM is no more applicable. In this case mesoscopic and lattice element type finite element modelling is more predictive where aggregate size and distribution are explicitly taken into account.

The objective of this thesis is to investigate experimentally and numerically the role of the ratio D/d_{\max} as the cause of the size effect. This can be done by two methods: Method 1 by scaling D , or Method 2 by scaling d_{\max} . In the thesis, the two methods are investigated by using three types of concrete mix (C05, C10, and C20) which are designed with the same aggregate to mortar volumetric ratio and the same mortar properties. Only the aggregate sizes are changed. Aggregate sizes are up-scaled in C05, C10, and C20 concretes such that the volumetric fraction of each aggregate (i.e. $d_a(i)/d_{\max}$) in each concrete remains same.

- In the first series $S1$, notched beam specimens are prepared using C10 (medium size aggregate) and C20 (large size aggregate) concrete on geometrically increasing sized specimens ($D1$, $D2$, $D3$). Besides, C05 (small size aggregate) concrete on geometrically increasing sized specimens ($D1$, $D2$) also investigated in the experiments. In this way, the ratio D/d_{\max} is up-scaled (Method 1).
- In the second series $S2$, three notched beams are prepared with the same dimensions (specimen height, $D1$ and $D2$), each with different concretes C05, C10, and C20 respectively. In this way, the ratio D/d_{\max} is up-scaled in each beam (Method 2).

The beams are tested in three-point bending. Fracture process is monitored with the help of digital image correlation (DIC) and acoustic emission (AE), crack lengths and crack openings are measured and the role of D/d_{\max} as the cause of the size effect is analysed.

The numerical investigation has been carried out by Discrete Element Method (DEM). DEM simulation has advanced advantages in simulating cemented material behaviours and exploring the microscopic mechanisms which attract increasingly researchers using it. Here the mechanical behaviour of the assemblage is dominated by the micro properties of particles and bonds between them. In this study, a three-phase model is adopted in modelling concrete. Aggregates are modelled by clumping smaller particles together as clusters. Micro parameters of matrix, aggregate and interface transitional zone are determined through inverse calibration using Levenberg-Marquardt

(LM) algorithm on compression and direct tension test for mortar and concrete. The crack propagation obtained by using DEM and the role of aggregate in concrete fracture processes are analysed.

Outline of the thesis

The problems lie in the fracture of concrete are illustrated above, so the thesis deals with these problems using the following five chapters.

The first chapter presents a review of main theoretical models used for fracture analysis and numerical modelling of concrete. Then the most widely used numerical methods for concrete are introduced. Among all those methods, the discrete element method is used to model the fracture behaviours of concrete.

The second chapter illustrates a comprehensive approach used in this study for modelling mechanical and fracture behaviour of concrete using the discrete element method (DEM). Concrete is modelled at mesoscale as a three-phase material composed of aggregates, mortar, and interface. The complete coarse aggregate grading curve is considered in the mesostructure. A systematic approach has been used in this study to determine local micro parameters for each phase of concrete using inverse calibration. An improved contact model that can satisfy the quasi-brittle behaviour and low tensile to compressive strength ratio (as in case of concrete) is used.

The third chapter investigates the size effect of concrete by experiment and numerical modelling. In the experimental part, acoustic emission (AE) and digital image correlation (DIC) are used in order to further study the fracture behaviours of concrete. Bažant's size effect law is used to analyse the size effect of concrete and the fracture parameters of concrete are also calculated. In the modelling part, discrete element method is used and the modified contact model developed in Chapter 2 is implemented to model the size effect of concrete.

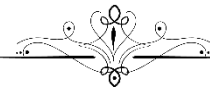
The fourth chapter analysed the effect of aggregate size. In this chapter, aggregate size (d_a) is scaled, three types of concrete mix are designed (C05, C10, and C20) with the same aggregate to mortar volumetric ratio and same mortar properties, only the aggregate sizes are changed. Aggregate sizes are up-scaled in C05, C10, and C20 concrete such that the volumetric fraction for each class of the aggregate with respect to maximum aggregate size in each concrete remains same. The experimental and numerical investigation is done to study the role of the ratio of the characteristic structural dimension (D) and the maximum aggregate size (d_{max}) in size effect. Also, the relationship between aggregate size effect and generally size effect has been studied.

The last chapter developed a displacement softening model in the framework of discrete element method in order to solve the post-peak fracture behaviour of concrete that remains a problem in the foregoing chapters. The influence of the microparameters is investigated through parametric studies. Then the proposed softening model is validated by the three-point bending test of mortar and the fracture behaviours are compared with the AE method. Finally, the model has been applied to model the aggregate effect which is the principal objective of this thesis.

Literature Review of Theoretical Models and Numerical Modelling of Concrete



The mechanical behaviour of quasi-brittle composites such as concrete, coarse grained ceramics, and fibre-reinforced composites, is manifested by mechanisms like strain localization and progressive fracture in the material. This is an intrinsic property of quasi-brittle materials due to the sizeable heterogeneity of the material microstructure. The modelling of the fracture behaviour of concrete is one of the main issues in durability and structural engineering problems. This chapter presents a review of the main theoretical models used for fracture analysis and numerical modelling of concrete.



1.1 Introduction to the fracture process in concrete

For concrete, the fracture is a fundamental phenomenon [8, 9]. There are a variety of reasons that cause the materials and structures made of concrete prone to cracking. In addition, for the fact that concrete is generally full of cracks, so the fracture of concrete is very complex. It consists of the main cracks with branches, secondary cracks, and microcracks. The coalescence of microcracks forms main cracks which propagate and finally lead to the rupture of concrete [9]. This is an intrinsic property for concrete and the fracture process zone (FPZ) is generally considered as a characteristic parameter which is used to analyse the failure process. However, the linear elastic fracture mechanics (LEFM) laws cannot be applied directly to the concrete due to the presence of the sizable FPZ [10].

Concrete although is a highly complex and heterogeneous composite material, it can be considered as a three-phase composite consisting of matrix, interface transition zone (ITZ), and aggregate. The individual properties of each phase and the interaction between phases affect the overall fracture process of concrete. Higher tangential, radial and/or shear stresses at ITZ, which are induced by the large difference between the elastic moduli of the matrix and the aggregate, have an influence on the crack initiation and propagation [11]. The thickness of ITZ in concrete has been measured by different researchers [12-14]. In general, its thickness varies in the range of 10 - 50 μm . When concrete is under compression or tension, the fracture of concrete can be roughly divided into three stages: (1) up to 30 - 40 % of peak compressive stress (or up to 60 % of peak tensile stress) [15], concrete is under quasi-elastic stage where the initial microcracks remain stable and some newly distributed microcracks are formed; (2) with the applied load increases (around 50 % of peak compressive stress) [16], new microcracks are formed in the high stressed zone and weak interfaces. Relative sliding of mortar and aggregates also occurs when ITZ is weaker (low and normal class concrete). Then it turns into the second stage, which is called a stable crack propagation stage. In this stage, numerous microcracks within the fracture process zone join together to form macrocrack which branches (due to the presence of aggregate in the crack path) and stably propagates; (3) the last stage occurs when the macrocrack propagates in an unstable way. At this stage, the concrete loses its strength and ruptures finally. The processes are illustrated in *Figure 1. 1*.

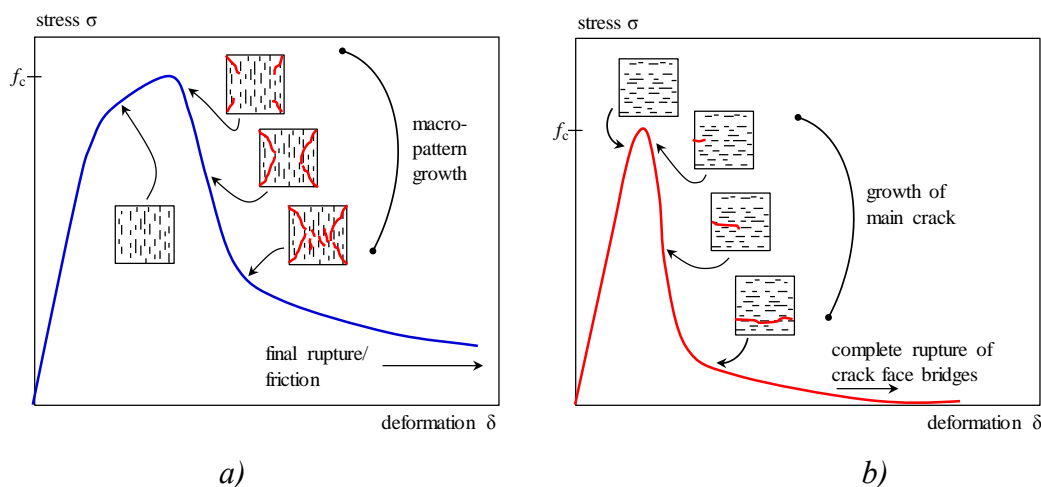


Figure 1. 1 Macroscopic failure modes under a) uniaxial compression; b) uniaxial tension [17]

1.1.1 Fracture process zone: observation and characterization

In recent decades, although researchers have proposed many concrete fracture models, the real physical state of the concrete fracture process zone is still unknown. For example, in the fictitious crack model [18], parameters such as the fracture energy dissipation in the fracture process zone and the critical opening displacement of the crack are the key parameters to almost all model calculations, but the values selected for those parameters are usually obtained from empirical methods or assumptions. In various theoretical and computational fracture models, several fracture criteria are adopted by assuming different fracture parameters. The calculation results also vary and the propagation of the fracture process zone is not the same. Therefore, researchers hope to observe the mechanical properties and propagation of the fracture process zone directly in the experiment and understand its real physical state. With further investigation of the fracture process zone, a large number of observational techniques have been developed. According to different methods of observation, the techniques are roughly divided into the direct observation method and indirect observation method.

Currently, the commonly used direct observation methods are highspeed photography [19], scanning electron microscope [20-23], and X-ray technique [24, 25]. Chabaat et al. [26] investigated the fracture process of a three-point bending beam specimen with pre-cracked concrete by scanning electron microscopy. In order to analyse the mechanical properties of the micro-cracks around the macro-cracks, the test specimens were cut along the crack propagation direction and the vertical crack propagation direction. The experimental observations showed that the failure mechanism of the concrete specimen is closely related to the development of the fracture process zone, and it is observed that the fracture process zone is actually formed by micro-cracks. In 1989, Otsuka [27, 28] measured the cracks inside the concrete by introducing contrast media based on the X-ray method. Based on this method, the research work on the concrete crack propagation process was carried out, the whole process of the concrete fracture process zone was measured [29]. The effect of aggregate size and specimen size on the core region of the fracture process zone was also studied [30]. The observation results showed that for the specimens with the same size and different aggregate particle size, the width of the core region of the fracture process zone increases with the increase of the aggregate size; for the specimens with the same aggregate size and different specimen sizes, the length and width of the core region of the fracture process zone increases with the increase of the specimen size, and the trend of increasing the length is more obvious than the width [30].

The indirect observation method refers to observing other physical parameters related to the process of fracture expansion, and indirectly obtaining the observation of the fracture process zone by relational calculation. At present, the indirect observation methods used by researchers are: dye penetration [31, 32], embedded graphite rods [33], laser speckle interferometer [34], ultrasonic measurement [35], infrared vibro-thermography [36], acoustic emission method [37-40] and digital image correlation method [41-43]. Among those methods, the acoustic emission method and digital image correlation method are the most common method that used for determining the fracture process zone. With the aid of three-dimensional acoustic emission technology, Otsuka and Date [30] measured the distribution range of the fracture process zone of concrete specimens. By analysing the experimental results, Otsuka defined the fracture process zone as containing the approximate area of the acoustic emission event greater than 95 % of the total energy. It can also be said that the distribution of acoustic emission events is very dense within this range. The test results showed that:

1) With the increase of load, the measurement results of acoustic emission indicated that micro-cracks are formed in the front part of the pre-formed crack; 2) If the initial ligament length is short, the core area of the fracture process zone will not be fully expanded. Muralidhara et al. [44] also used acoustic emission techniques to measure the size and fracture energy of the concrete fracture process zone. In this paper, the distribution area of the fracture process zone is also determined according to the position distribution of the acoustic emission events and the change of the energy release rate ratio corresponding to different load stages. Mihashi et al. [45] used three-dimensional acoustic emission technology in the double cantilever beam test to observe that the fracture process zone is actually a three-dimensional structure. The propagation of micro-cracks is not limited to the surface of the specimen but is randomly distributed around the main crack. Wu et al. [41] measured the size of FPZ and the corresponding crack opening displacement during the test loading process of concrete three-point bending beam specimens with different sizes and initial seam height ratios by digital image correlation method. The results showed that the FPZ length at the peak load and the maximum FPZ length increase with an increase in specimen height, but decrease by increasing the notch depth to specimen height ratio.

With the help of all the methods mentioned above, the mechanisms that are responsible for the fracture process in concrete have been reported. The toughening mechanisms [46] like micro-crack shielding, aggregate bridging, crack deflection, crack tip blunting, crack surface roughness induced closure and crack branching as shown in *Figure 1. 2*.

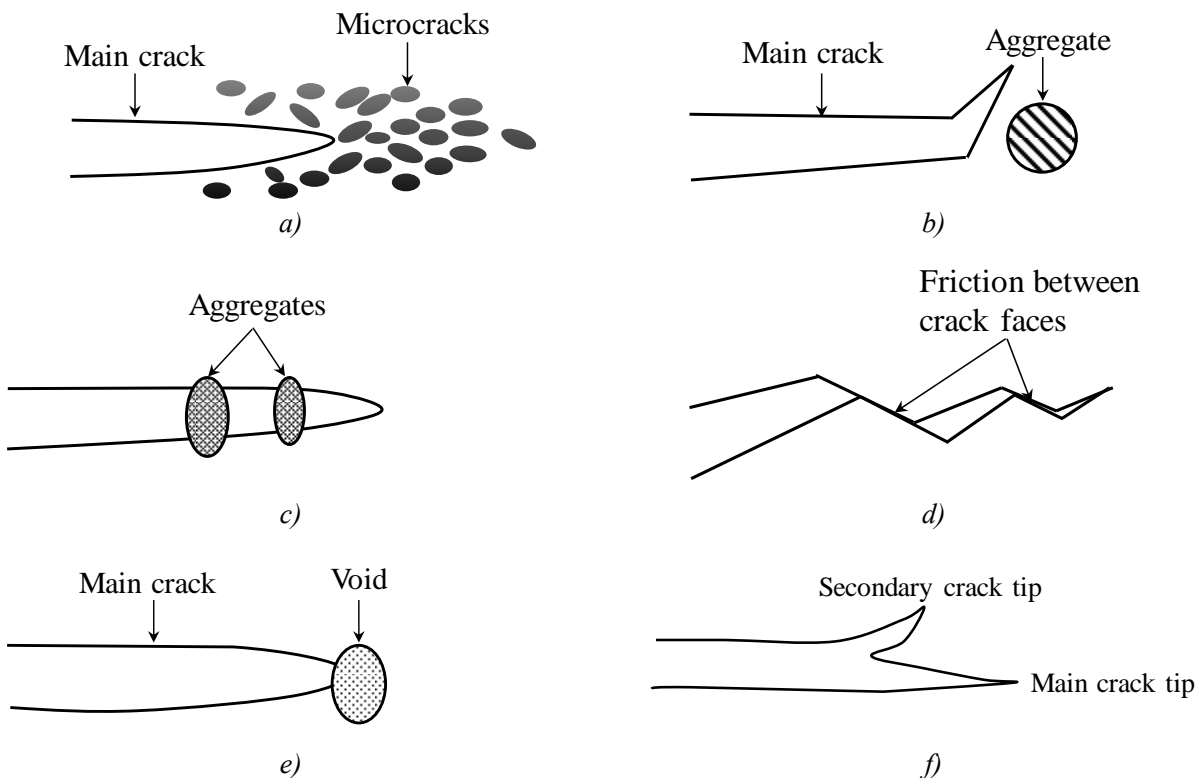


Figure 1. 2 Some toughening mechanisms in fracture process zone: a) crack shielding; b) crack deflection; c) aggregate bridging; d) crack surface roughness-induced closure; e) crack tip blunted by void; f) crack branching [8]

Usually, the influence of all these mechanisms mentioned above is lumped together and taken into account by a conceptual fracture process zone. So when one applies fracture mechanics to

concrete, the fracture process zone needs to be understood and determined. There are no standard methods to determine the width of FPZ experimentally, some researchers used the equation below to calculate the approximate width of the fracture process zone [47]. The value that calculated from the equation is just an effective width corresponding to linear stress-strain curve and uniform strain distribution within the fracture process zone is assumed.

$$w_{FPZ} = \frac{2G_f}{f_t^2} \left(\frac{1}{E} - \frac{1}{E_t} \right)^{-1} \quad (1.1)$$

Where E is the modulus of elasticity; E_t is the strain-softening modulus; f_t is the tensile strength of material; G_f is fracture energy.

Based on a banding microcrack model (BMM), Yao Wu and Li [48] proposed another equation to calculate the length and width of FPZ as presented below.

$$l_{FPZ} = \frac{1+k \cdot w_c}{2\pi} \left(\frac{K_{Ic}}{f_t} \right)^2 \quad (1.2)$$

$$w_{FPZ} = \frac{9}{8\pi} \left(\frac{K_{Ic}}{f_t} \right)^2 \quad (1.3)$$

Where k is softening degree; w_c is critical crack open displacement; f_t is tensile strength; K_{Ic} is fracture toughness.

Other researchers state that the width of FPZ is proportional to the maximum aggregate size. Bažant et al. [47] reported that the width of FPZ is about three times of the maximum aggregate size, while Chhuy et al. [49] assumed it is as wide as the maximum aggregate size and verified this with the help of ultrasonic detective test. Moreover, the length of FPZ is about 0.368 - 0.684 of specimen ligament as reported by Alexander [50, 51]. Shah [52] has studied the impact of specimen depth on the measured value of FPZ and reported that with the increase of specimen ligament, the length of FPZ increases and gradually approaches to a constant value. In the fictitious crack model [18], a parameter known as characteristic length (l_{ch}), is imported to combine tensile strength (f_t) and fracture energy (G_f) and can be expressed as:

$$l_{ch} = \frac{EG_f}{f_t^2} \quad (1.4)$$

It is assumed that characteristic length (l_{ch}) is a purely material property and is proportional to the length of the fracture process zone. The characteristic length value for concrete approximately ranges from 100 mm to 400 mm [53]. However, the length of the FPZ at a complete separation of the initial crack tip in concrete is in the range of $0.3l_{ch}$ and $0.5l_{ch}$ [8].

1.1.2 Impact of ITZ on fracture behaviour

It is now known that the properties of ITZ impact the mechanical properties of concrete. According to previous studies, the thickness of ITZ is controlled by the wall effect [54, 55]. There are also other factors that influence the thickness of ITZ like water-cement ratio, aggregate size, aggregate type, aggregate shape, aggregate surface conditions, cement, and admixtures [56-59]. Generally,

researchers consider that the lower the water-cement ratio, the thinner the ITZ [60]. Simenow et al. [57] found that the type of aggregate has a greater influence on the overall properties of ITZ. Moreover, for concrete with larger aggregate size, the thickness of ITZ becomes larger [60]. Elsharief et al. [61] concluded that when the aggregate size decreases, a lower porosity and higher unhydrated cement grains occurred in the ITZ. The researchers [56, 58, 59] also found that the interfacial bond is the deciding factor for tensile strength while has little influence on the compressive strength. Grondin and Matallah [62] numerically studied the effect of ITZs on the mechanical behaviour of concrete at the mesoscopic scale and found that the maximum strength of the concrete depends on the local tensile strength of the ITZs. Skarżyński et al. [14] investigated the cracking process in normal concrete through experiments and the results showed that the crack mainly propagates through ITZs and rarely propagate through a single weak aggregate. Nitka et al. [63] studied the effect of strength and number of ITZs by numerical modelling of the three-point bending test. They concluded that the strength and stiffness of the beam increase with the increase of ITZs strengths and with the decrease of the number of ITZs; however, the beam brittleness decreases with increasing number of ITZs and reducing the strengths of ITZs.

1.2 Theoretical models for quasi-brittle fracture in concrete

In order to investigate the issue of concrete fracture, researchers have mainly adopted three methods: 1) when fracture process zone size is relatively small when compared with the structure size, fracture toughness or energy release rate criterion based on linear elastic fracture mechanics can be used to analyse the fracture of concrete structure; 2) when the effect of fracture process zone needs to be considered, in order to simplify the calculation procedures, a nonlinear model based on linear elastic fracture mechanics can be used to describe the fracture process of concrete; 3) directly introducing non-linearity and/or considering FPZ when analysing fracture problems of concrete structures.

The main theoretical fracture or damage models able to describe the fracture characteristics of quasi-brittle materials such as concrete are successively presented in the following.

1.2.1 Cohesive Zone Model

The initial cohesive model was proposed by Dugdale [64] and Barenblatt et al. [65]. In the model, the propagation of a cohesive crack is considered as a fictitious crack which was able to transfer the stress from one face to the other. In 1976, based on the previous concepts, Hillerborg et al. [18] developed the fictitious crack model (FCM) to illustrate the nonlinear behaviour of the concrete material. The model assumed that: 1) there exists a fracture process zone ahead of a developed crack which is defined as a fictitious crack; 2) the stresses transfer through the fracture process zone depend on the opening width of the fictitious crack (w) following a characteristic strain softening behaviour of the material; 3) the fracture process zone begins when the maximum stress at the fictitious crack tip reaches the tensile strength of the material and after this stage the stress decreases according to the strain softening behaviour, as shown in *Figure 1. 3*, until the crack opening width becomes w_0 ; 4) outside the fracture process zone, the material is elastically deformed.

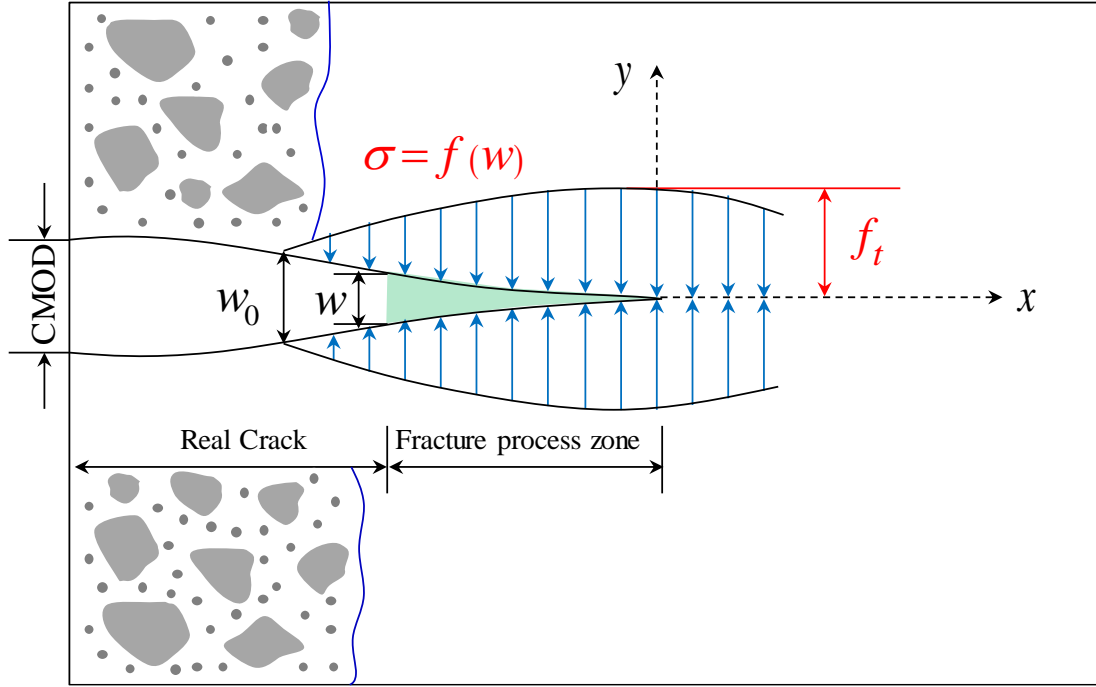


Figure 1. 3 Stress distribution and cohesive crack growth for fictitious crack model

As mentioned above, the stress transferred through the cohesive crack (σ) was assumed as a function of the crack opening displacement (w) expressed as:

$$\sigma = f(w) \quad (1.5)$$

Where f is a function characteristic of the material that must be determined from experiments.

According to *Figure 1. 3*, it should be noted that two properties are very important in the cohesive crack model: the tensile strength (f_t) and the cohesive fracture energy (G_f). The tensile strength is the stress at which the cohesive crack is created (formation of FPZ) and starts to open. The external energy required to create and fully break a unit surface area of cohesive crack is equal to the cohesive fracture energy. It can be given as the area under the softening curve by the following expression.

$$G_f = \int_0^{w_0} f(w)dw \quad (1.6)$$

The fictitious crack model considers that the softening curve is the fundamental parameter to represent the local microstructure based properties of the material and is independent of the geometry and size of the structure. When the tensile strength, fracture energy, and the shape of the softening curve are known, the softening behaviour of a material can be determined. Based on the experimental studies, softening curves with varies shape have developed, such as linear softening curve [18, 66], bilinear softening curve [53, 67-71], trilinear softening curve [72], exponential softening curve [73, 74] and power function softening curve [75].

1.2.2 Crack Band Model

Cracks in the concrete generally propagate tortuously and randomly around its aggregates instead of a straight line. Also at the crack tip, there exists an area named the fracture process zone,

which consists of distributed microcracks. Take into account these assumptions, Bažant and Oh [47] proposed a model called blunt crack band model (CBM) to simulate the fracture behaviour of concrete. The model considers the fracture process zone as a band of uniformly and continuously distribution microcracks with a fixed width h_c , as shown in *Figure 1. 4*. In this model, material fracture properties are characterized by three parameters: the fracture energy (G_f), the maximum uniaxial tensile strength (f_t) and the width of the crack band (h_c) which defines the fracture process zone ahead of a crack tip, and is represented in the model by the characteristic length (l_{ch}) of the material.

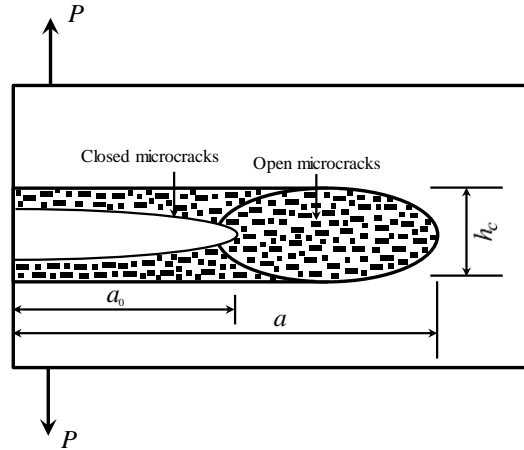


Figure 1. 4 Microcrack band fraction [47]

A simple stress-strain relationship is adopted to simulate the stable crack propagation as presented in *Figure 1. 5*.

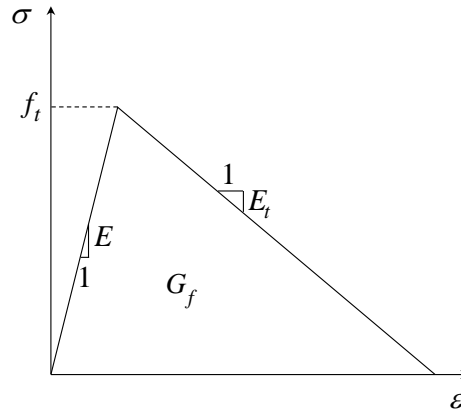


Figure 1. 5 Stress-strain curve for the micro crack band [47]

Then the energy consumed due to the crack advance per unit area of the crack band can be calculated from the area under the stress-strain curve and the width of the crack band.

$$G_f = h_c \left(1 + \frac{E}{E_t} \right) \frac{f_t^2}{2E} \quad (1.7)$$

Where E is the modulus of elasticity; E_t is the strain-softening modulus; f_t is the tensile strength of material; h_c is the width of the crack band.

1.2.3 Equivalent Elastic Crack Model

In the study of concrete fracture properties, in order to facilitate analytical analysis, many researchers have proposed various fracture models based on linear elastic fracture mechanics (LEFM), considering fracture toughness as parameters, such as two-parameter fracture model [76], equivalent fracture model [77], size effect model [78], etc.. Most of these models use the critical stress intensity factor K_{Ic}^s to determine the critical state of concrete cracks. However, K_{Ic}^s can only reflect the critical state of concrete crack instability. Another approach is to use the resistance-curve (R-curve) [79]. Based on the framework of equivalent LEFM, Morel et al. [80-82] assumed that the increase of the structure compliance due to the development of FPZ is attributed to the propagation of an elastically equivalent crack and the resistance to crack growth balances the elastic energy release rate. Thus, an R-curve behaviour can be obtained for quasi-brittle fracture corresponding to the dependence of the critical energy release rate required for fracture growth on the elastically equivalent crack length. Typically, the R-curve is described in terms of fracture energy, or stress intensity, and the stable and unstable crack growth can be distinguished by using this R-curve.

Two-parameter fracture model (TPFM) was developed by Shah and Jenq [76]. The model is based on the fracture mechanics and puts forward some nonlinear concrete mechanics assumptions. The fracture process of concrete is determined by two parameters: the critical stress intensity factor (K_{Ic}^s) and the elastic critical fracture tip opening displacement ($CTOD_c$). In 1990 RILEM [83] adopted this model as the standard experimental method to determine the fracture parameters. However, this model does not consider the influence of plastic deformation on the crack propagation when measuring the parameters.

Effective crack model (ECM) was proposed by Karihaloo and Nallathambi [77]. The model is based on the effective-elastic crack approach and the fracture toughness of concrete is determined by the three-point bending test. The basic concept of this model is similar to the two-parameter fracture model. The two fracture control parameters of the model are: the critical equivalent crack length (a_e) and the equivalent crack tip critical stress intensity factor (K_{Ic}^e). In this model, secant compliance at the maximum load is used to determine the effective-elastic crack length, while in the two-parameter fracture model using the elastic part of the unloading compliance. Due to the fact that the secant compliance at the maximum load includes effects of both elastic and inelastic deformation, so the value that calculated is greater than that obtained by the two-parameter fracture model.

Bazant and Kazemi [84] used a series of geometrically similar structures to investigate the fracture of quasi-brittle materials. The fracture behaviours of the materials are simulated by introducing an effective-elastic crack. The equations for the critical energy release rate and the critical crack extension for an infinitely large structure are given as below.

$$G_f = \frac{B^2 f_t^2 D_0}{E c_n^2} g\left(\frac{a_0}{D}\right) \quad (1.8)$$

$$c_f = \frac{g(a_0/D)}{g'(a_0/D)} D_0 \quad (1.9)$$

Where a_0 is the initial crack length; B and D_0 are constant; E is the modulus of elasticity; f_t is the size-independent tensile strength of a material; c_n is a coefficient representing different types of structures, $c_n = 1$ for a tensile plate and $c_n = 1.5S/D$ for a beam (S is the span and D the depth); $g(a_0/D)$ and $g'(a_0/D)$ are the functions.

1.2.4 Damage Models

Damage mechanics mainly deal with the macroscopic mechanical effects caused by the generation and development of microscopic defects in the material and the processes and laws that lead to material damage. The goal of damage mechanics is to predict the material response when damage initiates at a certain stress-strain state and propagates as the applied loads increase the stresses in the material. All materials show some level of damage at a very small scale. Damage is controlled by a state variable (D) which has a value between 0 (virgin material) to 1 (completely damaged material). Loss of stiffness as damage evolves is incorporated into the stiffness matrix (*Equation 1. 4*) and it is also a direct representation of the stress state of the material (*Equation 1. 5*).

$$C_{dam} = (1-D)C_{und} \quad (1.10)$$

$$\sigma = C_{dam} : \varepsilon = (1-D)C_{und} : \varepsilon \quad (1.11)$$

Where C_{dam} is damaged stiffness matrix; C_{und} is undamaged stiffness matrix; σ is stress tensor; ε is strain tensor.

The damage models can be roughly divided into two parts: 1) isotropic damage model [85-88]; 2) anisotropic damage model [89-95]. Løland [85], Krajcinovic [87, 88] and Mazars [86] considered damage as a scalar and established an isotropic damage model of concrete using the concept of effective stress. When dealing with the unilateral stress performance of concrete, Mazars [96] used two different damage variables to reflect tensile damage and compression damage. Ladevèze et al. [97] decomposed the Cauchy stress tensor into ‘positive’ and ‘negative’ parts, and the damage is still considered as a scalar, but a crack closure factor is introduced to account for the different effects of damage on stretching and compression. In the theory of anisotropic damage, Ortiz [95] first realized that although the average damage direction is perpendicular to the direction of compressive stress when concrete is subjected to uniaxial compression, the micro-cracks expand and merge along the coarse aggregate interface and the expansion direction is curved; so the damage has a lateral effect. According to this consideration, Suaris et al. [98] and Voyiadjis et al. [99] proposed the concept of effective compliance tensor, and established an anisotropic damage model of concrete. The evolution of damage is determined by the theory of the bounding surface.

1.3 Numerical modelling methods for concrete

In previous studies, the fracture behaviour of concrete has been studied using different numerical methods such as the finite element method (FEM) [18, 100, 101], the boundary element method (BEM) [102-104], the discrete element method (DEM) [105-107], the numerical manifold method [108-110], the discontinuous deformation analysis (DDA) method [111] and the mesh free method [112, 113]. All these methods mentioned can be roughly categorized as a continuum approach and discrete approach.

1.3.1 Continuum Approach

1.3.1.1 Finite Element Method

In the continuum approach, FEM is one of the most widely used modelling methods and can date back to the early 1960s [114, 115]. Firstly, Clough [115] used FEM to solve the problems of plane stress, now it has become the mainstream numerical tool in engineering sciences [18, 116]. The FEM is a numerical modelling method that tries to find approximate solutions to the boundary value problems of differential equations. The general principle of FEM is to divide the domain of the problem into smaller sub-domains called finite elements. Then it does the local approximation inside each finite element, performs the finite element assembly and finds the solution of the global matrix equation. FEM has great robustness and flexibility to deal with problems like material heterogeneity, non-linear deformability, complex boundary conditions, in situ stresses and gravity. These advantages make the FEM becoming the most successful numerical method used in engineering and science research [18, 116]. However, there are still some shortcomings for FEM, e.g., the continuum assumption in FEM makes it unsuitable to deal with complete detachment and large-scale fracture opening problems, which are the most concerning issues in the concrete fracture. Beside these demerits, the most difficult thing faced by FEM is the simulation of the fracturing process. Two available methods can be used for modelling of fracturing progress based on FEM: the element degradation approach and the element boundary-breaking approach.

1.3.1.1.1 Element Degradation Approach

The element degradation approach considers the fracturing process as a sequence of element degradation. In the software like ABAQUS [117] provides a deletion technique which removes the elements where the failure criterion is locally reached. Elements deleted can be visualized to mimic the crack progress. The continuum damage mechanics (CDM) is one of the most typical methods based on FEM and is widely applied to brittle fracturing analysis [118]. Based on the equivalent continuum concept, another degradation technique is developed. It considers cracks as elastic degradation and/or softening plasticity [119]. Smear crack model is one representative of this method, which is first introduced by Rashid [120].

No requirement of re-meshing and not adding new degrees of freedom in the calculation process is the principle merits of element degradation method. However, this method cannot give an explicit description of the fracture surface and has the demerits of mesh size and orientation dependency.

1.3.1.1.2 Element Boundary Breaking Approach

The element boundary-breaking approach represents the fracturing process by the separation of inter-element boundaries. Interface elements are inserted along the inter-element boundaries in this method. Failure of an inter-element boundary can be based on the fracture mechanics or failure criteria of the corresponding interface element. Cohesive Zone Model (CZM) [18] is the most successful development of the element boundary-breaking approach. Normally, in order to eliminate the element dependence and the problem of stress singularity which exists in the crack tip, the element

boundary-breaking approach should be combined with re-meshing techniques. However, for re-meshing techniques, a rather complex software package is needed to be developed and the use of re-meshing techniques also accumulates the calculation errors through the mapping of variables. The worst problem is that adaptive re-meshing can hardly be used to simulate complex crack development, such as crack coalescence and crack bifurcation.

1.3.1.2 Boundary Element Method

The boundary element method is a numerical method developed since the late 1970s [121], and an early application of the BEM to a crack problem was done by Cruse [122]. In BEM, the value of the field function at the boundary and at each point in the domain can be obtained by transforming the basic governing equations of the known boundary domain into boundary integral equations and then solving the corresponding algebraic equations by discretizing the boundary. The boundary element method only needs to be discretized on the boundary of the domain. Therefore, it is only necessary to arrange nodes on the boundary and crack surface when simulating cracks. It is not necessary to re-mesh when simulating crack propagation. BEM is more suitable for solving problems of homogeneous and linearly elastic bodies; however, it poses many problems in solving some problems like material heterogeneity, nonlinear material behaviour, and damage evolution process.

1.3.2 Discontinuum Approach

1.3.2.1 Discrete Element Method

The discrete element method (DEM) is the representative discontinuum method which was initially developed for solving rock mechanics problems by Cundall [123]. The key concept of DEM is to divide the domain of interest into an assemblage of rigid or deformable blocks/particles/bodies [124, 125]. DEM methods can be divided into two categories: explicit ones and implicit ones. There exist two kinds of approaches for the explicit DEM methods, namely the dynamic relaxation method and the static relaxation method. The static relaxation method uses equations of equilibrium to obtain the displacement of particles at the next time step. However, for dynamic problems, the static relaxation method cannot be used. Dynamic relaxation based DEM use Newton's second law to get the displacement of particles at the next time step, and it is generally called the distinct element method. The details of dynamic relaxation based DEM will be introduced in Chapter 2. The distinct element method can simulate the complex mechanical interactions of a discontinuous system. Now there are many researchers [126-130] who have successfully used DEM to model the fracture behaviours of concrete.

1.3.2.2 Lattice Method

The Lattice model is a simulation model of the grid system consisting of discrete continuum bodies separated into rods and beams. The Lattice model was first proposed by Hrennikoff [131] in 1941 and was called the framework method at that time. The method divides the continuum body into a truss, which is mainly used to solve classical elastic mechanics problems. The Lattice model has a

clear idea and a simple unit model. It is more suitable for the study of the failure mechanism of non-uniform materials such as rock [132] and concrete [133] under simple loading conditions.

One of the most widely used lattice models is the Beam Lattice model proposed by Schlangen et al. [134] as shown in *Figure 1. 6*. The Beam Lattice model assumes that the concrete is composed of meso-level beam elements, and the mechanical parameters of the beam elements are determined by the properties of the mesostructure components such as aggregates and cement mortar. The beam element can transmit axial force, shear force and bending moment. When the stress state of the beam satisfies the given strength criterion, the beam element is removed from the grid and the crack is generated and developed.

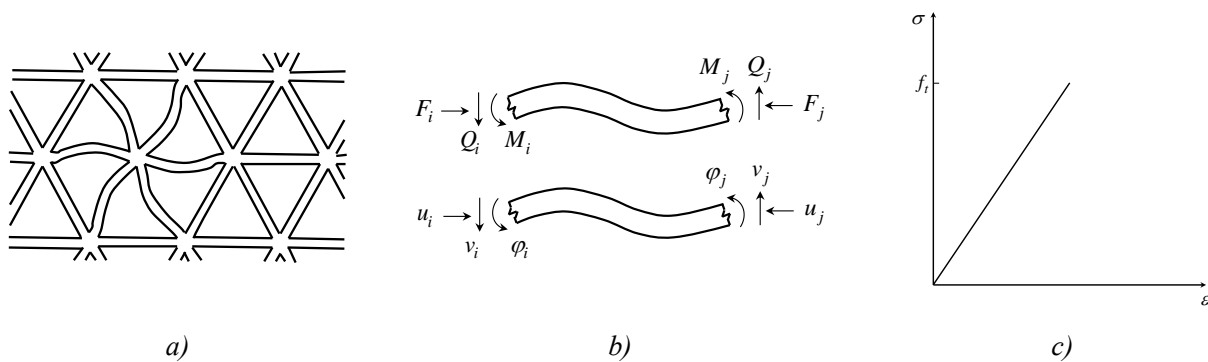


Figure 1. 6 Beam Lattice model diagram: a) Regular triangular lattice of beams; b) External forces and deformations on a single beam element; c) stress-strain relation for an element [134]

1.3.2.3 Extended Finite Element Method

Extended finite element method (X-FEM) is proposed by the research group of Belytschko [135, 136] in 1999, which is based on the unit decomposition theory to enhance the displacement function of the traditional finite element. Usually, Heaviside function and asymptotic functions are used to deal with the discontinuity and singularity. The level set method (LSM) [137], which is developed by Osher and Sethian [138], is introduced to describe the motion of interface, and the crack propagation is tracked in real time. So the X-FEM algorithm allows the crack passing arbitrarily through elements by incorporating enrichment functions to handle the field discontinuities. Particularly, elements containing a crack do not need to conform to crack edges and mesh generation are much simpler than in classical FEM [135]. Moreover, the X-FEM solves the problem that the finite element needs to continuously re-mesh the mesh when simulating crack propagation, and it is not necessary to separately divide the crack tip portion into a high-density mesh.

1.4 Numerical method used in the thesis

For those methods mentioned, some of them [139, 140] modelled concrete as a bi-phase material. It is not appropriate as aforementioned that the behaviour of ITZ is very important in the fracture of concrete. Hence, researchers now supposed concrete to be composed of three phases in their modelling. Trawiński [141] has successfully modelled the fracture of concrete by considering concrete as a three-phase material using 3D mesoscale finite element method (FEM). The parametric analysis of their studies has shown that the properties of matrix and ITZ have influences on the peak

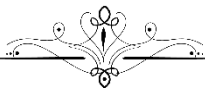
strength and brittleness of concrete beam under three-point bending test. Lilliu [142] used a lattice model to model the behaviour of concrete as three-phase and the results also revealed that the strength of ITZ affects the fracture process. Skarżyński [143] used DEM to simulate concrete as a three-phase composite and found that the mechanical properties of ITZs had a pronounced influence on the material strength and macro-cracking.

For the methods mentioned above, FEM is based on either continuum damage mechanics or fracture mechanics, and is being used for the description of deformable continuous bodies. On the contrary, DEM describes particulate materials, usually modelled by perfectly rigid particles and their interactions determined from fictitious overlaps of these rigid particles. The propagation of cracks in concrete is a discrete problem and should look into the local behaviours. Compared with FEM, DEM looks into micromechanics of problem and allows a grain level control and can solve the discontinuous problem. So it is suitable for modelling the fracture of concrete. In this thesis, DEM is adopted to model the size effect and the aggregate effect of concrete.

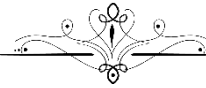
1.5 Summary

In this chapter, different fracture models of concrete behaviour are investigated. Fracture process zone is a key parameter that influences the fracture behaviours of concrete. Although different methods are proposed by researchers, it is still a problem that needs to be solved. Besides, the properties of ITZ seem to have a great impact on the mechanical properties of concrete. So the influence of ITZ needs to be studied later. Then the theoretical models and the numerical modelling methods used for concrete are presented. Based on fracture mechanics or damage mechanics, different theoretical models for concrete are proposed. Next, the most widely used numerical methods for concrete are introduced and those methods can be roughly divided into two categories: continuum models and discontinuum models. Compared with the continuum-based models, discontinuum based models seem more appropriate to model the fracture behaviours of concrete. So in the next chapter, the discrete element method is employed to model the fracture behaviours of concrete.

A Comprehensive Approach for Numerical Modelling of Concrete by Discrete Element Method



This chapter describes a comprehensive approach for modelling mechanical and fracture behaviour of concrete using discrete element method (DEM). Concrete is modelled at mesoscale as a three-phase material composed of aggregates, mortar, and interface. The complete coarse aggregate grading curve is considered in the mesostructure. A systematic approach has been used in this study to determine local micro parameters for each phase of concrete using inverse calibration. An improved contact model that can satisfy the quasi-brittle behaviour and low tensile to compressive strength ratio (as in case of concrete) is used.



2.1 Brief history of the development of Discrete Element Method

The discrete element method (DEM) is a method firstly proposed by Cundall [123] in the early 1970's to model the progressive failure of a discrete block system. The interaction between blocks was governed by friction and normal stiffness. However, whenever blocks were touching or separated, there was no limitation to the amount of displacement or rotation of each block in the model. It was designed for rigid body motion problems which were impossible to be solved by finite element methods (FEM) at that moment. The basic theory of DEM was also given Cundall, i.e. force-displacement law, the law of motion and computation cycles with time steps.

Cundall and Strack [124] then applied the DEM method to model the granular assemblies to study the particle contact force distributions in the assemblies. This granular medium was composed of distinct particles which displaced independently from one another and interacted with others at discrete contact points. Further development of DEM was made by Cundall, Drescher, and Strack [144] in the early 1980's who introduced the methodologies of measuring and observing granular assemblies using Ball simulation. In the late 1980's, Cundall extended 2D particle simulation to a 3D version which was known as TRUBAL [145]. The numerical modelling results were in accordance with the experimental results of Ishibashi et al. [146], except for the volumetric strain measured from tri-axial tests. Almost at the same period, Thorton et al. [147] developed a modified version called GRANULE. In their model, they attributed a surface energy to the balls in the agglomerates so that tensile forces between balls were defined as auto-adhesive. The program was able to model the fracture of an agglomerate of spherical balls bonded together. After that, the DEM has been developed rapidly, with applications in different domains like rock/soil mechanics [128], chemical engineering [148] and pharmacy [127].

2.2 State of the art on Discrete Element Method

The initial application of DEM to study the fracture of brittle materials such as concrete is dated back to the 1980s. Meguro and Hakuno [149, 150] developed a modified distinct element method (MDEM), based on the basis of Iwashita's model, to study the dynamic fracture of a masonry concrete wall. The results were in accordance with the actual seismic damage observed after past earthquake. Then Takada and Hassani [151] used MDEM to investigate compression failure of reinforced concrete in the 2D aspect, the quantitative results were in reasonable agreement with the experimental ones. After that, interest in using DEM to model the behaviours of concrete increased rapidly. DEM was mainly applied to investigate the fracture of concrete at a high strain rate [152]. Monteiro et al. [153] combined FEM and DEM to model the development of cracks when concrete was under the effect of the moment. Pan et al. [154] modelled the deterioration of concrete at meso-scale caused by the alkali-aggregate reaction. Although DEM is now widely used to model the behaviours of concrete, there still remain some problems.

Aforementioned, concrete is three-phase composite and coarse aggregate occupies about 45 % of the volume of concrete. How to model the coarse aggregate properly? Generally there exist three methods to generate aggregates: 1) each aggregate is represented as a single big ball; 2) each aggregate is represented as a clump of several small balls joined together with no breakage of inter-

particle bonds within aggregate; 3) each aggregate is represented as a cluster of several small balls joined together, breakage of inter-particle bonds within aggregate is allowed. The first approach is not suitable for the materials like concrete with relatively high compressive strength but low tensile strength. Nitka and Tejchman [155] modelled the behaviour of concrete in uniaxial compression and tension. In their modelling, single big balls used as the coarse aggregates. Although they obtained a satisfactory agreement between experiments and calculations, the micro parameters (cohesive stress and tensile normal stress) used for compression and tension are not the same. The micro-parameters used could not satisfy both compressive strength and tensile strength simultaneously. By using the same approach, the results of Diederichs [156] showed that when the model is calibrated to match the experimental unconfined compressive strength (UCS) of rock, the tensile strength of rock was significantly overestimated. Before Diederichs, Potyondy [157] and Schopfer [158] also got similar results when simulating brittle rock. As pointed out by Katsaga [152], the inserted contact models for concrete modelling were only calibrated to match the uniaxial compression test, the use of these models to perform tensile fracture propagation was only qualitative. The reason is that the tensile strength and compressive strength are increased at the same time with the increase of bond tensile strength (the main micro parameter). While for the brittle materials like rock and concrete, the compressive strength is about one order of magnitude larger than tensile strength. As a result, the micro parameter (normal tensile strength) for compressive strength is also about one order of magnitude larger than tensile strength. So “cluster logic” and “clump logic” were proposed (*Figure 2. 1*). The investigation of Cho [159] and Cundall [160] found that if combining the small balls together either as clump or cluster can effectively increase the particle interlocking and thus increase the compressive to tensile stress ratio in 2D simulations. However, there exist two main differences between clump and cluster. First, the most important difference is the particle rotation mechanism. Intra-cluster particles of a material have rotational velocities, while rotational velocities of particles in the clumped assembly are fixed as shown in *Figure 2. 1*. Only the clumped body itself can have rotational velocities. The second difference is that clump cannot break while cluster can break during the loading processes. For the experiments that performed in laboratories, aggregate breakage can be seen during the test. So from this point of view, compared with a clump, the cluster is more suitable to model aggregate behaviour in concrete

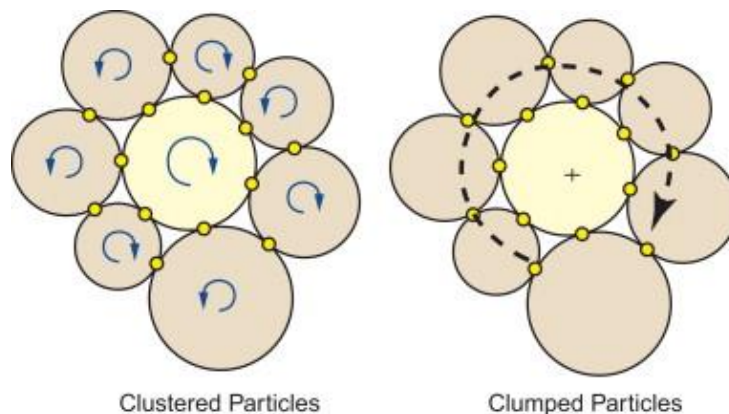


Figure 2. 1 Particle rotation mechanisms in clustered and clumped particles [159]

Another practice to simulate quasi-brittle response is by using appropriate contact models with

cementitious behaviour. In the existing literature by using modelling code PFC 2D, parallel bond model [152, 161, 162] or contact bond model [163, 164] are the most used contact models. The detail of these models will be presented in the later part (Section 2.4.3). These investigations are often focused on a specific mechanical behaviour of concrete and mainly paid more attention to the mechanical response only up to the peak load.

Nguyen et al. [165] used DEM method to model the three-point bending test of notched beam for soft rock and pointed out that although the parallel bond model could match the load - CMOD curve, it could not capture the softening behaviour as the contact cohesion was totally lost at the moment the contact strength was reached as showed in *Figure 2. 2*.

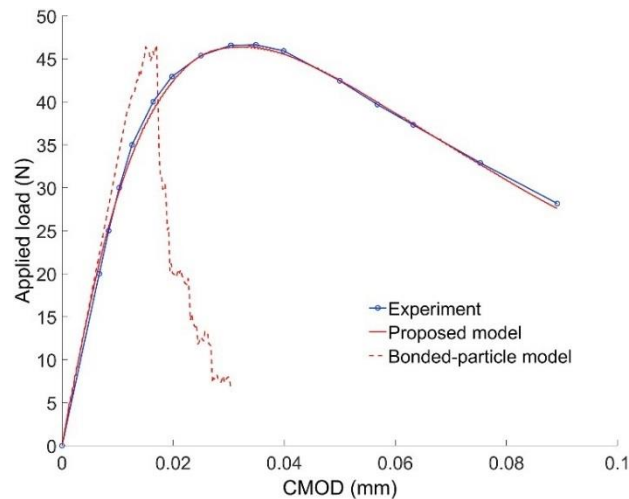


Figure 2. 2 Experimental and numerical load-CMOD results of three-point bending test [165]

Therefore, they proposed a damage-plasticity cohesive model for DEM as presented in *Figure 2. 3*. The modelling result was in accordance with the experiment when using the contact model proposed by Nguyen et al. [165].

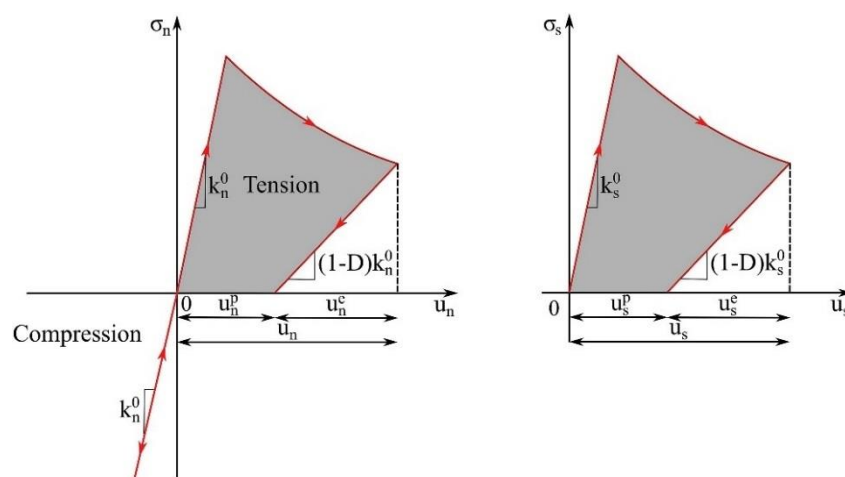


Figure 2. 3 The constitutive relationships in normal and shear directions of the model [165]

Kim et al. [130, 166-168] also employed an intrinsic linear softening model in DEM (*Figure 2. 4*) to study the fracture behaviour of asphalt concrete under compact tension test but no fracture

properties related to quasi-brittle materials were studied.

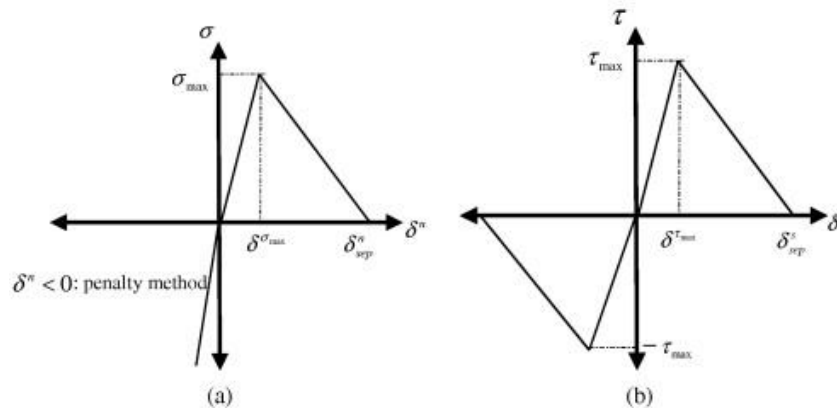


Figure 2. 4 Constitutive laws of cohesive zone model. (a) Normal. (b) Tangential [130, 166-168]

Similar with the model of Kim et al. [130, 166-168], Ma and Huang [169] modified the parallel bond model in the normal direction to obtain a displacement-softening contact model (Figure 2. 5) which was used to simulate the failure behaviours of quasi-brittle materials. The study illustrated the softening coefficient that defined in the model could satisfy the material compressive over tensile strength ratio.

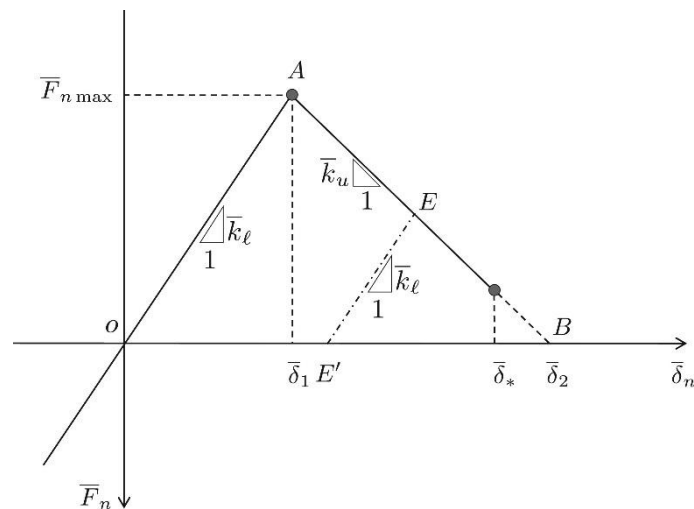


Figure 2. 5 Normal force-displacement contact law for the modified parallel bond [169]

Recently, Sinaie et al. [129] developed a cohesive bond model (Figure 2. 6) for concrete under cyclic loading. The model is more complex compared with others. In their study, the model performed well under cyclic loading, even though the material parameters were only calibrated against a monotonic stress-strain response.

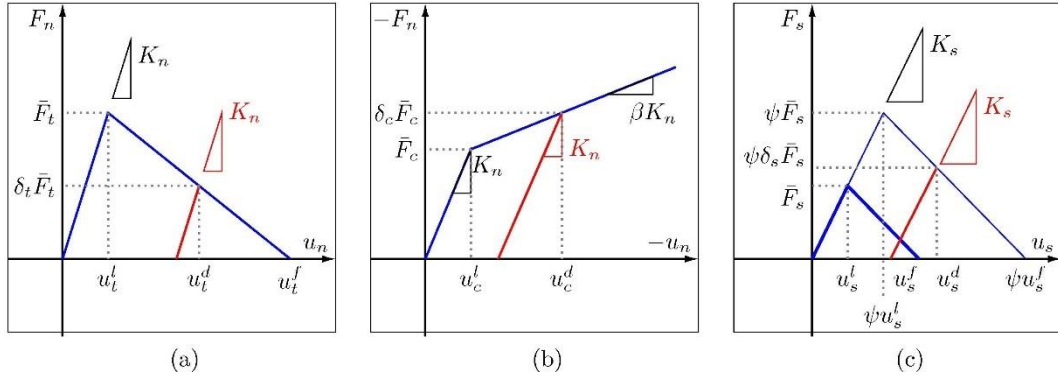


Figure 2. 6 Micro-mechanical damage models under (a) tension, (b) compression and (c) shear using the constant-stiffness formulation.

In DEM, most works in the literature are carried out to study the behaviours of rock and sand. Only a few literary works have been carried out so far for the modelling of brittle materials like concrete; a systematic study on how the contact models presented in the introduction section could improve the modelling for concrete, especially for its mechanical and fracture behaviour, is still lacking.

2.3 Theory of Discrete Element Method

The mechanical loop of DEM calculation processes is illustrated in Figure 2. 7. At every numerical iteration time step, the properties of a stressed assembly of rigid spherical particles are updated in DEM simulations. The contact forces between particles are calculated according to the force-displacement contact law models well-defined in DEM. Then the translational and rotational displacements of each particle are obtained by explicitly integrating the governing differential equations based on Newton's second law of motion. As all forces F_i acting on the particle i either from other particles, from boundaries or from external forces, are known, the equations can be expressed as Equation 2.1.

$$\begin{aligned}
 m_i \frac{d^2}{dt^2} x_i &= F_i + m_i g \\
 I_i \frac{d}{dt} \omega_i &= M_i
 \end{aligned}
 \tag{2.1}$$

With the mass m_i of particle i , its position x_i , the total force $F_i = \sum_c f_i^c$ acting on it due to contacts with other particles or with the walls, the acceleration due to volume forces like gravity g ; the spherical particles moment of inertia I_i , its angular velocity ω_i and the total torque $M_i = \sum_c (l_i^c \times f_i^c + q_i^c)$, where q_i^c are torques/couples at contacts other than due to a tangential force, e.g., due to rolling and torsion.

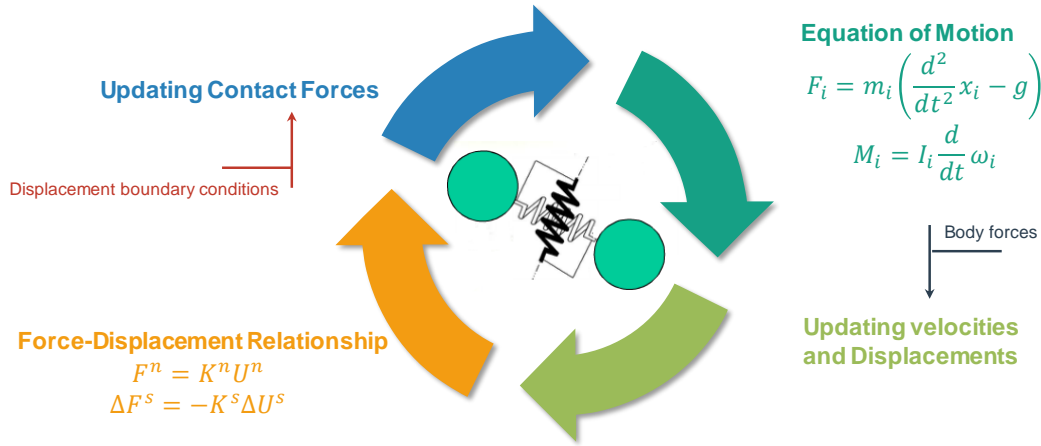


Figure 2. 7 The mechanical loop of DEM calculation processes [170]

So the interactions between particles are monitored at all contacts and the movement of each individual particle is traced. Among those codes that are used to apply DEM, the Particle Flow Code 2D (PFC 2D) which was developed by ITASCA is one of the widely used DEM code. In PFC 2D, two types of objects may be simulated in PFC 2D, “balls” and “walls”. Balls may either be spheres whose centroids lie in a plane or disks of a specified thickness. Walls are straight and rigid and interact only with balls, but not with each other.

Except for the aforementioned theory of DEM, some important assumptions are made in order to solve those equations: 1) Particles may be represented as rigid disks or balls; 2) Contacts (ball-ball and ball-wall) occur at a point; and 3) Particle overlap is allowed at contacts (soft-contact approach) but these overlaps are small relative to particle size.

Given these assumptions, the calculation cycle begins with determining the unit normal vector of the contacts in the assembly (the following derivation is after Itasca, 2014, but is included here for completeness):

$$n_i = \begin{cases} \frac{x_i^{[B]} - x_i^{[A]}}{d} & (\text{ball} - \text{ball}) \\ \frac{x_f - x_i^{[A]}}{d} & (\text{ball} - \text{facet}) \end{cases} \quad (2.2)$$

Where n_i is the normal vector, $x_i^{[A]}$ and $x_i^{[B]}$ are the locations of particle centres for particles A and B , respectively; x_f is the point on the wall facet that is closest to $x_i^{[A]}$, and d is the distance between particle centres or the distance between the centre of particle and the wall as can be expressed as Equation 2. 3.

$$d = \begin{cases} \|x_i^{[B]} - x_i^{[A]}\| & (\text{ball} - \text{ball}) \\ \|x_f - x_i^{[A]}\| & (\text{ball} - \text{facet}) \end{cases} \quad (2.3)$$

The overlap at contacts, U^n , may then be calculated as:

$$U^n = \begin{cases} R^{[A]} + R^{[B]} - d & (\text{ball-ball}) \\ R^{[A]} - d & (\text{ball-wall}) \end{cases} \quad (2.4)$$

Where $R^{[i]}$ is the radius of the ball i . The location of the contact point, $x_i^{[C]}$, may then be calculated and used to determine the relative distance between particles or distance between particle and wall facet:

$$x_i^{[C]} = x_i^{[A]} + \left(R^{[A]} - \frac{1}{2} U^n \right) n_i \quad (2.5)$$

Now that the contact location is known, it is straightforward to calculate velocities and invoke the constitutive relation for contact theory (linear or Hertz-Mindlin) to calculate normal and shear forces on each particle. First, particle forces are resolved into normal and shear components:

$$F_i = F_i^n + F_i^s \quad (2.6)$$

Where F_i is the total contact force vector and F_i^n and F_i^s are the normal and shear components, respectively.

Force in the normal direction is then calculated as:

$$F^n = K_n \cdot U^n \quad (2.7)$$

Where K_n is contact normal stiffness (secant modulus).

For the linear contact model, the two types of contact stiffness are assumed to act in series.

The contact normal stiffness is given by:

$$K_n = \frac{k_n^{[A]} k_n^{[B]}}{k_n^{[A]} + k_n^{[B]}} \quad (2.8)$$

Where the superscripts A , B denote two entities in contact.

To calculate shear forces, first the shear contact velocity, V^s , must be determined:

$$V^s = \left(\frac{d}{dt} x_i^{[\Phi^2]} - \frac{d}{dt} x_i^{[\Phi^1]} \right) t_i - \omega_i^{[\Phi^2]} \cdot \left| x_i^{[C]} - x_i^{[\Phi^2]} \right| - \omega_i^{[\Phi^1]} \cdot \left| x_i^{[C]} - x_i^{[\Phi^1]} \right| \quad (2.9)$$

Where ω_i is rotational velocity and $[\Phi^k]$ is used to denote either a wall or ball at the given contact as follows:

$$(\Phi^1, \Phi^2) = \begin{cases} (A, B) & (\text{ball-ball}) \\ (b, w) & (\text{ball-wall}) \end{cases} \quad (2.10)$$

The incremental shear force (ΔF^s) over a time increment (Δt) is calculated as:

$$\Delta F^s = -K_s V^s \Delta t \quad (2.11)$$

Where K_s is the tangent shear stiffness for the contact and is given by:

$$K_s = \frac{k_s^{[A]} k_s^{[B]}}{k_s^{[A]} + k_s^{[B]}} \quad (2.12)$$

Forces and moments for the particles are then updated as follows:

$$\begin{aligned} F^s &\leftarrow F^s + \Delta F^s \leq \mu \cdot F^n \\ F_i &= F^n \cdot n_i + F^s \cdot t_i \\ F_i^{[\Phi^1]} &\leftarrow F_i^{[\Phi^1]} - F_i \\ F_i^{[\Phi^2]} &\leftarrow F_i^{[\Phi^2]} - F_i \\ M_i^{[\Phi^1]} &\leftarrow M_i^{[\Phi^1]} - e_{ijk} \cdot \left(x_i^{[C]} - x_i^{[\Phi^1]} \right) \cdot F_i \\ M_i^{[\Phi^2]} &\leftarrow M_i^{[\Phi^2]} - e_{ijk} \cdot \left(x_i^{[C]} - x_i^{[\Phi^2]} \right) \cdot F_i \end{aligned} \quad (2.13)$$

Where μ is the friction coefficient at the contact; M_i is moment, and e_{ijk} is the permutation operator.

Note that there is only one rotational degree of freedom in two dimensions. The new particle forces and moments are used to calculate the new acceleration and angular momentum using the following relationships:

$$\begin{aligned} F_i &= m \cdot \left(\frac{d^2}{dt^2} x_i - g \right) \\ M_i &= \beta \cdot m \cdot R^2 \cdot \frac{d}{dt} \omega_i \end{aligned} \quad (2.14)$$

Where m is particle mass, g is acceleration due to gravity, and β is 0.4 for spheres and 0.5 for disks. The equations of motion (*Equation 2. 14*) are discretized and solved using central finite differences:

$$\begin{aligned} \frac{d^2}{dt^2} x_i^{[t]} &= \frac{1}{\Delta t} \left(\frac{d}{dt} x_i^{[t+0.5\Delta t]} - \frac{d}{dt} x_i^{[t-0.5\Delta t]} \right) \\ \frac{d}{dt} \omega_i^{[t]} &= \frac{1}{\Delta t} \left(\omega_i^{[t+0.5\Delta t]} - \omega_i^{[t-0.5\Delta t]} \right) \\ \frac{d}{dt} x_i^{[t+0.5\Delta t]} &= \frac{d}{dt} x_i^{[t-0.5\Delta t]} + \left(\frac{F_i^{[t]}}{m} + g \right) \cdot \Delta t \\ \omega_i^{[t+0.5\Delta t]} &= \omega_i^{[t-0.5\Delta t]} + \frac{M_i^{[t]}}{\beta \cdot m \cdot R^2} \cdot \Delta t \\ x_i^{[t+\Delta t]} &= x_i^{[t]} + \left(\frac{d}{dt} x_i^{[t+0.5\Delta t]} \right) \cdot \Delta t \end{aligned} \quad (2.15)$$

Where all terms are as previously defined.

The critical value of the time step (Δt) for a stable solution to a DEM problem depends on the minimum eigen period of the entire system. Calculating this value is computationally expensive, so PFC 2D uses a simplified spring and mass logic to calculate the time step and then applies a safety factor. A complete discussion of critical time step calculations is provided in Itasca [170].

2.4 Contact model in the Discrete Element Method

The constitutive model acting at a particular contact consists of three parts: a stiffness model, a slip model and a bonding model as shown in *Figure 2. 8*. The stiffness model provides an elastic relation between the contact force and relative displacement. The slip model enforces a relation between shear and normal contact forces such that the two contacting balls may slip relative to one another. The bonding model serves to limit the total normal and shear forces that the contact can carry by enforcing bond-strength limits. Normally there are two typical bond model given in PFC 2D called as built-in contact bond model, namely contact bond model and parallel bond model. However, when the bond models provided cannot meet material behaviours, users can define their own model in C++ language and insert into PFC 2D. All these models defined by users are called user-defined contact bond models. In the PFC 5.0, the stiffness model, slip model and bond model have been combined together. Here, the three models will be introduced separately.

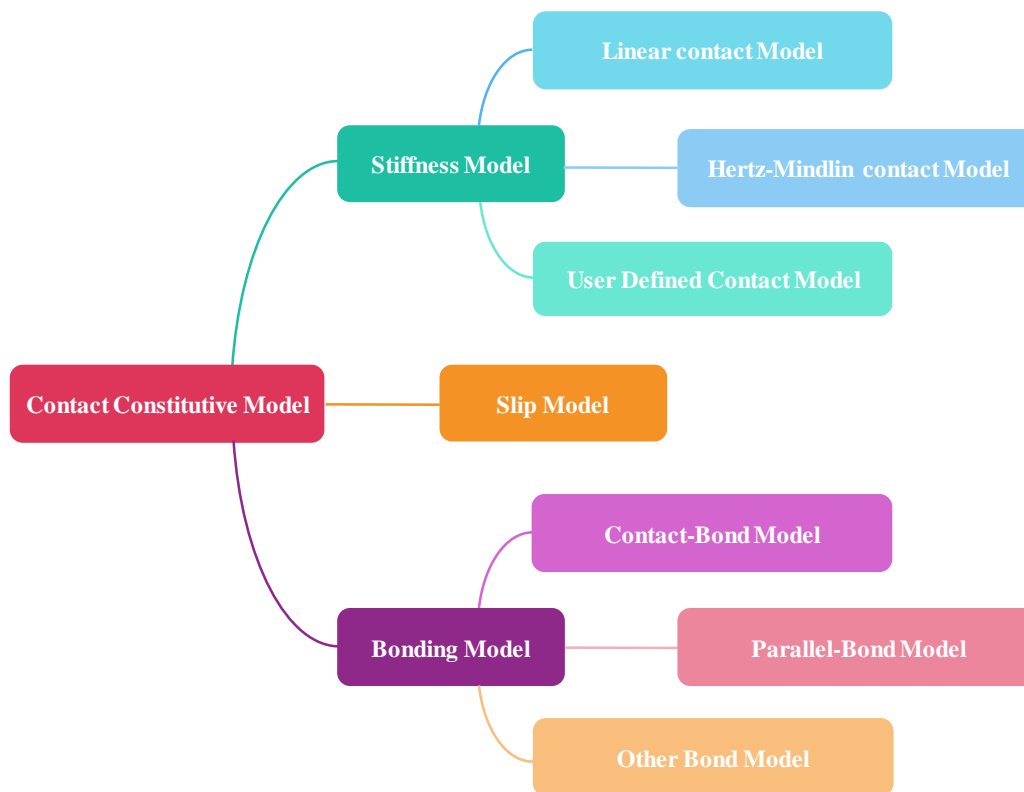


Figure 2. 8 Contact Constitutive Model

2.4.1 Stiffness Model

There are two types of basic models in PFC: the linear model and the nonlinear model. Linear models can be just simplified as a spring, while non-linear normal model usually refers to hertz model, which is more complicated.

For the linear contact model, each entity is given a constant normal and shear stiffness so that there is a linear relationship between the force and displacement. The total stiffness at contact then is

calculated by assuming the individual stiffness's work in series. The equations for normal tangent stiffness and shear tangent stiffness are given as *Equation 2. 8* and *Equation 2. 12*.

For both these equations A and B denote the two entities in contact. For the linear model, the normal secant stiffness, k_n , is equal to the normal tangent stiffness, since

$$k_n = \frac{dF^n}{dU^n} = \frac{d(K_n U^n)}{dU^n} = K_n \quad (2.16)$$

The Hertz-Mindlin contact model is one of the built-in options and is based on the model by Mindlin and Deresiewicz [171]. It is strictly applicable only to the case of spheres in contact. The only two input parameters are the shear modulus G and the Poisson's ratio ν of the particles in contact. The normal and shear stiffness are calculated as:

$$\begin{aligned} K_n &= \alpha_h \left(\frac{2G\sqrt{2R}}{3(1-\nu)} \right) (U^n)^{\alpha_h-1} \\ K_s &= \frac{2(1-\nu)}{2-\nu} \alpha_h \left(\frac{2G\sqrt{2R}}{3(1-\nu)} \right) (F_i^n)^{(\alpha_h-1)/\alpha_h} \end{aligned} \quad (2.17)$$

Here F^n and U^n are the normal force and particle overlap as defined before, respectively; α_h is a non-dimensional exponent and default value is 1.5; G , ν and R are the effect shear modulus, Poisson's ratio, and contact radius, respectively.

For the Hertz model, the normal-secant stiffness, k_n , is related to the normal-tangent stiffness by the relation:

$$k_n \equiv \frac{dF^n}{dU^n} = \frac{3}{2} K_n \quad (2.18)$$

2.4.2 Slip Model

This model allows slip, due to friction. The maximum allowable shear contact force is calculated:

$$F_{\max}^s = \mu |F_i^n| \quad (2.19)$$

If $|F_i^s| > F_{\max}^s$ then slip is allowed to occur (during the next calculation cycle) by setting the magnitude of F_i^s equal to F_{\max}^s via:

$$F_i^s \leftarrow F_i^s \left(\frac{F_{\max}^s}{|F_i^s|} \right) \quad (2.20)$$

The slip friction model is an intrinsic property of the two entities in contact (ball-ball or ball-wall) that governs frictional sliding of unbonded or debonded particles. The slip and bond model describe the constitutive behaviour governing the response of particle contact points. The slip model is defined by the friction coefficient at the contact. For bonded assemblies, if the applied force becomes larger than the maximum allowable shear contact force, then slip is allowed to occur.

2.4.3 Bond Model

PFC 2D allows particles to be bonded together at contacts. The two basic bonding models supported in PFC 2D are contact-bond model and parallel-bond model. Bonds can only be formed between particles and not between particles and walls. Once a bond is formed at a contact between two particles, the contact will remain intact until the bond is broken. The bond will be broken when the normal or shear force in the bond exceed the maximum allowable force. According to O’Sullivan [172], Scanning electron microscope (SEM) images show that the microstructure of cemented sands has a finite contact area in the contact surface. The contact force within this area would result in a resistance against moment acting on the particles. Therefore, parallel bond contact is thus introduced in DEM to overcome the lack of resistance at the moment at the contact. In the parallel bond model, not only the contact normal force and shear force could be transmitted, which is the same as the above contact bond model, but also the moments between particles can be transmitted. In this aspect, the parallel bond model seems suitable for cementitious materials.

In previous studies, Zhou et al. [162] used parallel bond model successfully to model the breakage mechanism of microcapsules in concrete. Murali et al. [173] also investigated the strength and size effect in concrete under tension by parallel bond model. Thus parallel bond model seems to be a suitable contact model for modelling the behaviours of concrete. The parallel-bond model describes the constitutive behaviour of a finite-sized piece of cementitious material deposited between two balls as shown in *Figure 2. 9*.

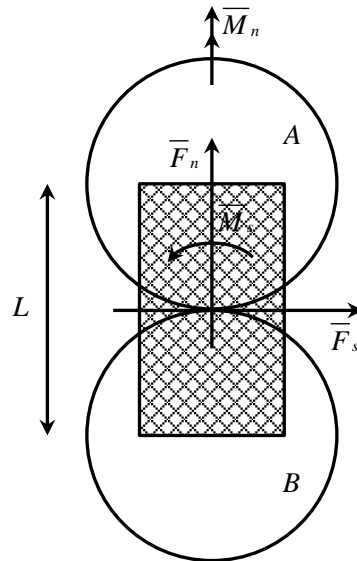


Figure 2. 9 Parallel bond illustration

To define parallel bond, five parameters are required: normal and shear stiffness per unit area \bar{k}_n and \bar{k}_s ; tensile and shear strength $\bar{\sigma}_t$ and $\bar{\tau}_s$; and bond-radius multiplier, λ , which defines the bond radius $\bar{R} = \lambda \min(R_A, R_B)$, with R_A and R_B being the radii of the bonded particles. The force and moment increments occurring over a time step of Δt in 2D are calculated by:

$$\begin{cases} \Delta \bar{F}_n = -\bar{k}_n A \Delta U_n \\ \Delta \bar{F}_s = -\bar{k}_s A \Delta U_s \end{cases} \quad (2.21)$$

and

$$\begin{cases} \Delta \bar{M}_n = 0 \\ \Delta \bar{M}_s = -\bar{k}_n I \Delta \theta_s \end{cases} \quad (2.22)$$

Where \bar{F}_n , \bar{F}_s and \bar{M}_n , \bar{M}_s are the contact forces and moments at the centre of the contact zone respectively in the normal (n) and shear (s) directions; U_n , U_s and θ_s are the relative displacements and rotations between the two bonded particles respectively in the normal (n) and shear (s) directions; A and I are the area and moment of inertia, determined by:

$$\begin{cases} A = 2\bar{R}t \\ I = \frac{2}{3}t\bar{R}^3 \\ t = 1 \end{cases} \quad (2.23)$$

The normal bond stiffness \bar{k}_n is in relation with bond modulus \bar{E}_c as follows:

$$\bar{k}_n = \frac{\bar{E}_c}{L} \quad (2.24)$$

$$L = \begin{cases} R_A + R_B & \text{ball-ball} \\ R_A & \text{ball-facet} \end{cases} \quad (2.25)$$

The maximum tensile and shear stresses, $\bar{\sigma}_{\max}$ and $\bar{\tau}_{\max}$, acting on the parallel bond periphery are calculated using the beam theory as follows:

$$\begin{cases} \bar{\sigma}_{\max} = \frac{\bar{F}_n}{A} + \frac{\bar{M}_s \bar{R}}{I} \\ \bar{\tau}_{\max} = \frac{\bar{F}_s}{A} \end{cases} \quad (2.26)$$

As aforesaid, a parallel bond model approximates the physical behaviour of a cement-like material combining the two adjacent particles. The bond acts like a beam that resists the moment induced by particle rotation or shearing within the bonded area. If $\bar{\sigma}_{\max} \geq \bar{\sigma}_t$ or $\bar{\tau}_{\max} \geq \bar{\tau}_s$, the bond breaks by tension or shear and the bond along with its forces, moments and stiffness is then removed from the model and the model is updated at each calculation as shown in *Figure 2. 10*.

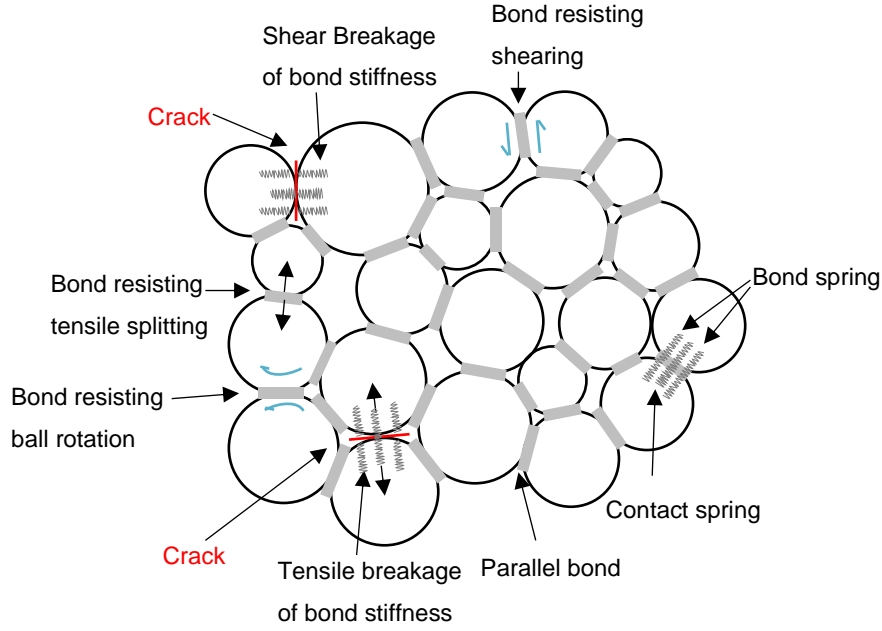


Figure 2. 10 Illustration of the parallel bond model breakage [174]

2.5 Stress measurement

In a DEM model, the term “stress” refers to the average stress in a specific volume since it is, in fact, a quantity in the continuum theory and does not exist at each point in an assembly of discrete particles. Newton Second’s Law and Force-Displacement Law act only between particles at the microscale. Thus, it is necessary to convert the particle behaviour at the micro level to a continuum term using an average process. Measurement circles are used to define local volumes so that a number of quantities such as the porosity, coordination number and stress can be calculated within the volume. The stress distribution in an assembly can be obtained by defining a number of measurement circles at different locations in the assembly and calculating the average stress in each measurement circle. The average stress tensor in a volume V is defined by:

$$\bar{\sigma}_{ij} = \frac{1}{V} \int_V \sigma_{ij} dV \quad (2.27)$$

Where $\bar{\sigma}_{ij}$ is average stress tensor; σ_{ij} is stress tensor acting throughout the volume V .

For a particulate material, stresses exist only in particles, thus above formulation can be replaced by:

$$\bar{\sigma}_{ij} = \frac{1}{V} \int_{Np} \bar{\sigma}_{ij}^p V^p \quad (2.28)$$

Where $\bar{\sigma}_{ij}^p$ is the average stress tensor in particle p ; Np is the number of particles; V^p is the volume of particle p .

Assuming the stress in each particle is continuous and in equilibrium, the average stress tensor in a particle can be written as:

$$\bar{\sigma}_{ij}^p = -\frac{1}{V^p} \sum_{Nc} x_i^c F_j^c = -\frac{1}{V^p} \sum_{Nc} |x_i^c - x_i^p| n_i^{c,p} F_j^c \quad (2.29)$$

Where x_i^c , F_j^c and x_i^p are the location, force at contact c and location of particle p respectively; $n_i^{c,p}$ is the unit-normal vector directed from the particle centroid to the contact location, and is a function of both the contact and particle.

A correction factor C is needed to compute the average stress when applying the above formulations because only the particles with centroids contained within the measurement circle are considered in the above computation process.

$$C = \frac{1-n}{\sum_{Np} V^p} V_m \quad (2.30)$$

Where n is porosity of the assembly; Np is number of particles; V_p is volume of particle p ; V_m is volume of the measure circle.

Applying Equation 2. 29 and 2. 30 to Equation 2. 28, the expression of the average stress can be obtained:

$$\bar{\sigma}_{ij} = -C \sum_{Np} \sum_{Nc} |x_i^c - x_i^p| n_i^{c,p} F_j^c \quad (2.31)$$

Where x_i^c , F_j^c and x_i^p is location, force at contact c and location of particle p respectively; $n_i^{c,p}$ is unit-normal vector directed from the particle centroid to the contact location; C is correction factor; Np is number of particles; Nc is number of contacts.

2.6 Strain rate measurement

Because the velocity field in voids of an assembly is non-zero, the strain rate cannot be expressed as an average strain rate directly in terms of the velocity field. Instead, a strain-rate tensor based on a best-fit procedure is determined, which can minimize the error between the predicted and measured velocity of all balls within the measurement circle. A velocity-gradient tensor α_{ij} is referred to the strain-rate tensor for a given measurement circle:

$$\begin{aligned} \alpha_{ij} &= e_{ij} - \omega_{ij} \\ e_{ij} &= \frac{1}{2} (v_{i,j} + v_{j,i}) \\ \omega_{ij} &= \frac{1}{2} (v_{j,i} - v_{i,j}) \end{aligned} \quad (2.32)$$

Where α_{ij} is strain rate tensor; e_{ij} is rate-of-deformation tensor; ω_{ij} is spin tensor; $v_{i,j}$ is velocity gradient.

The predicted relative velocity can be written as

$$\begin{aligned} \tilde{v}_i^{[p]} &= \dot{\alpha}_{ij} x_j^{[p]} \\ x_i^{[p]} &= x_i^{[p]} - \bar{x}_i \end{aligned} \quad (2.33)$$

Where $x_i^{[p]}$ is the central location of the particle p ; \bar{x}_i is mean position of the Np particles in the measurement circle, $\bar{x}_i = \frac{\sum_{Np} x_i^{[p]}}{Np}$.

The error for the predicted value is given by:

$$SS = \sum_{Np} \left| \tilde{v}_i^{[p]} - V_i^{[p]} \right|^2 = \sum_{Np} \left(\tilde{v}_i^{[p]} - V_i^{[p]} \right) \left(\tilde{v}_i^{[p]} - V_i^{[p]} \right) \quad (2.34)$$

Where SS is the sum of the square of the deviation between predicted and measured velocities. $\tilde{v}_i^{[p]}$ is predicted the relative velocity of particle p ; $V_i^{[p]}$ is measured relative velocity of particle p ; Np is number of particles within the measurement sphere.

The condition for minimum SS is that:

$$\frac{\partial SS}{\partial \dot{\alpha}_{ij}} = 0 \quad (2.35)$$

Substituting Equation 2. 34 into Equation 2. 35 and differentiating, the following set of four equations is obtained.

$$\begin{bmatrix} \sum_{Np} x_1^{[p]} x_1^{[p]} & \sum_{Np} x_2^{[p]} x_1^{[p]} \\ \sum_{Np} x_1^{[p]} x_2^{[p]} & \sum_{Np} x_2^{[p]} x_2^{[p]} \end{bmatrix} \begin{Bmatrix} \dot{\alpha}_{i1} \\ \dot{\alpha}_{i2} \end{Bmatrix} = \begin{Bmatrix} \sum_{Np} V_i^{[p]} x_1^{[p]} \\ \sum_{Np} V_i^{[p]} x_2^{[p]} \end{Bmatrix} \quad (2.36)$$

These four equations are solved by performing a single LU-decomposition upon the 2×2 coefficient matrix and performing two back-substitutions for the two different right-hand sides obtained by setting $i = 1$ and then 2. In this way, all four components of the strain-rate tensor are obtained.

2.7 Parallel bond model for the behaviour of the cementitious material

Generally, concrete can be considered as a three-phase composite, namely matrix (or mortar), interface and aggregate. The cementitious phase is the mortar which bonds the aggregate particles together. Generally, the fracture in concrete is also initiated in the mortar. Therefore, in order to check whether the parallel bond model is suitable for modelling the behaviours of concrete, the behaviours of mortar need to be determined first. Hence, the results of the compression test and the direct tension test for mortar are taken [175]. Numerical simulations are performed in 2D. Based on a previous study [176], the behaviours of the specimen are greatly affected by particle size, when it is relatively large ($L/R < 80$). The particle size cannot be chosen too small, because of the computational limitations. Thus, the particle radius used in the modelling of mortar was ranging from 0.5 mm to 0.75 mm. The density of particles was given as 2100 kg/m^3 as the same density of mortar measured from the experiment. A local damping coefficient of 0.7 was used, which is commonly used for mortar and concrete. The high damping coefficient was used to ensure a quasi-static loading condition [177]. The applied loading rate in the test should be given sufficiently low to ensure the specimen remains in quasi-static equilibrium throughout the test. As aforesaid, PFC 2D is based on Newton's second law. To ensure the computed solution produced by the model remains stable, the time step (Δt) in each

calculation cycle should not exceed a critical time step that is related to the minimum eigen period of the total particle assembly. Hence the critical time step is controlled by the stiffnesses, densities, and geometry of the particles. The critical time step is computed first and a reasonable time step is assigned before each cycle. Taking the time step equal to $1e^{-8}$ s/step for example. 0.2 m/s can be translated to $2e^{-6}$ mm/step, implying that it requires 500,000 steps to move the loading plate for 1 mm. This loading velocity is in the range of 0.016 - 0.2 m/s used by different researchers and selecting a lower loading velocity will result in essentially no difference for the simulation results [178]. Considering the calculation time and based on the previous studies [155, 177, 179, 180], a loading rate of 0.01 m/s was adopted for compression test and direct tension test in this study. Micro parameters (E_c (\bar{E}_c), k_n/k_s (\bar{k}_n/\bar{k}_s), $\bar{\sigma}_t$, \bar{C} , and ϕ) for mortar obtained through the calibration process are listed in *Table 2. 1*. Note that the calibrated values obtained bear no resemblance to mortar macro properties. Finally, the samples with 1137 particles for 40×40 mm² (compression) specimen; and with 35029 particles for 110×450 mm² (direct tension) specimen are generated respectively as shown in *Figure 2. 11*. For the direct tension test, some particles at the top and bottom of mortar specimen are clumped together to simulate the steel plates in the loading machine.

Table 2. 1 Micro parameter obtained through the calibration process

Micro Parameters	Value	Micro Parameters	Value
Minimum particle diameter d_{\min} (mm)	0.5	Radius multiplier λ	1.0
Ratio of maximum to minimum particle diameter d_{\max}/d_{\min}	1.5	Ratio of normal to shear bond stiffness \bar{k}_n/\bar{k}_s	3.0
Effective modulus E_c (GPa)	31.4	Effective bond modulus \bar{E}_c (GPa)	31.4
Ratio of normal to shear stiffness k_n/k_s	3.0	Moment contribution factor β_1	1.0
Friction angle ϕ (°)	0	Tensile strength $\bar{\sigma}_t$ (MPa)	32.7
Maximum shear strength multiplier γ	1.0	Residual friction angle ϕ_r (°)	26.6
Cohesion strength \bar{C} (MPa)	32.7		

The computational models either discrete or continuum approach experience difficulties to describe mechanical and fracture phenomena occurring in mortar and concrete. The complexity is often in determining the link between laboratory test data at structural scale and computational parameters of the constitutive behaviour at the material local level. Several investigations have been carried out with respect to the problem of extracting intrinsic material properties (model parameters), however, the main issues remain the assessment of the uniqueness of the estimated parameter set, the experimental data needed for the well-posedness of the inverse problem (global and/or local data) and the predictive capabilities of the calibrated model. Another issue of objectivity of micro parameters arises in DEM due to arbitrarily size particles used for modelling, which makes the determination of micro parameters very challenging. In most cases, a try-and-error method is used for the calibration procedures for a given loading condition, but the method is time-consuming and gives a non-unique estimation. In this study, based on simple experimental tests on mortar and concrete, model parameters are identified for each phase of concrete taking use of the inverse problem given below.

Firstly, the micro parameters need to be calibrated are assembled in a vector x and given the initial values x_{ini} , then the corresponding counterpart $y_{comp}(x_{ini})$ can be computed by DEM and the

error $e(x_{ini})$ between numerical vector $y_{comp}(x_{ini})$ and experimental vector y_{exp} can be calculated by the minimization of the objective function;

$$f(x_{ini}) = ((y_{exp} - y_{comp}(x_{ini})), x_{ini}) = (e(x_{ini}), x_{ini}) \quad (2.37)$$

Next, a new vector x_{new} can be obtained and put this new vector to the numerical model to the next cycle is started. When the function $f(x)$ is minimized, the suitable microparameters used for DEM are obtained. The minimization of the function $f(x)$ is performed by using the Levenberg-Marquardt (LM) algorithm [181, 182], which is also known as the damped least-squares method. The LM algorithm is a modification of the Gauss-Newton method, which is based on a local linearization of the residuals.

$$r_m(x + \delta x) \approx r_m(x) + J_{m\mu} \delta x^\mu \quad (2.38)$$

Where J is the Jacobian matrix; x is the vector of unknown parameters; r is an M -dimensional nonlinear vector function of N parameters, x , where $M \geq N$. The Gauss-Newton method then iterates according to

$$\delta x = -(J^T J)^{-1} \nabla C = -(J^T J)^{-1} J^T r \quad (2.39)$$

The Gauss-Newton method will usually converge quickly if it begins sufficiently near a minimum of C . While in order to solve the problem that $J^T J$ is often ill-conditioned, Levenberg and Marquardt suggested damping the $J^T J$ matrix by a diagonal cut-off. Therefore, LM algorithm steps according to

$$\delta x = -(J^T J + \chi D^T D)^{-1} \nabla C \quad (2.40)$$

Where $D^T D$ is a positive-definite, diagonal matrix representing the relative scaling of the parameters and χ is a damping parameter adjusted by the algorithm. Where small values of the algorithmic parameter result in a Gauss-Newton update and large values of χ the result in a gradient descent update. The parameter χ is initialized to be large so that first updates are small steps in the steepest descent direction.

For DEM modelling, many micro parameters need to be determined, while these parameters are difficult to obtain. Consequently, in order to reduce the time for parameters determination processes, the initial normal stiffness k_n and shear stiffness k_s for calibration process can be roughly calculated from Young's modulus and Poisson's ratio by *Equations 2. 41* and *2. 42* [168].

$$k_n = \frac{E}{\sqrt{3}(1-\nu)} \quad (2.41)$$

$$k_s = \frac{E(1-3\nu)}{\sqrt{3}(1-\nu^2)} \quad (2.42)$$

Where E is Young's modulus and ν is Poisson's ratio of mortar respectively.

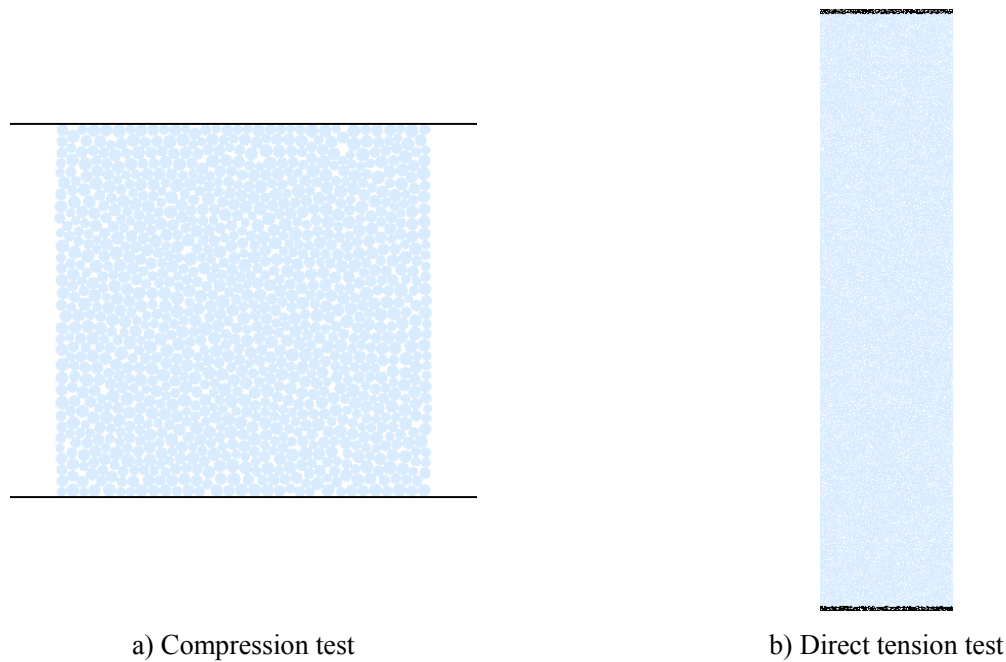


Figure 2. 11 Specimens for calibration procedures

Table 2. 2 Comparison between laboratory tests and modelling results using parallel bond model

Mechanical Properties	Mortar	
	Laboratory tests	Modelling Results
Compressive strength (σ_c) (MPa)	50.0±0.88	49.8
Young's modulus (E) (GPa)	24.0±1.30	24.0
Poisson's ratio (ν)	0.3±0.64	0.28
Direct tensile strength (σ_t) (MPa)	2.0±0.1	9.59

As shown in Table 2. 2, the micro-parameters of the parallel bond model could not satisfy both compressive strength and tensile strength simultaneously. The tensile strength is extremely higher when compared with the experimental results. The results of Diederichs [156] showed that when the model is calibrated to match the UCS experiment of rock, the tensile strength of rock is significantly overestimated. Before Diederichs, Potyondy [157] and Schopfer [158] also got similar results when simulating brittle rock. As pointed out in [152], the inserted contact models for concrete modelling only calibrated to match the uniaxial compression test, the use of these models to perform tensile fracture propagation was only qualitative. The reason is that the tensile strength and compressive strength are increased at the same time with the increase of bond tensile strength ($\bar{\sigma}_t$). While for the brittle materials like rock and concrete, the compressive strength is about one order of magnitude larger than tensile strength. As a result, the micro parameter $\bar{\sigma}_t$ for compressive strength is also about one order of magnitude larger than tensile strength. Therefore, the classical parallel bond model becomes no longer suitable for the simulation of brittle material with low tensile to compressive strength (σ_t/σ_c) material, like rock and concrete.

2.8 Modified Parallel Bond Model

2.8.1 Description of contact model

Aforementioned, the parallel bond contact model cannot meet overall mechanical behaviours of material like mortar and concrete with high compressive to tensile strength ratio. So, the parallel bond model cannot apply to the cementitious material directly. It is due to the reason that in the generic formulation of the parallel bond (*Equation 2. 26*) the full contribution of moments to maximum contact stresses is considered and constant normal and shear strengths are used without considering their inter-dependence. This limitation can be overcome by introducing a new parameter β_1 to control the contribution of moments to the maximum normal and shear contact stresses [183], as expressed below:

$$\begin{cases} \bar{\sigma}_{\max} = \frac{\bar{F}_n}{A} + \beta_1 \frac{\bar{M}_s R}{I} \\ \bar{\tau}_{\max} = \frac{\bar{F}_s}{A} \end{cases} \quad (2.43)$$

Where $\bar{\sigma}_{\max}$, $\bar{\tau}_{\max}$, \bar{F}_n , \bar{F}_s , \bar{M}_n and \bar{M}_s are as defined earlier; and β_1 is ranging from 0 to 1. When β_1 equals to 1 i.e. full contribution, *Equation 2. 43* reduces to *Equation 2. 26* of the default contact model.

It is also assumed that the shear strength follows the Coulomb criterion which is according to [183] as shown in *Figure 2. 12*. The shear strength is determined by:

$$\begin{cases} \bar{\tau}_s = \sigma_n \tan \phi + \bar{C} & \text{if } \sigma_n \tan \phi < (\gamma - 1) \bar{C} \\ \bar{\tau}_s = \gamma \bar{C} & \text{if } \sigma_n \tan \phi \geq (\gamma - 1) \bar{C} \end{cases} \quad (2.44)$$

Where σ_n is the normal contact stress; \bar{C} is the cohesion strength; ϕ is the friction angle and γ is the parameter that determines the ratio of the maximum shear strength over the cohesion strength.

After shear failure, the cohesion is set to zero and the frictional angle can decrease to residual angle ϕ_r and the shear strength is determined by:

$$\bar{\tau}_s = \sigma_n \tan \phi_r \quad (2.45)$$

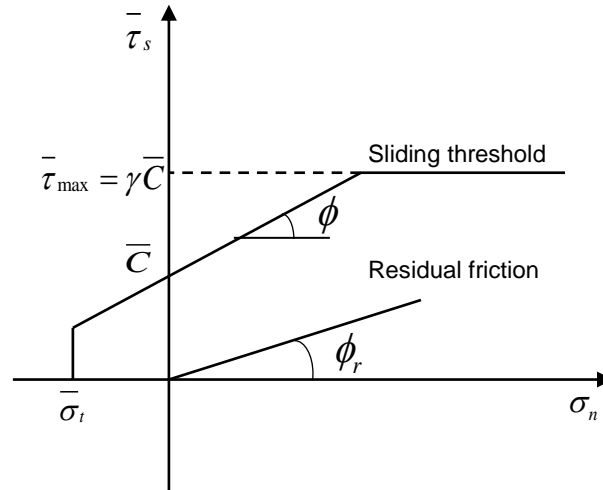


Figure 2. 12 Shear strength criterion

Thus, the new contact model contains the following microscopic parameters:

$$\lambda, \bar{E}_c, \bar{k}_n/\bar{k}_s, \bar{C}, \bar{\sigma}_t, \beta_1, \gamma, \phi, \phi_r$$

The effects of each parameter on the ratio of UCS/T can be seen in the paper [183].

2.8.2 Validation of new contact model

The calibration procedures for mortar are now by using the new modified contact model. The micro parameters obtained through the inverse calibration scheme (already presented) are given in Table 2. 3.

Table 2. 3 Micro parameters obtained through the calibration process

Micro Parameters	Value	Micro Parameters	Value
Minimum particle diameter d_{\min} (mm)	0.5	Radius multiplier λ	1.0
Ratio of maximum to minimum particle diameter d_{\max}/d_{\min}	1.5	Ratio of normal to shear bond stiffness \bar{k}_n/\bar{k}_s	1.77
Effective modulus \bar{E}_c (GPa)	22.1	Effective bond modulus \bar{E}_c (GPa)	22.1
Ratio of normal to shear stiffness k_n/k_s	1.77	Moment contribution factor β_1	0.1
Friction angle ϕ (°)	0	Tensile strength $\bar{\sigma}_t$ (MPa)	5.0
Maximum shear strength multiplier γ	1.0	Residual friction angle ϕ_r (°)	26.6
Cohesion strength \bar{C} (MPa)	38.1		

The comparison between the experimental results and modelling results obtained from calibrated parameters are listed in Table 2. 4.

Table 2. 4 Comparison of laboratory tests and modelling results

Mechanical Properties	Mortar	
	Laboratory tests	Modelling Results
Compressive strength (σ_c) (MPa)	50.0±0.88	49.9
Young's modulus (E) (GPa)	24.0±1.30	24.0
Poisson's ratio (ν)	0.3±0.64	0.33
Tensile strength (σ_t) (MPa)	2.0±0.1	2.06
Tensile maximum displacement (μm)	29.0±2.8	28.3

Table 2. 4 demonstrates that the new approach can satisfy compressive, tensile/bending behaviour of mortar using the same microscopic parameters. Therefore, this approach can be easily used to model the complex behaviour of mortar under multi-axial loadings. The failure patterns of the sample are given in Figure 2. 13. The failure patterns show a correct description of the fracture process in each test when compared with the experiments.

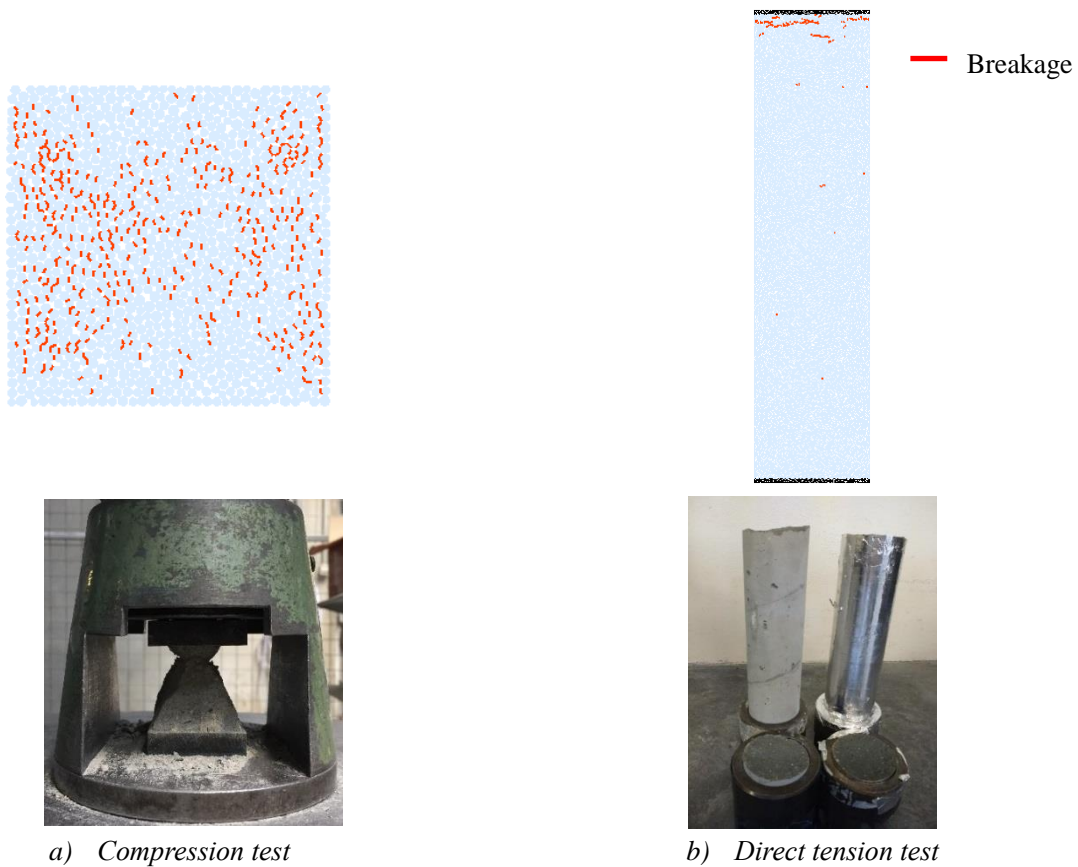


Figure 2. 13 Failure patterns for each calibration mortar sample

2.8.3 Application to concrete: microstructure description and mechanical behaviour

Concrete is a highly complex and heterogeneous composite material. The comprehensive and correct description of concrete behaviour through a macroscopic constitutive law is a difficult task

due to the heterogeneous microstructure. Mesoscopic modelling is an efficient way to describe the heterogeneous microstructure where concrete is considered as a three-phase material: Mortar, Aggregate and Interfacial Transition Zone (ITZ). Thus, it triples the microscopic parameters need to be determined for concrete. However, some estimation of the elastic properties can be made from the literature review. According to the results of Mondal [184], Young's modulus of ITZ is about 70 % - 85 % of that of bulk paste, thus parameters of ITZ can be obtained from that of mortar. In this section, normal concrete studied by Saliba [37] is considered; the mix design is presented in *Table 2. 5*.

Table 2. 5 Mortar mix design details (kg/m³)

w/c	Cement	Sand	Water	Sp
0.56	350	780	219.5	1.9

The microparameters like Young's modulus, stiffness ratio, normal strength and cohesive strength of ITZ are taken as 50 % of mortar. The elastic properties of aggregates can also be known based on the mineral composition e.g. Young's modulus of limestone is in the range of 22 - 55 GPa [52]. Therefore, the parameters for mortar need to be determined first using the approach already presented in the previous section. Experiments on equivalent mortar with same properties to that mortar in concrete [37] are used to determine micro parameters of mortar. Thus the only remaining micro parameters (E_c (\bar{E}_c), k_n/k_s (\bar{k}_n/\bar{k}_s), $\bar{\sigma}_t$, \bar{C} and ϕ) need to be determined were of coarse aggregates. The compressive strength, Young's modulus and Brazilian strength on cylindrical specimen $\phi 110 \times 220$ mm² are used as target values in the calibration. The calibrated micro parameters for aggregate are given in *Table 2. 6*.

Table 2. 6 Parameters determined for ITZ and aggregates

Micro Parameters	ITZ	Coarse aggregate
Effective modulus E_c (GPa)	/	44.2
Normal to shear stiffness ratio k_n/k_s	/	1.4
Radius multiplier λ	1.0	1.0
Friction angle ϕ (°)	18.0	18.0
Effective bond modulus \bar{E}_c (GPa)	11.1	44.2
Ratio of bond normal to shear stiffness \bar{k}_n/\bar{k}_s	1.0	1.4
Moment contribution factor β_1	0.1	0.1
Tensile strength $\bar{\sigma}_t$ (MPa)	2.3	15.5
Cohesion strength \bar{C} (MPa)	21.5	118.5
Maximum shear strength multiplier γ	1.0	1.0
Residual friction angle ϕ_r (°)	26.6	26.6

2.8.3.1 Generation of mesostructure: behaviour, form, and classes of aggregates

The key point for mesoscopic modelling of concrete is to consider the behaviour of aggregates in the local and overall response. In discrete element modelling, there are many ways to model the coarse aggregates, like using single particle [161] acting as aggregate or using a clump of unbreakable

bonded rigid particles [185] or cluster [152] particles. Single circular particles are unrealistically easy to rotate after the bonds with the matrix are broken and this behaviour affects the overall response of the specimen. Clump act similar to single particles and also it does not allow aggregate rupture when the local stresses are too high. In this study, cluster particles were adopted to model coarse aggregates. A cluster is defined as a set of particles that are bonded to one another (*Figure 2. 1*) and intra-cluster particles have rotational velocities. Using clusters to form irregular grain shapes in DEM specimens can also overcome the problem of easy particle rotation.

The shape of the aggregates is simply modelled as a circle. In order to simplify the generation process, a procedure to classify the coarse aggregate and the bulk matrix were developed. Namely, the coarse aggregates are firstly generated randomly using a Matlab program so that the information of coarse aggregates can be recorded. The main function of Matlab was to classify the bulk matrix particles and coarse aggregate particles. After achieving these steps, the information was imported into DEM software to classify the coarse aggregate particles. Finally, the coarse aggregate particles were bonded together. The procedures are illustrated in *Figure 2. 14*.

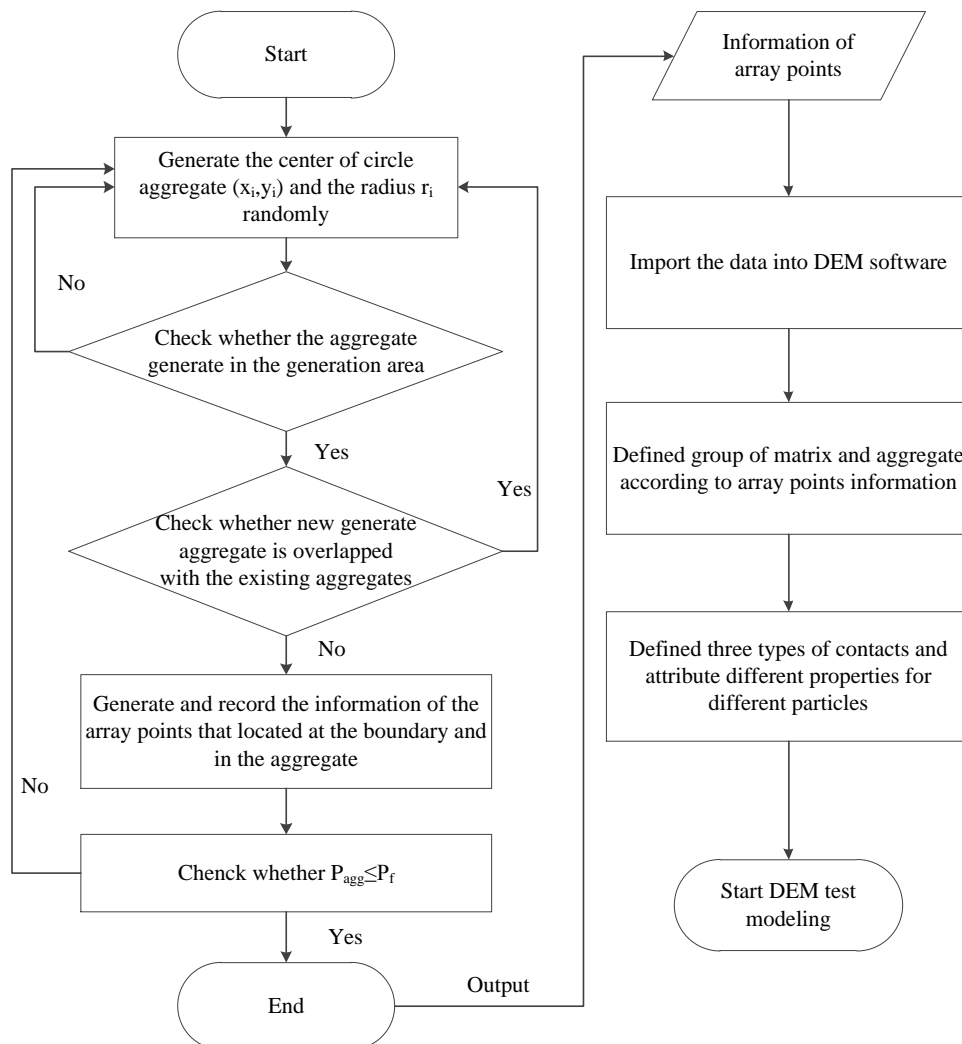


Figure 2. 14 Combination of Matlab and DEM to generate coarse aggregates in a specimen

In order to generate the mesostructure, the spatial distribution of aggregate cluster particles is carried out randomly in the matrix on the basis of a stochastic-heuristic algorithm. Overlapping was not allowed and the aggregates are placed one by one from the largest to the smallest. The size distribution of the aggregates follows the aggregate grading curve of the concrete studied. Comparison of experimental [175] and numerical aggregate distribution is provided in *Figure 2. 15* and *Table 2. 7*. Five classes of aggregates are generated accounting for about 37 % of the total volume of concrete.

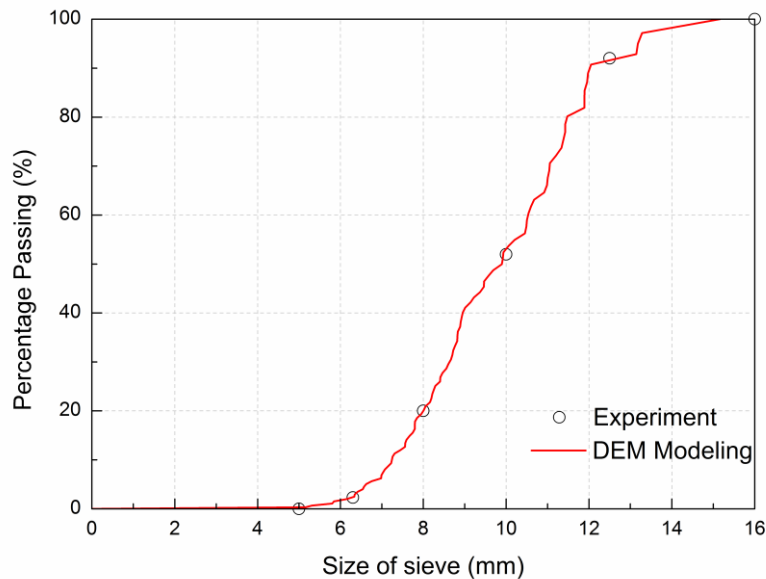


Figure 2. 15 Grading curve of coarse aggregate

Table 2. 7 The coarse aggregate size distribution of concrete

$\Phi(\text{mm})$	5-6.3	6.3-8	8-10	10-12.5	12.5-16.0
$V_f(\%)$ Experiment	3.0	7.0	11.0	14.0	2.0
$V_f(\%)$ Modelling	2.9	7.1	11.0	14.1	1.9

2.8.3.2 Generation of the specimen

For compression test, 17118 particles are directly generated inside the rectangular specimen area. However, in order to generate a Brazilian test specimen in 2D, common practice is to first generate a square sample, particles are then inserted and finally trimming is performed to form a circle. In this way, the circumference of the specimen does not remain smooth, which means when loaded, the loading platens apply strip loading rather than point loading and cause a discrepancy in the results as shown by Nakashima et al. [186]. The effect can also be seen in *Figure 2. 16* where two peaks appear for trimmed specimen irrespective of the loading platen type. In order to avoid these problems, the sample is generated directly in a circular area and the specimen contains 6828 particles. It can be seen in *Figure 2. 16* that by using circular specimen the post behaviour does not show the second peak irrespective of the type of loading platen and unlike the results obtained in [186] no extra local peak

Table 2. 8 Results of using clusters and laboratory tests

Property	Concrete	
	Laboratory tests	Modelling Results
Unconfined compressive strength(σ_c) (MPa)	42.6±0.64	42.8
Young's Modulus(E) (GPa)	35.0±2.0	28.8
Brazilian tensile strength(σ_b) (MPa)	3.8±0.36	3.97

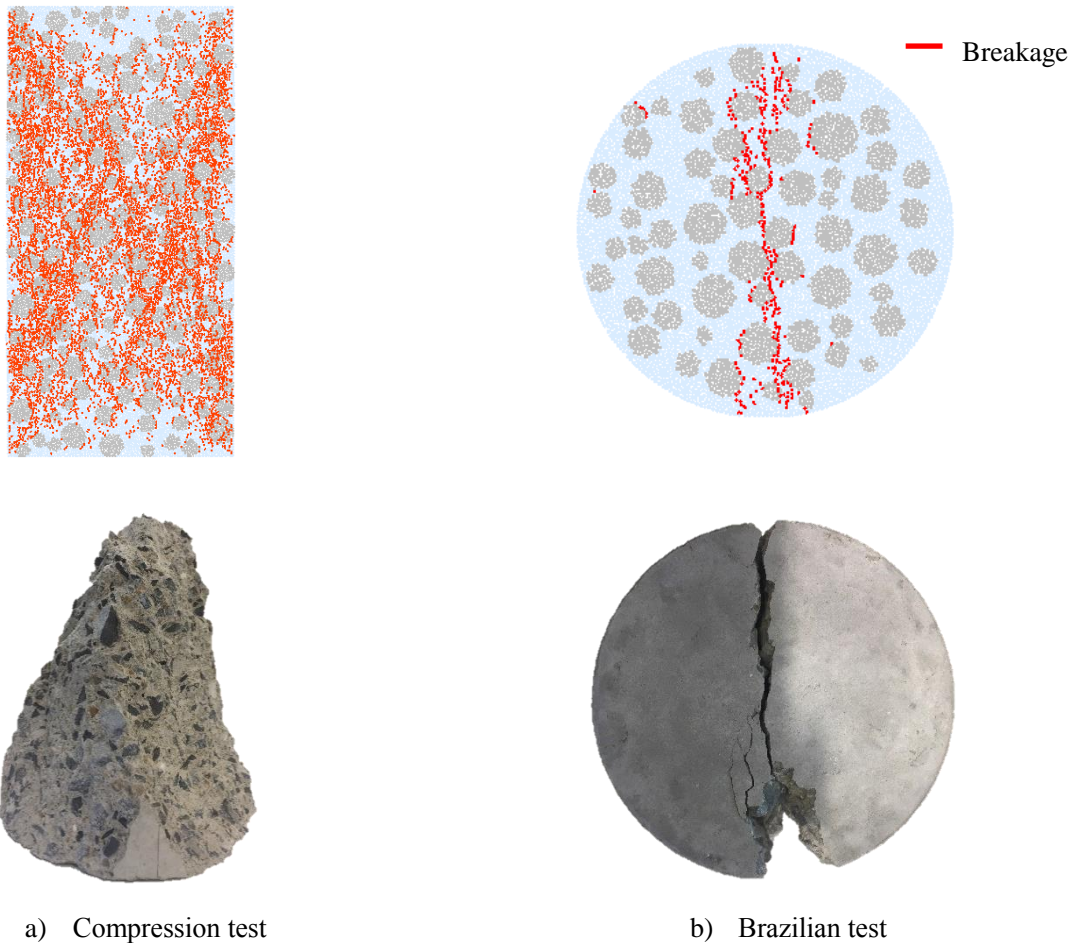


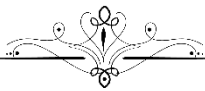
Figure 2. 18 Numerical and experimental failure patterns of concrete

2.9 Summary

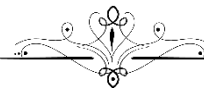
In this chapter, the concepts and theories of the DEM method were presented. A state of the art on the development of DEM models for quasi-brittle cementitious materials is also presented. With the advantages of that DEM looked into micromechanics of problem and allowed a grain level control and could solve the discontinuous problem, it seems suitable to analyse the local behaviours of concrete. Main contact models are explained, however, the parallel bond is further considered to perform numerical simulations in this chapter. It is shown that using parallel bond contact model, the behaviour of concrete with high UCS/T ratio cannot be modelled with the same set of microparameters. It is due to the reason that in the generic formulation of the parallel bond, full

contribution of moments to maximum contact stresses was considered and constant normal and shear strengths were used without considering their inter-dependence. A modified contact model was applied where the contribution of the moment is considered and a new model parameter is defined. Besides, for concrete modelling, three types of contacts are determined for three phases (matrix, interface, and aggregate) and aggregates are modelled using cluster particles and bonded together by connecting with Matlab. For micro parameters determination, Levenberg-Marquardt (LM) algorithm is used. The application of this modified parallel bond model on mortar and concrete showed that numerical results of mechanical behaviour show good reproduction of experimental results. Fracture patterns are also correctly described. A more detailed analysis of the fracture process will be described in Chapter 4.

Experimental Investigation and Discrete Element Modelling of Concrete Fracture through Size Effect



This chapter investigates the size effect of concrete by experiment and numerical modelling. In the experimental part, acoustic emission combined and digital image correlation was used in order to further study the fracture behaviours of concrete. Bazant's size effect law was used to analyse the size effect of concrete and the fracture parameters of concrete were also calculated. In the modelling part, discrete element method was used and the modified contact model was applied to model the size effect of concrete.



3.1 Size effect in concrete

Size effect refers that the mechanical properties of the material are no longer constant but change with the geometrical dimensions of the material. Based on the previous studies, the size of the specimen has an influence on the nominal strength and fracture toughness of concrete. So, the strength determined by experiment is not just a property of the material, but the parameter that based on the dimensions of the structure. However, the structures used in the laboratory are adjusted according to the real structures. Whether the experimental results of these small-scale structures have the extensive applicability and practical significance to the actual structures have become one of the challenges faced by the majority of researchers, namely the problem of size effect.

3.1.1 Review of size effect theories

The study of size effect was originated in the 15th century, first proposed by Leonardo de Vinci [188], who pointed out that “Among cords of equal thickness, the longest is the least strong.”. Experiments involving size effect had been carried out on many materials [68, 189-191] and was first applied to the study of concrete materials by Gonnerman [192]. At present, the research on the size effect of concrete strength mainly uses the theory of size effect caused by energy release, namely energetic-statistical theory [9, 68, 193]. In addition, the Weibull statistical theory [194-197] and the Carpinteri multifractal size effect theory [198-200] have also been proposed. Each of these three theories has its own advantages and disadvantages, and it is still being continuously improved.

3.1.1.1 Theory of size effect caused by energy release

This theory is mainly represented by Bažant's size effect law [193]. The basic assumptions are [193]: i) The extension of a fracture or crack zone requires that the energy provided per unit area of the fracture plane be approximately constant; ii) The energy released by the fracture or crack zone expansion of the structure can be described by fracture length and the size of fracture process zone; iii) Different sizes of geometrically similar structures are geometrically similar to the failure mode; iii) The structure does not fail at the crack initiation. Although these assumptions have never been fully satisfied experimentally, Bažant's size effect law is the most commonly used size effect model for quasi-brittle materials.

Bažant [9] pointed out that most quasi-brittle materials do not break immediately when they start cracking. After extensive investigation on concrete, rock, sea ice, composites, toughened ceramics, bones, grouting soils, coal, and other quasi-brittle materials, Bažant believes that the size effect of such quasi-brittle materials is achieved at the maximum load. The gravitational redistribution and stored energy release caused by the development of cracks or microcracking zones, i.e., the size effect is caused by the dispersion of strain energy when the macroscopic microcracks propagate.

3.1.1.2 Statistical size effect

In 1926, Peirce [201] proposed the weakest link model and introduced extreme value theory proposed by Tippet [202] in 1925. Subsequently, Weibull [194-197] reached a crucial conclusion in 1939: the Weibull distribution of minimum intensity with a very small probability cannot be described using any existing distribution; it is recommended that the distribution of extremal intensity should describe by a power function with a threshold value. Freudenthal et al. [203] theoretically confirmed Weibull distribution through the probability model of microcracking distribution in the material. With the efforts of Weibull and other researchers, the basic framework of the statistical theory of size effect is established. The statistical theory of material strength is based on the following four assumptions: i) As long as a small unit in the material reaches the strength limit, the structure will fail; ii) The failure of each unit is independent; iii) The materials are isotropic and statistically uniform; iiiii) The entire chain consists of N units, all of which have the same probability of failure.

3.1.2.3 Multi-fractal scaling law

The theory is represented by the Carpinteri [198-200] multifractal size effect theory. Due to the disorder of the mesostructure of concrete materials and the existence of various micro-defects (micro-cracks, micro-holes) interactions, macro-fracturing mechanics theory is no longer applicable to describe its fracture behaviour. In quasi-brittle materials, the random and discontinuous distribution of defects and the anisotropy of their internal structure can result in the non-uniform distribution of strengths inside the material. Under the same external force field, the stress intensity factors at different points are different, and the points with weaker strength will produce cracks first. Therefore, the cracks caused by external force sites are discontinuous and random. Before the material fractures, the internal microcrack evolution process has fractal characteristics. Fractal theory is particularly suitable for describing irregular and disordered materials, such as pore structures, cement hydration particles, or micro-cracks in amorphous materials. Carpinteri [204] believed that the difference in the fractal characteristics of microcracks is the source of the size effect of the material at different observation scales.

Although each theory is applicable to investigate size effect, there are much evidence to show that the main reason that results in size effect is the release of strain energy due to the fracture growth [205].

3.1.2 Literature review of size effect in concrete

The main investigations on the size effect can be divided into three categories, namely the size effect on compressive strength, size effect on tensile strength and size effect on flexural strength.

3.1.3.1 Size effect on compressive strength

Neville [206] tested about 300 cubic concrete specimens with the compressive strength in the range of 13 - 48 MPa. The results showed that the strength of a small specimen is higher. Lessard

[207] analysed the compressive strength results of high strength concrete and found that there obviously existed size effect. J.R. del Viso et al. [208] studied size effects on the compressive strength of high-strength concrete using different shape specimens. The results illustrated that large specimens resist less stress than the small ones and the size effect in the cubes is quite stronger than in cylinders. Bažant et al. [209] reported the results of the geometrically similar pin-ended tied reinforced concrete columns under eccentric axial load. The results were in good agreement with the size effect law proposed by Bažant [193].

Based on the microplane model, Brocca and Bažant [210] used the finite element method to study the size effect of the compressive failure of geometrically similar concrete columns with different sizes. The results showed that the numerical modelling is captured with good approximation the size effect observed experimentally. Cusatis and Bažant [211] investigated the size effect on compression fracture of concrete with or without V-notches. Confinement-shear lattice model (CSL model) is adopted in the numerical modelling. The results illustrated that the size effect on compressive strength is significant in notched structures but almost negligible for unnotched structures and a strong size effect is observed on the post-peak behaviour for both notched and unnotched structures.

Except for the experimental and numerical studies on the size effect phenomena in compressive strength, many attempts had been made to propose the fracture-mechanics-based model of compression failure. Based on the size effect law given by Bažant [193], Kim and Eo [212] added independent strength to Bažant's size effect law (SEL) and proposed a modified size effect law (MSEL). The similar equation was also proposed by Bažant and Xiang [213]. The analytical expression of the refined MSEL model is given as *Equation 3. 1*.

$$f_c(D) = \frac{Bf_c'}{\sqrt{1 + \frac{D}{D_0}}} + Cf_c' \quad (3.1)$$

Where $f_c(D)$ is the nominal compressive strength of specimen; B , D_0 and C are empirical coefficients obtained from fitting experimental data of geometrically similar specimens of various sizes; f_c' is the compressive strength of standard cylinder; D is the characteristic dimension of the specimen.

Based on the crack band theory and more influencing parameters were considered, Sim et al. [214] proposed a generalized model to predict the fracture behaviour of concrete specimen. The analytical expression of Sim et al. [214] model was expressed as follows.

$$f_c(D) = \frac{A\sqrt{(n_1)^{X_4} f_c'}}{\sqrt{1 + BD\left(\frac{\rho_c}{\rho_0}\right)^{-X_2}}} f_c' + Cf_c' \quad (3.2)$$

Where $f_c(D)$ is the nominal compressive strength of specimen; A , B , C , X_2 and X_4 are empirical coefficients obtained from fitting experimental data of geometrically similar specimens of various sizes; f_c' is the compressive strength of standard cylinder; n_1 is the aspect ratio of specimens; ρ_c is the unit weight of concrete; ρ_0 is the reference value for concrete unit weight and equals to 2300 kg/m^3 ; D is the characteristic dimension of specimen.

Kim et al. [215] proposed an equation (*Equation 3.3*) to predict the compressive strength of plain and spirally reinforced concrete cylinders with different aspect ratios. They reported that the effect of maximum aggregate size on size effect is negligible.

$$f_{oc} = 0.8f'_c + \frac{0.4f'_c}{\sqrt{1 + \frac{(h-d_c)}{50} \left[1 - \frac{8000A_{sp}(1-s/d_c)}{d_c s f'_c} \right]}} + \frac{5.4A_{sp}f_y}{d_c s} (1-s/d_c) \quad (3.3)$$

Where A_{sp} is the cross section area of the spiral reinforcement; f_y is the yield strength of the spiral reinforcement; f'_c is the compressive strength of standard cylinder; d_c is the outer diameter of the spiral reinforcement; s is the spacing of the spiral reinforcement; f'_c and f_y are in MPa and d_c , h and s are in mm.

3.1.3.2 Size effect on tensile strength

It is very difficult to determine the tensile strength of concrete using the direct tension test. Generally, researchers [216-218] used the splitting test to obtain the indirect tensile strength of concrete. Changing the diameter of the concrete specimen is the main approach to study size effect on Brazilian splitting strength. Although most results [212, 219] have proved that Brazilian tensile strength decreases with the specimen size increasing, there exist some different conclusions. The results of Bažant et al. [220] illustrated that when the specimen size increased, Brazilian tensile strength decreased at first and then increasing. The same results were also obtained by Hasegawa et al. [221]. Chen et al. [222] pointed out that splitting tensile strength showed a slight increase when specimen size increasing. Rocco et al. [223] tested cylindrical and prismatic specimens with the sizes in the range of 17 mm and 300 mm, the results showed that splitting tensile strength decreased monotonously as the size of the specimen increased and tended to be constant at large sizes. Zhou et al. [224] tested the splitting tensile strength of high strength concrete with normal aggregate (crushed limestone) and lightweight aggregate (sintered fly ash) using prismatic specimens, the results obtained the conclusion that tensile strength decreased with increasing size.

The influence of bearing strips also has been studied by previous researchers. Rocco et al. [225] found that with the decreasing of the width of the bearing strip, the size effect was not obvious. If the width of bearing strips smaller than 4 % of the specimen diameter, the size effect was negligible. Based on the cohesive crack model, Rocco et al. [225] also theoretically analysed the size effect in the Brazilian test and proposed the size effect equation for Brazilian splitting strength as follows.

$$f_{st} = \frac{f_t}{c_1 + c_2 (D/l_{ch})} + c_3 f_t \quad (3.4)$$

Where f_t is the tensile strength which obtained from an ideal uniaxial tensile test; l_{ch} is the characteristic length. D is the specimen size; c_1 , c_2 and c_3 depend on the geometry and the relative width of the bearing strips (b/D); b is the width of the bearing strip.

3.1.3.3 Size effect on fracture characteristics

Three-point bending test is the main method to perform the size effect behaviour of concrete. Generally, geometrically similar beams, with or without the notch are used. Many results showed that there exist size effect in flexural strength, but the main investigation focused on the influence on fracture energy and fracture toughness. Mindess [226] studied the effect of specimen size on the fracture energy of notched beams. The results showed that the value of fracture energy and fracture toughness for the small two size beams seemed to be independent of specimen size but increased considerably for the largest size beams. Alexander and Blight [227] found that the fracture toughness and microcrack zone increase as the depth of the beams increases. Brameshuber and Hilsdorf [228] concluded that when the depth of the beam increased from 100 mm to 800 mm, the fracture energy experienced about 20 % increasing. However, Linsbauer and Sajna [229] found that the fracture energy showed a slight increase with increasing specimen size, but the fracture toughness showed an increase when specimen size increasing. On the contrary, Jueshi and Hui [230] noticed that the fracture energy decreased by about 19 % when the specimen size increases.

Mazars et al. [231] pointed out that the fracture properties of the material depend on the ratio of the crack size versus the structure size based on their numerical and experimental results. Skarżyński and Tejchman [232] used FEM to perform the size effect. In their numerical modelling, concrete was treated as a one-phase material with a heterogeneous three-phase section at the central part of the beams. The results illustrated that there was no effect of beam height on characteristic length, but the beam strength increased with decreasing beam height.

Although the size effect has been studied by many researchers, many results have given the opposite conclusions. There are still many problems still need to be explained and understood through those phenomena occur in the experiments.

3.2 Experimental approach to characterize size effect

3.2.1 Material

Ordinary Portland cement (CEM I 52.5 N) was used as a binder. Natural aggregate and sand with maximum size 2 mm were used. Water-cement ratio (w/c) was 0.40 for concrete. The influence of size effect was investigated by using three different sizes of specimens. Besides, in order to calibrate the microparameters for DEM, compression test and Brazilian test were also tested. The maximum sizes of aggregate were 5.25 mm, 10.5 mm and 21.0 mm, respectively. Bažant [193] considered the size of FPZ as a material property and multiple of maximum aggregate size (d_{\max}). Aggregate plays a key role in the microstructure and regards as the skeleton of concrete. Thus, it can be inferred that the ratio between the structure size and the aggregate size is a fundamental factor causing the size effect. The objective of the experiments performed in the thesis considered the ratio of the characteristic structural dimension and the maximum aggregate size (D/d_{\max}) as a key factor in investigating the size effect. The aggregate effect is investigated by taking the ratio of the characteristic structural dimension (D) and the maximum aggregate size (d_{\max}) as a key parameter. In previous studies [233-236], only the maximum aggregate size (d_{\max}) is scaled. Here, the aggregate size (d_a) of the complete grading curve is scaled with the same factor. The percentage retained for

each aggregate is presented in *Figure 3. 1*. The grading curves for sand and all aggregates can be seen in the appendixes.

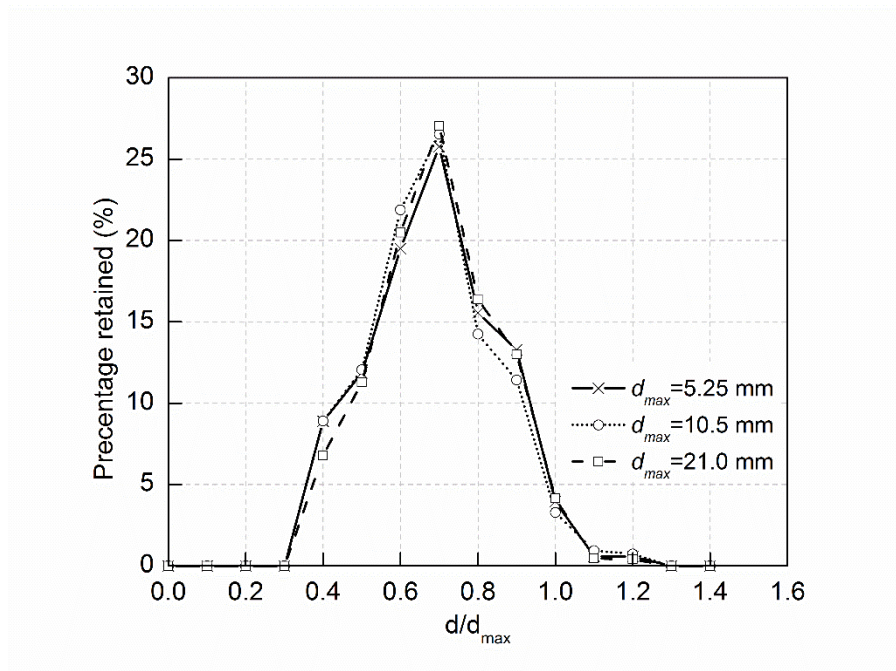


Figure 3. 1 Aggregate gradation

Table 3. 1 shows mixture proportions of concrete. For the small aggregate size concrete, more superplasticizer (SP) was needed. This is due to the reason that for concrete with smaller aggregate, aggregate specific surface area increases. It means that water needed to wet the surfaces of aggregates augments. Since the water content is maintained constant, slightly more SP was added to keep the same workability of concrete with larger aggregate size. By dividing the portion of aggregate into cement, water, sand, and SP, i.e. using the same cement, water, sand and SP ratio in concrete, the mix design of mortar can be obtained.

Table 3. 1 Mix proportions of concrete

Series	Unit content (kg/m ³)					SP	
	Water	Cement	Sand	Gravel			
				2-5.25mm	4-10.5mm	8-21.0mm	
M02	258	645	1134				7.45
C05	176	439	772	926			8.02
C10	176	439	772		926		5.07
C20	176	439	772			926	5.07

3.2.2 Specimen preparation and testing procedure

The dimensions of specimens for compression tests and Brazilian tests were $\phi 110 \times 220$ mm² cylinders. The cylinders for uniaxial compression tests (UCS) were ground at both ends before testing in order to remove any surface irregularity and also ensure the ends to be perpendicular to the sides

of the specimens. Elastic modulus and compressive strength of the cylinders were measured using of a Universal Testing Machine (UTM) with a capacity of 3000 kN according to ASTM C469 [237] and ASTM C39 [238], respectively. Three sets of linear voltage differential transducers (LVDTs) were attached to two fixed rings were used to measure deformation as shown in *Figure 3. 2*. The apparatus consisted of two aluminum rings with screws for attachment to the specimens. The spacing between screws on the top and bottom rings was 80 mm for $\phi 110 \times 220$ mm² cylinders, which served as a gauge length for calculating axial strain from the measured deformations as shown in *Figure 3. 2*. The static elastic modulus of concrete is defined as a chord modulus from the stress-strain curve with a first point at a strain level of 0.00005 (ε_1) and the second point at 40 % of the maximum stress as follows:

$$E_c = \frac{0.4f_c - \sigma(\varepsilon_1)}{\varepsilon(0.4f_c) - \varepsilon_1} \quad (3.5)$$



Figure 3. 2 Instrumentations for measuring the properties of concrete

The three-point bending test was performed on beams with a constant width (t), however, length and height of beams varied such that the ratio of length to depth (L/D) and span to depth (S/D) were maintained constant. According to RILEM-TC 89 recommendation [239], the ratio of vertical notch depth to the depth of each beam in all cases was 0.2 ($a_0 = 0.2D$). The geometrical properties of the specimens were given in *Table 3. 2*. All the three-point bending tests were performed with the same controlled crack mouth opening displacement ($CMOD$) rate of $0.2 \mu\text{m}/\text{sec}$.

Table 3. 2 Dimensions of beam specimens

Series	D (mm)	t (mm)	a_0/D	S/D	L/D
M02	100	100	0.2	3.0	4.0
C05	100	100	0.2	3.0	4.0
	200				
C10	100	100	0.2	3.0	4.0
	200				
	400				
C20	100	100	0.2	3.0	4.0
	200				
	400				

Series C10 and C20 with the depth of 100 mm, 200 mm and 400 mm were used to perform the general size effect. Series C05 with a depth of 100 mm, 200 mm was also used to perform size effect. Series M02 specimen with the depth of 100 mm was used to calibrate the DEM microparameters DEM.

According to RILEM-TC 89 [239] in SEM, the weight of each bending specimen should be added to the peak load recorded by testing equipment. Thus, peak loads recorded for each bending beam is corrected according to RILEM-TC 89 [239] recommendation as:

$$P_{\max} = P_{\max}^0 + \frac{2S-L}{2S} \cdot g_g \cdot m \quad (3.6)$$

Where P_{\max} the corrected peak load, P_{\max}^0 is the peak load recorded by the testing equipment, m is the mass of each specimen, S is the specimen span, L is the specimen length, g_g is the gravity acceleration.

Then the nominal strength is calculated based on the corrected ultimate load for each specimen using Equation 3. 7.

$$\sigma_N = \frac{3P_{\max}S}{2b(D-a_0)^2} \quad (3.7)$$

3.3 Methods to analyse the fracture of concrete

3.3.1 Acoustic emission

Acoustic emission technique (AET) is a non-destructive testing (NDT) method to evaluate the damage in the materials. The oldest report on a scientifically planned AE experiment was known as the experiments did by F. Kishinouye [240] in Japan. The first investigation into acoustic emission was carried out by J. Kaiser [241] to do the research work for metal in 1950. While the term ‘acoustic emission (AE)’ was initiated by B. H. Schofield [242] in 1954. The next major effort in AE research was made by A. Tatro [243] who foresaw the unique potential of AE as a nondestructive testing procedure. After that, with the reforming of computerized test instrumentations and evolving, AET was complemented during the next several decades. To date, AE technique is being applied into detecting structures flaws, inspecting weld quality, detecting loose particles, aerospace and aircraft industry, detecting and locating leakage, manufacturing fibre reinforced plastic (FRP) tanks, and pressure vessels, bridges, etc. However, with regard to AE research in concrete, the early scientific papers were published in the 1960s. In these papers, the relation between the fracture process and volumetric change in the concrete under uniaxial compression was mainly studied by Rosch [244], Lhermitte [245] and Robinson [246]. In the late 1970s, the most important applications of AET to structural concrete elements had drawn much attention of the researchers [247, 248]. The original technology developed for metals was modified to suit heterogeneous materials like concrete. At present, the AE methodology can also be used to study micro and crack propagation in concrete. Because AET is based on the generation of transient elastic waves produced by a sudden redistribution of stress in a material when undergoes cracking, so the crack sources can be located using the time differences between detection of the event at different sensors. The fracture process zone (FPZ) in the

concrete can also be visualized by analysing the localization of acoustic events during crack propagation [30, 44, 249-252]. Li and Shah [253] applied the AE source location to identify the FPZ for cementitious materials, mainly subject to strain-softening loads. Ohtsu [254] carried out further studies concerned on the AE source location in bending tests of reinforced concrete beams. Two failure modes, namely bending failure and diagonal shear failure, are clearly identified from 3-D maps of source location. Later, the AET is also used to categorize concrete cracks into two modes, namely tensile mode and shear mode [255-257].

Compared to other NDT methods, AET can monitor changes in material behaviours over a long time without moving one of its components (i.e. sensors) and the energy that is detected is released from within the test object rather than being supplied by the test method, as in radiographic or ultrasonic testing. The acoustic emission measurement system (Figure 3. 3) generally consists of sensors, preamplifier, filter, and amplifier, along with measurement, display, and storage equipment. The AE transducers are generally very sensitive piezoelectric sensors. As the traditional AE technique only uses AE features, the actual waveforms are not critical to this method. Resonance sensors are often used as AE sensors (transducers) used and are only very sensitive to a certain frequency. Since the AE signals are very weak, so after the AE transducer, a pre-amplifier is connected in order to minimize the noise interference and prevent the signal loss. Sometimes, the transducer and the preamplifier are built as a unit. Then, the noises in the signals are removed when passing through the filter. After that, the signals are amplified by the amplifier before being sent to the signal conditioner. The gain of the amplifier (dB) is expressed as:

$$dB = 20 \cdot \log_{10} \left(\frac{V_0}{V_i} \right) \tag{3.8}$$

Where V_0 is input voltage; V_i is output voltage. As a reference, the signals in concrete and rocks are usually magnified 60 dB to 100 dB. The filter of variable bandwidth ranging from 1 kHz to 2 kHz is recommended [258].

Finally, the AE features are subtracted and stored in a computer for further analysis. During investigations, other parameters, such as load, deformation, pressure, and temperature, can also be recorded as parametric inputs.

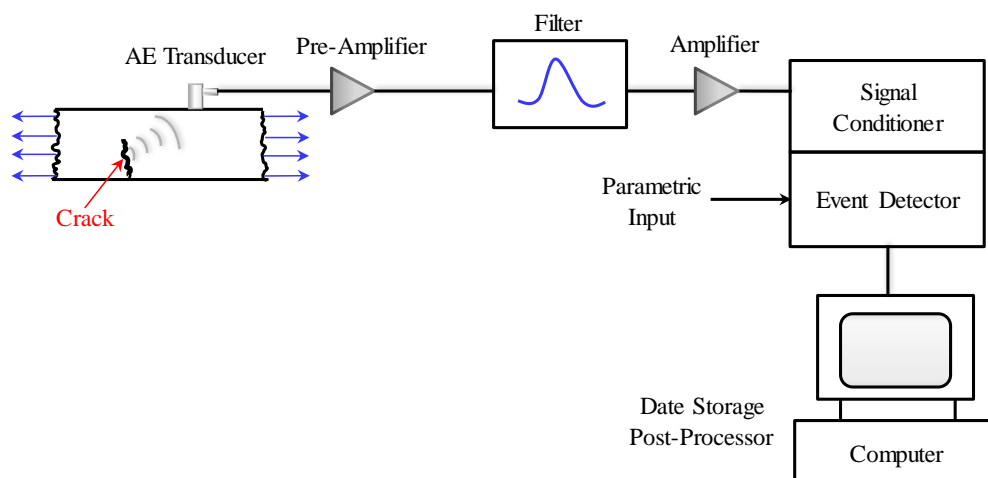


Figure 3. 3 Schematic of AE instrumentation [259]

In the experiment, when a crack develops in a material like concrete, energy is released and a portion of this energy is dissipated as an acoustic wave possessing different frequencies. Once the wave arrives the surface of the specimen, it can be noted by means of an acoustic emission sensor. In this way, the position of the crack can be determined in the case of homogeneous isotropic materials and appropriate sensor positioning. In order to evaluate measurements, several parameters of AE waveform (e.g., amplitude, rise time, duration, velocity, frequency, signal strength, and corresponding AE energy) need to be analysed. The AE waveform parameters are illustrated in *Figure 3. 4*. Amplitude determines the detectability of the signal and is defined as the greatest measured voltage in a waveform. Minimum threshold will not be recorded if signals with amplitudes below the operator-defined. Duration is the delay between the first and last threshold crossings and the energy is directly proportional to the area under the AE waveform [260]:

$$AE\ energy_i = \int_{t_0}^{t_1} V_i(t)^2 dt \quad (3.9)$$

Where i is the recorded voltage $V(t)$ transient of a channel; t_0 is the starting time of the voltage transient record; t_1 is the ending time of the voltage transient record.

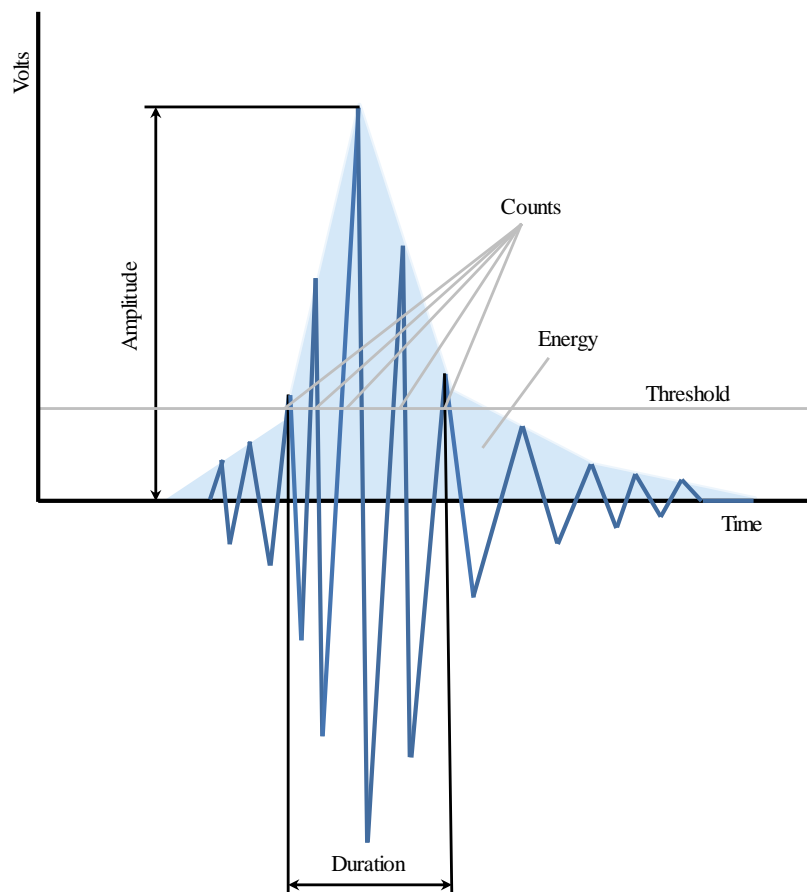


Figure 3. 4 Parameters reflected in an AE waveform [258]

Using the AE energy obtained, researchers defined a parameter called relaxation ratio (ratio of average energy during the unloading phase to the average energy during loading phase) to assess the damage state of concrete structures.

Before starting the AE testing, a test called pencil-lead breakage (PLB) is conducted first to test the performance of the AE system and determine the attenuation of AE signals when transmitting through concrete materials [261, 262]. This method is a long established standard as a reproducible artificial AE source known as the Hsu-Nielsen source or HSN-source [263]. Using a mechanical pencil, the lead of the pencil is pressed firmly against the structure surface under investigation until the lead breaks as shown in *Figure 3. 5*. During pressure application with the lead, deformed is occurred at the surface of the structure. When lead breaks, the accumulated stress is suddenly released; the surface of the structure will produce a microscopic displacement and causes propagation of an acoustic wave into the structure. Since this type of source is easy to handle both in laboratory environments and field testing, so it became the most common type of test source in AE testing.

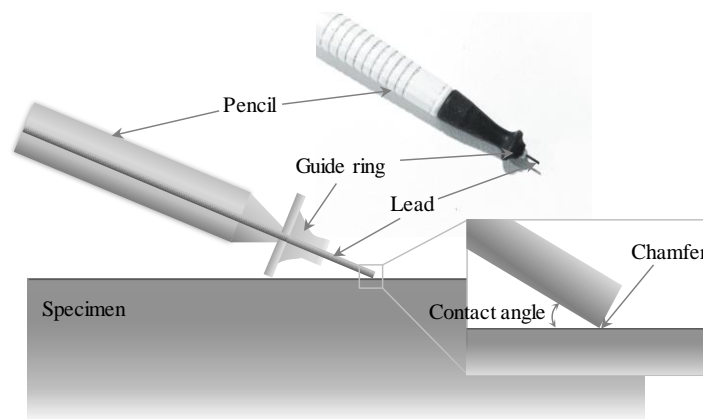


Figure 3. 5 Pencil-lead break test

Aforementioned, the traditional methods of AE source location are based on the time difference, wave velocity and distances between sensors. They can be divided into three categories: linear location, planar location, and 3D location.

The linear location is a time difference method and suitable locate AE source on linear structures whose lengths are much larger than their widths, such as pipes. The testing setup can be shown in *Figure 3. 6*. It is based on the arrival time difference between two sensors for the known velocity. If the time for sensor 1 and sensor 2 receiving the signal is t_1 and t_2 , then the difference of arrival times (Δt) can be defined as

$$\Delta t = t_2 - t_1 \quad (3.10)$$

As the wave velocity (V) is known, so the distance between the AE source and AE sensor 1 (d), which is closer to the AE source can be calculated as

$$d = \frac{1}{2}(D - \Delta tV) \quad (3.11)$$

Where D is the distance between sensor 1 and sensor 2 and V is the wave velocity.

Then, the location of the AE source can be determined as the distance between the AE sensors is known.

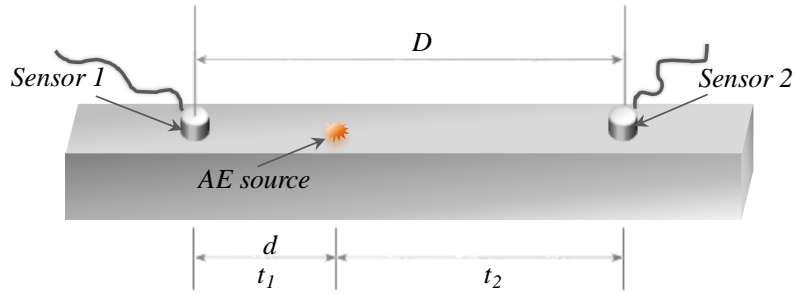


Figure 3. 6 The schematic of the 1D linear location [258]

The planar location is applied to 2D structures, where the thickness is small compared to the extent of the object, and the source coordinates are only required in two directions. The principle of 2D planar location is shown in *Figure 3. 7*. For a 2D localization, at least 3 sensors are needed and the AE source can be calculated by the hyperbola method [264, 265]. It supposed that in a uniform medium, there is an AE source $S(x_s, y_s)$ and the AE sensors are placed nearby. The coordinates of an arbitrary sensor i is (x_i, y_i) . Assume the AE signal is produced at the initial time of t_0 , and spread to any -sensor i at the time t_i , then the distance between the AE source S and sensor i can be obtained as follows:

$$d_{s-i} = \sqrt{(x_s - x_i)^2 + (y_s - y_i)^2} \quad (3.12)$$

Then the relationship between initial time t_0 and arrival time t_i for each sensor can be expressed by:

$$t_i - t_0 = \frac{d_{s-i}}{V} \quad (3.13)$$

As the initial time t_0 is difficult to measure accurately, so it needs to eliminate t_0 in the equation:

$$\Delta t_{i-j} = t_i - t_j = \frac{d_{s-i}}{V} - \frac{d_{s-j}}{V} \quad (3.14)$$

Using the *Equation 3. 12 – Equation 3. 14*, two analytic solutions can be got with the help of at least 3 sensors that are not placed in a straight line. Consequently, the coordinates of the source can be determined by the obtained solutions refer to its real situation or determined precisely by placing more sensors. At present, for 2D system, the numerical solution is usually obtained by using the iterative algorithm.

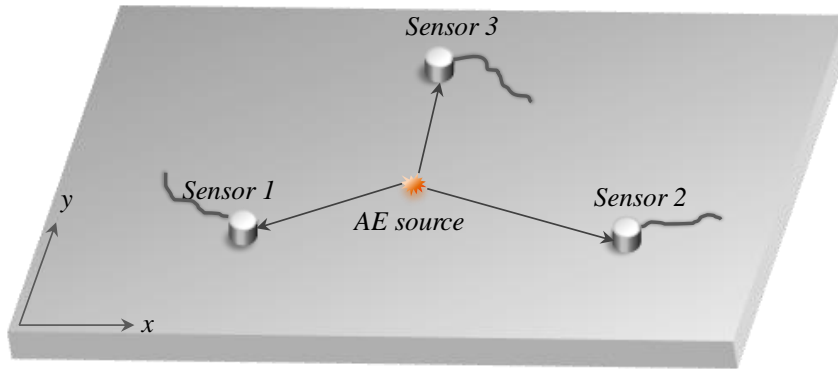


Figure 3. 7 Schematic of the 2D planar location [258]

For the source located in the 3D location, its principle similar to 2D planar location method as shown in *Figure 3. 8*. The standard technique for 3D localization is to linearize the problem [258]. The equations used to calculate a 3D location of an AE source are based on the assumptions that the material is homogeneous and isotropic and that the AE source resembles a point source. If this is not the case, the following approach has to be modified. The AE sensors are located around the AE source $S(x_S, y_S, z_S)$, and the coordinates of an arbitrary sensor i are (x_i, y_i, z_i) . The distance between the AE source S and sensor i can be written as:

$$d_{S-i} = \sqrt{(x_S - x_i)^2 + (y_S - y_i)^2 + (z_S - z_i)^2} \quad (3.15)$$

Then the relationship between initial time t_0 and arrival time t_i for each sensor can be expressed by:

$$t_i - t_0 = \frac{d_{S-i}}{V} \quad (3.16)$$

The time difference of arrival of any two sensors i and j can be described as follows:

$$\Delta t_{i-j} = t_i - t_j = \frac{d_{S-i}}{V} - \frac{d_{S-j}}{V} \quad (3.17)$$

According to the *Equation 3. 15 – Equation 3. 17*, two analytic solutions can be obtained when there are at least 4 sensors that are not placed in the same plane. Consequently, the coordinates of the source can be determined by the obtained solutions refer to its real situation or determined precisely by placing more sensors.

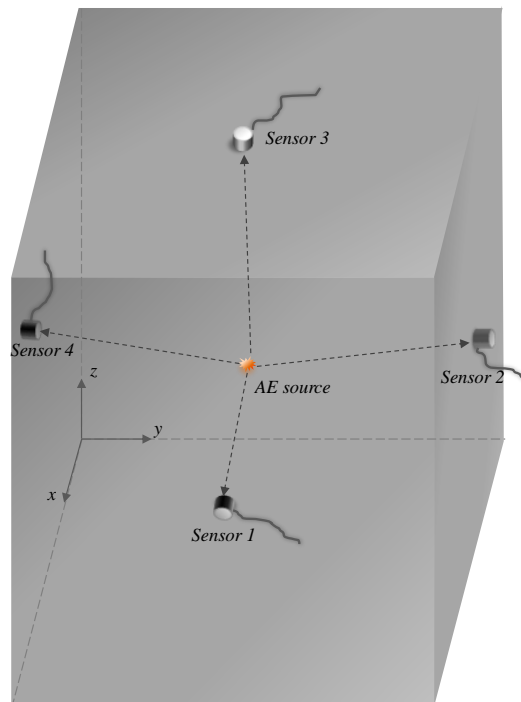


Figure 3. 8 The schematic of the 3D location of an AE source [258]

The AE system used in this study comprised of a general-purpose interface bus ($2 \times \text{PCI-DISP4}$ having 4 channels each). A 3D analysis is performed for the localization of AE events, for which 8 piezoelectric transducers of type R15a were used; all having a same frequency range of 50 - 200 kHz and the same resonance frequency of 150 kHz. The transducers were placed around the expected location of the fracture process zone (FPZ) to minimize errors in the AE event localization. Both sides of the specimen were pasted with transducers using silicon grease as the coupling agent. Thus, the sensors form a parallelogram grid location on one side of ($60 \times 150 \text{ mm}^2$) for D1 beam, ($131 \times 150 \text{ mm}^2$) for D2 beams and ($300 \times 150 \text{ mm}^2$) for D3 beams as shown in *Figure 3. 9*.

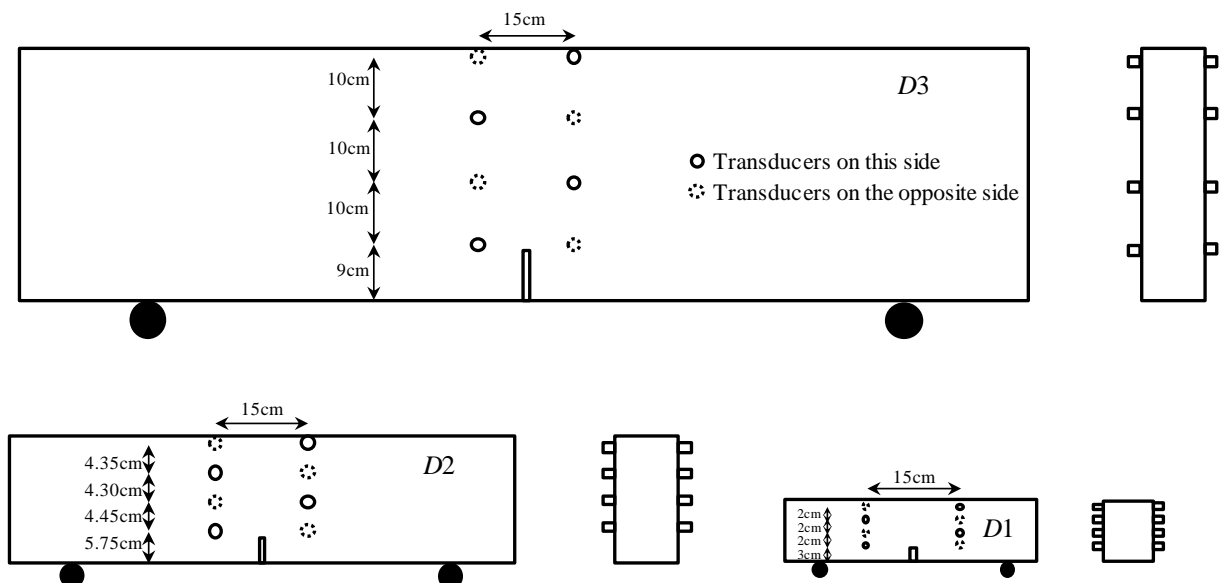


Figure 3. 9 Specimen geometry and AE transducers positions for D1, D2 and D3 beams

3.3.2 Digital image correlation

In the early 80's, the digital image correlation (DIC) was the first system developed at the University of South Carolina [266-269] and later has been subsequently improved by researchers [270-272]. The purpose of using this technique was to measure full-field in-plane displacements and displacement gradients of a strained body at the macro scale. In brief, DIC is computer-based process to obtain full field information in 2D aspect by recording deformation and motion of speckle patterns on a rectangular area of specimen surface, known as the so-called regions of interest (ROI), before and after an increment of deformation of the body. It determines displacements and cracks propagation in concrete structures as the fact that applied stresses change both the thickness and optical properties of materials. In this respect, the digital camera is one important tool. Camera with charge-coupled device (CCD) array has small photosensitive cells and high pixel count, records the intensity of light falling on a pixel. In high-resolution camera, the array is rectangular with thousand or more pixels per line and a thousand or more lines per image. The signal from CCD array is digitized and gives a reading of the light intensity for each pixel. Intensity readings are shown as 0 from dark pixels and 100 for the light pixel. Storage of image into pixel and combination of the pixel is called convolution. The sensor is an array of light-sensitive semi-conductors called pixels. Each pixel emits electrons when hit by photons. A number of electrons are proportional to the number of photons.

Aforesaid, DIC is a full-field image analysis method. It based on grey value digital images that can determine the contour and the displacements of an object under load in three dimensions. Due to rapid new developments in high-resolution digital cameras for static as well as dynamic applications, and computer technology, the applications for this measurement method has broadened and DIC techniques have proven to be a flexible and useful tool for deformation analysis.

In the routine implementation of the 2D DIC method, the ROI in the reference image should be specified or defined firstly. Later ROI is divided into evenly spaced virtual grids. The displacements are computed at each point of the virtual grids to obtain the full-field deformation. The schematic of the DIC testing setup can be seen in *Figure 3. 10*.

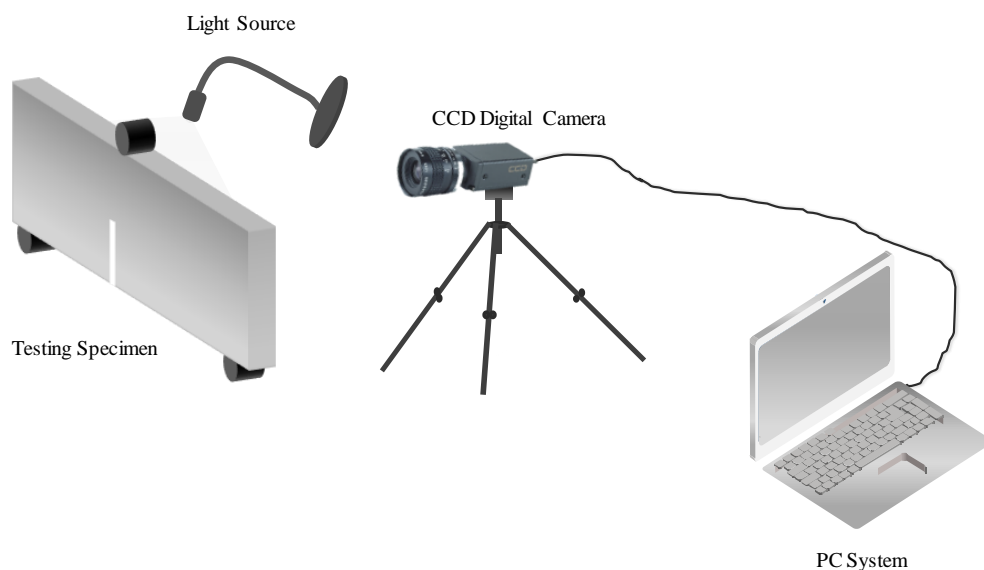


Figure 3. 10 A schematic plot of DIC testing setup

The basic principle of 2D DIC is the tracking (or matching) of the same points (or pixels) between the two images recorded before and after deformation as schematically illustrated in *Figure 3. 11*.

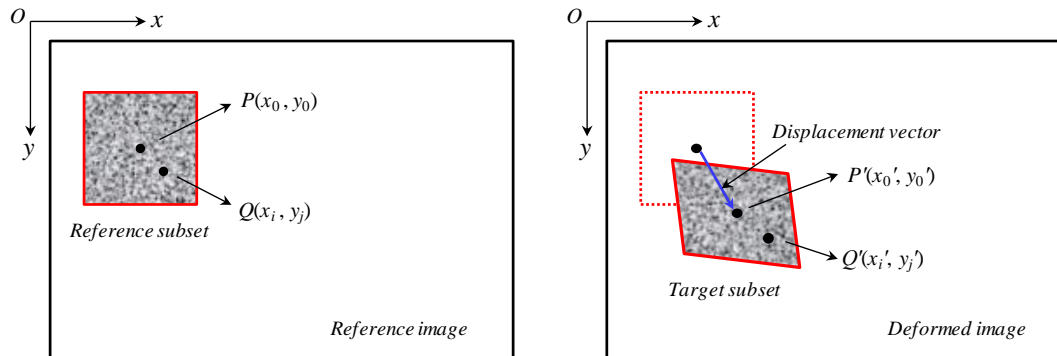


Figure 3. 11 Schematic representation of a reference subset and a deformed subset

Even though the images are captured at a very small-time interval, as the change of luminous intensity or the noise of electronic signals, there still remain differences. In order to evaluate the similarity between the reference and the deformed subsets with a similarity, an undeformed subset of pixel intensities (f_i) and a deformed subset of pixel intensities (g_i) are given respectively. In displacement measurement, various correlation criteria have been proposed and used, like the Cross-Correlation (CC), the Sum of Absolute Difference (SAD), the Sum of Squared Difference (SSD), the Parametric Sum of Squared Difference (PSSD), the Sum of Hamming distances (SHD) and the least-squares correlation criteria [273-276]. In order to decrease the error caused by the change of intensity, the criteria aforementioned are modified to Zero-Normalized Cross-Correlation (ZNCC) criterion, the Zero-Normalized Squared Sum of Differences (ZNSSD) criterion and the Parametric Sum of Squared Differences (PSSD_{ab}) criterion with two additional parameters. Among those criteria, CC criterion and SSD criterion with their normalized and zero-normalized criteria are commonly used as can be seen in *Table 3. 3* and *Table 3. 4*.

Table 3. 3 Commonly used CC criterion

CC criterion	Definition
Cross-Correlation (CC)	$C_{CC} = \sum f_i g_i$
Normalized Cross-Correlation (NCC)	$C_{NCC} = \frac{\sum f_i g_i}{\sqrt{\sum f_i^2 \sum g_i^2}}$
Zero-Normalized Cross-Correlation (ZNCC)	$C_{ZNCC} = \frac{\sum \bar{f}_i \bar{g}_i}{\sqrt{\sum \bar{f}_i^2 \sum \bar{g}_i^2}}$

Table 3. 4 Commonly used SSD criterion

SSD criterion	Definition
Sum of Squared Differences (SSD)	$C_{SSD} = \sum (f_i - g_i)^2$
Normalized Sum of Squared Differences (NCC)	$C_{NSSD} = \sum \left(\frac{f_i}{\sum f_i^2} - \frac{g_i}{\sum g_i^2} \right)^2$
Zero- Normalized Sum of Squared Differences (ZNSSD)	$C_{ZNSSD} = \sum \left(\frac{\bar{f}_i}{\sum \bar{f}_i^2} - \frac{\bar{g}_i}{\sum \bar{g}_i^2} \right)^2$

Where in Table 3. 3 and Table 3. 4, $\bar{f}_i = f_i - \bar{f}$ and $\bar{g}_i = g_i - \bar{g}$; $\bar{f} = \frac{1}{n} \sum_{i=1}^n f_i$ and $\bar{g} = \frac{1}{n} \sum_{i=1}^n g_i$.

In order to compute the displacements of a point P from the reference image, a square reference subset of $(2M + 1) \times (2M + 1)$ pixels centered at the interrogated point $P(x_0, y_0)$ is chosen and used to track its corresponding location in the deformed image. To track the position of the reference subset in the deformed image accurately, a criterion must be established to evaluate the similarity or difference between the selected reference subset and the target subset. It can be done by sliding the reference subset in the searching area of the deformed image and computing the correlation coefficient at each location.

The reason why a square subset, rather than an individual pixel, is selected for matching is that the subset comprising a wider variation in gray levels will distinguish itself from other subsets, and can, therefore, be more uniquely identified in the deformed image [277].

Hence the target subset deformation induced by a shape function or displacement mapping function can be defined as:

$$\begin{aligned} x'_i &= x_i + \xi(x_i, y_j) \\ y'_j &= y_j + \eta(x_i, y_j) \end{aligned} \quad (i, j = -M : M) \quad (3.18)$$

If only rigid body translation exists in the reference subset and deformed subset, in other words, the displacements of each point in the subset are the same, and then a zero-order shape function can be used:

$$\begin{aligned} \xi_0(x_i, y_j) &= u \\ \eta_0(x_i, y_j) &= v \end{aligned} \quad (3.19)$$

Obviously, the zero-order shape function is not sufficient to depict the shape change of the deformed subset. Thus, the first-order shape function that allows translation, rotation, shear, normal strains and their combinations of the subset is most commonly used:

$$\begin{aligned} \xi_1(x_i, y_j) &= u + u_x \Delta x + u_y \Delta y \\ \eta_1(x_i, y_j) &= v + v_x \Delta x + v_y \Delta y \end{aligned} \quad (3.20)$$

Besides, the polynomial second-order shape functions, proposed by Lu et al. [75] can be used to depict more complicated deformation states of the deformed subset:

$$\begin{aligned}\xi_2(x_i, y_j) &= u + u_x \Delta x + u_y \Delta y + \frac{1}{2} u_{xx} \Delta x^2 + \frac{1}{2} u_{yy} \Delta y^2 + u_{xy} \Delta x \Delta y \\ \eta_2(x_i, y_j) &= v + v_x \Delta x + v_y \Delta y + \frac{1}{2} v_{xx} \Delta x^2 + \frac{1}{2} v_{yy} \Delta y^2 + v_{xy} \Delta x \Delta y\end{aligned}\quad (3.21)$$

Where $\Delta x = x_i - x_0$, $\Delta y = y_j - y_0$, u , v are the x- and y-directional displacement components of the reference subset center, $P(x_0, y_0)$, u_x , u_y , v_x , v_y are the first-order displacement gradients of the reference subset and u_{xx} , u_{xy} , u_{yy} , v_{xx} , v_{xy} , v_{yy} are the second-order displacement gradients of the reference subset.

The DIC method in this study was applied and images were continuously obtained during the whole loading branch. Displacement fields were calculated and crack opening were derived. Camera with 50 mm macro lens was mounted in order to image a complete ligament area above the notch of the beam. The digital camera has a resolution of 2452×2056 pixels and gives 256 levels of grey output. A speckle pattern of black and white paint was sprayed onto the surface of the specimen to improve the displacement resolution. The commercial package Vic2D by Correlated Solution is used to perform digital image correlation analysis and NCC correlation criterion is adopted. Gaussian weight functions that provide the best combination for spatial and displacement resolutions are used [278].

3.3.3 AE and DIC investigation

In quasi-brittle material, the main reason for the size effect is the existence of a non-linear zone of micro-cracking ahead of the crack tip called the fracture process zone (FPZ) as showed in *Figure 3. 12*. A relatively large FPZ length occurs in concrete compared to other quasi-brittle materials. So due to the existence of the large size of the FPZ in concrete structures, a strong size-effect is produced [279]. Generally, in small specimens (with a FPZ larger than the cross-sectional dimensions), the FPZ cannot develop to its full length, the energy consumed by fracture is less than in a large specimen [280]. It is necessary to analyse the FPZ in order to have a better understanding of the size effect. The size of the fracture process zone has been studied by many researchers using different methods [30] such as X-rays, Acoustic emission (AE) and Digital image correlation (DIC). Here for comparison, AE and DIC are adopted.

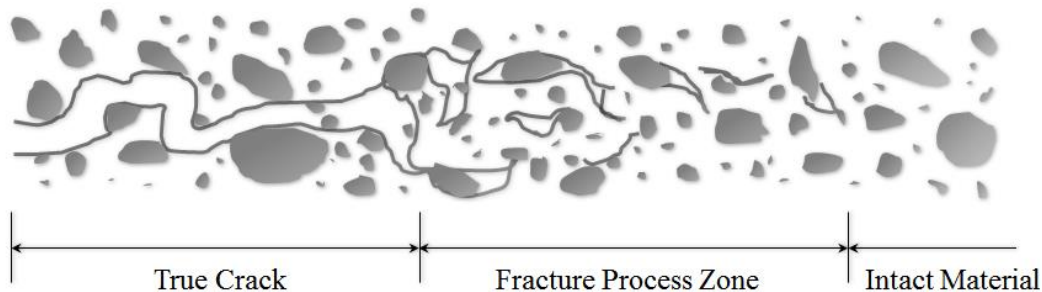


Figure 3. 12 Fracture Process Zone in concrete

The zone of FPZ corresponds to the area with the high number of AE events. So the length and width of fracture process zone are evaluated according to the method used by Alam et al. [43] and

Saliba et al. [37]. The boundary of the FPZ is assumed where number AE events are reduced to 20 % of the peak of the cumulative AE events (N_{max}). Thus, the average width of the FPZ at a certain loading instant can be defined as the width where cumulative AE events at each x location are more than or equal to 20 % of N_{max} . Similarly, the average length of the FPZ at a certain loading instant can be defined as the length where cumulative AE events at each y location are more than or equal to 20 % of N_{max} . Figure 3. 13 shows an example of the cumulative number of events in the post-peak loading step. It can be seen that the number of events is more important in the zone above the notch ($x_{notch} = 125 \text{ mm}$) and decreases gradually on both sides.

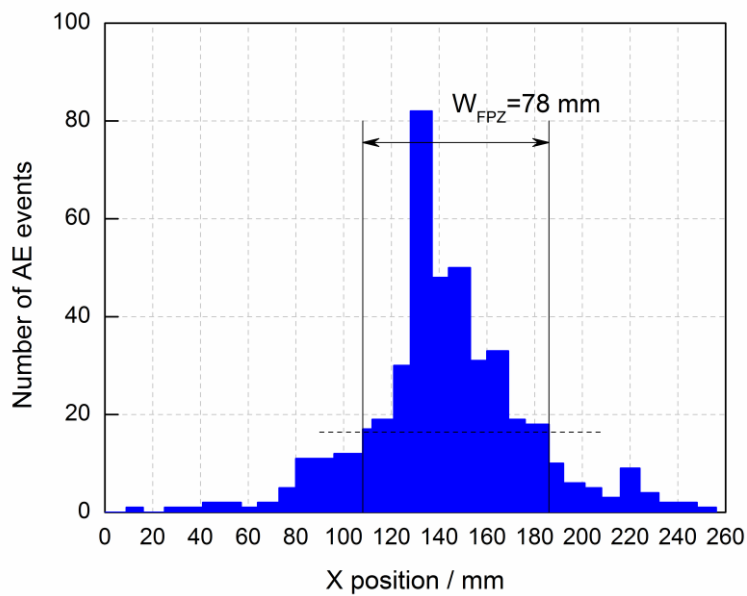
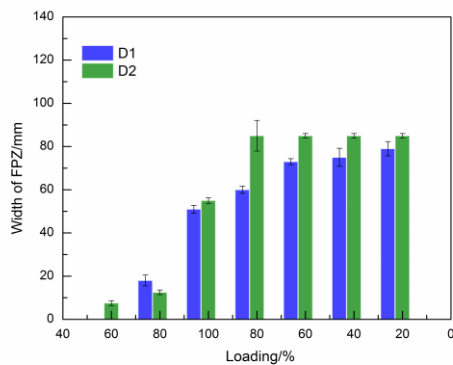
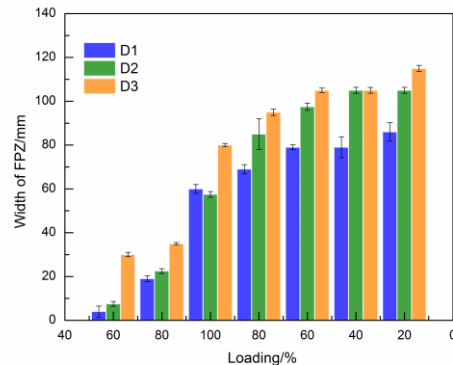


Figure 3. 13 Example of cumulative AE events at each x location and calculation of W_{FPZ}

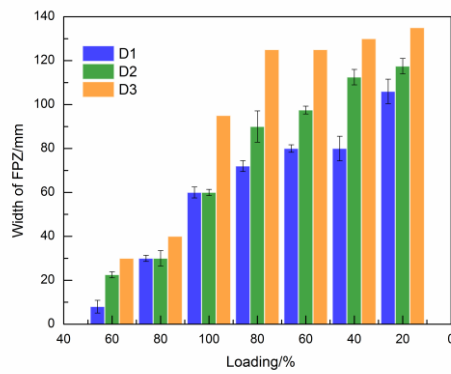
The width of FPZ and the relative fracture length ($L_{crack}/L_{ligment}$) at different loading intervals obtained with the AE technique are plotted in Figure 3. 14 and Figure 3. 15, respectively.



a) Width of FPZ for series C05

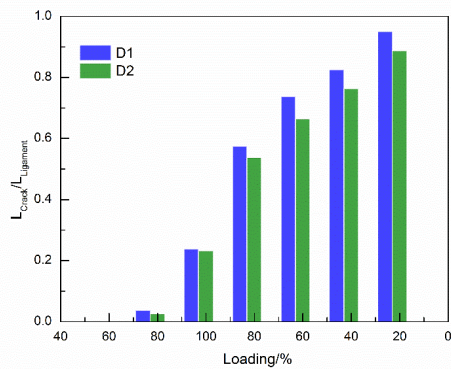


b) Width of FPZ for series C10

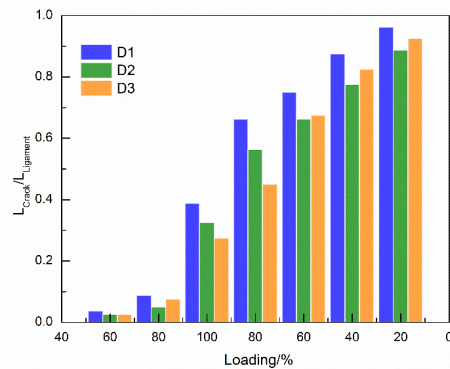


c) Width of FPZ for series C20

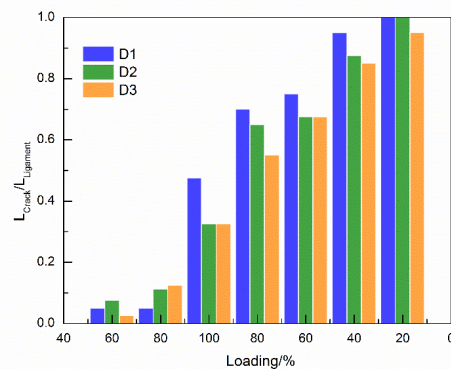
Figure 3. 14 Evolution of width of FPZ with loading steps for each concrete series



a) Relative crack length for series C05



b) Relative crack length for series C10



c) Relative crack length for series C20

Figure 3. 15 Evolution of relative crack length with loading steps for each concrete series

It can be seen that the width of FPZ increases with the loading steps before the peak force and then it starts becoming stable in the post-peak regime. The same trend is observed for all beam sizes. However, the width of FPZ is greater for the larger beam size in the post-peak loadings. The relative crack length also increases with the loading steps but decreases with the size of the specimen. This

can be explained by the decrease of the stress gradient with increasing specimen size [281] and with the specimen size increasing, the mechanical behaviour becomes more brittle. In larger specimen, more strain energy is available to make the failure zone propagates. Besides, the fracture growth can be divided into three stages. The first stage is range from the crack initiation to 80 % of peak load. In this period, the growth of crack is smooth. Then in the second stage, which is in the range of 80 % of pre-peak load and 80 % post-peak load, the growth of crack experiences a steep increase. In the last stage, when the crack approaches the backface of the specimen, the crack propagation is becoming relatively slow. These stages of crack propagation have been studied by Alam et al. [43]. They found out that in the first phase, the energy dissipation process is active. In the second phase, continuum-discontinuum transition occurs. However, in the third phase, crack opening phase becomes active and energy dissipation rate decreases. For each concrete type, the trend of FPZ width and length growth is similar when the size of the specimen is varied.

For comparison, the analysis of FPZ using DIC technique is also presented. When a macrocrack is formed, there is a sudden jump in the axial displacement field across the crack. The crack opening refers to the displacement jump between two points located at each side of the crack can be termed as local crack opening displacement. The displacement jump increases with the loading steps as shown in *Figure 3. 16*.

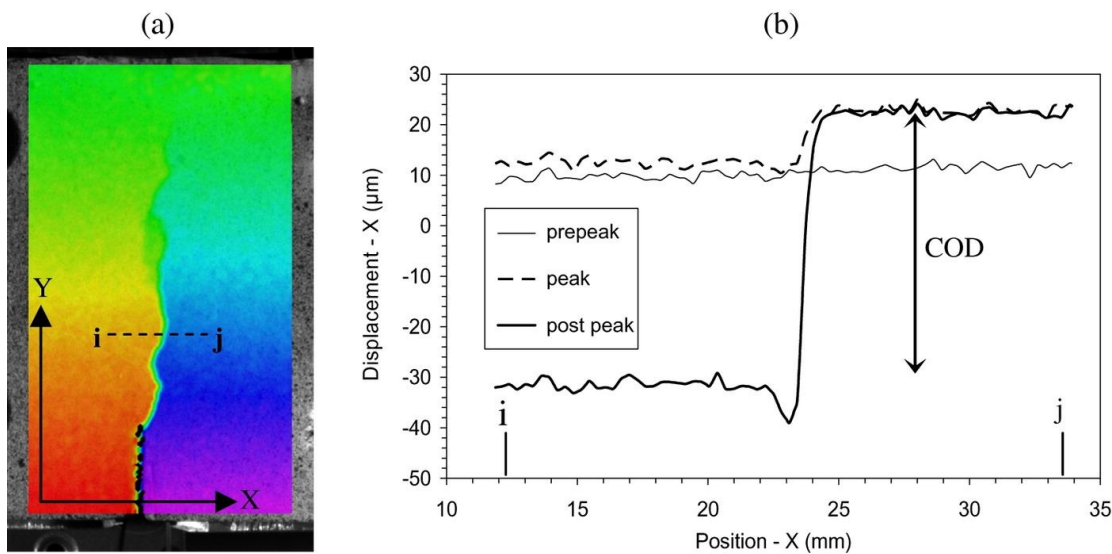


Figure 3. 16 Measurement of COD from the DIC method: (a) displacement field and definition of line i-j; (b) displacement profile plotted along the line i-j. [42]

As the crack path obtained by experiments is very tortuous, so the crack opening displacement at different crack length is calculated from the displacement vectors located at 5 mm of the crack path, as shown in *Figure 3. 17*.

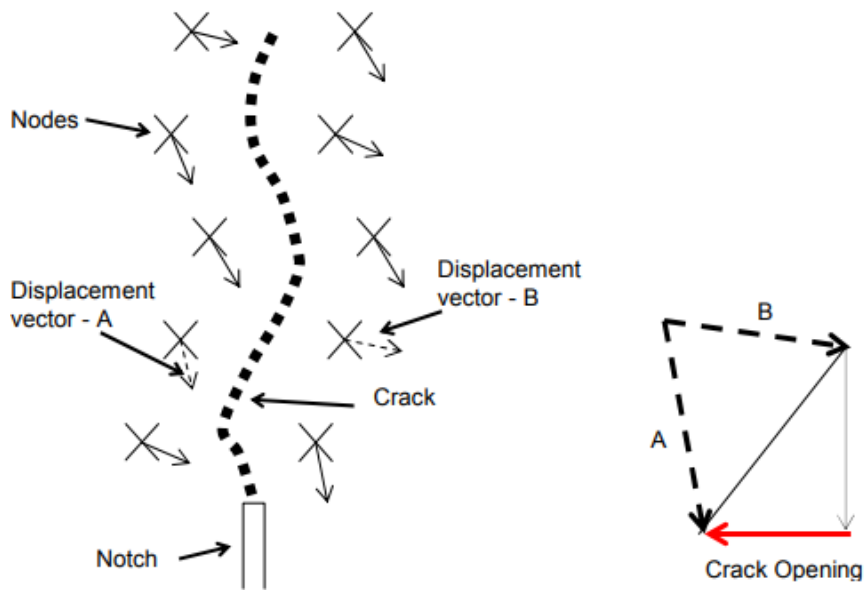
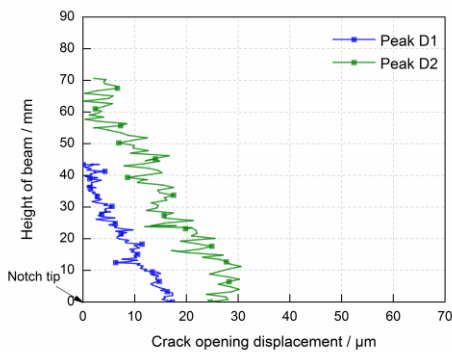
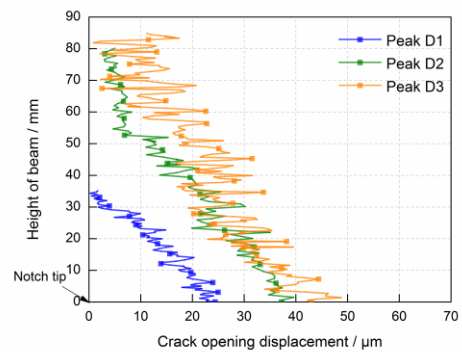


Figure 3. 17 Determination of the crack profile from a displacement field [282]

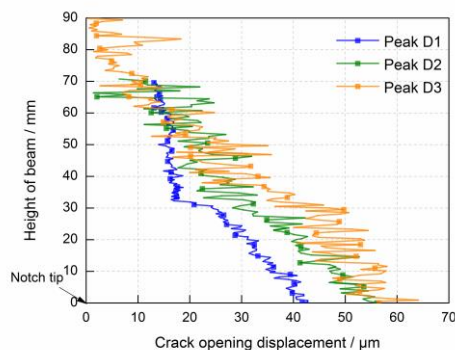
The digital camera captures the surface of the specimen above the notch, thus the complete opening profiles can be obtained from the axial displacement field data using VIC-2D. The crack opening profiles at peak load for each concrete series are presented in Figure 3. 18.



a) Crack opening profiles for C05



b) Crack opening profiles for C10



c) Crack opening profiles for C20

Figure 3. 18 Crack opening displacement profiles at peak load for each series

The crack opening displacement throughout the crack length is greater with the specimen size increases. It should be noticed in *Figure 3. 18 c)*, crack opening profile of D1 beam deflects which is caused by the formation of aggregate interlock at the peak loading stage. This is due to the fact that an aggregate comes into the path and causes the deflection of crack [282]. The fracture tip can be assumed where the COD profile approaches to zero crack opening displacement. From *Figure 3. 18*, it can be seen that the fracture length at peak load increases with the increase of the specimen height. The same results are obtained by the experimental results of Wu et al. [283] and modelling and analytical investigation of Aissaoui and Matallah [284].

3.4 Discussion and experimental exhibition of size effect

Size effect is the most important fracture phenomena of quasi-brittle material like concrete. Using geometrically similar concrete specimens will exhibit a pronounced size effect on their failure loads. Therefore, it is worthwhile to relate the size effect behaviour to their fracture properties. Bažant and Oh [193] proposed size effect method (SEM) based on the ductile-brittle transition of the failure mode of geometrically similar fracture specimens. According to linear elastic fracture mechanics (LEFM), the normal stress (σ_N) decreases in proportion to the square root of the depth of the specimen ($D^{-1/2}$). Hence the plot of $\log(\sigma_N)$ versus $\log(D)$ is an inclined line with a slope of $-1/2$. However, in concrete structures, size effect is transitional between the strength criterion representing the horizontal line and size effect of LEFM represented by the inclined line. According to Bažant [193], the equation of nominal strength can be written as follows:

$$\sigma_N = \frac{Bf_t}{\sqrt{1 + \frac{D}{D_0}}} \quad (3.22)$$

Where: f_t is the size-independent tensile strength of concrete;

B and D_0 are the parameters depending on structural geometry;

D is the characteristic structural dimension;

Therefore, the size effect can be analysed by using a linear regression of the stresses of geometrically similar specimens of varying sizes, and according to *Equation 3. 22*, the coefficients Bf_t and D_0 can be determined as:

$$Y = AX + C \quad (3.23)$$

$$X = D, Y = (1/\sigma_N)^2, D_0 = C/A, Bf_t = 1/\sqrt{C} \quad (3.24)$$

Based on the concept of LEFM, Bažant and Kazemi [285] concluded that in the failure of structures of infinite size, the two major fracture parameters, fracture energy (G_f) and the effective length of process zone (c_f) can be determined through:

$$G_f = \frac{g(\alpha_0)}{AE_c} \quad (3.25)$$

$$c_f = \frac{g(\alpha)}{g(\alpha)} \cdot \frac{C}{A} \quad (3.26)$$

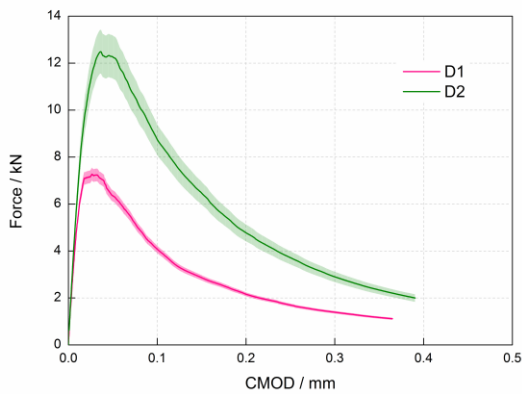
Where E_c is the modulus of elasticity of concrete; A is the angular coefficient of regression line; C is the y-intercept of the regression line, $g(\alpha)$ is the non-dimensional energy release rate and $g'(\alpha)$ is the derivative of $g(\alpha)$ with respect to the relative crack length ($\alpha = a/D$). These functions ($g(\alpha)$ and $g'(\alpha)$) are geometry dependent and obtained according to RILEM-TC 89 recommendation [239].

Except the fracture parameters mentioned above, there are some other parameters can also indicate the fracture behaviours of concrete. For example, the brittleness of concrete can be represented by the parameter known as characteristic length (l_{ch}) [193]. The critical stress intensity factor (K_{IC}) has been used to represent the fracture toughness in previous investigations [52]. K_{IC} and l_{ch} can be calculated using the equations below.

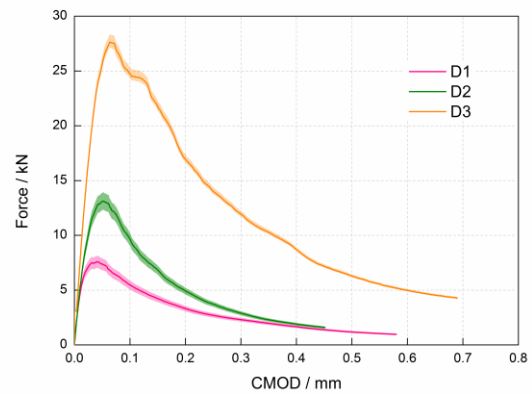
$$K_{IC} = \sqrt{E_c G_f} \quad (3.27)$$

$$l_{ch} = \frac{E_c G_f}{f_t^2} \quad (3.28)$$

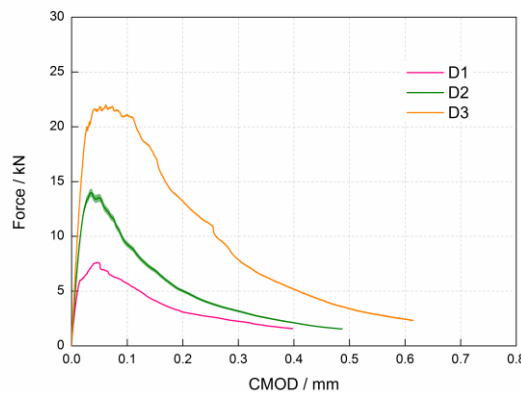
Figure 3. 19 shows the mechanical response between the average force and the mouth opening displacement for each specimen size.



a) Average Force-CMOD curves for C05



b) Average Force-CMOD curves for C10



c) Average Force-CMOD curves for C20

Figure 3. 19 Average Force-CMOD curves for each mix design

It can be observed in *Figure 3. 19*, the relationship between the force and the notch mouth opening displacement is different to each specimen size. In the pre-peak regime, the slope is indifferent to specimen size. After the peak stage, the applied load dropped sharply, showing a larger rate of decrease with increasing D .

Based on the aforesaid method, the size effect plots for each concrete are presented in *Figure 3. 20*. All the size effect law curves obtained are the same. Therefore, all the results data can be plotted in *Figure 3. 21*.

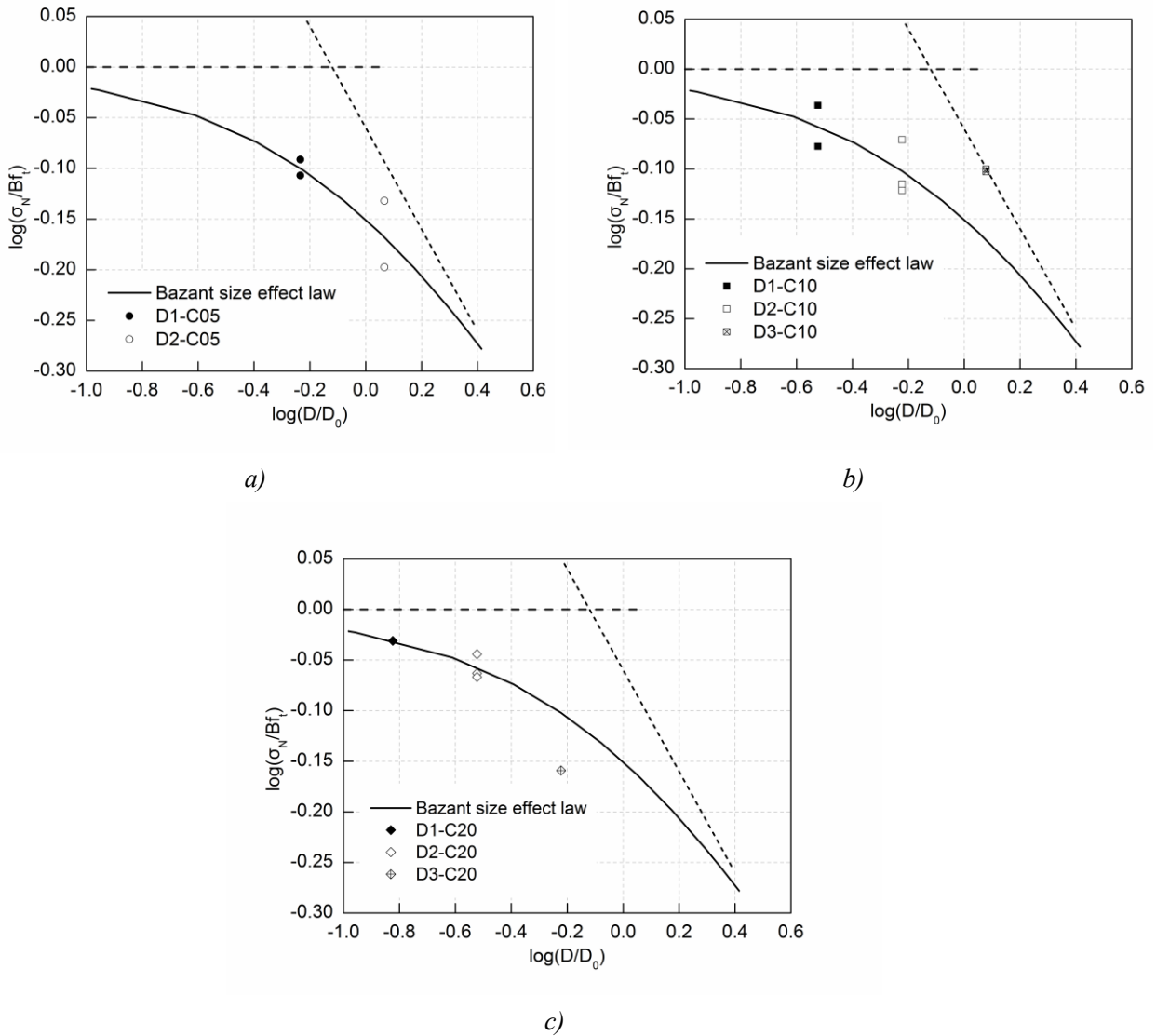


Figure 3. 20 Size effect law for each concrete series: (a) C05; (b) C10; (c) C20

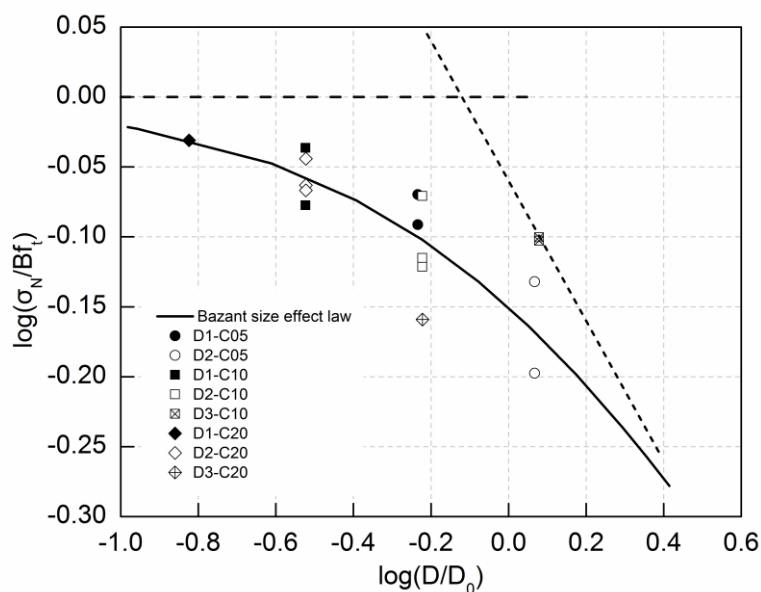


Figure 3. 21 Size effect for different maximum aggregate size

Table 3. 5 Fracture parameters for each concrete mix according to RILEM size effect method

Series	C05	C10	C20
Properties			
d_{\max} (mm)	5.25	10.5	21.0
Bf_t	4.21	4.08	3.69
D_0	166.26	333.56	666.18
K_{IC} (MPa \sqrt{m})	1.11	1.50	1.92
c_f (mm)	29.9	60.1	119.9
l_{ch} (mm)	134.1	225.6	305.3
G_f (N/m)	42.9	74.5	114.0

As can be seen in Figure 3. 21, with the increase of d_{\max} , the behaviour of specimens approached the hypotheses of strength criterion, which means that the specimens are more ductile when compared with specimens with smaller d_{\max} . Besides, the size effect on the nominal strength is not very pronounced between $D1$ and $D2$, but more prominent between $D2$ and $D3$. A smooth transition from $D1$ to $D3$ can be shown when using Bazant size effect law. The size effect curve passes well through the $D3$ specimens (near to LEFM line for $D3-C10$), but a slight discrepancy for $D1$ and $D2$ specimens. The undesirable results for $D3$ beams may be due to the limitation of the experimental conditions, the $D3$ beams, the loading roller and supports used for the experiment are rotated in order to perform the test using MTS, thus may leading to the unexpected mix mode loading condition during the test. Besides, the number of testing specimens maybe not enough as there exist the scatter of the experimental results. The results of $D3$ the beams need to be further repeated again.

Besides, it can be noticed that the results of $D2-C20$ and $D1-C10$; $D2-C10$ and

D1–C05 ; D3–C10 and D2–C05 have the similar results. So apart from using the geometrically similar specimens, changing the depth of the specimen and the maximum size of aggregate at the same time can also obtain the similar trend. The relation between the aggregate effect and size effect will be discussed detailed in Chapter 4.

It can be seen that from Table 3. 5, effective fracture process zone length (c_f) is increased by increasing the maximum aggregate size. It means that concrete with small coarse aggregate is more brittle than that with bigger coarse aggregate [286]. This may be also attributed to the changes in fractal dimensions and longer cracking path. Yan et al. [234] showed that in concrete, ductility index is related to fractal dimensions, while coarse aggregate is debonded and fractal dimensions are increased when the maximum aggregate size is increased. Besides, concrete with larger aggregate contains more weakened ITZ. It also exhibits a larger process zone and relatively more deviation in cracking path. In other words, when the maximum aggregate size becomes smaller, the effect of bridging and aggregate interlocking in the crack path is attenuated. The fracture toughness (K_{IC}) and fracture energy (G_f) also increase with an increase of maximum aggregate size d_{max} . This may be due to reason that during the process of crack propagation, microcracking and matrix-aggregate debonding consumes considerable energy, therefore, the increase of aggregate size causing a larger crack area, thus increasing the energy demand required for crack growth. The reason explained for the variation of fracture energy is also responsible for the variation of fracture toughness. The same tendency for fracture toughness mentioned above also has observed in previous researches [287-289]. Jeng et al. [290] reported that when d_{max} increases from 4.75 to 19 mm, G_f increases from 21.1 N/m to 35.4 N/m for normal concrete (NC). Rao et al. [289] found that for high-strength concrete (HSC), when d_{max} increases from 4.75 to 20 mm, G_f increases from 76.6 to 142 N/m. Karamloo et al. [235] also obtained the similar results for self-compacting lightweight concrete (SCLC) with w/c of 0.35 and 0.4; it showed that when d_{max} increases from 9.5 to 19 mm, G_f increases from 25.5 N/m to 36.26 N/m and 16.9 N/m to 31.5 N/m. Except c_f and G_f increased by increasing the maximum aggregate size, the characteristic length (l_{ch}) also showed the same trend. Petersson [291] studied the normal vibrated concrete (NVC) with w/c ratio of 0.5 and reported that with increasing aggregate size from 8 mm to 16 mm, l_{ch} increases from 233.5 mm to 332.2 mm. Beygi et al. [292] studied self-compacting concrete (SCC) with two different strength levels, medium strength (M-series) and high strength (H-series). They found that an increase of aggregate size from 9.5 mm to 19 mm causes l_{ch} to augment from 263.9 mm to 466.4 mm and from 209.2 mm to 394.7 mm for M-series and H-series concrete respectively. The D_0 obtained for C05, C10 and C20 are 166.26, 333.56 and 666.18. It is almost 2 times when the maximum aggregate size used for concrete is doubled. So, with the increase of d_{max} , leading to a higher value for D_0 , which is corresponding to lower brittleness of concrete. The study of Moseley et al. [293] also concluded that with an increase of d_{max} , concrete ductility increases. The parameter c_f and l_{ch} , are related to concrete brittleness and with an increase of c_f , concrete brittleness is decreased.

In order to investigate the failure mode of the structure, β known as brittleness number, is introduced in SEM. The expression to calculate the brittle number is given below [294].

$$\beta = \frac{g(\alpha)D}{g'(\alpha)c_f} \quad (3.29)$$

Figure 3. 22 shows the variation of β with the variation of the depth of the beam specimens. As it can be seen, all data lie in the range of nonlinear fracture mechanics ($0.1 \leq \beta \leq 10$). The failure

should be analysed according to LEFM when $\beta > 10$ and the method of the analysis approaches strength criterion when $\beta < 0.1$ as reported by Bažant and Kazemi [84].

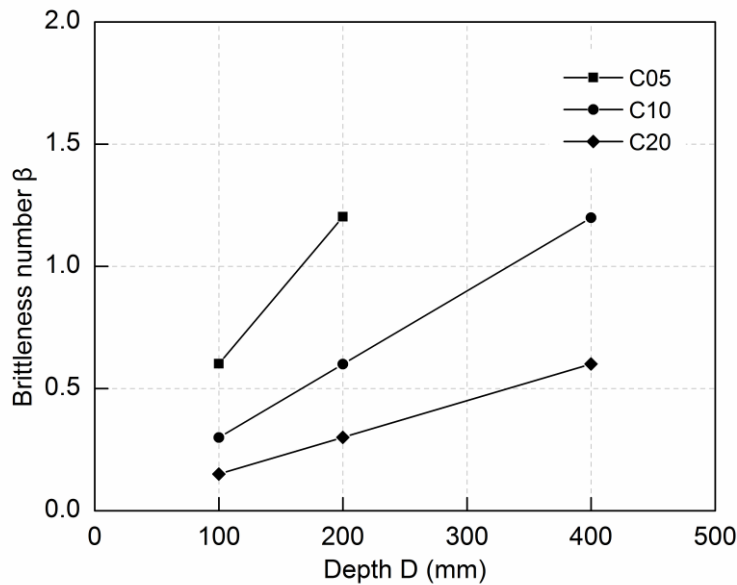


Figure 3. 22 Variation of brittleness number with depth

3.5 Numerical modelling for size effect using Discrete Element Method

Due to the fact that DEM has advanced advantages in stimulating cemented material behaviour, grain level control and exploring the microscopic mechanisms, in this section, the general size effect is modelled by a discrete element. The disadvantage of DEM is time-consuming, so here only series C10 concrete is performed and the positions of the aggregates are fixed during the calibration processes. The influence of aggregates positions will be studied in the near future. The modified parallel bond model that developed in Chapter 2 is applied in this modelling. The microparameters for mortar are firstly determined by LM method. Then the microparameters for ITZ and aggregate are determined. Finally, the general size effect is performed by using all the microparameters obtained. The detailed procedures have been introduced in Chapter 2.

3.5.1 Calibration of microparameters for mortar phase

The generation procedures and calibration were the same as illustrated in the first chapter. The calibration of mortar parameters is performed on the standard tests: compression test on $40 \times 40 \times 40$ mm³ specimen and, bending strength on $40 \times 40 \times 160$ mm³ specimen and Young's modulus was determined by $\phi 110 \times 220$ mm² cylindrical specimen in compression. The particle radius used in the modelling of mortar was ranging from 0.25 mm to 0.5 mm. The density of particles was given as 2100 kg/m³ as the same density measured from the experiment. A local damping coefficient of 0.7 was used, which is commonly used for mortar and concrete. This high damping coefficient was used to ensure a quasi-static loading condition [177]. The applied loading rate in the test should be

sufficiently low to ensure that the specimen remains in quasi-static equilibrium throughout the test. Considering the calculation time and based on the previous studies [155, 177, 179, 180], a loading rate of 0.01 m/s was adopted for compression test and the constant vertical velocity 0.002 m/s [143] was given for three-point bending test. Micro parameters (E_c (\bar{E}_c), k_n/k_s (\bar{k}_n/\bar{k}_s), $\bar{\sigma}_t$, \bar{C} , and ϕ) for mortar obtained through the calibration process are listed in Table 3. 7. Note that the calibrated values obtained bear no resemblance to mortar macro properties. Finally, the samples with 4877 particles for $40 \times 40 \text{ mm}^2$ (compression) specimen; with 49627 particles $110 \times 220 \text{ mm}^2$ (compression) specimen; and with 13134 particles for $40 \times 160 \text{ mm}^2$ (bending) specimen are generated respectively. Then the compressive strength, Young's modulus, and three-point bending force are used in the procedures for finding the microparameters using the Levenberg Marquardt (LM) algorithm.

The comparison between the experimental results and modelling results obtained from calibrated parameters are listed in Table 3. 6.

Table 3. 6 Comparison of laboratory tests and modelling results

Mechanical Properties	Mortar	
	Laboratory tests	Modelling Results
Compressive strength (σ_c) (MPa) $40 \times 40 \times 40 \text{ mm}^3$	64.9±1.34	66.3
Compressive strength (σ_c) (MPa) $\phi 110 \times 220 \text{ mm}^2$	55.4±4.20	60.1
Young's modulus (E) (GPa)	25.1±0.31	25.1
Three-point bending force (F) (kN)	2.40±0.05	2.37

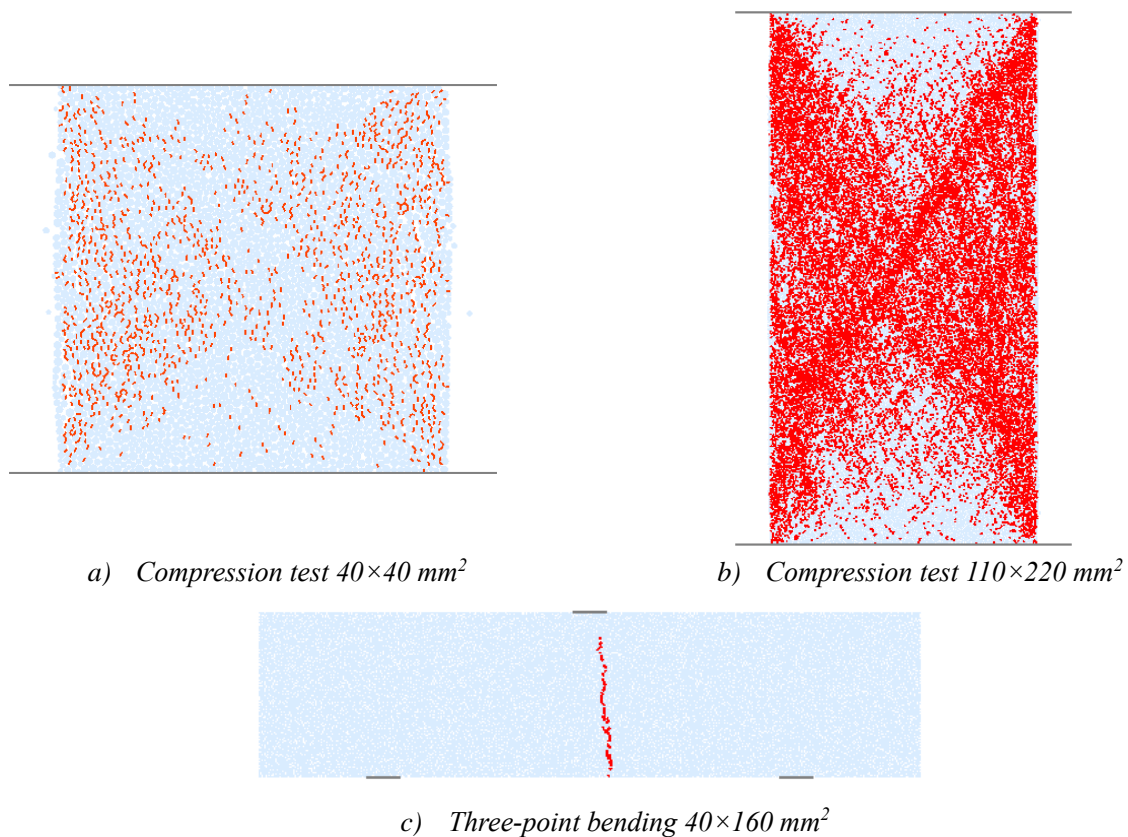


Figure 3. 23 Failure patterns for each calibration mortar sample

Table 3. 6 demonstrates that the modified parallel bond model can satisfy compressive, tensile/bending, stiffness properties and behaviour of mortar using the same microscopic parameters. Therefore, this approach can be easily used to model the complex behaviour of mortar under multi-axial loadings. The failure patterns of the sample are given in Figure 3. 23. The failure patterns show a correct description of the fracture process in each test. The comparison between experiment and numerical compressive stress-strain curves is shown in Figure 3. 24. The numerical curve is almost the same trend with the experimental curve.

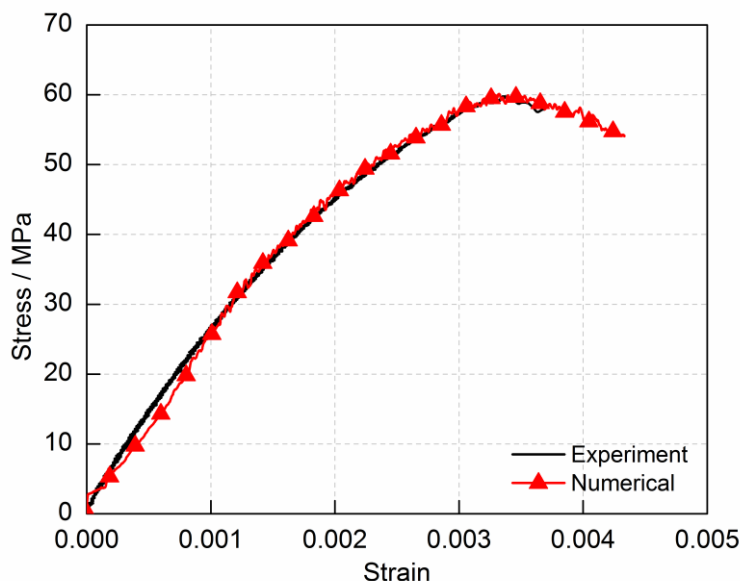


Figure 3. 24 Comparison experimental and numerical stress-strain curves for mortar

Table 3. 7 Micro parameters obtained through the calibration process

Micro Parameters	Value	Micro Parameters	Value
Minimum particle diameter d_{\min} (mm)	0.5	Radius multiplier λ	1.0
Ratio of maximum to minimum particle diameter d_{\max}/d_{\min}	2.0	Ratio of normal to shear bond stiffness \bar{k}_n/\bar{k}_s	1.77
Effective modulus E_c (GPa)	18.3	Effective bond modulus \bar{E}_c (GPa)	18.3
Ratio of normal to shear stiffness k_n/k_s	1.77	Moment contribution factor β_1	0.1
Friction angle ϕ ($^\circ$)	18.0	Tensile strength $\bar{\sigma}_t$ (MPa)	8.0
Maximum shear strength multiplier γ	1.0	Residual friction angle ϕ_r ($^\circ$)	26.6
Cohesion strength \bar{C} (MPa)	51.3		

3.5.2 Effect of 2D and 3D

In comparison with 2D simulation, the 3D simulation is generally more accurate because the 3D

microstructure and boundary conditions are closer to the realistic microstructure and state of the material. However, the 2D simulation results may perform good and close to the actual results under the assumption that material is isotropic in the third dimension. At present few studies have been carried out to compare the 2D and 3D simulations with the same model parameters. In order to confirm the conclusions made from 2D simulations, 3D simulations are performed in this study. Compression test on $40 \times 40 \times 40 \text{ mm}^3$ specimen is chosen to study the effect of 2D and 3D. Finally, 4877 particles are generated for the 2D specimen and 244120 particles are generated for the 3D specimen as shown in *Figure 3. 25*. The computer used in the simulation is Intel(R) Core(TM) i5-4590 CPU @ 3.30GHz.

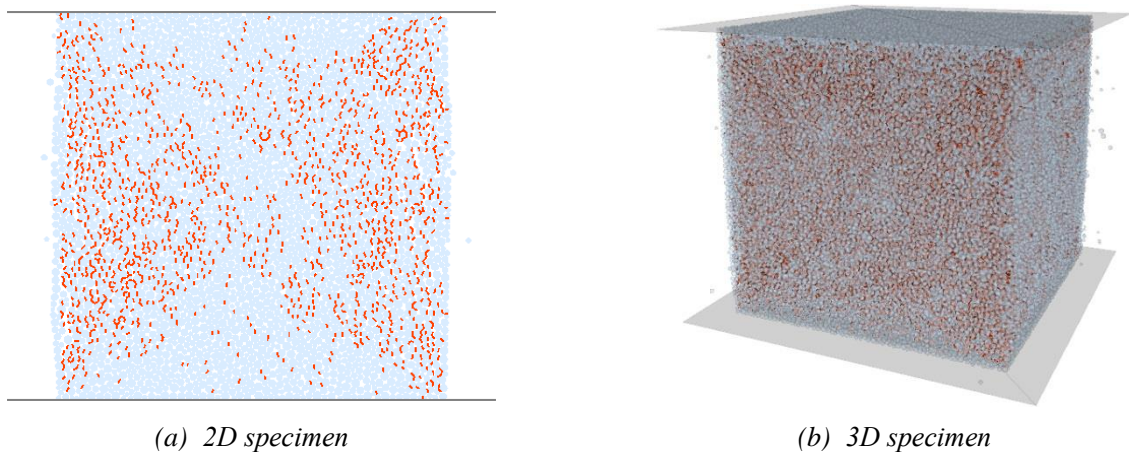


Figure 3. 25 Failure patterns for 2D and 3D specimen

The stress-strain curve for 2D and 3D are presented in *Figure 3. 26*. Notably, the stress-strain curve for 2D specimen fluctuates more than that of 3D specimen, nevertheless, the overall response for 2D and 3D is almost the same.

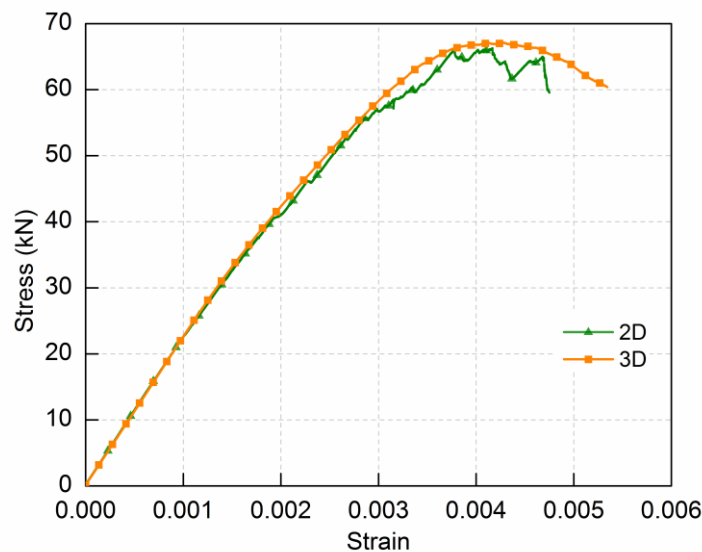


Figure 3. 26 Stress-strain curves for 2D and 3D modelling

Due to the fact that the growing number of particles, it is difficult to simulate real-time large-scale granular flow scene on CPU. So, when the particle size is very small or the system is very large, excessive memory requirements and simulation time are needed for the calculation of DEM. Therefore, the modelling procedures of this study are based on 2D simulation. However, in order to obtain more realistic behaviour, concrete microstructure should be considered in 3D using real aggregate shape.

3.5.3 Microparameters for concrete: ITZ and aggregate phases

Here, the numerical modelling of size effect is only presented for the series C10. Mesoscopic modelling is an efficient way to describe the heterogeneous microstructure where concrete is considered as a three-phase material: Mortar, Aggregate and Interfacial Transition Zone (ITZ) [281, 295]. It makes the microscopic parameters for concrete also three times. However, some estimation of the elastic properties can be made from the literature review. According to the results of Mondal [55], Young's modulus of ITZ is about 70 % - 85 % of that of bulk paste, thus parameters of ITZ can be obtained from that of mortar. Here Young's modulus of ITZ can be taken equal to 80 % of mortar. The local mechanical properties of ITZ are determined using micro-indentation and micro-hardness testing [56-58]. The study of Asbridge et al. [56] found that the micro-hardness of ITZ was about 14 % - 22 % lower than the bulk matrix at w/c of 0.4 and 0.5. The hardness test on cement paste found that there exists a linear relationship between hardness and strength [59, 60]. Therefore, due to the limited experimental results support, it is assumed that a linear relationship between indentation hardness and strength existed for ITZ. In order to reduce the parameters for calibration, tensile strength and cohesive strength of ITZ were also adopted as 80 % of mortar and other parameters kept the same to the mortar. Thus the only micro parameters (E_c (\bar{E}_c), k_n/k_s (\bar{k}_n/\bar{k}_s), $\bar{\sigma}_t$, \bar{C} and ϕ) need to be determined were of coarse aggregates. The compressive strength, Young's modulus, and Brazilian strength are used as target values in the LM approach. Concrete compression test and Brazilian tests on cylindrical specimen $\phi 110 \times 220 \text{ mm}^2$ are adopted for the calibration process. For compression test, 46428 particles are directly generated inside the rectangular specimen area for all concrete series. For the Brazilian test, 19639 particles are directly generated in the circular area for all concrete series. The specimen used for calibration procedures are presented in *Figure 3. 27*. The calibrated micro parameters for aggregate are given in *Table 3. 8*.

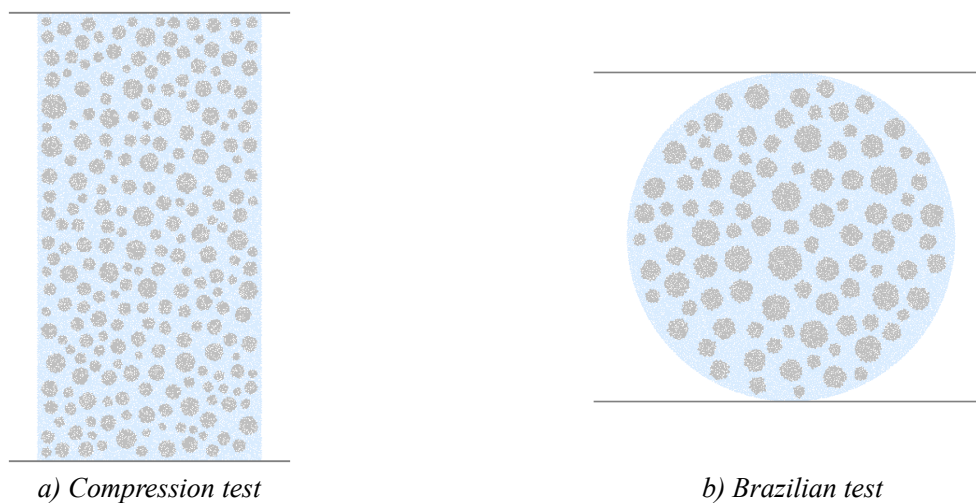


Figure 3. 27 Specimens for calibration procedures for each concrete

Table 3. 8 Parameters determined for ITZ and aggregates

Micro Parameters	ITZ	Coarse aggregate
Effective modulus E_c (GPa)	/	30.1
Normal to shear stiffness ratio k_n/k_s	/	1.6
Radius multiplier λ	1.0	1.0
Friction angle ϕ (°)	18.0	18.0
Effective bond modulus \bar{E}_c (GPa)	14.6	30.1
Ratio of bond normal to shear stiffness \bar{k}_n/\bar{k}_s	1.4	1.6
Moment contribution factor β_1	0.1	0.1
Tensile strength $\bar{\sigma}_t$ (MPa)	6.4	45.0
Cohesion strength \bar{C} (MPa)	41.0	288.6
Maximum shear strength multiplier γ	1.0	1.0
Residual friction angle ϕ_r (°)	26.6	26.6

The comparison between the experimental results and modelling results obtained from calibrated parameters are listed in Table 3. 9.

Table 3. 9 Comparison numerical results with experimental results

Mechanical Properties	Experimental Results	Numerical Results
Compressive strength (σ_c) (MPa)	69.1±1.49	67.5
Young's modulus (E) (GPa)	30.3±1.14	28.8
Brazilian strength (σ_b) (MPa)	3.81±0.32	3.56

The comparison between experimental and numerical stress-strain curves is shown in Figure 3. 28. The numerical curve is almost the same trend with the experimental curve.

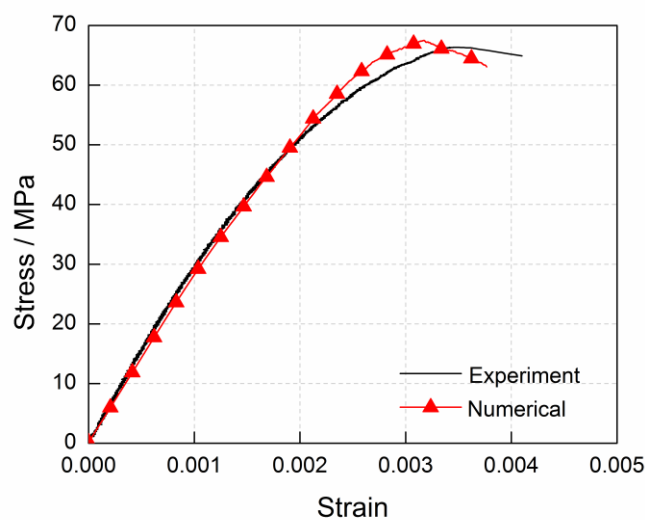


Figure 3. 28 Comparison between experimental and numerical stress-strain curves of C10 concrete

In the Brazilian test, the stress distribution is shown schematically in *Figure 3. 29*. Hertz [296] based on two assumptions: the behaviour of the material is elastic-brittle and it obeys Griffith failure criterion, proposed an analytical solution to calculate the stress distribution for Brazilian test as following.

$$\sigma_x = -\frac{2F}{\pi l} \left(\frac{x^2(R-y)}{\alpha_1^4} + \frac{x^2(R+y)}{\alpha_2^4} - \frac{1}{2R} \right) \quad (3.30)$$

$$\sigma_y = -\frac{2F}{\pi l} \left(\frac{(R-y)^3}{\alpha_1^4} + \frac{(R+y)^3}{\alpha_2^4} - \frac{1}{2R} \right) \quad (3.31)$$

$$\tau_{xy} = -\frac{2F}{\pi l} \left(\frac{x(R-y)^2}{\alpha_1^4} + \frac{x(R+y)^2}{\alpha_2^4} \right) \quad (3.32)$$

and

$$\alpha_1^4 = (R-y)^2 + x^2 \quad (3.33)$$

$$\alpha_2^4 = (R+y)^2 + x^2 \quad (3.34)$$

Where F is the force; R is the radius of the Brazilian disc; l is the thickness of the Brazilian disc.

While Hondros [297] considered the distribution of the loads uniformly over strips of finite width and derived a complete stress solution along the loading diameter as follows.

$$\sigma_\theta = \frac{F}{\pi R l \alpha} \left\{ \frac{[1-(r/R)^2] \sin 2\alpha}{1-2(r/R)^2 \cos 2\alpha + (r/R)^4} - \tan^{-1} \left[\frac{1-(r/R)^2}{1+(r/R)^2} \tan \alpha \right] \right\} \quad (3.35)$$

$$\sigma_r = -\frac{F}{\pi R l \alpha} \left\{ \frac{[1-(r/R)^2] \sin 2\alpha}{1-2(r/R)^2 \cos 2\alpha + (r/R)^4} + \tan^{-1} \left[\frac{1-(r/R)^2}{1+(r/R)^2} \tan \alpha \right] \right\} \quad (3.36)$$

Where F is the force; R is the radius of Brazilian disc; l is the thickness of Brazilian disc; 2α is the angular distance over which is assumed to be distributed radially (usually $\leq 15^\circ$) and r is the distance from the centre of the Brazilian disc. Tensile stress is taken positively.

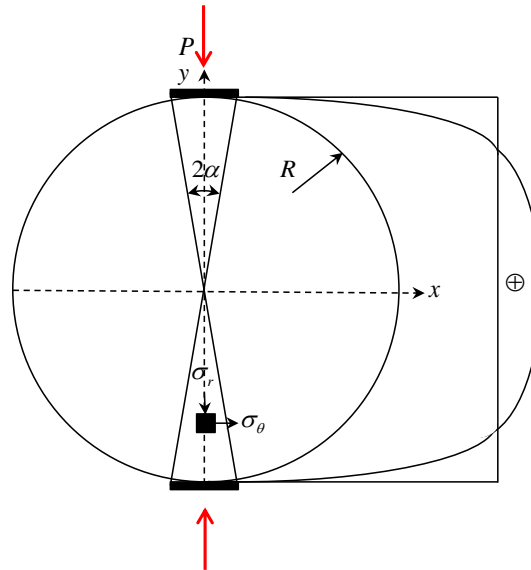


Figure 3. 29 Stress distribution in Brazilian test

In the DEM modelling, the stresses are calculated in measurement circles distributed uniformly over the horizontal and vertical axes as shown in Figure 3. 30.

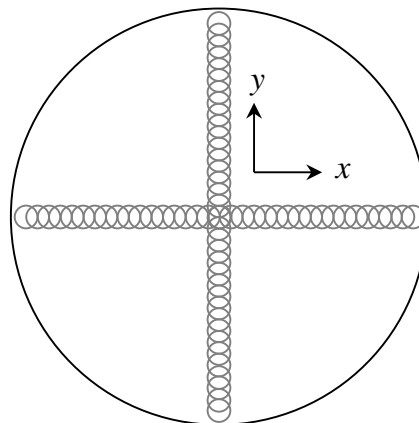


Figure 3. 30 Positions of the measurement circles in the numerical sample

The numerical modelling results are compared with the theoretical results as shown in Figure 3. 31. The principle stress is normalized by $F/(\pi Rl)$. Because the micro parameters for different group particles in the numerical specimen are different, so the numerical stress distribution across the loading diameter is not uniform and fluctuates around the theoretical curves. The compressive stress σ_{yy} shows good agreement with Hondros' solution; however, the tensile stress σ_{xx} is systematically less than the theoretical solution over mid-height. Variation in the results is understandable, due to heterogeneity of concrete as the analytical solution proposed by Hondros is based on the assumption that the material is an equivalent isotropic continuum medium.

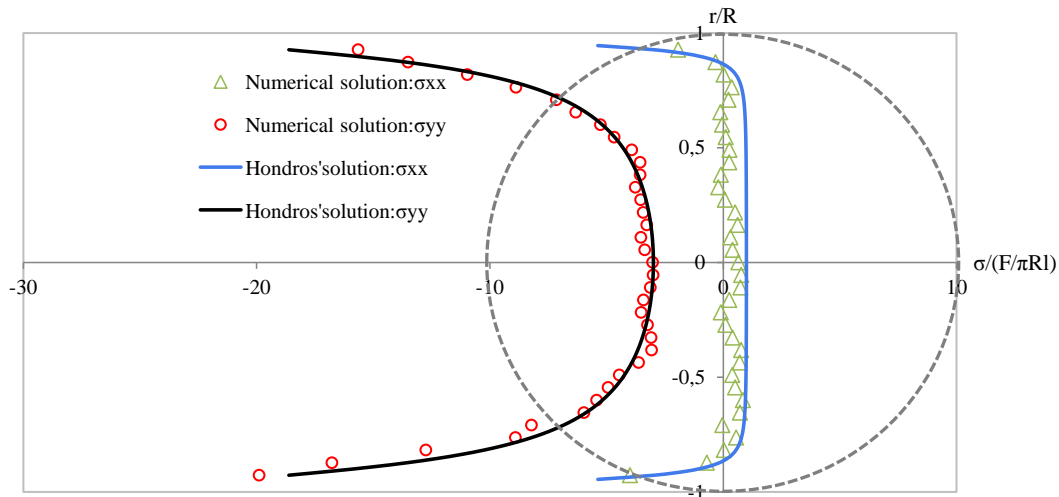


Figure 3.31 Comparison of normalized stresses between numerical modelling and Hondros' solutions in Brazilian test

3.5.4 Numerical modelling of size effect

Once the model parameters for each phase of concrete are determined, the model capability to simulate size effect is analysed in this section. The coarse aggregate used in the concrete mixture had a maximum size equals to 10.5 mm. The generation procedure is almost the same with the mortar specimens, except deleting particles to form the notch after the generation of the specimen. All the loading velocities are kept the same with those used for mortar in the previous section (Section 3.5.1). Three-point bending specimens are generated are shown in *Figure 3.32*.

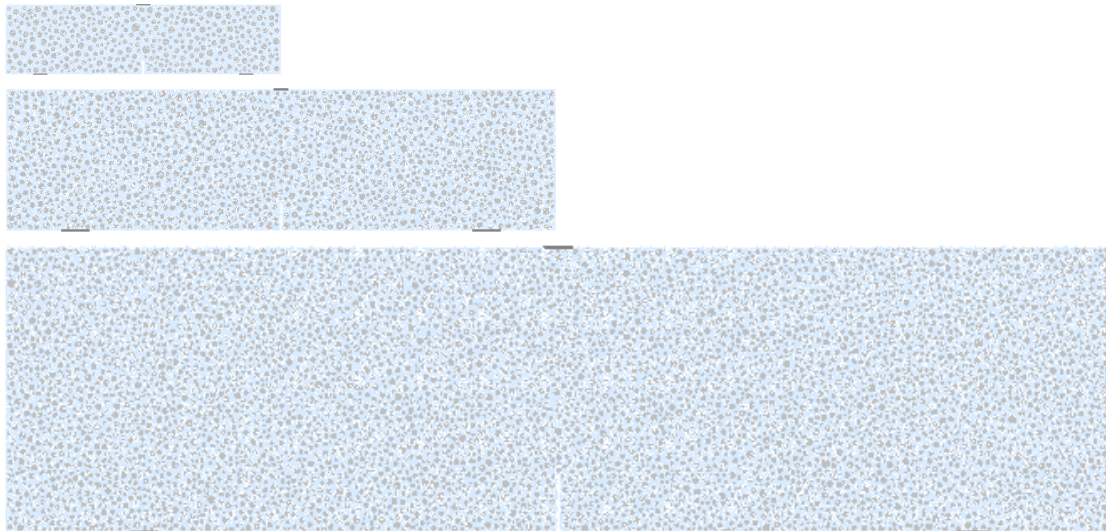


Figure 3.32 Specimens used for the size effect

From the peak load obtained from the modelling results, as given in *Table 3.10*.

Table 3. 10 Comparison between laboratory tests and modelling results

Series	Force / kN	Experimental Results	Numerical Results
D1		7.55±0.76	7.28
D2		13.43±0.14	12.72
D3		26.95±0.12	24.17

The corresponding peak nominal stress can be calculated using Equation 3. 6 and Equation 3. 7. Then the results are summarized in a σ_N versus D size effect plot (Figure 3.14 b)) based on Bažant’s size effect law. The DEM results predict well the peak load for each specimen size and obey the size effect law as shown in Figure 3. 33. The numerical result of D3 specimen also lies precisely on the size effect curve. This shows that the presented discrete element approach and the modified parallel bond model can correctly predict the size effect on concrete.

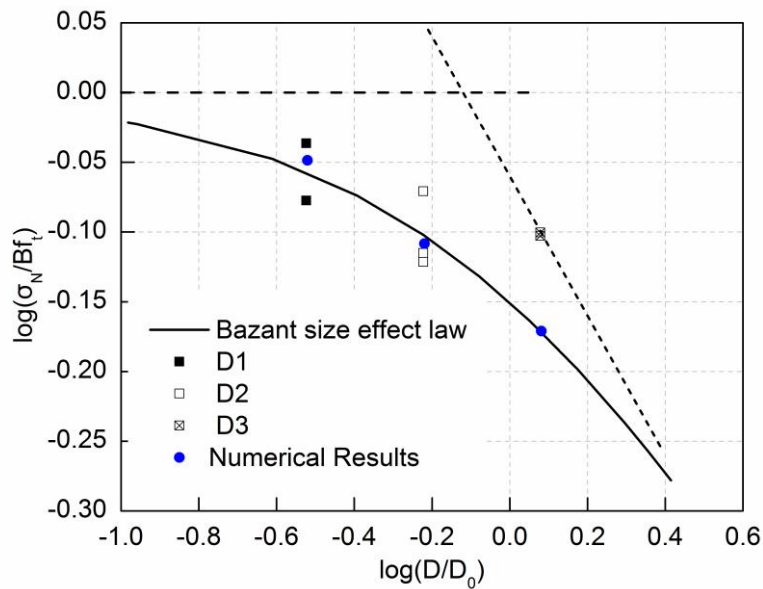
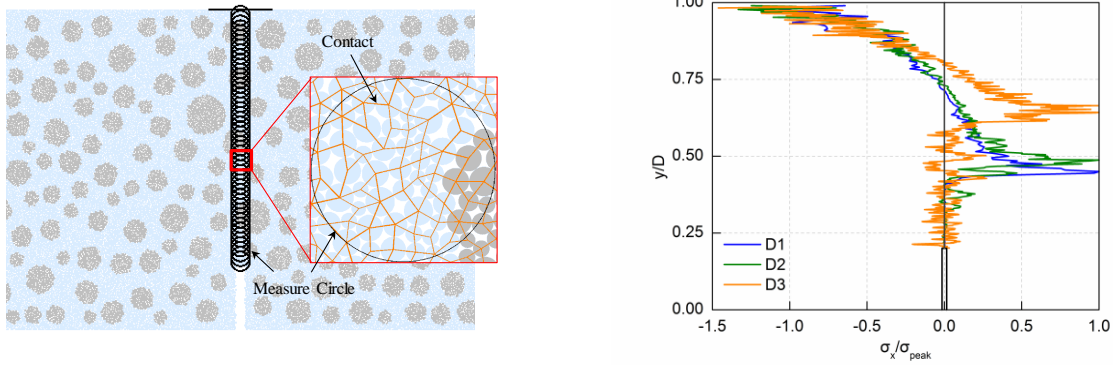


Figure 3. 33 Size effect plot and fitted curves for notched beams

The corresponding normal stress distributions at the midsection of the beams above the crack tips at peak loads are summarized by generating the measure circles at the middle of the beams. At each point, a circle as shown in Figure 3. 34 a) presents a measure circle and it is small enough to make sure that σ_x at the tip of fracture process zone is very close to the tensile strength.



a) Location of measure circles

b) Normal Stress distribution at peak load

Figure 3. 34 Stress measurement and stress distribution at mid-span

The stress distributions clearly show the normalized fracture zone (FZ) lengths change with the size of concrete specimens. The normalized FZ lengths at the peak load experience a decrease when the size of concrete specimen increase. Because of the crack length can be obtained from the results, thus the fracture process zone length can be determined. The comparison of numerical FPZ length and experimental length are given in *Table 3. 11*. The experimental results are much larger when compared with the numerical results at the peak load especially for the larger beams. The reason can be explained by the fact that the modified parallel bond model is a linear elastic model, the force decreases to zero when reaching the peak force. However, for concrete, there exists a softening behaviour. Thus, the differences between experimental results and numerical results occur. So, a softening model needs to be established in order to study the size effect further. In the modelling, the positions of the aggregates are randomly generated first and kept the same position in the modelling. Thus, for the small beams, the positions of the aggregates may play important role that leading some deviations in the modelling.

Table 3. 11 The comparison of FPZ length

Series	l_{FPZ} / mm	Experimental Results	Numerical Results
D1		31 ± 0.39	7
D2		52 ± 0.33	16
D3		88 ± 0.30	21.5

3.6 Summary

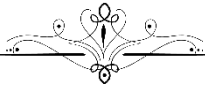
An experimental approach is presented to study the size effect for various concretes with increasing maximum aggregate size. The characteristic structural dimension and the maximum aggregate size (D/d_{\max}) is considered as a key factor in investigating size effect. In this chapter, the ratio D/d_{\max} was up-scaled by using upscaling the structural dimension and keeping d_{\max} constant. Geometrically increasing sized specimens ($D1$, $D2$, $D3$) in accordance with RILEM recommendations. Fracture and Size effect parameters are obtained from size effect analysis. It is

found that as the maximum aggregate size is increased from 5.25 to 21.0 mm, the fracture energy, fracture process zone length, and fracture toughness increases. The results of *D2-C20* and *D1-C10*; *D2-C10* and *D1-C05*; *D3-C10* and *D2-C05* have the similar results. So apart from using the geometrically similar specimens, having the depth of specimen and the maximum size of aggregate at the same time can also obtain the similar trend.

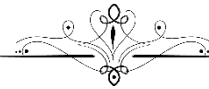
Analysing the results by AE and DIC, it found that the width of FPZ is greater for the larger beam size in the post-peak loadings. The relative crack length also increases with the loading steps but decreases with the size of the specimen. It is due to the fact that the decrease of the stress gradient with increasing specimen size and with the specimen size increasing, the mechanical behaviour becomes more brittle.

Then DEM was used to model the size effect behaviours. The modified parallel bond model developed in Chapter 2 was adopted here. Firstly, compressive and tensile tests were used at the same time in the calibration algorithm. Matrix parameters were determined on mortar specimens. Aggregate particles are considered breakable and parameters are obtained by calibration on concrete specimens. This objective approach gives a good prediction of experimental results under different loading conditions. Then the size effect was modelled by using concrete with a maximum aggregate size 10.5 mm. The numerical results were in compliance with experimental results.

A New Approach to Size Effect by Scaling Microstructure



In this chapter, size effect is analysed by scaling of aggregate size (d_a). Three types of concrete mix are designed (C05, C10, and C20) with the same aggregate to mortar volumetric ratio and same mortar properties, where only the aggregate sizes are changed. Aggregate sizes were up-scaled in C05, C10 and C20 concrete such that the volumetric fraction for each class of aggregate with respect to maximum aggregate size in each concrete remains same. The experimental and numerical investigation is done in order to study the role of the ratio of the characteristic structural dimension (D) and the maximum aggregate size (d_{max}) in size effect.



4.1 Introduction

It is known that the mechanical behaviour of quasi-brittle composites such as concrete, coarse-grained ceramics, and fibre-reinforced composites, is manifested by mechanisms like strain localization and progressive fracture in the material. This is an intrinsic property of quasi-brittle materials due to the sizeable heterogeneity of the material microstructure. The heterogeneity in the concrete material is generally manifested by the presence of coarse aggregate. Generally, as an inert filler, aggregate accounts for 60 % - 80 % of the volume and 70 % - 85 % of the weight of concrete [1], of which, coarse aggregate occupies about 45 % of the volume of concrete [2]. Thus, the properties of coarse aggregate seem to have a significant effect on the performance of concrete. Coarse aggregate properties, such as grading, surface area, particle size and shape, angularity, surface texture, mineralogy, water absorption, and strength have been investigated [3-7]. The results showed that maximum aggregate size (d_{\max}) can affect properties of fresh and hardened concrete. The effect on the mechanical properties of hardened concrete, however, is a complex problem which is the main subject of this chapter. In concrete materials, coarse aggregates act as the rigid skeleton, since the compressive strength of coarse aggregates is higher than that of mortar and can reach up to about 100 MPa [298]. Also, the elastic modulus of coarse aggregate can reach up to about 100 GPa [299], while the elastic modulus of mortar is in the range of 10 - 30 GPa [300]. When concrete is bearing the load, the stresses are transmitted through coarse aggregates, which improves the strength of concrete and increase the strain capacity. Previous researchers have done many investigations on the role of aggregate size on hardened concrete properties and a state of the art is presented in the following section.

4.2 Review of the aggregate size effect on the hardened concrete properties

In hardened state, concrete generally cracks when stresses exceed the tensile strength of the material. It is generally considered that the coarse aggregate plays an important role in increasing the tensile strength by preventing the crack propagation. When the maximum aggregate size is increased up to a certain extent, the fracture toughness will be enhanced, leading to the improvement of concrete strength [287]. Nevertheless, once maximum aggregate size is out of this range, with its increasing, the possibility of failure of the surface between coarse aggregate and matrix is increased [301, 302]. This surface is known as the interface transition zone (ITZ), which is generally the weakest zone in concrete. With the appearance of the cracks in ITZ, the bond strength of coarse aggregate is decreased, resulting in a marked decrease of concrete strength.

4.2.1 Effect on tensile strength

The bond strength between aggregate and cement matrix seems to control the tensile strength of the concrete [303]. Although the tensile strength obtained from the direct tension test is more reliable, the method requires more care compared to the indirect tensile test. So one of the most common indirect tests for measuring the tensile strength of concrete is the split cylinder test [304]. It was developed firstly in Brazil by Carneiro and Barcellos [305], and developed independently by Akazawa [306] in Japan. In direct contradiction to concrete failures under direct tensile load, the

fracture plane often passes through the coarse aggregate particles instead of following the ITZ in the splitting test. This may be due to the fact that the tensile stress reaches its maximum value only within a narrow strip along the central vertical plane, essentially forcing failure to occur along this route. The results of some researchers [3, 307] demonstrated that splitting tensile strength of concrete is influenced by the splitting tensile strength of aggregates to a small extent. On the other side, Hannant et al. [308] studied the effect of aggregate size on the tensile strength of the concrete and found that an increase in maximum aggregate size causes a greater increase in the splitting strength than in the direct tensile strength. This trend was also obtained by Rao [289] and Chen [286] for high strength concrete.

In the study of Osidez [309], the effect of aggregate size on the tensile strength was investigated. The results showed an opposite trend for splitting strength when maximum aggregate size. An empirical equation for splitting strength considering aggregate size is proposed as *Equation 4. 1*.

$$f_{bt} = \alpha_t k_t f_{st}^{D_{\max}} \quad (4.1)$$

Where f_{bt} is the splitting tensile strength of concrete; α_t is conversion factor for the tensioning of a standard specimen; k_t is a constant that takes into account the effects of the maximum size of coarse aggregate on the tensile strength of concrete; f_{st} is the mean splitting tensile strength of a nonstandard specimen.

Kadlecek et al. [310] also obtained the relationship considering the effect of aggregate on Brazilian strength of concrete as shown in *Equation 4. 2 - Equation 4. 4*.

For coarse aggregate concrete (max. aggregate size 32 mm),

$$R_{bt,st} = 239A^{-0.160} \quad (4.2)$$

For medium aggregate concrete (max. aggregate size 16 mm),

$$R_{bt,st} = 188A^{-0.116} \quad (4.3)$$

For fine aggregate concrete (max. aggregate size 4 mm).

$$R_{bt,st} = 157A^{-0.083} \quad (4.4)$$

Where $R_{bt,st}$ is the ratio of tensile strength between the standard cubic specimen and nonstandard specimen (%); A is the fracture size (cm^2).

Ibragimov [311] investigated the compressive and splitting strength of concrete with maximum aggregate size in the range of 40 - 80 mm and the water-cement ratio is from 0.4 - 0.68. The results showed up to 9 % increase of compressive strength and up to 10 % decrease of splitting strength.

Uddin et al. [312] studied compressive and splitting strength for concrete using brick aggregate. They concluded that with lower cement content (375 kg/m^3) and the water-cement ratio of 0.45 and 0.50, the compressive strength increases with the increase of maximum aggregate up to 37.5 mm and then decrease. While at higher cement content (400 kg/m^3), the compressive strength reduces with the increase of maximum aggregate size regardless of water-cement ratio and sand to total aggregate volume ratio (s/a). The trend of the results related to splitting strength is different from the results of compressive strength. With an increase of maximum aggregate size, the splitting strength decreases irrespective of variation of cement content and s/a ratio.

Benkemoun et al. [313] numerical modelled the fracture energy for concrete with different maximum aggregate size (4 - 16 mm) using the Brazilian test. The aggregate and the results showed

that the splitting stress is increased with the increase of maximum aggregate size and the width of fracture process zone is in relation to aggregate size as shown in *Figure 4. 1*.

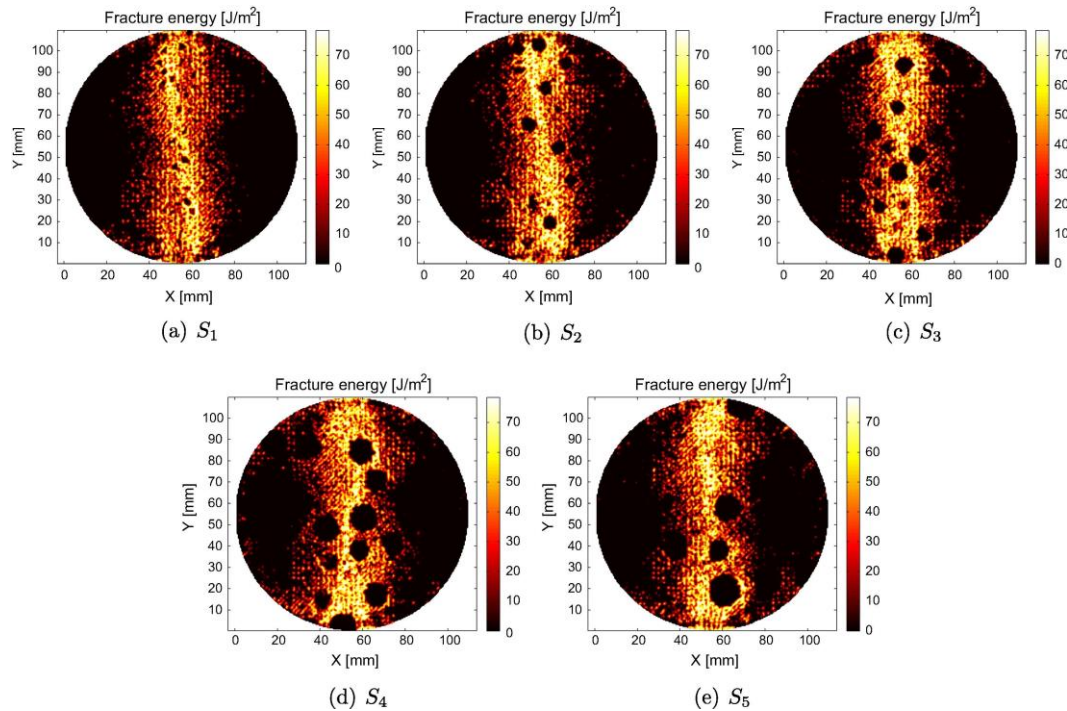


Figure 4. 1 2D fracture energy [$J m^{-2}$] for $D=4,8,10,14$ and $16mm$ in cylinder slices located at $Z=25mm$ at the end of the computation [313]

4.2.2 Effect on flexural strength

Walker and Bloem [314] studied the effect of coarse aggregate size on the properties of normal-strength concrete under flexure. The results demonstrate that at a fixed water-cement ratio, an increase in aggregate size from 9.5 - 63.5 mm ($\frac{3}{8}$ - $2\frac{1}{2}$ in.) seems to have negligible effects on flexural strength. Sim et al. [315] investigated lightweight concrete by varying the size of the specimen and maximum aggregate size. The results illustrated that when maximum aggregate size is larger than 8 mm, there is an insignificant effect of maximum aggregate on the peak force and fracture parameters.

Later Strange and Bryant [288] investigated the interaction of matrix cracks and aggregate particles in concrete with compressive strengths greater than 70 MPa. The results showed an increase in fracture toughness with an increase in aggregate size. This belongs to that as a crack meets an aggregate particle, it passes along the matrix-aggregate interface and then re-enters the matrix. Larger aggregate particles result in a greater increase in crack surface than smaller particles and, thus, require more energy for crack propagation. Although an increase in fracture toughness with an increase in aggregate size was found, the investigation shows a decrease in flexural strength with an increase in aggregate size. The investigation of Kellerman [316] on how altering the size of the aggregate can influence the value of the flexural strength of concrete also concluded that when the water-cement ratio is constant, the flexural strength was higher for the concrete with smaller aggregate. Besides, with the smaller aggregate size, the variability of the flexural strength results decreased. For high strength concrete, Yan et al. [234] got similar results. Alam [282] reported that the peak load increases with the decrease of the aggregate size and the post-peak characteristics are more brittle for concrete

with smaller aggregate size. However, Beygi et al. [236] and Karamloo et al. [235] studied self-compacting concrete (SCC) and found that with an increase of the size of coarse aggregate, the peak force, the fracture toughness and energy increased.

4.2.3 Effect on fracture characteristics

Hillerborg [317] showed that the maximum aggregate size has effects on fracture energy (G_f). The same results have been noticed by Walsh [318], Bažant and Oh [47], Nallathambi et al. [319]. Bažant and Oh [47] developed a formula as follows.

$$G_f = \left(2.72 + 0.0214 f_t'\right) f_t'^2 \frac{d_{\max}}{E} \quad (4.5)$$

Where f_t' is the tensile strength; d_{\max} is the maximum aggregate size; E is Young's modulus.

Nallathambi et al. [319] also proposed a non-linear relationship for energy release rate (G_c).

$$G_c^* = \alpha_1 \left(\frac{d_{\max}}{b}\right)^{\alpha_2} \left(\frac{d}{L}\right)^{\alpha_3 + \alpha_4 \left(\frac{a}{d}\right)} \quad (4.6)$$

Where the non-dimensional energy release rate G_c^* is given by

$$G_c^* = G_c / (\sigma_c^2 b / E) \quad (4.7)$$

Here, σ_c and E are the compressive strength and Young's modulus; d , b and L are depth, width, and span of the specimen respectively; α_i ($i = 1, 4$) are constants; d_{\max} is the maximum size of the aggregate and a is the notch depth.

Later, in the late 1980s, Comité Euro-International du Béton [320] proposed an equation in the CEB-FIP Model Code to estimate total fracture energy (G_F). In Equation 4. 8, G_F is in relation to the maximum size of aggregate (d_{\max}) and cylindrical compressive strength (f_c').

$$G_F = \left(0.0469 d_{\max}^2 - 0.5 d_{\max} + 26\right) \left(\frac{f_c'}{10}\right)^{0.7} \quad (4.8)$$

While the results were not recognized by Petersson [291] and Kleinschrodt and Winkler [321], as the results of them showed that the fracture energy was not affected by maximum aggregate size. Therefore, more investigations have been done to study the role of maximum aggregate size by researchers, but some of them reported the opposite tendency. Wolinski et al. [322] reported that the crack surface of smaller aggregate (2 - 4 mm) is smoother than larger aggregate (8 - 32 mm) and there is no monotonic influence of aggregate size on fracture mechanics parameters. The similar results are also reported by Barr et al. [323] for aggregate size from 5 to 20 mm. Regnault et al. [324] investigated the fracture process zone of mortar ($d_{\max} = 3 \text{ mm}$) and concrete ($d_{\max} = 8 \text{ mm}$) and obtained that the size of aggregate affects both strain distribution and formation of microcracks; fracture process zone is more pronounced in concrete than mortar. Mihashi et al. [45] showed that the fracture energy is significantly increased with the increase of the aggregate size and larger aggregates create a wider fracture process zone (FPZ). Besides, Mihashi [325] also reported that the length of the fracture process zone seems to be independent of the maximum aggregate size but the width is influenced by the maximum aggregate size. However, Tasdemir et al. [326] found that fracture energy and characteristic length (l_{ch}) increases when the aggregate size is increased. While Otsuka and Date [30]

showed that the width of fracture core zone (FCZ) and fracture process zone (FPZ) increases with the increase of the maximum aggregate size and the length of them shows an opposite trend.

Bazant and Becq-Giraudon [327] developed empirical relations for initial fracture energy, the effective length of the fracture process zone and total fracture energy based on 238 tests data. The proposed formulae as follows:

$$G_f = \alpha_0 \left(\frac{f'_c}{0,051} \right)^{0.46} \left(1 + \frac{d_{\max}}{11.27} \right)^{0.22} \left(\frac{w}{c} \right)^{-0.30} ; \quad \omega_{G_f} = 17.8\% \quad (4.9)$$

$$c_f = \exp \left[\gamma_0 \left(\frac{f'_c}{0.022} \right)^{-0.019} \left(1 + \frac{d_{\max}}{15.05} \right)^{0.72} \left(\frac{w}{c} \right)^{0.2} \right] ; \quad \omega_{c_f} = 47.6\% \quad (4.10)$$

$$G_F = 2.5\alpha_0 \left(\frac{f'_c}{0.051} \right)^{0.46} \left(1 + \frac{d_{\max}}{11.27} \right)^{0.22} \left(\frac{w}{c} \right)^{-0.30} ; \quad \omega_{G_F} = 29.9\% \quad (4.11)$$

Where f'_c is a cylindrical compressive strength; $\alpha_0 = \gamma_0 = 1$ for rounded aggregates, while $\alpha_0 = 1.44$ and $\gamma_0 = 1.12$ for crushed or angular aggregates; ω_{G_f} , ω_{c_f} and ω_{G_F} are the coefficients of variation of the ratios G_f^{test}/G_f , c_f^{test}/c_f and G_F^{test}/G_F .

Skarżyński and Tejchman [232] numerical modelled three-point bending test using single notched beams with two aggregate sizes and reported that the width of fracture process zone is not affected by aggregate size, but the shape of fracture process zone is affected by aggregate size as shown in *Figure 4. 2*.

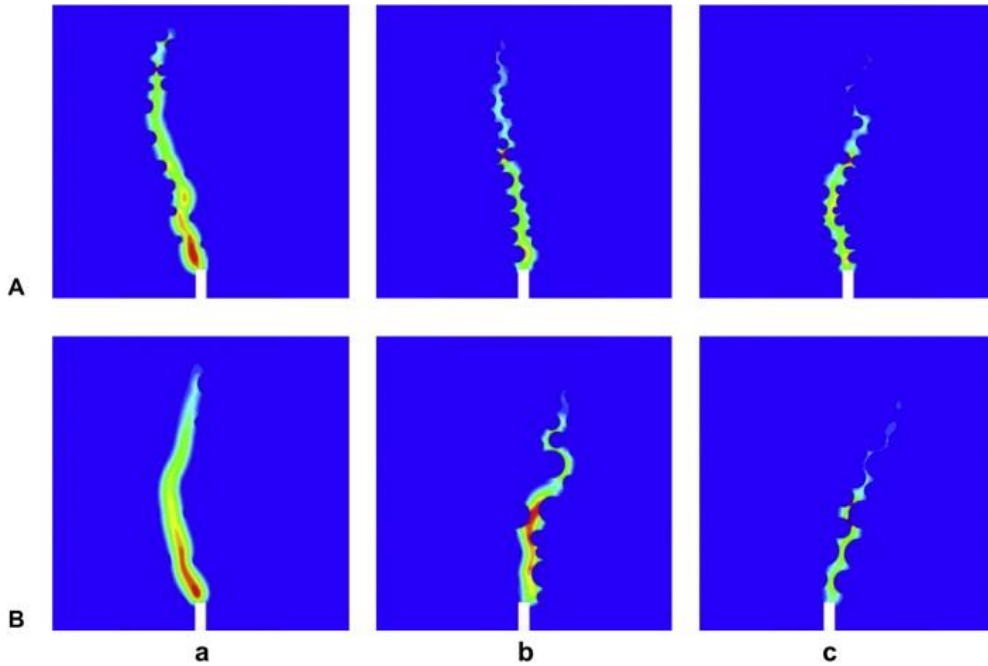


Figure 4. 2 Calculated distribution of non-local strain measure for different aggregate density (small-size beam $80 \times 320 \text{mm}^2$): a) $\rho=30\%$, b) $\rho=45\%$, c) $\rho=60\%$, A) sand concrete ($d_{50}=0.5\text{mm}, d_{\max}=3\text{mm}$), B) gravel concrete ($d_{50}=2\text{mm}, d_{\max}=8\text{mm}$)

Issa et al. [328, 329] reported that the fracture energy and fracture toughness increase with the increase of aggregate size and the fracture surface changes from smooth to rough and complex when

aggregate size increasing. The same trends were also obtained by Chen et al. [330] and Zhou et al. [331] for high strength concrete. Wu et al. [233] and Chen et al. [332] used acoustic emission (AE) technique to investigate the effect of maximum aggregate size. Except obtaining the similar features for fracture surfaces, the results also found that the fracture energy and the total number of hits increased with the increase of aggregate size

Issa et al. [333] then used fractal dimension method to investigate the fracture parameters of concrete and defined the area under $P_c - \Delta_t$ envelopes truncated at P_c and Δ_t corresponding to $a/W = 0.65$ as modified fracture energy \overline{G}_F . The results showed that the fractal dimension and modified fracture energy increases with an increase in maximum aggregate size, the equation can be written as follows.

$$D^2 = \alpha_1 + \alpha_2 \ln(d_{\max}) \quad (4.12)$$

$$\overline{G}_F^2 = \alpha_3 + \alpha_4 \ln(d_{\max}) \quad (4.13)$$

Where D is fractal dimension; d_{\max} is maximum aggregate size; α_i ($i=1,4$) are experimental constants.

4.2.4 The role of aggregate size in classical size effect analysis

Size effect has been rigorously analysed by comparison of nominal strength (σ_N) of geometrically similar structures of different sizes. Considering the conditions of the laboratory, the tests, however, become difficult when the specimen becomes sufficiently large. Due to distinctive fracture process in quasi-brittle materials, size effect is transitional between plasticity (strength-based theories) and LEFM. The transitional behaviour is caused by the fact that the fracture process zone (FPZ) size, equal to several heterogeneity sizes (or maximum aggregate size) is not negligible compared to the cross sectional dimension of the member. It is well described by Bažant size effect law [193] and can be written as follows in the generalized:

$$\sigma_N = \frac{Bf_t}{\sqrt{1 + \frac{D}{D_0}}} \quad (4.14)$$

Where Bf_t and D_0 are the empirical constants of the model obtained by the fitting plot;

D is the characteristic structural dimension.

D_0 is also considered as the transitional structural dimension between the plasticity and LEFM [193]. In Bažant size effect law [193], D_0 is related to the maximum aggregate size (d_{\max}) and relative crack length (a/D) at the peak load. It is expressed as follows:

$$D_0 = \frac{n_a d_{\max}}{2} \cdot \frac{D}{a} = c_f \frac{D}{a} \quad (4.15)$$

Where $n_a d_{\max}$ is the width of fracture band front which represents the width of FPZ.

Equation 4.14 was derived by simple energy release analysis. SEL law has also been derived by asymptotic matching [9] based on the simple asymptotic power scaling laws for very large and very small D , where Equation 4.14 will take the following form:

$$\sigma_N = \sqrt{\frac{E_c G_f}{g(\alpha)D + g'(\alpha)c_f}} \quad (4.16)$$

Where $\alpha = a/D$ is the relative crack length; $g(\alpha)$ is the dimensionless energy release rate function of LEFM; $g'(\alpha) = dg(\alpha)/d(\alpha)$; G_f is the fracture energy; $E_c = E/(1-\nu^2)$ is the Young's modulus for plane strain (ν is Poisson's ratio) and c_f is the effective length of fracture process zone. By setting Equation 4.16 into the form of classical Equation 4.14, one would get:

$$D_0 = c_f \frac{g'(\alpha)}{g(\alpha)} \quad (4.17)$$

and

$$Bf_t = \sqrt{\frac{E_c G_f}{c_f g'(\alpha)}} \quad (4.18)$$

Similar to Equation 4.15, Equation 4.18 reveals that transitional size D_0 is directly proportional to the effective length of FPZ which is proportional to the heterogeneity size (or maximum aggregate size). From Equation 4.18, the parameter B can also be written as a function of heterogeneity size or characteristic length ($l_{ch} = E_c G_f / f_t^2$) as follows:

$$B = \frac{1}{\sqrt{g'(\alpha)}} \sqrt{\frac{l_{ch}}{c_f}} \quad (4.19)$$

Equation 4.19 shows that B is also a function of material heterogeneity size (or maximum aggregate size). Aggregate size thus plays an important role in the size effect on mechanical and fracture behaviour of quasi-brittle materials like concrete. Thus, it can be inferred that ratio between the structure size and the aggregate size maybe the fundamental factor which is causing the size effect. When the structure size increases, D/d_{max} , the ratio between the characteristic structural dimension D and the maximum aggregate size d_{max} increases and approaches D , the material behaviour approaches linear elastic fracture mechanics (LEFM). However, when the structure size is small i.e. at laboratory scale where D and d_{max} are of the same magnitude, LEFM is no more applicable. So, in this chapter, the ratio of the characteristic structural dimension and the maximum aggregate size (D/d_{max}) is regarded as a key factor in investigating the size effect. Three notched beams of the same dimensions were prepared, each with different concretes C20, C10, and C05 respectively. As explained in Chapter 3, aggregate size is scaled down in these concretes and the ratio D/d_{max} was up-scaled in each beam. The detailed procedures will be introduced in the next section.

4.3 A new approach to study aggregate size effect on the mechanical behaviour of concrete: An experimental study

In this Section, an experimental study is presented where the aggregate size (d_a) is considered as scaling factor. The size effect is investigated by taking the ratio of the characteristic structural dimension (D) and the maximum aggregate size (d_{max}) as a key parameter. In previous studies as

shown in literature review (section 4.2), only the maximum aggregate size (d_{max}) is scaled. However, in this study all the aggregate sizes (d_a) of the grading curve are scaled with the same factor. In order to perform the scaling of d_a , three types of concrete mix are designed (C05, C10, and C20) with the same aggregate to mortar volumetric ratio and same mortar properties, only the aggregate sizes are changed. Aggregate sizes were up-scaled in C05, C10 and C20 concretes such that the volumetric fraction for each class of aggregate with respect to maximum aggregate size (i.e. $d_a(i)/d_{max}$) in each concrete remains same as shown in Figure 4. 3. The experimental materials and test procedures have been introduced in the past chapter.

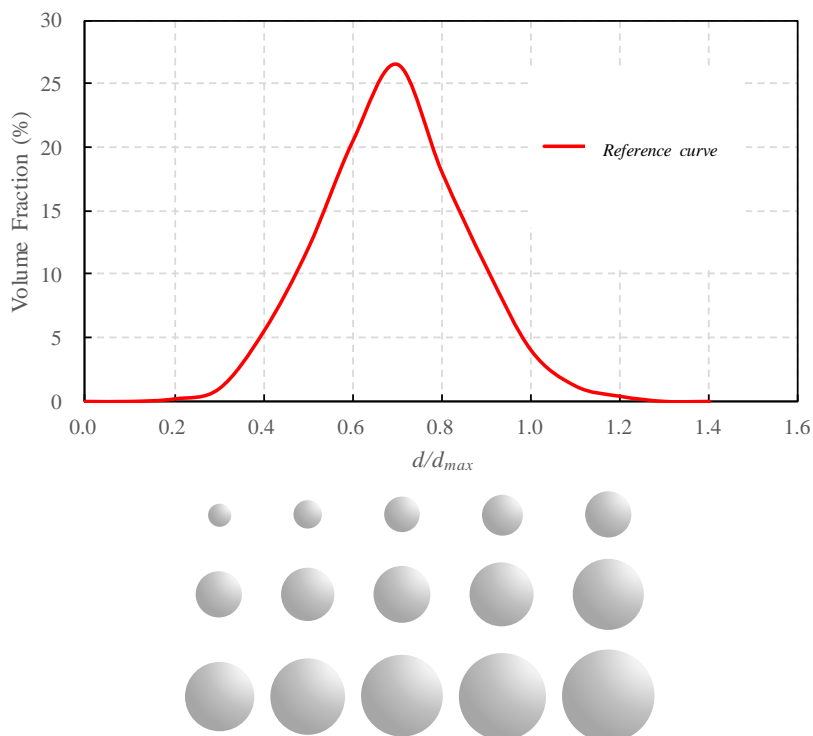


Figure 4. 3 Reference volume fraction curve for concrete series C05, C10 and C20

4.3.1 Effect of aggregate scaling on Brazilian strength

Table 4. 1 shows the results of the Brazilian test for concrete with different aggregate sizes. In the table, the mean value of the splitting tensile strength f_{bt} , the standard deviation s and the coefficient of variation $C_v = s/f_{bt}$ are given.

Table 4. 1 Results for Brazilian test

Series	f_{bt} (MPa)	$s^{(1)}$ (MPa)	$C_v^{(2)}$ (%)
C05	3.65	0.17	5
C10	3.81	0.32	8
C20	4.19	0.49	12

Note: (1) standard deviation and (2) coefficient of variation $C_v = s/f_{bt}$

It can be seen in Table 4. 1, the splitting tensile strength slightly increases with the increase of

maximum aggregate size. This trend was also obtained by Rao [289] and Chen [286] for high strength concrete. The reason is that, the splitting failure is mainly as a result of the opening of a single crack and development of fracture process zone in the surrounding. The up-scaling of aggregate size increases the size of the fracture process zone and energy dissipation which slows down the crack opening, crack propagation and increase the strength.

Benkemoun [313] used the split cylinder strength to study the effect of aggregate size by using the size effect parameter $\beta = \frac{d_0}{d_{max}}$ (d_0 is the empirical parameter). By using numerical analysis they found that increasing aggregate size has similar but opposite effect to the structural size effect. Using Bažant size effect equation rewritten in the form of Equation 4. 15 transitional size effect can be obtained.

$$\sigma_N = \frac{Bf_t}{\sqrt{1+\beta}} \tag{4.20}$$

Experimental results are plotted on the size effect plot as shown in Figure 4. 4. The results show a good correspondence with Bažant size effect law.

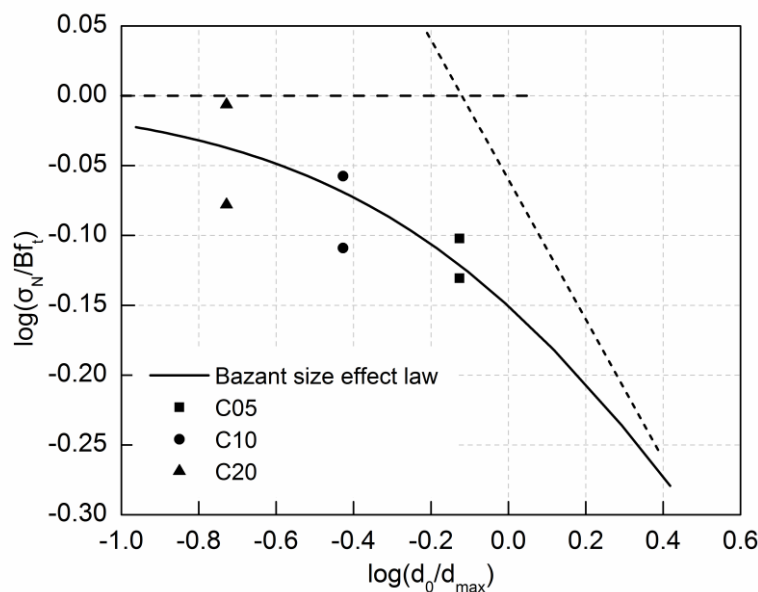


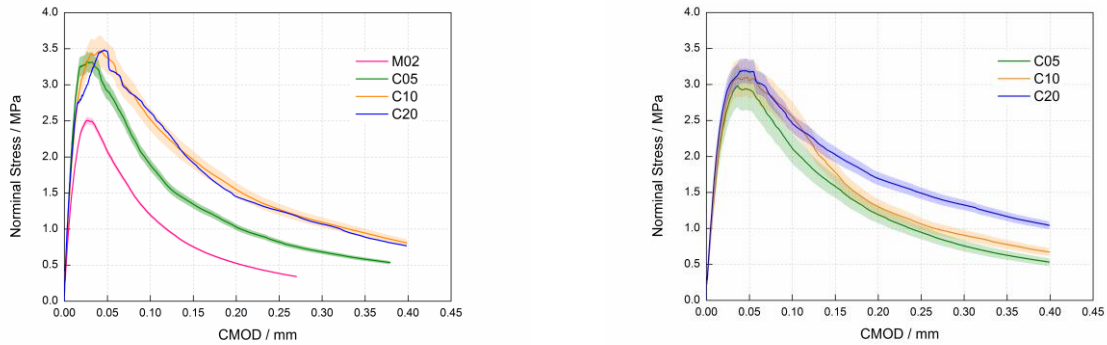
Figure 4. 4 Bažant size effect law with modified $\beta = \frac{d_0}{d_{max}}$ versus experimental results

4.3.2 Aggregate size effect on flexural behaviour: transition from strength-based laws to LEFM

In this section, $D1$ ($100 \times 100 \times 400$ mm³) beams and $D2$ ($100 \times 200 \times 800$ mm³) beams each made with three concretes having maximum aggregate size ($d_{max} = 5.25, 10.5, 21.0$ mm) are analysed. For $D1$ beam, mortar specimen ($M02$) was also prepared and analysed. $M02$ for mortar was taken equal to 2 mm.

Flexural behaviour is generally considered as the most representative of the real structural

loadings. Aforesaid in Section 4.2.4, maximum aggregate size considerably affects the crack propagation, size of the fracture process zone and flexural strength. Nominal stress is calculated using Equation 3. 6 and Equation 3. 7. Figure 4. 5 presents the experimental Stress-CMOD curves obtained from each beam. It can be observed that the slope of the ascending branch of curves is independent of d_{max} , while the maximum peak force is dependent on d_{max} . When a visible crack occurred at the tip of the notch, CMOD is sharply increased; this shows that the rate of increase is affected by d_{max} owing to the aggregate interlock along the crack. After reaching peak load, the crack opening gradually grows, and the applied load drop sharply, showing a larger rate of stress decrease with decreasing d_{max} . Besides, as can be seen in Figure 4. 5 a), for D1 beams the softening part for C20 concrete is almost the same with C20 concrete. In previous investigations [334, 335], the thickness of fracture mechanics specimens were chosen larger than four times the maximum aggregate size to minimize the thickness effect. However, whether four times maximum aggregate size can rule out any thickness effect or not is very difficult to justify. The boundary limit study of Duan et al. [336] indicates that one cannot rule out the impact of thickness even if the specimen thickness is four times the maximum aggregate size. So for C20 concrete with a thickness of 100 mm, the ratio of specimen thickness and the maximum aggregate size is about 4.76, the effect of thickness may be more notable when compared with M02, C05 and C10. Another possible reason may be due to the wall effect. The thickness of the boundary layer increases due to the increase of d_{max} , thus affecting the softening part, especially for small specimens.



a) Average Stress-CMOD curves for D1

b) Average Stress-CMOD curves for D2

Figure 4. 5 Average Stress-CMOD curves of each beam

According to the Size Effect Law (SEL) proposed by Bažant, D_0 is a transitional size between two principal theories of solid mechanics: strength laws and LEFM. In classical form of SEL, D_0 is in a relationship with the maximum aggregate size d_{max} as expressed by Equation 4. 15. If the same specimen is used to study the aggregate size effect, D remains constant. So, the Bažant’s size effect equation (Equation 4. 14) can be reduced to the following form:

$$\sigma_N = \frac{Bf_t}{\sqrt{1 + \frac{2}{n} \cdot \frac{a}{d_{max}}}} \quad (4.21)$$

It can be observed that the above equation is independent of the size of the structure. The nominal strength is intrinsically dependent on the heterogeneity size (d_{max}) and the crack length at the failure point (assumed as notch length). The above equation can not only be applied for aggregate size effect

keeping the heterogeneity size (or maximum aggregate size d_{agg}) constant and varying size of the structure (D), one arrives at the well-known size effect problem (Figure 3. 14 and Figure 3. 15). Here, the strength of the structure decreases by increasing D . However, by scaling the heterogeneity size (or maximum aggregate size d_{agg}) and keeping D constant, one can observe the aggregate size effect (Figure 4. 6). In this study, while scaling the maximum aggregate size (d_{agg}) complete grading curve is scaled with the same factor. Here the results of bending experiments show an increase of strength by increasing aggregate size.

In order to build the relationship between classical size effect and aggregate size effect, D_0 in the Bažant’s size effect law can be expressed in relationship with the maximum aggregate size d_{max} (Equation 4. 15). As shown in Table 3. 5 from classical size effect analysis, one can obtain D_0 (hereafter called D_{0-size}) equals to 166.26, 333.56 and 666.18, respectively for concrete series C05, C10, and C20. Similarly, from aggregate size effect analysis, the value of D_0 can now be obtained (hereafter called D_{0-agg}) by using Equation 4. 15 equals to 191.63, 383.25 and 766.5 for D1 beams with different aggregate size; 386.93, 773.85 and 1547.7 for D2 beams with different aggregate size. By using regression analysis (shown in appendixes), an empirical relationship can now be developed for D_{0-size} and D_{0-agg} as given below with an accuracy of 0.99. The calculated values and the experimental values for are given in Table 4. 2 and Table 4. 3.

$$D_{0-size} = \gamma(D) \cdot D_{0-agg} \tag{4.24}$$

Where D is the height of beam (mm) used to perform aggregate size effect analysis; $\gamma(D)$ is a parameter of D .

Table 4. 2 Experimental values and calculated values for D_{0-size}

Series \ Size	C05		C10		C20	
	Exp.	Cal.	Exp.	Cal.	Exp.	Cal.
D1	166.26	165.19	333.56	330.39	666.18	660.78
D2	166.26	165.19	333.56	330.39	666.18	660.78

Table 4. 3 Experimental values and calculated values for D_{0-agg}

Series \ Size	D1		D2	
	Exp.	Cal.	Exp.	Cal.
C05	191.63	192.18	386.93	384.37
C10	383.25	385.57	773.85	771.14
C20	766.50	770.05	1547.7	1540.11

A similar relationship between Bf_t obtained from classical size effect analysis and aggregate size effect can also be concluded. The calculated values using the empirical relationship and the obtained experimental results are compared in Table 4. 4.

$$Bf_{t-size} = \alpha(D) \cdot (Ad_{max} + C) Bf_{t-agg} \tag{4.25}$$

Where $\alpha(D)$ is the parameter in a relationship with the height of beam (D) used to perform aggregate size effect analysis; d_{max} is the maximum aggregate size of concrete on which classical

size effect is performed; parameters A and C are the regression parameters.

Table 4. 4 Experimental values and calculated values for Bf_{t-size}

Series Size	C05		C10		C20	
	Exp.	Cal.	Exp.	Cal.	Exp.	Cal.
D1	4.21	4.22	4.08	4.05	3.69	3.70
D2	4.21	4.23	4.08	4.05	3.69	3.70

From the above analysis the Bažant’s size effect law can be rewritten as the equation below.

$$\sigma_N = \frac{Bf_{t-size}}{\sqrt{1 + \frac{D}{D_{0-size}}}} = \frac{\alpha(D) \cdot (Ad_{max} + C) Bf_{t-agg}}{\sqrt{1 + \frac{D}{\gamma(D) \cdot D_{0-agg}}}} \quad (4.26)$$

The empirical equation proposed here (Equation 4. 28) is based on the preliminary result obtained by current experimental study. The parameters in the equation, i.e. α , A , C , and γ need more experimental data in order to get stable values. More experimental studies are required for deeper understanding of the relationship between the classical size effect and the aggregate size effect.

4.3.4 AE and DIC investigation

In order to gain an insight into the fracture process zone, AE and DIC methods are adopted. The way for determining the length and the width of fracture process zone using AE method is the same as introduced in Chapter 3. The results are illustrated in Figure 4. 7 and Figure 4. 8.

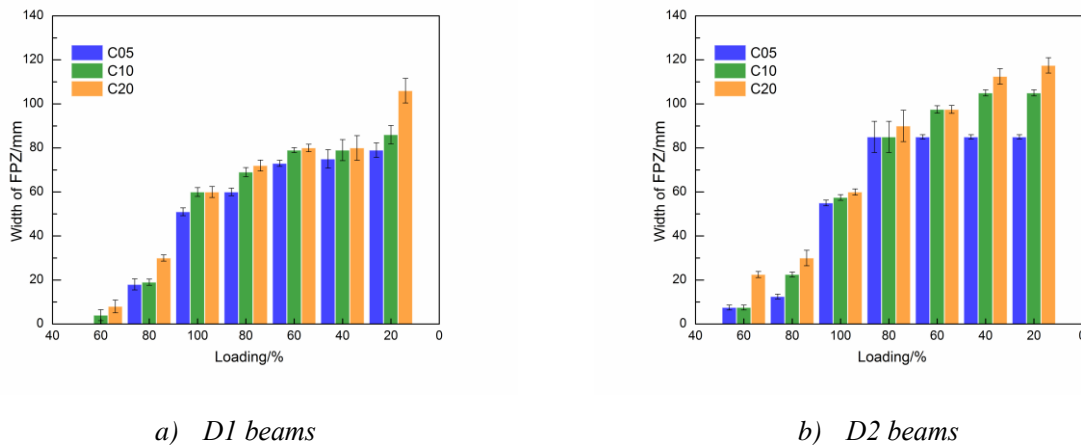
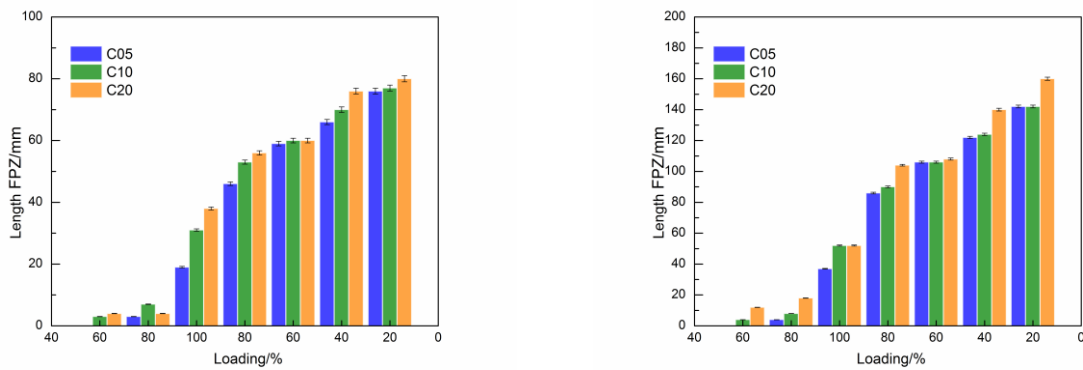


Figure 4. 7 Evolution of width of FPZ with loading steps for each aggregate size

As presented in Figure 4. 7, the width of FPZ is increasing with the increase of maximum aggregate size and the result is supported by Otsuka and Date [30]. The possible reason for the influence of aggregate on the width of FPZ is the non-uniform distribution of local fracture [337]. The presence of larger aggregate prevents the crack from opening and results in bridging of cracks and a wider FPZ.

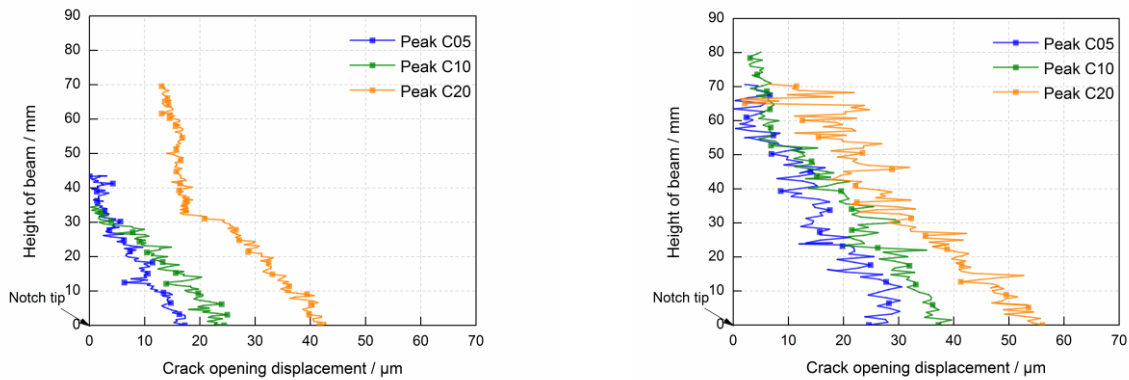


a) D1 beams

b) D2 beams

Figure 4. 8 Evolution of length of FPZ with loading steps for each size of the concrete

Unlike the previous results [30, 45], the length of FPZ experiences an increase with the increase of maximum aggregate size. It may be due to the reason that in previous studies only the maximum aggregate size is scaled and the volumetric proportion for each class of aggregate size in an aggregate mix was not kept constant while scaling the aggregate size. This result is supported by the study of Rao et al. [338]. They used three cement content, i.e. 400, 450 and 500 kg/m³, and three maximum aggregate sizes, namely 10, 16 and 20 mm to investigate the size of FPZ. The results indicated that the size of FPZ was in the order of magnitude of the size of coarse aggregate. The fracture process monitoring is further extended by applying simultaneously DIC technique. Crack openings are extracted at each location of the crack profile as explained in Chapter 3. The crack opening profiles for each concrete are compared at peak loadings as shown in Figure 4. 9.



a) D1 beams

b) D2 beams

Figure 4. 9 Crack opening displacement profiles at peak load for each series

It can be observed in Figure 4. 10 that crack opening displacement at each location of the crack is higher for larger aggregate size. The higher crack opening of the macrocrack can be due to higher microcracking in the vicinity and efficient crack bridging when the aggregate size is larger. One can also estimate the crack tip by location when crack opening profile shows an insignificant change in the crack opening. Analysing the results, it can be seen that the crack length at peak load increases with the increase of aggregate size which is in consistency with the AE results.

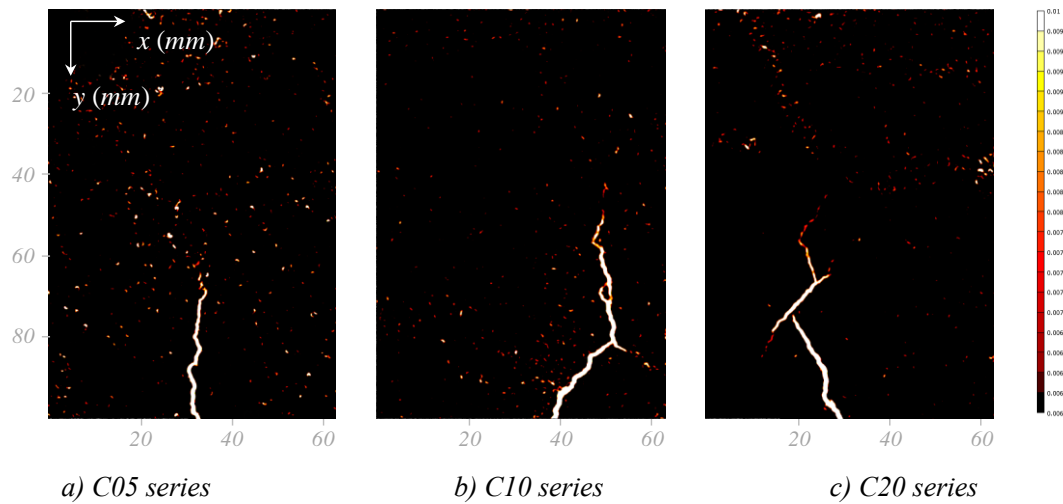


Figure 4. 10 Experimental principle strain maps in D1 beams showing strain localized damaged zone at different loading steps at peak load for different concrete series

According to the previous study [328], the aggregate size also impacts the tortuosity of crack. Strain maps shown in Figure 4. 10 confirm that compared with the concrete with smaller aggregate, the crack trajectory for concrete with larger aggregate deviates from the rectilinear path.

4.4 Modelling for aggregate effect

The objective of this section is to model behaviour and failure process of plain concrete with different aggregate size at mesoscale using DEM. The modified parallel bond model established in Chapter 2 is used for modelling in this chapter the aggregate size effect. The microparameters for matrix and aggregate have already been determined using mortar and C10 concrete in Chapter 3. Here only the microparameters that need to be determined are ITZs for C05 and C20 concrete. By applying inverse calibration using LM method (introduced in Chapter 2) on Brazilian tests, the microparameters (Young’s modulus, stiffness ratio, tensile stress, and cohesive stress) of ITZ are obtained for C05, C10 and C20, respectively. Here, only the modelling results of D1 beams are presented. The beam M02 which represents mortar beam is also modelled. The generation procedures of matrix and aggregate particles are the same as presented in Chapter 3. The specimens used for modelling the aggregate effect are presented in Figure 4. 11.

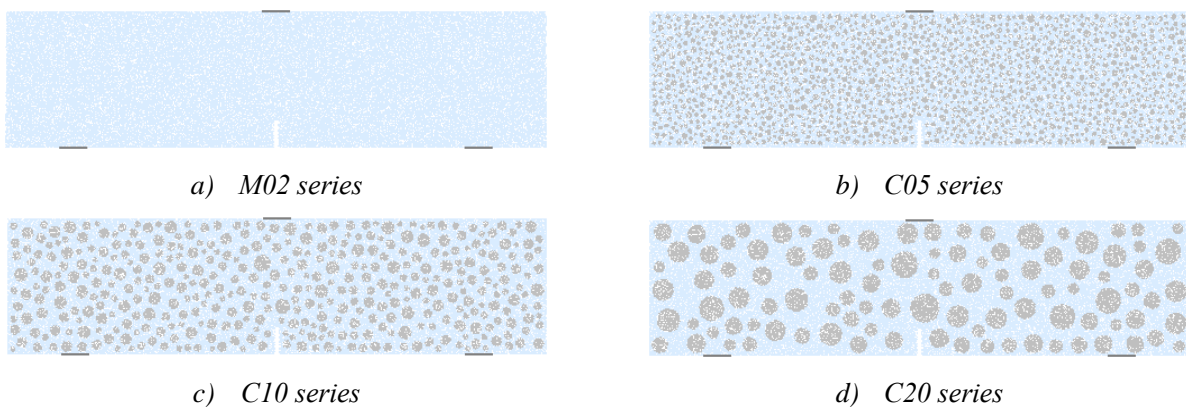


Figure 4. 11 Specimens for each concrete series

The comparison between the numerical and experimental peak force is given in *Table 4. 5*. For C20 concrete, one result is deleted as it is obtained by the beam that may have initial microcracks.

Table 4. 5 Comparison of laboratory tests and modelling results

Series	Force / kN	Experimental Results	Numerical Results
M02		5.58±0.22	5.40
C05		7.42±0.34	7.04
C10		7.55±0.76	7.28
C20		7.61	7.59

The results in *Table 4. 5* show that the numerical results are in agreement with the experimental results. Using *Equation 4. 22*, the numerical results are plotted on the aggregate size effect plot along with the experimental results as illustrated in *Figure 4. 12*. The numerical results obtained are well described by the aggregate size effect curve.

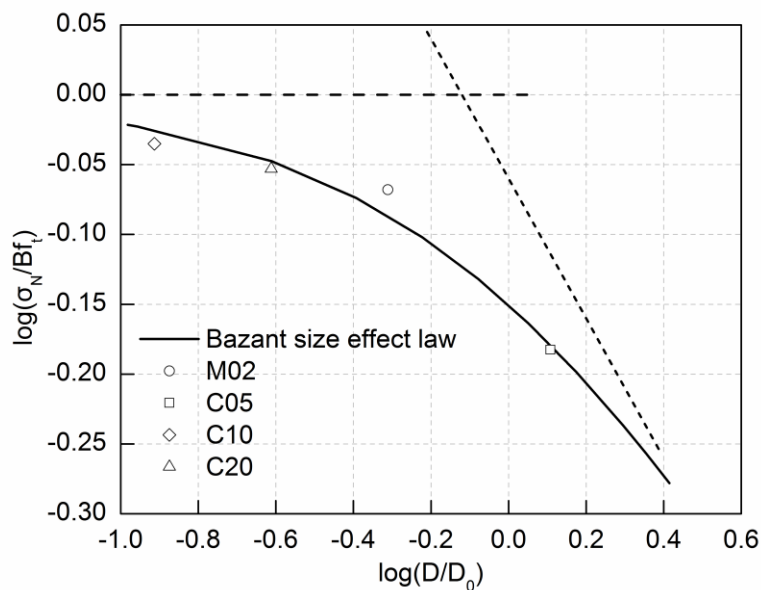


Figure 4. 12 Numerical aggregate size effect on D1 beams.

4.5 Local behaviours of concrete

The ability to model local behaviour of a material at microstructures levels is one of the outstanding features of DEM. So, in this section, the local behaviours of concrete are investigated.

Since cracking in concrete mainly occurs due to local failure in tension, the fracture zone can be obtained by mapping the tensile force distribution as illustrated in *Figure 4. 13*. F_{\max} in the figure

means the maximum tensile contact force. The thicknesses of the lines represent the value of the force. At the peak loading, significant tensile stress is dominant around the top area of the crack. The tensile stress level is noticeably higher than that in the surrounding areas.

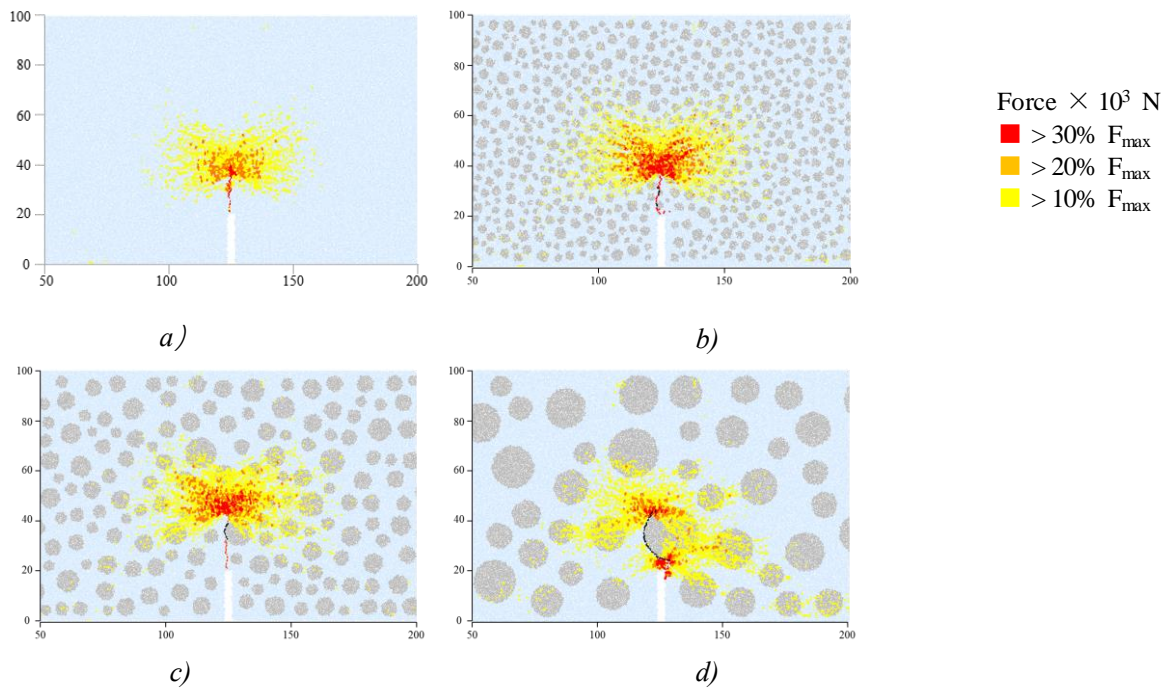


Figure 4. 13 Numerical tensile force distribution at peak stress for each concrete series: a) M02; b) C05; c) C10; d) C20

The crack path for each series is extracted and plotted together in Figure 4. 14. The deviation of the crack path for M02, C05 and C10 is less when compared with C20 series. It can be noticed that there exists a large aggregate directly at the notch tip which prevents the straight crack propagation.

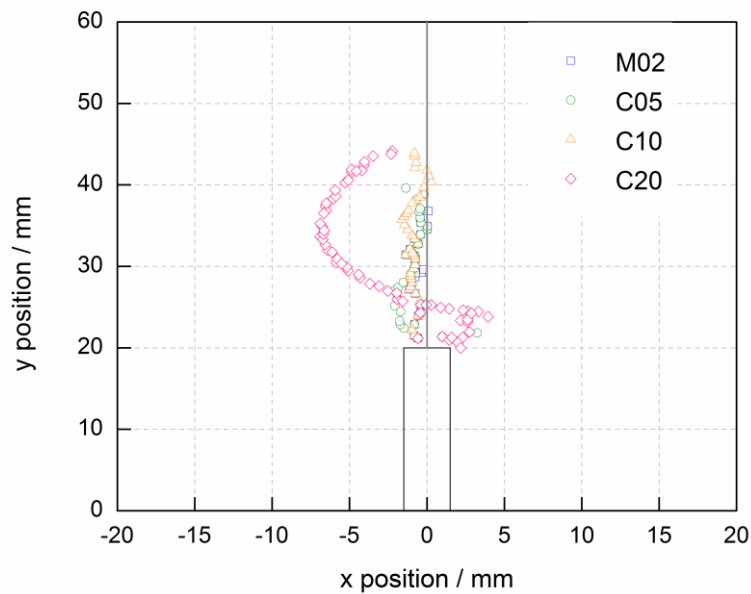


Figure 4. 14 Crack path for each concrete series at peak loading

Measure circles are placed at the middle of the beams to measure the stress distribution (See Section 2. 5), so the stress distribution at the peak force for each concrete series is given in *Figure 4. 15*.

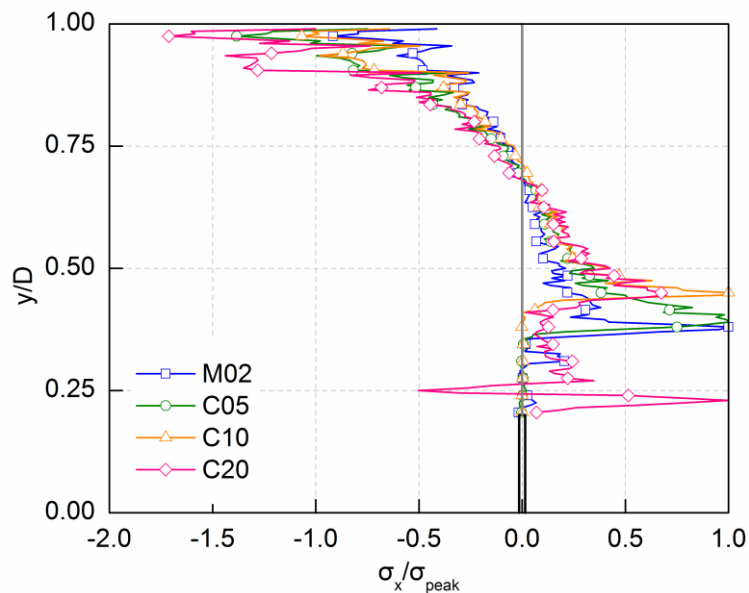


Figure 4. 15 Stress distribution at peak load at the mid-span

The stress distributions show the normalized complete fracture zone length (crack length + FPZ length) change with the aggregate size. Specifically, the normalized complete fracture lengths at the

peak load experience a little increase with the increase of maximum aggregate size. The trend is the same with the result observed using AE and DIC, but the change is not clear. The reason is that the weak ITZ between aggregate and matrix is the place where the crack is always initiated. The crack is propagated by connecting the notch and the broken contacts (in the ITZs) and formed the macrocracks. However, sometimes an aggregate is located just in front of the notch (See *Figure 4. 13 d*) and it plays a role of an obstacle that prevents the rupture of contacts in the vicinity of the notch. Therefore, it disconnects the macrocracks from the notch. In this case, by mainly connecting the broken ITZ contacts, the macrocrack is finally formed. Therefore, the position of the aggregate particles actually has an important role on the FPZ size in conjunction with the size of the aggregate particles. Nevertheless, when the volume fraction of aggregate is kept constant, the spacing between the aggregates is constant regardless of the size of aggregate, and thus the position of aggregates seems to be more important than the size of aggregates in the producing the size of FPZ. Therefore, the impact of aggregate positions needs to be studied in the later investigations. Another reason can be explained by the fact that contact bond model between the two adjacent particles is a linear elastic model, the force decreases to zero when reaching the peak force. It means that the FPZ size developed in this type of model (brittle elastic) may not always be related to the aggregate size itself. So, in order to further investigate the influence of the maximum aggregate on the FPZ length, a softening model needs to be developed. In the next chapter, an exponential softening contact model will be introduced in detail and used to model the aggregate size effect.

4.6 Summary

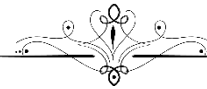
In this chapter, the effect of the aggregate size is investigated on the size effect. In previous studies, when investigated the size effect, the characteristic size of the structure (D) is a variable parameter without considering the role of ratio between D and maximum aggregate size (d_{\max}). The effect of aggregate size was thus ignored. So, this study size effect is analysed based on the scaling of the ratio of the characteristic structural dimension and the maximum aggregate size (D/d_{\max}). Based on this approach, Brazilian test, and three-point bending test are used to investigate the mechanical behaviours of concrete with different maximum aggregate size and keeping D constant. The Brazilian strength showed an increase when maximum aggregate size increased and obeyed the modified Bažant's size effect law. It is due to the fact that the splitting failure is mainly as a result of the opening of a single crack and development of fracture process zone in the surrounding. The upscaling of aggregate size increases the size of the fracture process zone and energy dissipation which slows down the crack opening, crack propagation and increase the strength. Three-point bending results are performed on notched specimens of constant D by varying d_{\max} . A modified size effect law is proposed and the results are plotted on the classical size effect plot. It is observed that the concrete behaviour transitions from LEFM to strength criterion when the maximum size of coarse aggregates increases (or by decreasing D/d_{\max}). This is the same effect when D is scaled with constant d_{\max} (classical size effect). Based on regression analysis and empirical relationship between aggregate size effect and classical size effect is proposed. With the help of AE and DIC methods, the size of FPZ and the crack trajectory were investigated. It found that the width and the length of FPZ are increasing with the increase of maximum aggregate size. The non-uniform distribution of local fracture and increased crack bridging may be the possible reason for these phenomena. The crack trajectory for concrete with larger aggregate deviates from the rectilinear path compared with the concrete with smaller aggregate.

A modified linear elastic parallel bond model is used to model the concrete mechanical behaviour and fracture process of three-point bending beams with concretes of different aggregate sizes. Numerical bending strength is in accordance with the experimental results. Also, the numerical fracture pattern matches with the fracture obtained by experiments. However, the differences of the crack lengths of different concrete series are not obvious when using linear elastic contact model, so in order to investigate the influence of maximum aggregate on the FPZ length, a softening model needs to be developed (see Chapter 5).

A Displacement Softening Model for DEM and its Application



In this chapter, a local crack opening displacement softening model is developed in the framework of discrete element method in order to improve the post-peak fracture behaviour of concrete that remains a problem in linear elastic parallel bond model. The influence of the microparameters is investigated through a parametric study. The proposed softening model is validated by three-point bending test of mortar and the fracture behaviour is compared with the AE method. Finally, the model is applied to study the concrete fracture behaviour and more specially the aggregate size effect which is the main objective of this thesis.



5.1 Development of local softening bond model

In this chapter, a softening contact bond model based on the work of Liu et al. [339] is introduced to model the post-peak behaviours of concrete. Previous researchers [106, 170, 340] have proposed some implementations of softening bonds to model the quasi-brittle materials, but most of them are linear softening models. Here, an exponential softening model is developed which better represents the cementitious material behaviour [341]. In continuum modelling, the relationship between tractions and relative displacements of two virtual surfaces in the fracture process zone is determined by the softening laws [64, 65]. The concept is applied to DEM modelling by defining the fracture process zone as an area containing inter-particle bonds undergoing failure. A relationship between stress σ (σ_n , σ_s) in each bonding contact and the relative displacement u (u_n , u_s) of the corresponding interaction pairs are established.

5.1.1 Yield surface

A correspondence between bond stresses in DEM and stress field of a continuum near a crack tip by LEFM theory is established by Potyondy and Cundall [157]. Here, this concept is also adopted to build the yield surface.

Griffith [342] was the pioneer who analysed the propagation of pre-existing cracks based on energy considerations for the fracture of brittle materials. He assumed that the stresses and strains at the crack tip tend to infinity and the energy is only dissipated at the crack tip. In 1957, Irwin [343] introduced the concept of the stress intensity factor or so-called “Irwin Criterion for fracture of brittle materials”. Three fundamental modes have been defined for the crack opening as shown in *Figure 5.1*. Mode I and Mode II are known as planar modes. Mode I fracture is caused by normal stresses perpendicular to the crack face and Mode II fracture is due to shear stresses parallel to the crack face. Mode III is an anti-plane mode caused by tearing load. A stress intensity factor for each mode will be required for the full description of generalized fracture. For Mode I, II and III, respectively, the stress intensity factors are termed K_I , K_{II} and K_{III} .

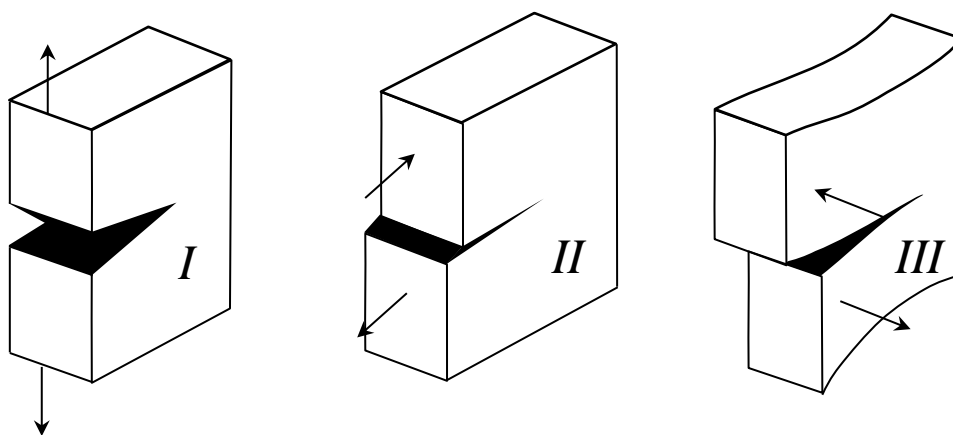


Figure 5.1 The three opening modes for cracks [74]

Based on the work of Griffith, Irwin [343] studied the so-called Mode I fracture. For mode I stress field for a sample with a crack length in a two-dimensional infinite linear elastic isotropic solid, subjected to uniform normal stress at infinity in all directions as shown in *Figure 5.2*.

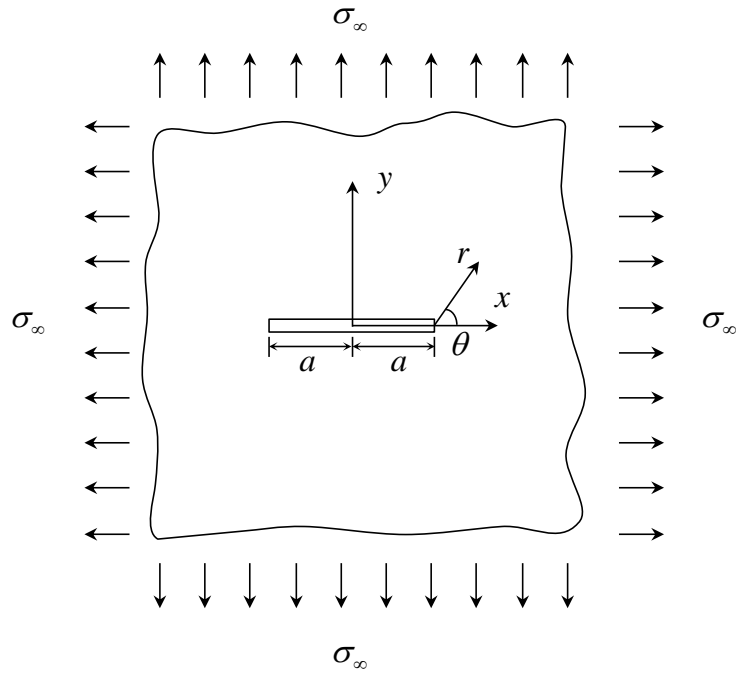


Figure 5. 2 Centre cracked infinite panel subjected to remote equiaxial tension

By introducing a polar coordinate system with the origin at the crack tip, the leading terms of the Williams [344] expansion, for the stresses and displacements as a function of the distance r and the angle θ for Mode I, are expressed as:

$$\begin{aligned}\sigma_{xx} &= \frac{K_I}{\sqrt{2\pi r}} \cos \frac{\theta}{2} \left(1 - \sin \frac{\theta}{2} \sin \frac{3\theta}{2} \right) \\ \sigma_{yy} &= \frac{K_I}{\sqrt{2\pi r}} \cos \frac{\theta}{2} \left(1 + \sin \frac{\theta}{2} \sin \frac{3\theta}{2} \right) \\ \sigma_{xy} &= \frac{K_I}{\sqrt{2\pi r}} \cos \frac{\theta}{2} \sin \frac{\theta}{2} \sin \frac{3\theta}{2}\end{aligned}\quad (5.1)$$

$$\begin{aligned}u &= \frac{K_I(1+\nu)}{E} \sqrt{\frac{2r}{\pi}} \cos \frac{\theta}{2} \left(\frac{k-1}{2} + \sin^2 \frac{\theta}{2} \right) \\ v &= \frac{K_I(1+\nu)}{E} \sqrt{\frac{2r}{\pi}} \sin \frac{\theta}{2} \left(\frac{k-1}{2} + \cos^2 \frac{\theta}{2} \right)\end{aligned}\quad (5.2)$$

Where u and v are the horizontal and vertical components of the displacement field. The parameter k is equal to $(3-4\nu)$ for plane strain and to $(3-\nu)/(1+\nu)$ for plane stress.

Irwin's fracture criterion introduces a new material parameter known as the critical stress intensity factor K_{IC} . When $K_I > K_{IC}$, the crack propagates and leading to the appearance of brittle crack, otherwise the crack will not propagate. Griffith [342] has given the solution to this problem. The asymptotic near-tip ($r/a \rightarrow 0$) stress is expressed as a function of the distance to the right crack tip, the expression for σ_y is given below. It should be noted that LEFM is valid only in the singularity-dominated zone ($r \ll a$).

$$\sigma_y = \frac{K_I}{\sqrt{2\pi r}} \quad (5.3)$$

Where r is the distance from the crack tip; K_I is the stress intensity factor.

As shown in *Figure 5. 3*, in a square area with a uniform particle of radius R , the normal stress exerted on the particle can be calculated by integration over the tributary area as follows.

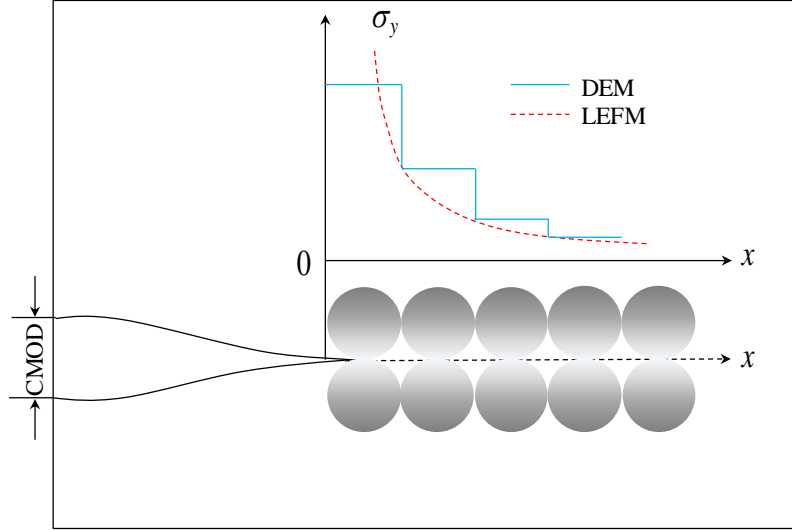


Figure 5. 3 Stress distribution ahead of the crack tip: Continuum v.s. DEM[339]

$$\sigma_n^i = \frac{F_n^i}{2Rt} = \frac{1}{2Rt} \int_{2R(i-1)}^{2Ri} \sigma_y t dr = \frac{K_I}{\sqrt{2\pi r_{eq}}} \quad (5.4)$$

Where $2Rt$ is the tributary area for each bond; t is the particle thickness and $t=1$ for 2D DEM modelling; r_{eq} is the equivalent distance of the particle i to crack tip given by the following equation.

$$\sqrt{r_{eq}} = \frac{\sqrt{R}}{\sqrt{2}(\sqrt{i} - \sqrt{i-1})} \quad (5.5)$$

According to *Equation 5. 4*, the stress intensity factor can be expressed by using the normal force at the first particle. For the first particle, $r_{eq} = R/2$.

$$K_I = \frac{F_n^1}{2t} \sqrt{\frac{\pi}{R}} \quad (5.6)$$

Where F_n^1 is the normal force at first particle; R is the radius of the particle.

The crack will propagate when the stress factor reaches a certain critical value K_{IC} , so this critical value is expressed in terms of the tensile strength S_n .

$$K_{IC} = \frac{S_n}{2t} \sqrt{\frac{\pi}{R}} \quad (5.7)$$

This equation is derived by assuming all particles have the same size and are assembled in squared packing. Potyondy and Cundall [157] introduced two correction factors to correct the

influence of microstructure and bond type.

$$K_{IC} = \beta \frac{S_n}{2t} \sqrt{\alpha \frac{\pi}{R}} \quad (5.8)$$

Where α is a non-dimensional factor that increases with packing irregularity, strength heterogeneity and bond ductility; β is a non-dimensional factor that accounts for the weakening effect of the bending moment.

The equation illustrates that for a given strength, in order to keep the same fracture toughness, particle size has to remain the same for brittle bonds. For softening model, there is no such constraint as confirmed by Liu et al. [339].

From the equations above (*Equation 5. 6* and *Equation 5. 7*), the following equation can be obtained. The similar equation can also be established for mode II.

$$\frac{K_I}{K_{IC}} = \frac{F_n^1}{S_n} \quad (5.9)$$

$$\frac{K_{II}}{K_{IIC}} = \frac{F_s^1}{S_s} \quad (5.10)$$

Where F_s^1 is the shear force at first particle; S_s is the shear strength.

When the stress intensity factors increase under mixed mode loading, the fracture is assumed to occur when a certain combination of the two stress intensity factors (K_I and K_{II}) reaches a critical value. Many fracture envelopes have been proposed for in-plane loadings, like linear form [345], elliptic form [346] and general quadratic form [347]. In practice, the energy consumption for creating fracture surfaces under mode I is different from that under mode II, namely $K_{IC} \neq K_{IIC}$. So, an elliptical failure envelope is adopted here to satisfy the condition $K_{IC} \neq K_{IIC}$. In 2D modelling, the ellipsoidal failure envelope in LEFM can be expressed as follows.

$$\left(\frac{K_I}{K_{IC}} \right)^2 + \left(\frac{K_{II}}{K_{IIC}} \right)^2 = 1 \quad (5.11)$$

Combined the *Equations 5. 9 - 5. 11* and dropping the reference to the first particle, the yielding surface used for DEM is derived.

$$\left(\frac{F_n}{S_n} \right)^2 + \left(\frac{F_s}{S_s} \right)^2 = 1 \quad (5.12)$$

5.1.2 Model formulation

When the yield surface is reached, the bond strength follows the softening path rather than decrease to zero directly. It decreases according to a damage law which is proposed by Jirásek and Bauer [348]. The damage parameter in normal and shear directions have the same value. It means that there is only one damage parameter (D_f), which is widely accepted in quasi-brittle materials modelling [96, 349, 350].

$$D_f = \max(D_f^n, D_f^s) = \begin{cases} 0 & u_{n,s} \leq u_e^{n,s} \\ 1 - \frac{u_e^{n,s}}{u_{n,s}} \exp\left(-\frac{u_{n,s} - u_e^{n,s}}{u_f^{n,s} - u_e^{n,s}}\right) & u_{n,s} > u_e^{n,s} \end{cases} \quad (5.13)$$

Where $u_{n,s}$ is the relative normal or shear displacement between two particles; $u_e^{n,s}$ is the displacement corresponding to elastic limit in normal or shear direction; $u_f^{n,s}$ is the parameter which controls the slope of softening curve in normal or shear direction.

The normal spring subjected to tensile force and the shear spring subject to shear force obey the exponential softening law. The elastic exponential softening model is presented in *Figure 5. 4*.

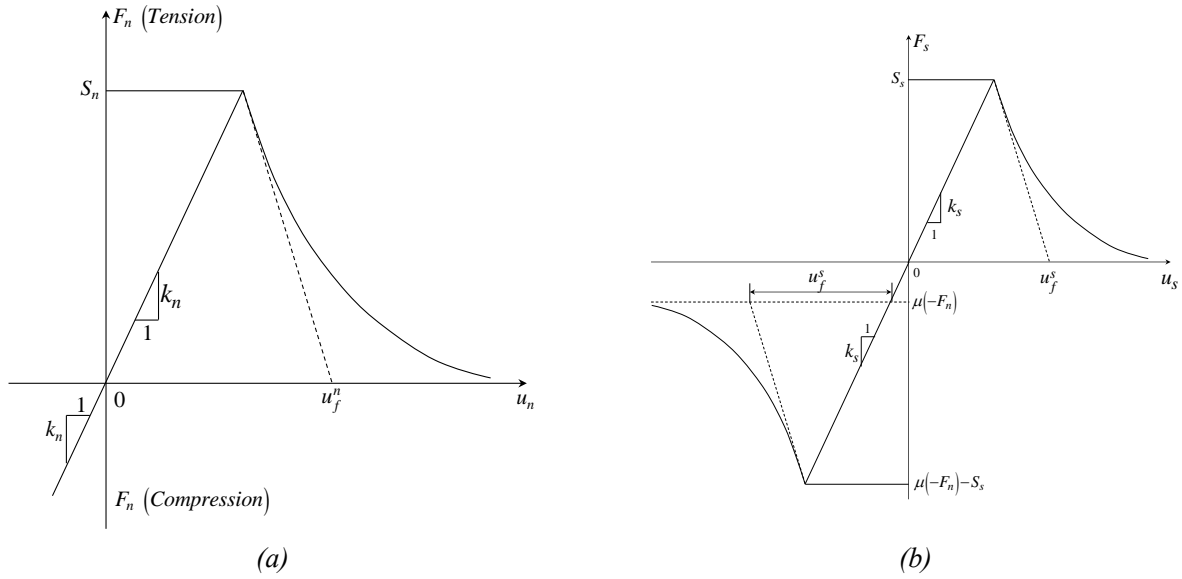


Figure 5. 4 Constitutive behaviour of contact displacement-softening model: (a) normal behaviour; (b) shear behaviour

The equation for calculating the bond force in normal or shear direction is given below.

$$F_{n,s} = (1 - D_f) k_{n,s} u_{n,s} = \begin{cases} k_{n,s} u_{n,s} & u_{n,s} \leq u_e^{n,s} \\ k_{n,s} u_e^{n,s} \exp\left(-\frac{u_{n,s} - u_e^{n,s}}{u_f^{n,s} - u_e^{n,s}}\right) & u_{n,s} > u_e^{n,s} \end{cases} \quad (5.14)$$

Then, at a certain damage condition, the reduced normal strength and shear strength are calculated by the equations as follows.

$$\begin{aligned} S_{n,sof} &= (1 - D_f) k_n u_n \\ S_{s,sof} &= (1 - D_f) k_s u_s \end{aligned} \quad (5.15)$$

Bond fails either in tension or shear, and when the particles are in compression, shear strength is augmented by the slip which is contributed by compression.

$$S'_{s,sof} = \mu \langle -F_n \rangle + S_{s,sof} \quad (5.16)$$

Where $\langle \cdot \rangle$ is Macaulay brackets; $S_{s,sof}$ is the softened shear strength.

Thus, the softening model is established by the above equations. The bond behaviour of this

softening model is controlled by seven parameters: μ ; S_n and S_s ; k_n and k_s ; u_f^n and u_f^s .

5.1.3 Model behaviour

The softening model established above is inserted into PFC as a user-defined model. To illustrate the constitutive response of the proposed model, two contacted particles under mode I/II and mixed-mode loading conditions are performed. The simulation of two particles under different loading paths illustrate in *Figure 5. 5*. The diameter of two particles is 0.1 m and the other microparameters are listed in *Table 5. 1*. For mode I, mode II and tension-shear tests, a constant velocity is given to one particle until the contact is broken and the other particle is always fixed. For the compression-shear test, a constant velocity in shear direction is applied and a constant compressive force (0.2 kN) is maintained at the contact. Then the force-displacement curve for each test is recorded to verify the softening model.

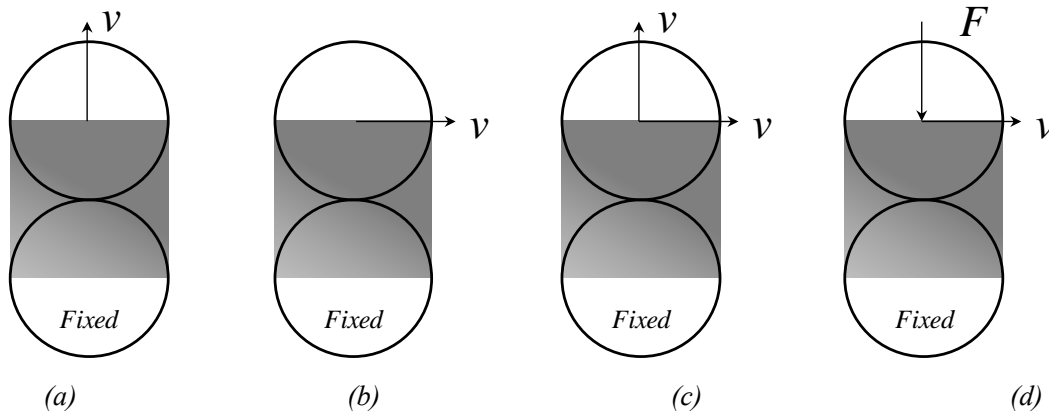


Figure 5. 5 Model behaviour tests: a) Mode-I test; b) Mode-II test; c) Tension-shear test; d) Compression-shear test

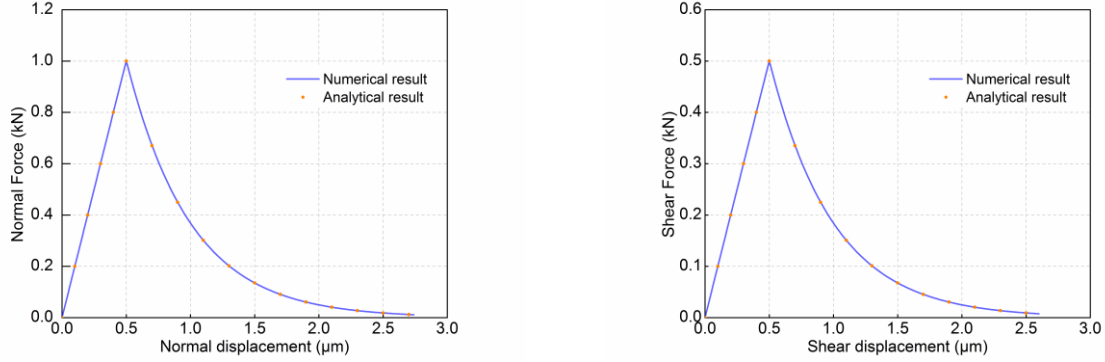
Table 5. 1 Model parameters of the behaviour tests

Model microparameters	
Friction coefficient, μ	0.5
Normal stiffness, k_n (GPa/m)	2.0
Shear stiffness, k_s (GPa/m)	1.0
Tensile strength, S_n (kN)	1.0
Shear strength, S_s (kN)	0.5
Normal softening parameter, u_f^n (μm)	1.0
Shear softening parameter, u_f^s (μm)	1.0

5.1.3.1 Pure mode-I and mode-II loading tests

Based on these equations, the explicit function relating to normal (shear) force and normal (shear)

displacement in yielding contact can be obtained base on *Equation 5. 14*. Mode-I and mode-II results of stress-displacement curves are illustrated in *Figure 5. 6*. The results give a complete agreement between the analytical solution and numerical solution, which verifies the stress update algorithm for mode-I and mode-II loading paths using the developed model.



a) Mode-I test

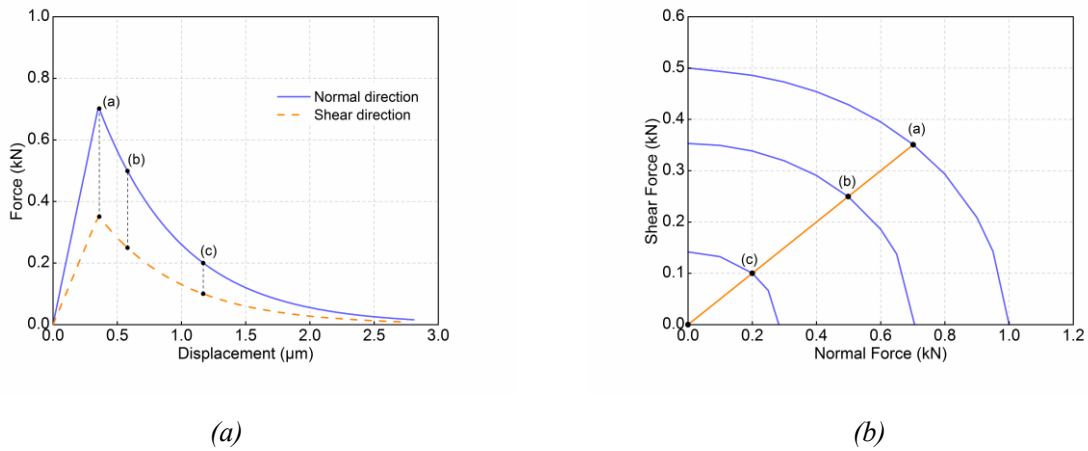
b) Mode-II test

Figure 5. 6 The analytical and numerical results of force-displacement curves

5.1.3.2 Mix-mode loading tests

Tension-shear test results are presented in *Figure 5. 7*. The normal force and shear force experience an increase and then follow an exponential decrease when the normal and shear displacements further increase. Three loading stages corresponding to different damage states are recorded to draw the corresponding yield surfaces. The results show that all the points located exactly on their corresponding yield surfaces. It should be noticed that the yield surfaces at different damage states are parallel if satisfying the following condition,

$$\frac{k_n u_f^n}{S_n} = \frac{k_s u_f^s}{S_s} \tag{5.17}$$

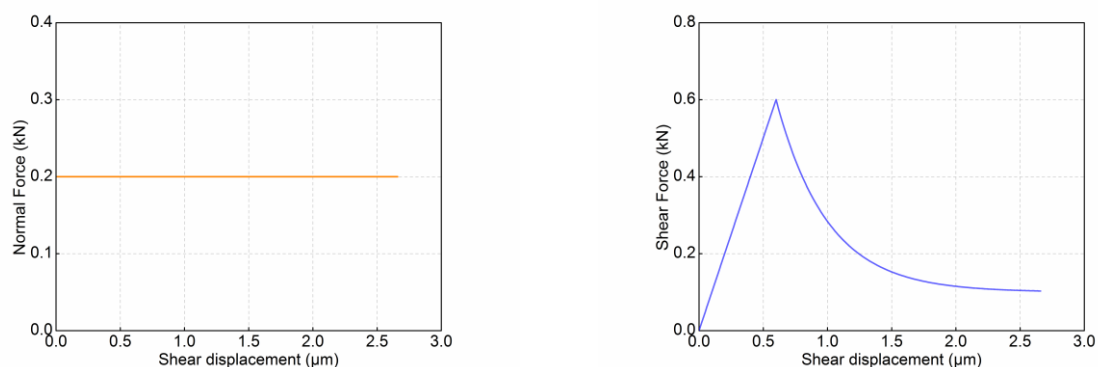


(a)

(b)

Figure 5. 7 Simulation results of the tension-shear test: (a) Normal and shear force-displacement relationship; (b) The evolution of force states with respect to the shrinking of the yield surface

The results of the compression-shear test are illustrated in *Figure 5. 8*. The compression induced frictional resistance. Due to frictional slip, complete damage does not occur at the contact.



a) Normal force-displacement curve

b) Shear force-displacement curve

Figure 5. 8 Simulation results of the compression-shear test

5.2 Parametric study

As aforementioned, the bond behaviour of this model is controlled by seven parameters: μ ; S_n and S_s ; k_n and k_s ; u_f^n and u_f^s , so the influence of these microparameters needs to be investigated. In this section when studying the effect of one parameter, others are kept constant during the modelling. Three point bending test on a mortar beam is chosen to perform the parametric study. Beam dimension is $40 \times 40 \times 160 \text{ mm}^3$ with as central notch as shown in *Figure 5. 9*. The small size of the beam is selected to reduce the computational cost.

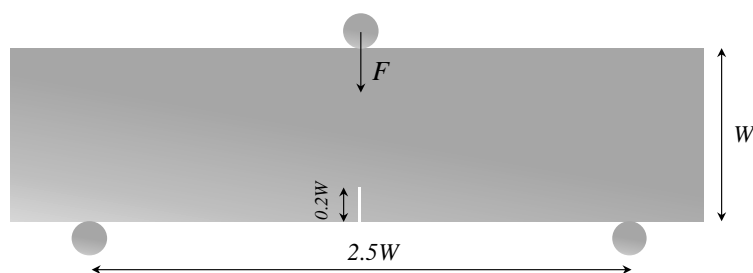


Figure 5. 9 Specimen geometry and boundary condition for the small beam

After the calibration procedures mentioned in Chapter 2, the micro parameters obtained for the mortar beam is given in *Table 5. 2*.

Table 5. 2 Micro parameters obtained for small mortar beam

Micro Parameters	Value	Micro Parameters	Value
Minimum particle diameter d_{\min} (mm)	0.5	Normal stiffness k_n (GPa)	6.2
Ratio of maximum to minimum particle diameter d_{\max}/d_{\min}	1.5	Ratio of normal to shear bond stiffness k_n/k_s	1.77
Normal strength S_n (kN)	1.0	Shear strength S_s (kN)	1.0
Normal softening parameter u_f^n (μm)	20	Shear softening parameter u_f^s (μm)	20
Friction coefficient μ	0.5		

5.2.1 Effect of friction coefficient

The effect of friction coefficient on the numerical behaviour is investigated. Three values of the friction coefficient are chosen (0.3, 0.5 and 0.7) and the results are illustrated in Figure 5. 10.

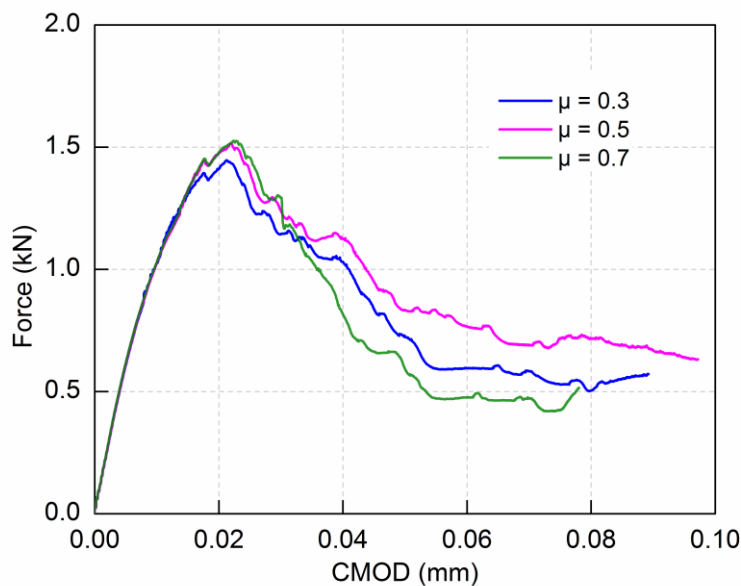


Figure 5. 10 Effect of different friction coefficient in DEM on Force-CMOD curve

The coefficient of friction has no effect on the initial slope of the Force-CMOD curve. As explained before, the friction coefficient is an effective parameter on the shear force. When the shear force exceeds the maximum shear force limit, shear strength ($S'_{s,sof}$) is augmented by the slip. Before reaching the peak force, few cracks occur in the specimen, so this coefficient has no obvious effect on the system slope. The peak force is slightly affected by the friction coefficient. With the increase of the friction coefficient, the peak force increases, however the increase is very small when friction coefficient varies from 0.5 to 0.7. The post-peak behaviour is significantly influenced by the friction coefficient. When friction coefficient varies from 0.3 to 0.5, the post peak response is almost the same;

however, when friction coefficient varies from 0.5 to 0.7, the post peak behaviour becomes more brittle. The reason can be concluded that the friction coefficient between particles influences the initial generation of the specimen, leading to the different compactness of the assembly. When the interparticle friction coefficient is set to very small values, the interparticle sliding is permitted resulting in a dense packing of the particles [351]. Due to the fact that the test specimen used is small, the arrangement of particles changes the numbers of the contact, which impact the redistribution of the stress when the crack propagates leading to the difference in the post-peak part.

5.2.2 Effect of normal and shear strength

The effect of normal and shear strength on the numerical behaviour is investigated. Three values of strengths are chosen ($0.5S_{n,s}$, $1.0S_{n,s}$ and $2.0S_{n,s}$) and the results are illustrated in *Figure 5. 11*.

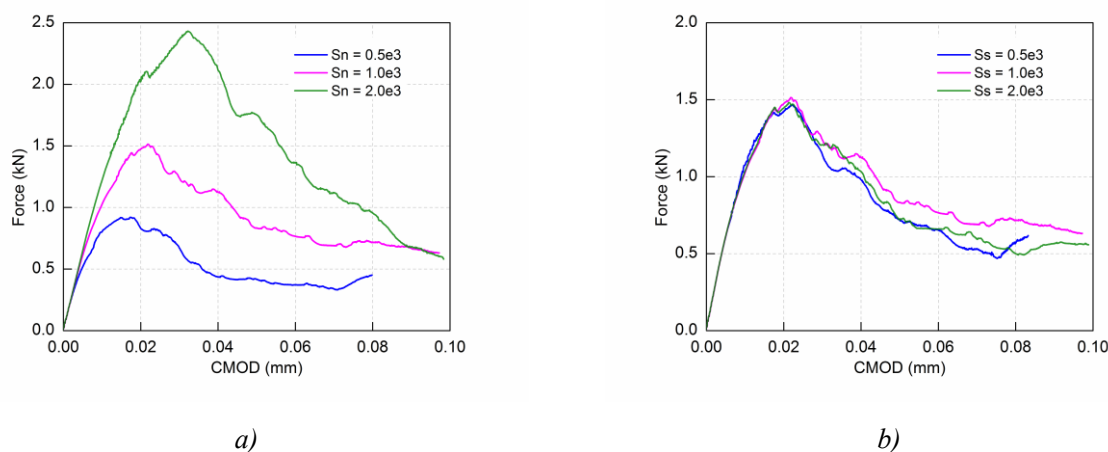


Figure 5. 11 Effect of different strengths in DEM on Force-CMOD curve: a) normal strength; b) shear strength

With the increase of normal strength, the peak force is increasing. However, the increase of shear strength seems to have no obvious impact on the Force-CMOD curve. The reason is that during the fracture in three-point bending test, the tensile behaviour dominates. Therefore, when the normal strength increases, the peak force also increases.

5.2.3 Effect of normal and shear stiffness

The influence of normal and shear stiffness on Force-CMOD curve is given in *Figure 5. 12*.

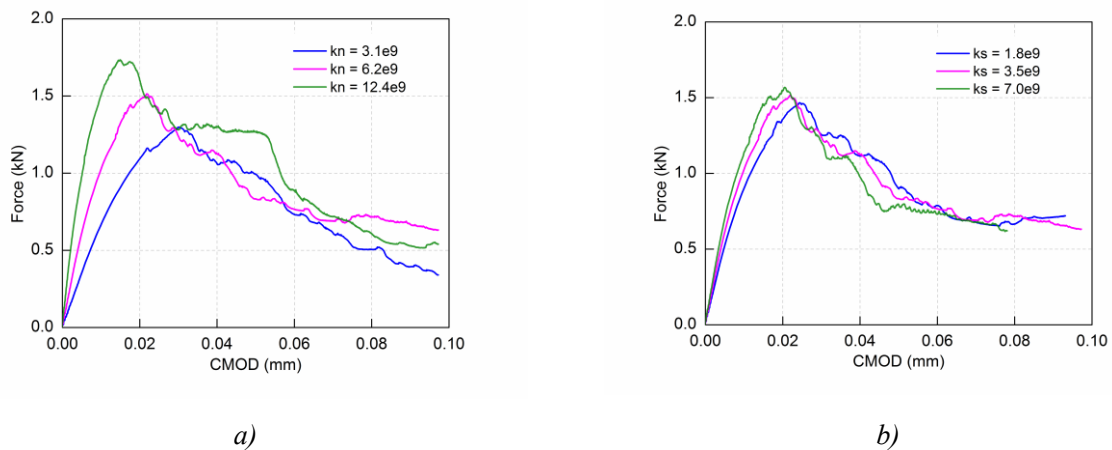


Figure 5.12 Effect of different stiffnesses in DEM on Force-CMOD curve: a) normal stiffness; b) shear stiffness

The normal stiffness has a significant impact not only on the initial slope of the curve but also the peak force. As can be seen in Equation, 5.14, the force is in a relationship with the stiffness, so if the stiffness increases, the force that can bear also increases. By increasing the shear stiffness, the effect is same as that of normal stiffness, but the increase in peak force and initial slope is relatively very small.

5.2.4 Effect of softening parameters

In the softening model described in the previous section, the normal and shear softening parameters control the slope of the softening part. So, the influence of normal and shear softening parameters on Force-CMOD curve is investigated. The results are presented in Figure 5.13.

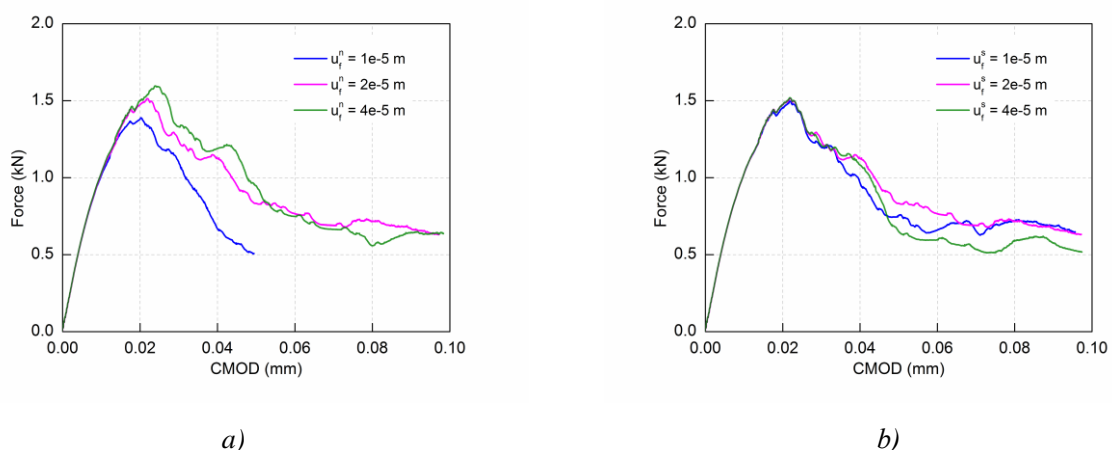


Figure 5.13 Influence of different softening parameters in DEM on Force-CMOD curve: a) normal softening parameter; b) shear softening parameter

The results show that the peak force and the slope of softening part increase with the increase of the normal softening parameter. The reason is that when the normal softening parameter is increasing,

the bearing force at the contact is increasing according to *Equation 5. 14*. So it impacts the bearing force of the beam at the macro level, leading to a smoother descent of the Force-CMOD curve. However, the influence of shear softening parameter is not obvious on the three-point bending test. Since the failure belongs to the Mode I type, the softening behaviour of shear part has limited influence.

5.3 Model validation at local and macroscopic scale

Firstly, the microparameters are determined using inverse calibration scheme presented in Chapter 2 using standard mortar tests: compressive strength of $40 \times 40 \times 40 \text{ mm}^3$ specimen and bending strength of $40 \times 40 \times 160 \text{ mm}^3$ specimen. The calibrated parameters are given in *Table 5. 3*. The mortar used in study is the same which is used in Chapter 3 (section 3.2.1).

Table 5. 3 Micro parameters obtained through the calibration process

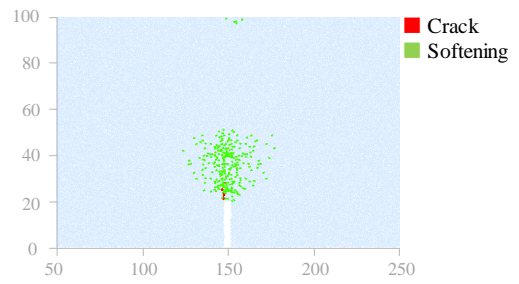
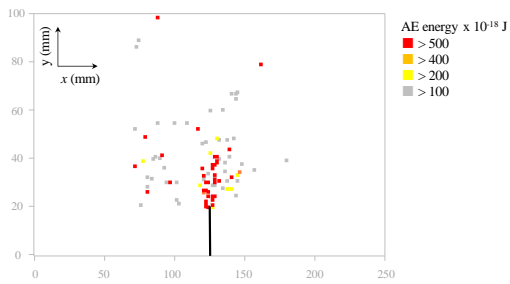
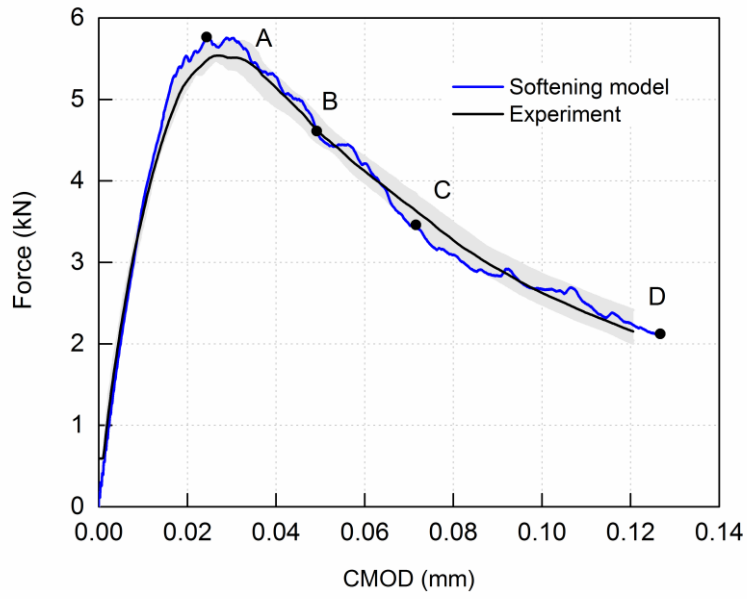
Micro Parameters	Value	Micro Parameters	Value
Minimum particle diameter d_{\min} (mm)	0.5	Normal stiffness k_n (GPa)	24.5
Ratio of maximum to minimum particle diameter d_{\max}/d_{\min}	1.5	Ratio of normal to shear bond stiffness k_n/k_s	1.77
Normal strength S_n (kN)	1.8	Shear strength S_s (kN)	2.0
Normal softening parameter u_f^n (μm)	30	Shear softening parameter u_f^s (μm)	40
Friction coefficient μ	0.5		

Once the parameters are obtained, the model is applied to predict the behaviour of notched three-point bending beam of size and geometrical properties similar to series *D1* ($100 \times 100 \times 400 \text{ mm}^3$) presented in Section 3.5.4. The numerical beam is created by generating 80821 particles inside the rectangular specimen area for the SENB test as shown in *Figure 5. 14*. The constant vertical velocity of the wall is the same as the one used in Chapter 2, namely 0.002 m/s. The result of Force-CMOD curve obtained from modelling is compared with the experimental results as illustrated in *Figure 5. 15*.

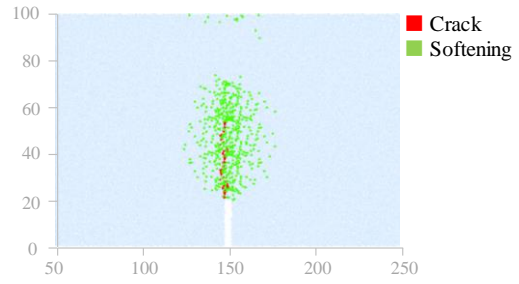
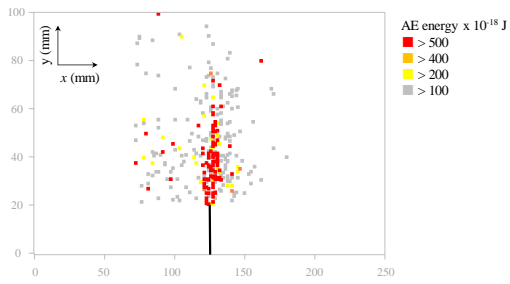


Figure 5. 14 Specimen geometry and boundary condition of the mortar

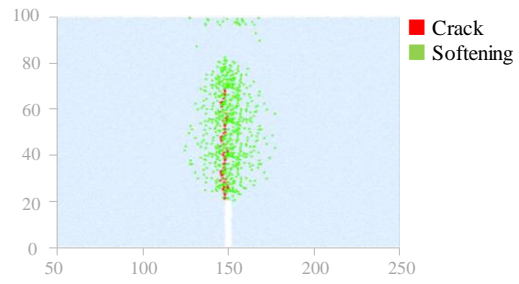
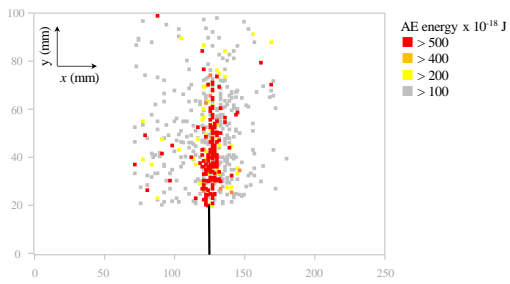
The Force-CMOD curve obtained by the softening model matches well with the experimental results. Then cumulative events of local fracture recorded by acoustic emission during the experiment are compared with the modelling results as presented in *Figure 5. 15*. Four stages of fracture process, namely 100%, post-80%, post-60% and post-36% of peak force are chosen.



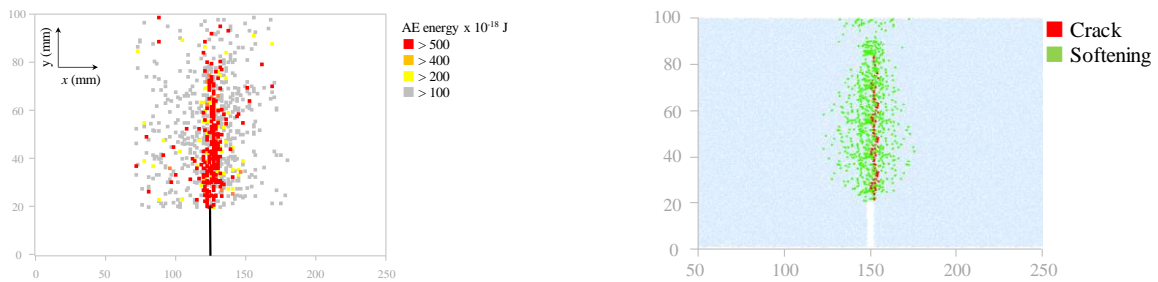
a) Point A : peak force



b) Point B : post-80% of peak force



c) Point C : post-60% of peak force



d) Point D : post-36% of peak force

Figure 5. 15 Central part of SENB specimen displaying four selected stages of the fracture process in comparison to the damage zone estimated experimentally by means of AE

The previous researchers [40, 43] have shown that the scattering zone of AE signal can provide valuable information on the fracture process zone of concrete. Thus, the 2D localization maps of AE events are classified in terms of levels of energy. Four energy levels are defined. High energy levels of AE events are located in the core of the FPZ region outlining the crack path. As defined by Bažant [9], the distribution of tensile stress within the FPZ gradually increases from the initial crack tip and reaches the tensile strength at the end of FPZ. In the DEM modelling, two groups of fractures are defined. Group 1 - Softening: where the contact between two adjacent particles shifts the softening part; Group 2 - Fracture: where the contact has been totally broken. When AE events locations are compared with the numerical local fracture zone, it can be clearly shown that the DEM modelling using softening model can clearly illustrate the fracture process zone and is consistent with the results of AE.

The length of the FPZ can be defined as the length of the softening zone ahead of the crack tip as shown in *Figure 5. 16*. Based on this definition of FPZ, the FPZ length at selected stages of loading (pre-40%, pre-60%, pre-80%, 100%, post-80%, post-60% and post-40% of peak load) is measured. The obtained lengths of FPZ are shown in *Figure 5. 17*.

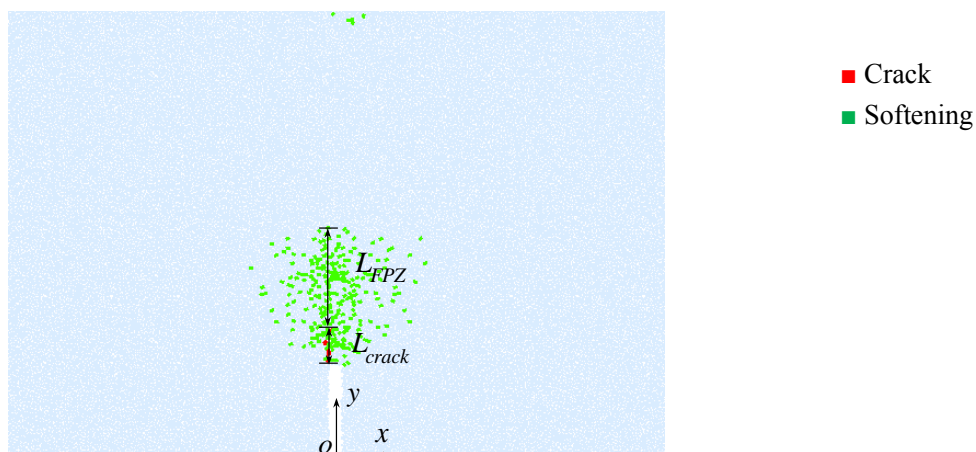


Figure 5. 16 The definition of fracture process zone in DEM modelling

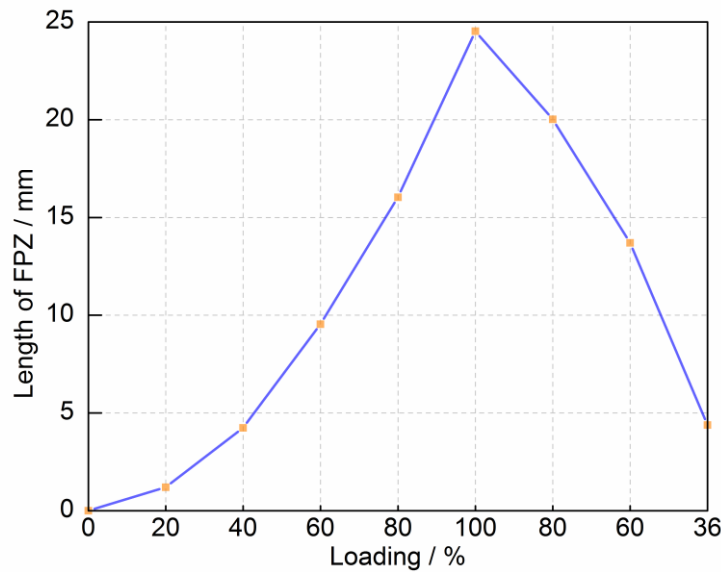


Figure 5. 17 Length of FPZ vs. Loading stage for mortar

When the load is applied to the specimen, the length of the fracture process zone initially increases from the initial notch. Then when the applied load reaches the maximum, the process zone size reaches its maximum length. Afterwards, the length of the fracture process zone decreases when the loading increases. Ha et al. [352] also computationally obtained the similar results by utilizing a cohesive zone modelling approach.

5.4 Application to concrete: study of aggregate grain size effect

The remaining problem in the foregoing chapters is that the model used for concrete is a linear elastic model. Although it can be adapted to investigate the peak loading behaviours and the fracture patterns, the fracture process zone size and the post-peak behaviours of concrete cannot be modelled properly. The size of the fracture process zone length may be largely dependent upon the size of the aggregates [353]. Thus, a softening model has been developed in this chapter. The impact of aggregate size on the fracture process zone is examined. So, the softening model that has established above is employed in this section. The microparameters of mortar matrix have been determined in section 5.3. The next step is to identify the microparameters of aggregate and ITZs based on the same process mentioned in Chapter 3. Firstly, the compressive test and Brazilian test are used for C10 concrete on the purpose of obtaining the microparameters of aggregate. It should be noted that for C10 concrete, Young's modulus, bond strengths and softening parameters of ITZ are taken equal to 80 % of the mortar. Then the microparameters of aggregate can be obtained from the calibration procedures on C10 concrete. Once the microparameters of aggregate and mortar matrix have obtained, the microparameters (Young's modulus, stiffness ratio, softening parameters and bond strengths) of ITZ for C05 concrete and C20 concrete can be determined by inverse calibration procedure using LM method on Brazilian test. The specimens used for the modelling can be found in Figure 5. 18.

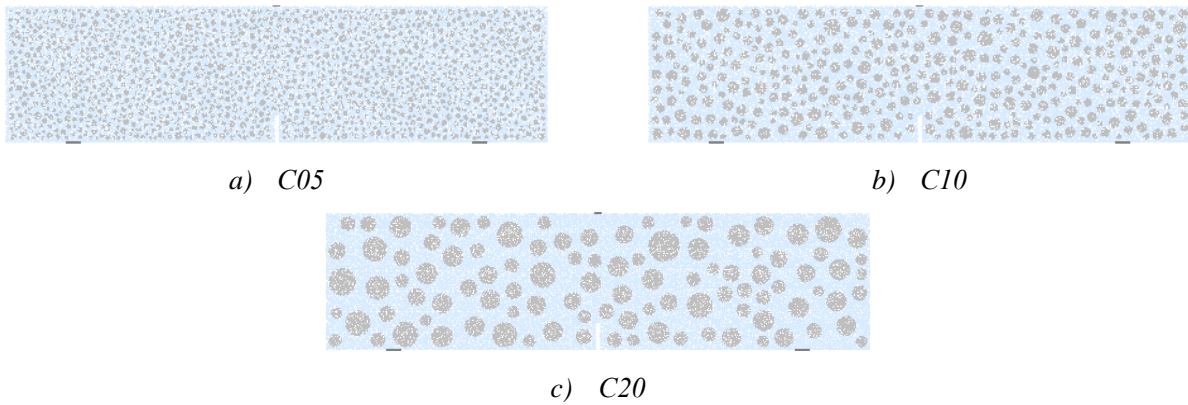


Figure 5.18 Specimens for each concrete series

The Force-CMOD curves for each concrete series are illustrated in Figure 5.19. The calculated maximum vertical forces for each concrete series are given in Table 5.4.

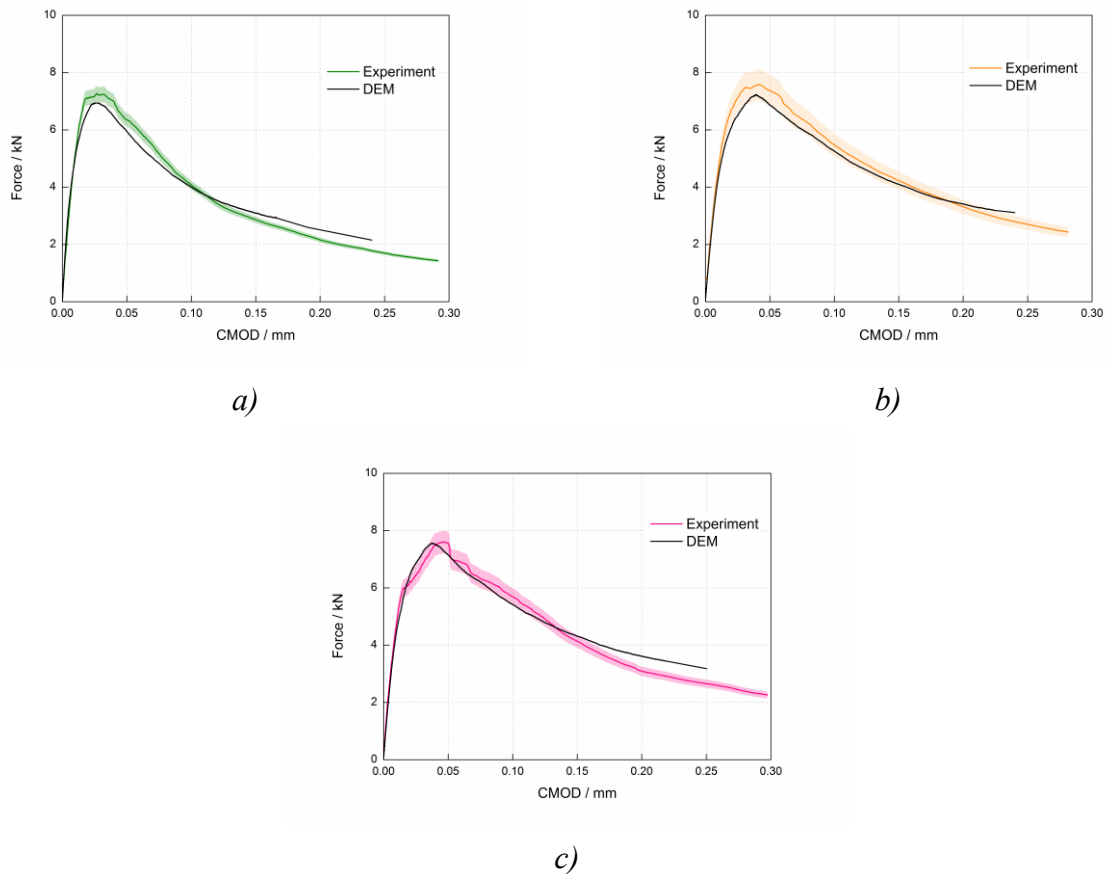


Figure 5.19 Comparison between experimental and numerical Force-CMOD curves for different concrete series: a) C05; b) C10; c) C20

Table 5. 4 Comparison of laboratory tests and modelling results

Series	Force / kN	Experimental Results	Numerical Results
C05		7.42±0.34	6.94
C10		7.55±0.76	7.23
C20		7.61	7.56

The Force-CMOD curves in the simulation using the proposed softening model match well with the experimental curves. There is a little deviation at the end of the curves which can be explained due to the boundary effect. In the softening model used in this section, the fracture energy is constant along the ligament length. However, the studies of Duan and Hu [354-357] showed that the specific fracture energy (G_f) is dependent on ratio between ligament length and initial crack length. The local fracture energy (g_f) at the crack-tip decreases when approaching the boundary at the later stage of fracture. From the *Figure 5. 19*, it can also be observed that with the load increases, all the specimens experience three stages, namely linear elastic at the beginning, hardening until reaching the peak force and softening until the totally failure. So, the softening model developed above is capable to model the fracture behaviour of concrete. Then the fracture path for each DEM concrete series was studied. *Figure 5. 20* presents fracture paths for each DEM concrete series at 60% of the maximum force.

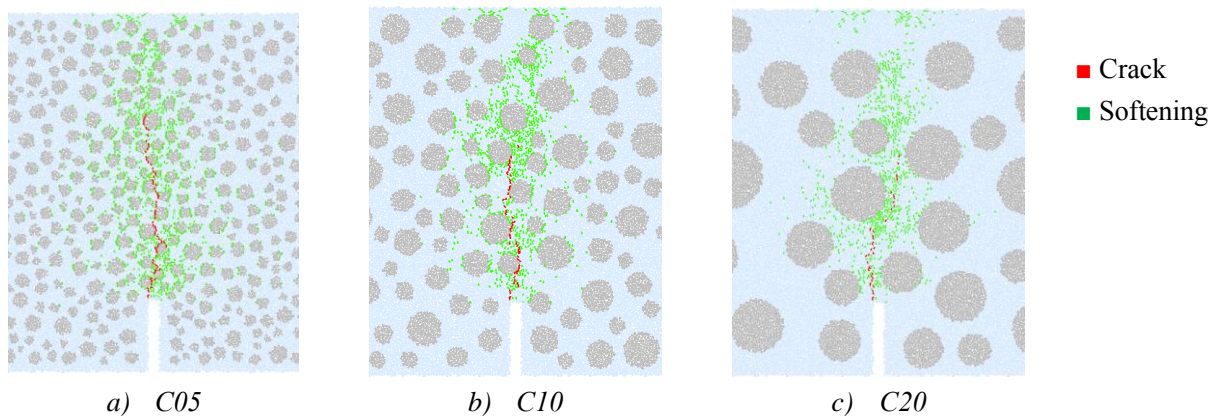


Figure 5. 20 Crack path for each DEM concrete series at 60% of the maximum force

The roughness of the fracture path increases as the aggregate size increases (*Figure 5. 20*) which is also supported by Issa et al. [328]. Overall, the fractures tend to follow the weakest part of concrete, namely interface transition zone (ITZ). More aggregates are placed at the crack path for concrete with smaller aggregate. It means that there exists more ITZs compared with concrete with larger concrete and it is easier to form the crack path. The lower mechanical strengths of ITZs decrease the loading capacity of concrete beam. So, the loading capacity of C05 is smaller than C20.

Based on the method aforesaid (*Figure 5. 16*), the FPZ length at selected stages of loading (pre-40%, pre-60%, pre-80%, 100%, post-80%, post-60% and post-40% of maximum force) is measured for each concrete series.

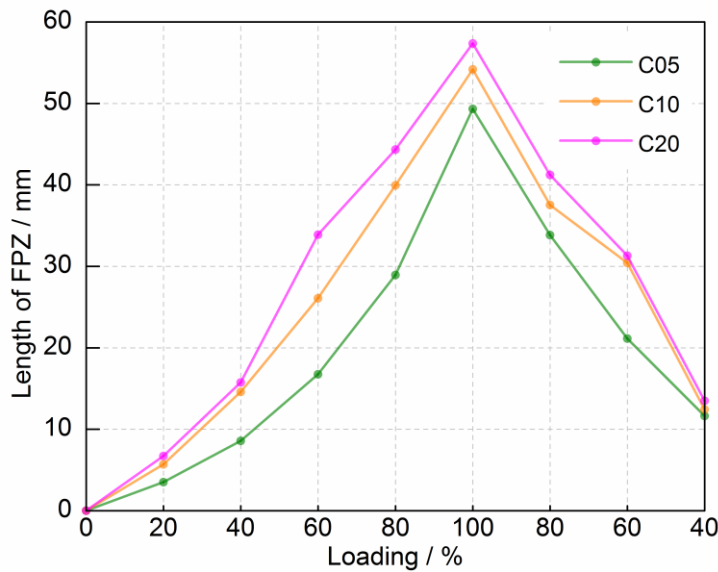


Figure 5. 21 Length of FPZ vs. Loading stage for each concrete series

The length of FPZ experiences an increase with the increase of maximum aggregate size as illustrated in *Figure 5. 21*. The phenomenon is in accordance with the results of AE that showed in *Figure 4. 8*. The possible reason is that the crack path contains more aggregates placed for concrete with smaller aggregate size. It means that there exists more ITZ and the weaker strength of ITZ is easier to form the macrocrack. So, the length of FPZ increases with the increase of aggregate.

5.5 Summary

In Chapter 4, it has been mentioned that with a linear elastic model, the influence of the maximum aggregate on the FPZ length and the post-peak behaviours of concrete cannot be investigated. However, the size of the fracture process zone length may be large depending upon the size of the aggregates. So, in this section, to solve the remained problem, a crack opening displacement softening model is developed. In this softening model, the shear and normal strength are combined with an elliptic form fracture envelope. Thus, the softening model can handle both pure modes and mixed mode fracture behaviours of the materials. Before modelling, the impact of microparameters on the numerical modelling results is also investigated in order to see how each parameter affects the behaviours first, thus can decrease the workload of microparameters calibration procedures. Through a comparison between numerical and experimental results, it can be shown that the proposed model can be used for numerical analysis of quasi-brittle materials like mortar and concrete. It is demonstrated that the fracture process zone experiences an increase until the peak load and then decreases with increasing loading stages. Finally, the aggregate effects are analysed using the proposed softening model, the crack path and the length of FPZ for each concrete series are investigated. It can be concluded that the length of FPZ and the roughness of the fracture path increase with the increase of maximum aggregate size. The reason is that more aggregates placed at the crack path for concrete with smaller aggregate, leading to the weaker ITZ areas. The weaker strength of

ITZ is easier to form the macrocrack, thus the roughness of the fracture path and the length of FPZ increases as the aggregate size increases.

Conclusions and Perspectives

Conclusions

In order to understand the effect of aggregate size on the size effect phenomenon, experimental and numerical studies have been carried out in this work.

The modelling of the fracture behaviour of concrete properly is still a problem, although there exist many approaches to model the fracture behaviours of concrete. Different fracture models for concrete behaviour are presented in the Chapter 1. It clearly shows that the fracture process zone is an important property that influences the fracture behaviours of concrete. These models are generally based on the principles of fracture mechanics or damage mechanics, the numerical methods can be roughly classified into two categories: continuum approach and discontinuum approach. Discrete Element Method (DEM) is one of discontinuum approach that looks into micromechanics of the problem, allows a grain level control and could solve the discontinuous problem. So DEM is suitable to analyse the local behaviours of concrete. Thus, compared with the continuum-based models, discontinuum based models seem more appropriate to model the fracture behaviours of concrete.

Parallel bond model inserted in the DEM code provides the mechanical behaviour of a finite-sized piece of cement-like material deposited between the two contacting particles, thus the parallel bond is considered as a suitable model to perform numerical simulation at first when compared to all the main contact models. However, the modelling results show that the behaviour of concrete with high compressive strength/tensile strength ratio cannot be modelled with the same set of microparameters. The reason is that in the generic formulation of the parallel bond, full contribution of moments is considered and constant normal and shear strengths are used without considering their inter-dependence. Thus, the parallel bond model cannot be used for concrete directly. Therefore, a modified parallel bond model is developed. In the model, the contribution of the moment is considered and a new model parameter is defined in order to control problems in parallel bond model. Concrete is seen as a three-phase composite, hence three types of contacts are determined for three phases (matrix, interface, and aggregate) and aggregates are modelled using cluster particles and bonded together by connecting DEM with Matlab. Levenberg-Marquardt (LM) algorithm is adopted to deal with the time-consuming method (try and error method) used for micro parameters determination. When applied to this modified parallel bond model on mortar and concrete, the numerical results of mechanical behaviour can well reproduce experimental mechanical results and fracture patterns are also correctly described. The modified parallel bond model is then applied in the following chapters to illustrate the local fracture behaviours of concrete related to dimensional size effect and aggregate size effect.

In Chapter 2, an experimental approach is presented to study the general size effect for various concretes with increasing maximum aggregate size. The characteristic structural dimension and the maximum aggregate size (D/d_{\max}) is regarded as a key factor while investigating the size effect. The classical approach is first applied by up-scaling the ratio D/d_{\max} through upscaling the structural dimension and keeping d_{\max} constant. Geometrically increasing sized specimens ($D1$, $D2$, $D3$) in accordance with RILEM recommendations. The experimental results points are located on the Bažant's size effect curve, thus obeying the size effect behaviour. The size effect curves for all concrete series are found to be the same. So, when putting all the points together, it can be concluded that with the increase of d_{\max} , the behaviour of specimens transitions from LEFM to the hypotheses of strength criterion. It means that the specimens with larger d_{\max} are more ductile when compared

with specimens with smaller d_{\max} . Fracture parameters are also obtained from the size effect analysis. The results illustrated that when the maximum aggregate size increased from 5.25 to 21.0 mm, the fracture energy, fracture process zone length, and fracture toughness increases. It means that concrete with small coarse aggregate is more brittle than that with bigger coarse aggregate. It should be pointed out that same results (non-dimensional nominal strength) are obtained from specimens with the same D/d_{\max} ratio: $D2-C20$ and $D1-C10$ ($D/d_{\max}=9.5$); $D2-C10$ and $D1-C05$ ($D/d_{\max}=19$); $D3-C10$ and $D2-C05$ ($D/d_{\max}=38$). It means that increasing the depth of the specimen or decreasing the maximum size of aggregate obtains the same effect. Further investigation of this phenomenon as the most important goal of the thesis was then studied in the Chapter 4.

Through the results obtained by AE and DIC, it is found that the width of FPZ is greater for the larger beam size in the post-peak loadings. The relative crack length also increases with the loading steps but decreases with the size of the specimen. It is due to the decrease of the stress gradient with increasing specimen size. Besides, with the specimen size increasing, the mechanical behaviour becomes more brittle.

Size effect behaviours are modelled by the modified parallel bond model developed in Chapter 2. Only $C10$ concrete with maximum aggregate size of 10.5 mm is selected for the modelling. In the calibration procedures, conventional compressive and tensile tests on mortar are used to determine the microparameters of the matrix. Owing to the lack of experimental results supports, it assumed a linear relationship between hardness and strength. Thus, Young's modulus, tensile strength and cohesive strength of ITZ are simply adopted as 80 % of mortar properties. The other parameters of ITZ are kept the same to the mortar. Then the microparameters of aggregate particles are obtained by calibration on conventional compressive and tensile tests using LM method. After determining all microparameters for concrete, the size effect analysis on bending tests is performed. The numerical results are in compliance with experimental results.

Chapter 4 presents a new way to analyse size effect by another approach to up-scale the ratio D/d_{\max} . In this approach, the structural dimension is kept constant while up-scaling d_{\max} . Based on this approach, Brazilian test, and three-point bending test are used to investigate the mechanical behaviours of concrete with different maximum aggregate size. The indirect tensile strength showed an increase when maximum aggregate size increased and obeyed the modified Bažant's size effect law. It is explained by the fact that the splitting failure is mainly as a result of the opening of a single crack and development of fracture process zone in the surrounding. The increase of aggregate size increases the size of the fracture process zone and energy dissipation which slow down the crack opening, crack propagation and increases the strength. An aggregate size effect law is developed by rearranging Bažant size effect law. The three-point bending results followed well with the aggregate size effect law. The behaviour is plotted on the typical size effect curves; it can be stated that the concrete behaviour transitions from LFM to strength criterion when the maximum size of coarse aggregates increases. A relationship between general size effect and aggregate size effect has been proposed. On this point analysis of the relationship between the two size effects still needs to be further investigated as it is based only on the limited experimental support of this study.

With the help of AE and DIC methods, the size of FPZ and the crack trajectory are investigated. It is found that the width and the length of FPZ increase with the increase of maximum aggregate size. The non-uniform distribution of local fracture and the new upscaling maximum aggregate size approach may be the possible reason for these phenomena. The crack trajectory for concrete with larger aggregate deviates from the rectilinear path compared with the concrete with smaller aggregate.

Results of DEM modelling produced a similar fracture as obtained by experiments. The differences of the crack lengths for different concrete series are not obvious when using a linear elastic contact model. So, in order to investigate the influence of the maximum aggregate on the FPZ length, a more suitable model like softening model needs to be developed.

In Chapter 5 a displacement softening model is developed in the framework of discrete element method to solve the remained problem. In this model, the shear and normal strength are combined with an elliptic form fracture envelope. Thus, the model can handle both pure modes and mixed modes fracture behaviours of the materials. Then the impacts of microparameters on the numerical modelling results are also investigated in order to decrease the workload of microparameters calibration procedures. Through a comparison between numerical and experimental results, it can be demonstrated that the proposed model can be used for numerical analysis of quasi-brittle materials like concrete. Finally, the aggregate effects are analysed using the proposed model using *D1* beams, the crack path and the length of FPZ for each concrete series are investigated. Due to the reason that more aggregates are placed at the crack path for concrete with smaller aggregate size, leading to the weaker ITZ areas, the roughness of the fracture path and the length of FPZ increases as the aggregate size increases.

Perspectives

This study provides insight into the effects of aggregate size on the fracture behaviours of concrete. The current work should be extended in different directions. In the perspective of this work, further experimental research should be conducted to investigate the impact of ITZ on the aggregate size effect. The properties of ITZ can be analysed by scanning electron microscope (SEM) and backscattered electron images (BSE). Through these methods, changes in properties around the aggregate, changes in the spacing along the aggregate surface, and changes in the average chemical composition of the interface can be analysed. It is useful for the further investigation of the aggregate size effect under the level of microstructure.

In this study, only the mode I (tensile) failure is considered to study the effect of aggregate size. Similar relationships can be obtained e.g. between maximum aggregate size and compressive strength. The failure of the compression test is a complex fracture process, so in this study, the effect of aggregate size on the compressive strength is not included. The relationship between compressive strength and the aggregate size effect has yet to be studied, where many parameters related to concrete mix design, rheological, physical and mechanical properties need to be considered.

One of the most prominent outcomes of this experimental study is the relation of conventional size effect and aggregate size effect. Many conclusions have been drawn in this regard. Although an empirical equation has also been proposed, more investigation needs to be performed to obtain the fundamental law between these two size effects.

In the DEM modelling, few problems have still to be reckoned. The first one is that concrete is modelled in a three-phase material without considering the existence of the random pores. So, in the subsequent analysis, the pores will be modelled either simply by random delete the balls in the specimens or by multi-scale modelling where mortar is modelled at the scale of representative elementary volume (REV) where porosity will be considered. Also, in the work, the generation of aggregates in concrete is based on the random generation of circular balls and clumped the small balls together. However, the real shape and the real position of the aggregates may have an influence on the fracture behaviours of concrete. Images obtained from the X-ray micro-computed tomography (μ CT) can be used to produce the real shape and the actual position of the aggregates in concrete.

Appendixes

A. The grading curves for sand and aggregates

As illustrated in Chapter 3 (Section 3.2.1), sand with maximum size 2 mm used in this thesis. The maximum sizes of aggregate were 5.25 mm, 10.5 mm and 21.0 mm, respectively. The grading curves for sand and aggregates are given in *Figure A. 1*.

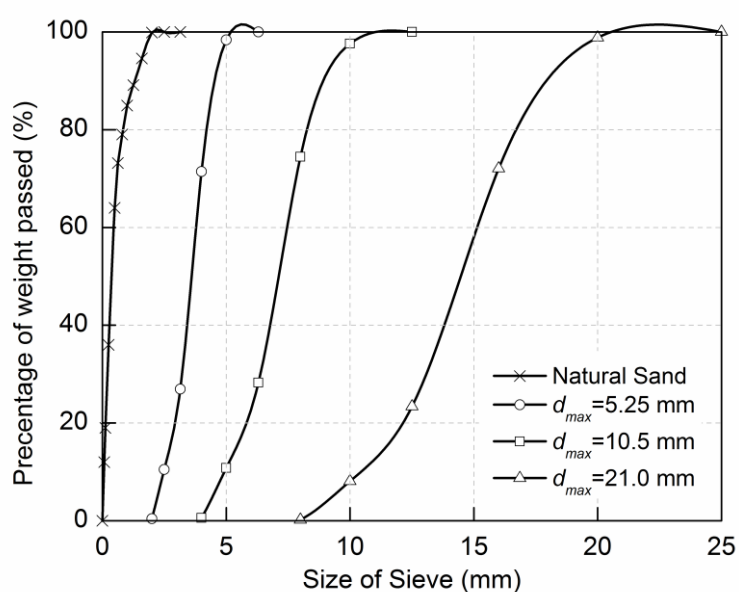


Figure A. 1 Grading curves for sand and aggregates

B. The regression curves

The results of general size effect and aggregate size effect have been given in Chapter 3 and Chapter 4, respectively. As elaborated in Chapter 4 (Section 4.3.3), there may exist a relationship between the two size effects. The regression curves have been made for the parameters obtained for the purpose of finding the empirical relationship between aggregate size effect and general size effect.

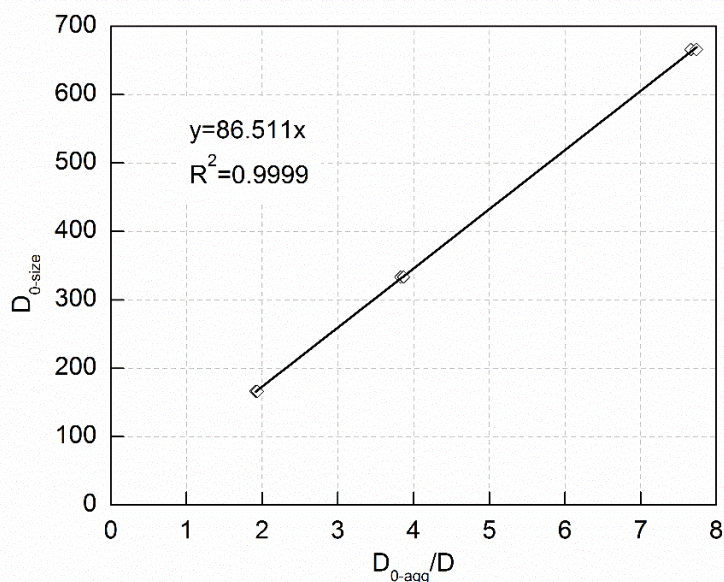


Figure B. 1 The relation between D_{0-agg} and D_{0-size}

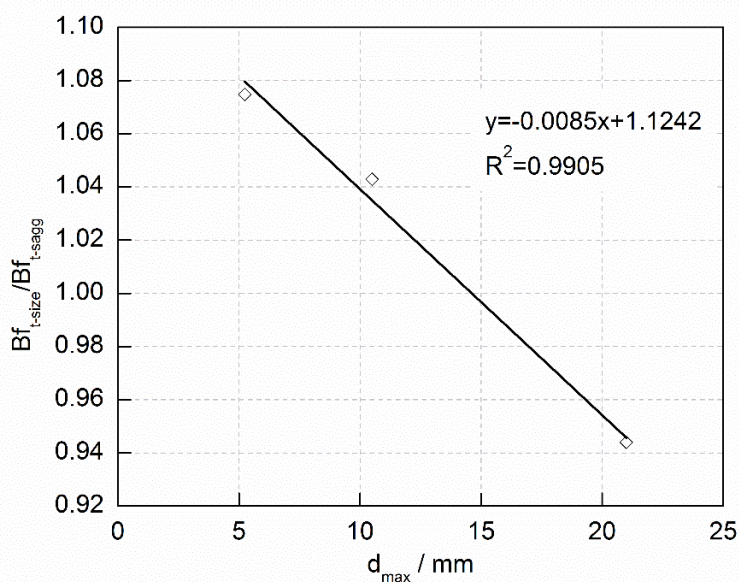


Figure B. 2 The relationship between d_{max} and Bf_{t-size} / Bf_{t-agg} for D1 beams

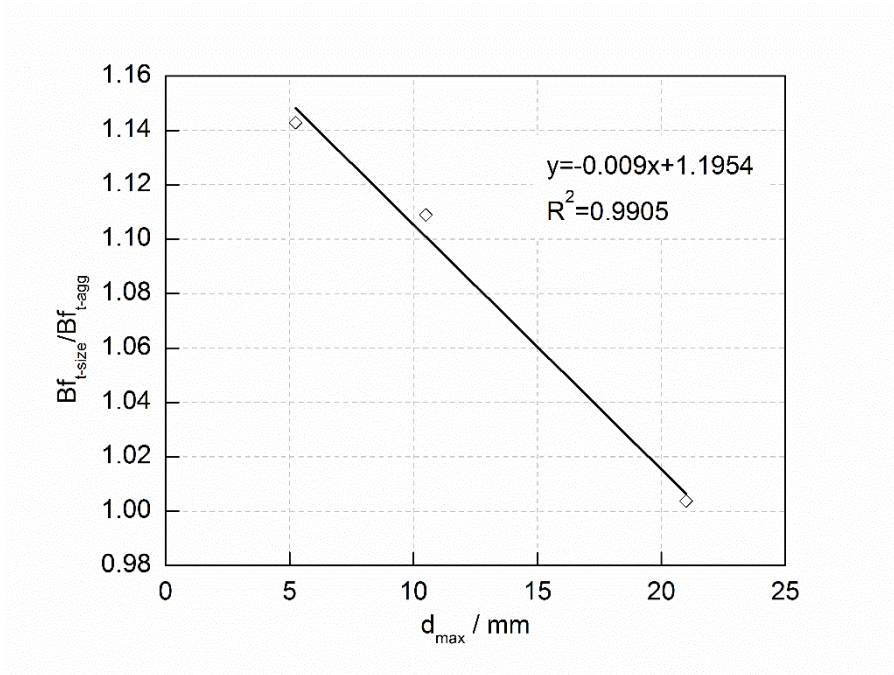


Figure B. 3 The relationship between d_{max} and Bf_{t-size} / Bf_{t-agg} for D2 beams

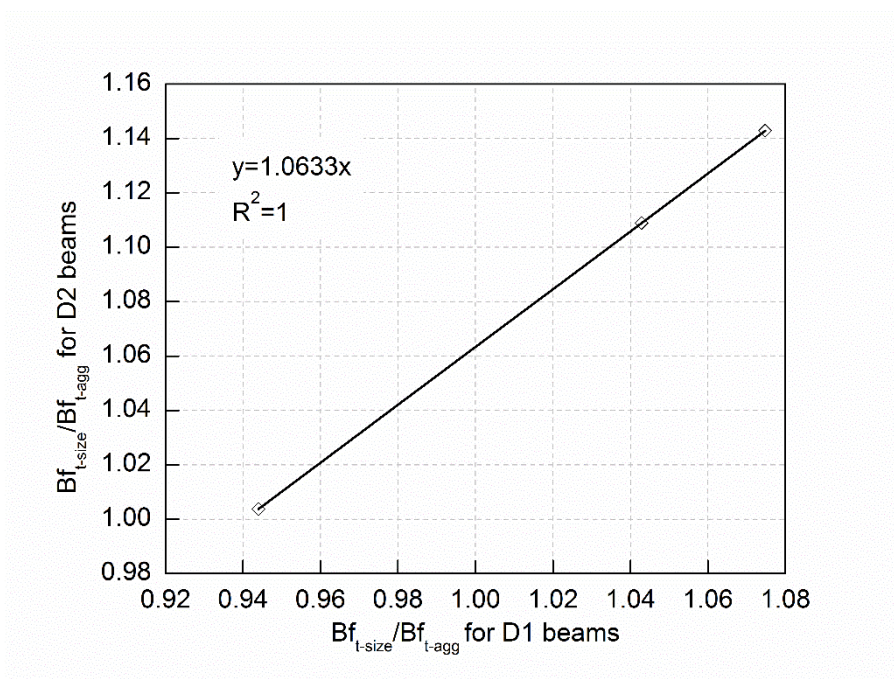


Figure B. 4 The relationship between Bf_{t-size} / Bf_{t-agg} for D1 beams and Bf_{t-size} / Bf_{t-agg} for D2 beams

Bibliographic References

- [1] P. Shafiqh, H. B. Mahmud, M. Z. Jumaat, and M. Zargar, "Agricultural wastes as aggregate in concrete mixtures—A review," *Construction and Building Materials*, vol. 53, pp. 110-117, 2014.
- [2] M. S. Meddah, S. Zitouni, and S. Belâabes, "Effect of content and particle size distribution of coarse aggregate on the compressive strength of concrete," *Construction and Building Materials*, vol. 24, pp. 505-512, 2010.
- [3] K.-R. Wu, B. Chen, W. Yao, and D. Zhang, "Effect of coarse aggregate type on mechanical properties of high-performance concrete," *Cement and Concrete Research*, vol. 31, pp. 1421-1425, 2001.
- [4] P.-C. Aitcin and P. K. Mehta, "Effect of coarse aggregate characteristics on mechanical properties of high-strength concrete," *Materials Journal*, vol. 87, pp. 103-107, 1990.
- [5] A. M. Neville and J. J. Brooks, *Concrete technology*. London: Pearson, 1987.
- [6] A. M. Neville, *Properties of concrete* vol. 4. London: Longman 1995.
- [7] C. F. Goble and M. D. Cohen, "Influence of aggregate surface area on mechanical properties of mortar," *Materials Journal*, vol. 96, pp. 657-662, 1999.
- [8] S. P. Shah, S. E. Swartz, and C. Ouyang, *Fracture mechanics of concrete: applications of fracture mechanics to concrete, rock and other quasi-brittle materials*. New York: John Wiley and Sons, 1995.
- [9] Z. P. Bažant and J. Planas, *Fracture and size effect in concrete and other quasibrittle materials*. Boca Raton: CRC press, 1998.
- [10] S. P. Shah and F. J. McGarry, "Griffith fracture criterion and concrete," *Journal of the Engineering Mechanics Division*, vol. 97, pp. 1663-1676, 1971.
- [11] W. Tasong, C. Lynsdale, and J. Cripps, "Aggregate-cement paste interface. II: Influence of aggregate physical properties," *Cement and Concrete Research*, vol. 28, pp. 1453-1465, 1998.
- [12] K. L. Scrivener, A. K. Crumbie, and P. Laugesen, "The interfacial transition zone (ITZ) between cement paste and aggregate in concrete," *Interface Science*, vol. 12, pp. 411-421, 2004.
- [13] J. Ollivier, J. Maso, and B. Bourdette, "Interfacial transition zone in concrete," *Advanced cement based materials*, vol. 2, pp. 30-38, 1995.
- [14] Ł. Skarżyński and J. Tejchman, "Experimental Investigations of Fracture Process in Concrete by Means of X-ray Micro-computed Tomography," *Strain*, vol. 52, pp. 26-45, 2016.
- [15] T. T. Hsu, F. O. Slate, G. M. Sturman, and G. Winter, "Microcracking of plain concrete and the shape of the stress-strain curve," in *ACI Material Journal*, 1963.
- [16] S. P. Shah and S. Chandra, "Critical stress, volume change, and microcracking of concrete," in *ACI material Journal*, 1968.
- [17] J. G. van Mier, "Framework for a generalized four-stage fracture model of cement-based materials," *Engineering fracture mechanics*, vol. 75, pp. 5072-5086, 2008.
- [18] A. Hillerborg, M. Modéer, and P.-E. Petersson, "Analysis of crack formation and crack growth in concrete by means of fracture mechanics and finite elements," *Cement and Concrete Research*, vol. 6, pp. 773-781, 1976.
- [19] J. Bhargava and Å. Rehnström, "High-speed photography for fracture studies of concrete," *Cement and Concrete Research*, vol. 5, pp. 239-247, 1975.
- [20] X. Hu and F. H. Wittmann, "Experimental method to determine extension of fracture-process zone," *Journal of Materials in Civil Engineering*, vol. 2, pp. 15-23, 1990.
- [21] K. M. Nemati, "Fracture analysis of concrete using scanning electron microscopy," *Scanning*, vol. 19, pp. 426-430, 1997.

- [22] S. Mindess and S. Diamond, "A device for direct observation of cracking of cement paste or mortar under compressive loading within a scanning electron microscope," *Cement and Concrete Research*, vol. 12, pp. 569-576, 1982.
- [23] S. Mindess and S. Diamond, "A preliminary SEM study of crack propagation in mortar," *Cement and Concrete Research*, vol. 10, pp. 509-519, 1980.
- [24] F. O. Slate and S. Olsefski, "X-rays for study of internal structure and microcracking of concrete," in *Journal Proceedings*, 1963, pp. 575-588.
- [25] G. S. Robinson, "Methods of detecting the formation and propagation of microcracks in concrete," in *international conference on the structure of concrete and its behavior under load*, London, 1965, pp. 131-145.
- [26] M. Chabaat and J.-F. Thimus, "Use of scanning electron microscope and the non-local isotropic damage model to investigate fracture process zone in notched concrete beams," *Experimental mechanics*, vol. 47, pp. 473-484, 2007.
- [27] K. Otsuka, "Detection of fine cracks in reinforced concrete through x-ray techniques using contrast media," *Doboku Gakkai Ronbunshu*, vol. 1992, pp. 169-178, 1992.
- [28] K. Otsuka, "X-ray technique with contrast medium to detect fine cracks in reinforced concrete," in *International Workshop on Fracture Toughness and Fracture Energy*, Balkema, 1988.
- [29] K. Otsuka, H. Date, and T. Kurita, "Fracture process zone in concrete tension specimens by X-ray and AE techniques," in *Fracture Mechanics of Concrete Structures-Proceedings FraMCoS-3*, Freiburg, 1998, pp. 1169-1182.
- [30] K. Otsuka and H. Date, "Fracture process zone in concrete tension specimen," *Engineering fracture mechanics*, vol. 65, pp. 111-131, 2000.
- [31] S. Swartz and T. Refai, "Influence of size effects on opening mode fracture parameters for precracked concrete beams in bending," in *Fracture of concrete and rock*, ed: Springer, 1989, pp. 242-254.
- [32] S. Swartz and C. Go, "Validity of compliance calibration to cracked concrete beams in bending," *Experimental mechanics*, vol. 24, pp. 129-134, 1984.
- [33] N. Lee, B. Mayfield, and C. Snell, "Detecting the progress of internal cracks in concrete by using embedded graphite rods," *Magazine of Concrete Research*, vol. 33, pp. 180-183, 1981.
- [34] F. Ansari, "Mechanism of microcrack formation in concrete," *ACI Materials Journal*, vol. 86, pp. 459-464, 1989.
- [35] Y. Sakata and M. Ohtsu, "Crack evaluation in concrete members based on ultrasonic spectroscopy," *Materials Journal*, vol. 92, pp. 686-698, 1995.
- [36] R. Dhir and R. Sangha, "Development and propagation of microcracks in plain concrete," *Matériaux et Construction*, vol. 7, pp. 17-23, 1974.
- [37] J. Saliba, M. Matallah, A. Loukili, J.-P. Regoin, D. Grégoire, L. Verdon, and G. Pijaudier-Cabot, "Experimental and numerical analysis of crack evolution in concrete through acoustic emission technique and mesoscale modelling," *Engineering fracture mechanics*, vol. 167, pp. 123-137, 2016.
- [38] A. Maji, C. Ouyang, and S. Shah, "Fracture mechanisms of quasi-brittle materials based on acoustic emission," *Journal of Materials research*, vol. 5, pp. 206-217, 1990.
- [39] A. Maji and S. Shah, "Process zone and acoustic-emission measurements in concrete," *Experimental mechanics*, vol. 28, pp. 27-33, 1988.
- [40] J. Saliba, A. Loukili, J.-P. Regoin, D. Grégoire, L. Verdon, and G. Pijaudier-Cabot, "Experimental analysis of crack evolution in concrete by the acoustic emission technique," *Frattura ed Integrità Strutturale*, 2015.
- [41] Z. Wu, H. Rong, J. Zheng, F. Xu, and W. Dong, "An experimental investigation on the FPZ properties in concrete using digital image correlation technique," *Engineering fracture mechanics*, vol. 78, pp. 2978-2990, 2011.
- [42] S. Alam, A. Loukili, and F. Grondin, "Monitoring size effect on crack opening in concrete by digital image

- correlation," *European Journal of Environmental and Civil Engineering*, vol. 16, pp. 818-836, 2012.
- [43] S. Y. Alam, J. Saliba, and A. Loukili, "Fracture examination in concrete through combined digital image correlation and acoustic emission techniques," *Construction and Building Materials*, vol. 69, pp. 232-242, 2014.
- [44] S. Muralidhara, B. R. Prasad, H. Eskandari, and B. L. Karihaloo, "Fracture process zone size and true fracture energy of concrete using acoustic emission," *Construction and Building Materials*, vol. 24, pp. 479-486, 2010.
- [45] H. Mihashi, N. Nomura, and S. Niiseki, "Influence of aggregate size on fracture process zone of concrete detected with three dimensional acoustic emission technique," *Cement and Concrete Research*, vol. 21, pp. 737-744, 1991.
- [46] S. Morel, "Size effect in quasibrittle fracture: derivation of the energetic Size Effect Law from equivalent LEFM and asymptotic analysis," *International Journal of Fracture*, vol. 154, pp. 15-26, 2008.
- [47] Z. P. Bažant and B. H. Oh, "Crack band theory for fracture of concrete," *Materials and Structures*, vol. 16, pp. 155-177, 1983.
- [48] W. Yao, K. Wu, and Z. Li, "Fracture process zone of composite materials as concrete," in *Third international conference on fracture mechanics of concrete and concrete structures (FRAMCOS-3)*, 1998.
- [49] S. Chhuy, G. Cannard, J. Robert, and P. Acker, "Experimental investigations into the damage of cement concrete with natural aggregates," in *Brittle Matrix Composites 1*, ed: Springer, 1986, pp. 341-354.
- [50] M. G. Alexander, "Use of ultrasonic pulse velocity for fracture testing of cemented materials," *Cement, concrete and aggregates*, vol. 10, pp. 9-14, 1988.
- [51] M. Alexander and G. Blight, "The use of small and large beams for evaluating concrete fracture characteristics," *Fracture toughness and fracture energy*. Elsevier, Amsterdam, pp. 323-332, 1986.
- [52] S. Shah, "Dependence of concrete fracture toughness on specimen geometry and on composition," in *Fracture mechanics of concrete: Material characterization and testing*, ed: Springer, 1984, pp. 111-135.
- [53] H. Hilsdorf and W. Brameshuber, "Code-type formulation of fracture mechanics concepts for concrete," *International Journal of Fracture*, vol. 51, pp. 61-72, 1991.
- [54] A. Bentur and M. Alexander, "A review of the work of the RILEM TC 159-ETC: Engineering of the interfacial transition zone in cementitious composites," *Materials and Structures*, vol. 33, pp. 82-87, 2000.
- [55] K. Scrivener, "Characterisation of the ITZ and its quantification by test methods," RILEM Reports 1369-4448, 1999.
- [56] W. A. Tasing, C. J. Lynsdale, and J. C. Cripps, "Aggregate-cement paste interface: Part I. Influence of aggregate geochemistry," *Cement and Concrete Research*, vol. 29, pp. 1019-1025, 1999.
- [57] P. Simeonov and S. Ahmad, "Effect of transition zone on the elastic behavior of cement-based composites," *Cement and Concrete Research*, vol. 25, pp. 165-176, 1995.
- [58] C. Perry and J. Gillott, "The influence of mortar-aggregate bond strength on the behaviour of concrete in uniaxial compression," *Cement and Concrete Research*, vol. 7, pp. 553-564, 1977.
- [59] R. Zimbelmann, "A contribution to the problem of cement-aggregate bond," *Cement and Concrete Research*, vol. 15, pp. 801-808, 1985.
- [60] P. Monteiro, J. Maso, and J. Ollivier, "The aggregate-mortar interface," *Cement and Concrete Research*, vol. 15, pp. 953-958, 1985.
- [61] A. Elsharief, M. D. Cohen, and J. Olek, "Influence of aggregate size, water cement ratio and age on the microstructure of the interfacial transition zone," *Cement and Concrete Research*, vol. 33, pp. 1837-1849, 2003.
- [62] F. Grondin and M. Matallah, "How to consider the Interfacial Transition Zones in the finite element modelling of concrete?," *Cement and Concrete Research*, vol. 58, pp. 67-75, 2014.
- [63] M. Nitka and J. Tejchman, "A three-dimensional meso-scale approach to concrete fracture based on combined DEM with X-ray μ CT images," *Cement and Concrete Research*, vol. 107, pp. 11-29, 2018.
- [64] D. S. Dugdale, "Yielding of steel sheets containing slits," *Journal of the Mechanics and Physics of Solids*, vol. 8, pp. 100-104, 1960.

- [65] G. I. Barenblatt, "The mathematical theory of equilibrium cracks in brittle fracture," in *Advances in applied mechanics*. vol. 7, ed: Elsevier, 1962, pp. 55-129.
- [66] L. Cedolin, S. D. Poli, and I. Iori, "Tensile behavior of concrete," *Journal of engineering mechanics*, vol. 113, pp. 431-449, 1987.
- [67] S. Morel, C. Lespine, J.-L. Coureau, J. Planas, and N. Dourado, "Bilinear softening parameters and equivalent LEFM R-curve in quasibrittle failure," *International Journal of Solids and Structures*, vol. 47, pp. 837-850, 2010.
- [68] S. Morel and N. Dourado, "Size effect in quasibrittle failure: Analytical model and numerical simulations using cohesive zone model," *International Journal of Solids and Structures*, vol. 48, pp. 1403-1412, 2011.
- [69] P. Roelfstra, "Numerical method to link strain softening with failure of concrete," presented at the Fracture toughness and fracture energy of concrete, Amsterdam, 1986.
- [70] F. Wittmann, K. Rokugo, E. Brühwiler, H. Mihashi, and P. Simonin, "Fracture energy and strain softening of concrete as determined by means of compact tension specimens," *Materials and Structures*, vol. 21, pp. 21-32, 1988.
- [71] P.-E. Petersson, *Crack growth and development of fracture zones in plain concrete and similar materials*: Division, Inst., 1981.
- [72] B. Liaw, F. Jeang, J. Du, N. Hawkins, and A. Kobayashi, "Improved nonlinear model for concrete fracture," *Journal of engineering mechanics*, vol. 116, pp. 429-445, 1990.
- [73] J. Planas and M. Elices, "Fracture criteria for concrete: mathematical approximations and experimental validation," *Engineering fracture mechanics*, vol. 35, pp. 87-94, 1990.
- [74] B. L. Karihaloo, "Fracture mechanics and structural concrete," presented at the Concrete Design and Construction Series, New York, 1995.
- [75] J. Du, J. Yon, N. Hawkins, K. Arakawa, and A. Kobayashi, "Fracture process zone for concrete for dynamic loading," *Materials Journal*, vol. 89, pp. 252-258, 1992.
- [76] Y. Jenq and S. P. Shah, "Two parameter fracture model for concrete," *Journal of engineering mechanics*, vol. 111, pp. 1227-1241, 1985.
- [77] B. Karihaloo and P. Nallathambi, "Effective crack model for the determination of fracture toughness (K_{ICe}) of concrete," *Engineering fracture mechanics*, vol. 35, pp. 637-645, 1990.
- [78] Z. P. Bažant, J.-K. Kim, and P. A. Pfeiffer, "Nonlinear fracture properties from size effect tests," *Journal of Structural Engineering*, vol. 112, pp. 289-307, 1986.
- [79] B. Lawn and T. R. Wilshaw, *Fracture of brittle solids*: Cambridge university press, 1993.
- [80] S. Morel, E. Bouchaud, J. Schmittbuhl, and G. Valentin, "R-curve behavior and roughness development of fracture surfaces," *International Journal of Fracture*, vol. 114, pp. 307-325, 2002.
- [81] S. Morel, G. Mourot, and J. Schmittbuhl, "Influence of the specimen geometry on R-curve behavior and roughening of fracture surfaces," *International Journal of Fracture*, vol. 121, pp. 23-42, 2003.
- [82] S. Morel, N. Dourado, and G. Valentin, "Wood: a quasibrittle material R-curve behavior and peak load evaluation," *International Journal of Fracture*, vol. 131, pp. 385-400, 2005.
- [83] R. D. Recommendations, "Determination of fracture parameters (K_{ICs} and CTOD_c) of plain concrete using three-point bend tests," *Materials and Structures*, vol. 23, pp. 457-460, 1990.
- [84] Z. P. Bažant and M. T. Kazemi, "Determination of fracture energy, process zone length and brittleness number from size effect, with application to rock and concrete," *International Journal of Fracture*, vol. 44, pp. 111-131, 1990.
- [85] K. Løland, "Continuous damage model for load-response estimation of concrete," *Cement and Concrete Research*, vol. 10, pp. 395-402, 1980.
- [86] J. Mazars, D. Boerman, and G. Piatti, "Mechanical damage and fracture of concrete structures," in *5th*

- International Conference on Fracture*, Cannes, France, 1981, pp. 1499-1506.
- [87] G. Fonseka and D. Krajcinovic, "The continuous damage theory of brittle materials, part 2: uniaxial and plane response modes," *Journal of applied mechanics*, vol. 48, pp. 816-824, 1981.
- [88] D. Krajcinovic and G. Fonseka, "The continuous damage theory of brittle materials, part 1: general theory," *Journal of applied mechanics*, vol. 48, pp. 809-815, 1981.
- [89] A. Sellier, G. Casaux-Ginestet, L. Buffo-Lacarrière, and X. Bourbon, "Orthotropic damage coupled with localized crack reclosure processing. Part I: Constitutive laws," *Engineering fracture mechanics*, vol. 97, pp. 148-167, 2013.
- [90] C. La Borderie, "Phénomènes unilatéraux dans un matériau endommageable: Modélisation et application à l'analyse de structures en béton," Paris 6, 1991.
- [91] S. Fichant, "Endommagement et anisotropie induite du béton de structures: modélisations approchées," Cachan, Ecole normale supérieure, 1996.
- [92] S. Fichant, G. Pijaudier-Cabot, and C. La Borderie, "Continuum damage modelling: approximation of crack induced anisotropy," *Mechanics Research Communications*, vol. 24, pp. 109-114, 1997.
- [93] R. Desmorat, F. Gatuingt, and F. Ragueneau, "Nonlocal anisotropic damage model and related computational aspects for quasi-brittle materials," *Engineering fracture mechanics*, vol. 74, pp. 1539-1560, 2007.
- [94] R. Desmorat, "Dissymétrie de comportement élastique anisotrope couplé ou non à l'endommagement," *Comptes Rendus de l'Académie des Sciences-Series IIB-Mechanics*, vol. 328, pp. 445-450, 2000.
- [95] M. Ortiz, "A constitutive theory for the inelastic behavior of concrete," *Mechanics of materials*, vol. 4, pp. 67-93, 1985.
- [96] J. Mazars, "A description of micro-and macroscale damage of concrete structures," *Engineering fracture mechanics*, vol. 25, pp. 729-737, 1986.
- [97] P. Ladeveze and J. Lemaitre, "Damage effective stress in quasi unilateral conditions," in *16th International congress of theoretical and applied mechanics*, Lyngby, Denmark, 1984.
- [98] W. Suaris, C. Ouyang, and V. M. Fernando, "Damage model for cyclic loading of concrete," *Journal of engineering mechanics*, vol. 116, pp. 1020-1035, 1990.
- [99] G. Z. Voyiadjis and T. M. Abu-Lebdeh, "Damage model for concrete using bounding surface concept," *Journal of engineering mechanics*, vol. 119, pp. 1865-1885, 1993.
- [100] J. M. Sancho, J. Planas, D. A. Cendón, E. Reyes, and J. Gálvez, "An embedded crack model for finite element analysis of concrete fracture," *Engineering fracture mechanics*, vol. 74, pp. 75-86, 2007.
- [101] G. Wells and L. Sluys, "A new method for modelling cohesive cracks using finite elements," *International Journal for Numerical Methods in Engineering*, vol. 50, pp. 2667-2682, 2001.
- [102] M. Aliabadi and A. Saleh, "Fracture mechanics analysis of cracking in plain and reinforced concrete using the boundary element method," *Engineering fracture mechanics*, vol. 69, pp. 267-280, 2002.
- [103] A. Saleh and M. Aliabadi, "Crack growth analysis in concrete using boundary element method," *Engineering fracture mechanics*, vol. 51, pp. 533-545, 1995.
- [104] S. G. F. Cordeiro, E. D. Leonel, and P. Beaurepaire, "Quantification of cohesive fracture parameters based on the coupling of Bayesian updating and the boundary element method," *Engineering Analysis with Boundary Elements*, vol. 74, pp. 49-60, 2017.
- [105] J. Kozicki and F. Donzé, "A new open-source software developed for numerical simulations using discrete modeling methods," *Computer Methods in Applied Mechanics and Engineering*, vol. 197, pp. 4429-4443, 2008.
- [106] F. Camborde, C. Mariotti, and F. Donzé, "Numerical study of rock and concrete behaviour by discrete element modelling," *Computers and Geotechnics*, vol. 27, pp. 225-247, 2000.
- [107] S. Hentz, L. Daudeville, and F. V. Donzé, "Identification and validation of a discrete element model for concrete," *Journal of engineering mechanics*, vol. 130, pp. 709-719, 2004.

- [108] D. Kourepinis, C. Pearce, and N. Bićanić, "Higher-order discontinuous modeling of fracturing in concrete using the numerical manifold method," *International Journal of Computational Methods*, vol. 7, pp. 83-106, 2010.
- [109] R.-J. Tsay, Y.-J. Chiou, and W.-L. Chuang, "Crack growth prediction by manifold method," *Journal of engineering mechanics*, vol. 125, pp. 884-890, 1999.
- [110] Y.-J. Chiou, Y.-M. Lee, and R.-J. Tsay, "Mixed mode fracture propagation by manifold method," *International Journal of Fracture*, vol. 114, pp. 327-347, 2002.
- [111] C. Pearce, A. Thavalingam, Z. Liao, and N. Bićanić, "Computational aspects of the discontinuous deformation analysis framework for modelling concrete fracture," *Engineering fracture mechanics*, vol. 65, pp. 283-298, 2000.
- [112] J. Tomiyama, S. Iraha, G. Yagawa, T. Yamada, and T. Yabuki, "Fracture analysis of concrete using free mesh method," in *Infrastructure regeneration and rehabilitation improving the quality of life through better construction*, 1999.
- [113] T. Rabczuk and J. Eibl, "Modelling dynamic failure of concrete with meshfree methods," *International Journal of Impact Engineering*, vol. 32, pp. 1878-1897, 2006.
- [114] J. H. Argyris and S. Kelsey, *Energy theorems and structural analysis* vol. 960: Springer, 1960.
- [115] R. W. Clough, "The finite element method in plane stress analysis," in *Proceedings of 2nd ASCE Conference on Electronic Computation, Pittsburgh Pa., Sept. 8 and 9, 1960*, 1960.
- [116] D. Ngo and A. Scordelis, "Finite element analysis of reinforced concrete beams," *ACI Journal*, vol. 64, pp. 152-163, 1967.
- [117] K. S. Hibbit and B. Karlsson, "ABAQUS Reference Manuals," *Dassault Systemes*, 2005.
- [118] D. Brooker and B. Ronalds, "Prediction of ductile failure in tubular steel members using ABAQUS," in *The Eleventh International Offshore and Polar Engineering Conference*, 2001.
- [119] O. Zienkiewicz, E. Hinton, N. Bićanić, and P. Fejzo, "Computational models for the transient dynamic analysis of concrete dams," in *Dams and earthquake*, ed London: Thomas Telford Publishing, 1981, pp. 171-178.
- [120] Y. Rashid, "Ultimate strength analysis of prestressed concrete pressure vessels," *Nuclear engineering and design*, vol. 7, pp. 334-344, 1968.
- [121] A. H.-D. Cheng and D. T. Cheng, "Heritage and early history of the boundary element method," *Engineering Analysis with Boundary Elements*, vol. 29, pp. 268-302, 2005.
- [122] T. Cruse, "Numerical evaluation of elastic stress intensity factors by the boundary-integral equation method," in *Surface cracks: physical problems and computational solutions*, ed, 1972, pp. 153-170.
- [123] P. Cundall, "A computer model for simulating systems," in *Proceedings of the Symposium of the International Society of Rock Mechanics*, Nancy, France, 1971.
- [124] P. A. Cundall and O. D. Strack, "A discrete numerical model for granular assemblies," *Geotechnique*, vol. 29, pp. 47-65, 1979.
- [125] P. A. Cundall, "A computer model for simulating progressive large scale movements in blocky rock systems," in *Proc. Symp. Rock Fracture (ISRM)*, Nancy, 2013.
- [126] S. Hentz, F. V. Donzé, and L. Daudeville, "Discrete element modelling of concrete submitted to dynamic loading at high strain rates," *Computers & structures*, vol. 82, pp. 2509-2524, 2004.
- [127] D. Kretz, S. Callau-Monje, M. Hitschler, A. Hien, M. Raedle, and J. Hesser, "Discrete element method (DEM) simulation and validation of a screw feeder system," *Powder Technology*, vol. 287, pp. 131-138, 2016.
- [128] L. Jing and O. Stephansson, *Fundamentals of discrete element methods for rock engineering: theory and applications* vol. 85: Elsevier, 2007.
- [129] S. Sinaie, T. D. Ngo, and V. P. Nguyen, "A discrete element model of concrete for cyclic loading," *Computers & structures*, vol. 196, pp. 173-185, 2018.

- [130] H. Kim, M. P. Wagoner, and W. G. Buttlar, "Simulation of fracture behavior in asphalt concrete using a heterogeneous cohesive zone discrete element model," *Journal of Materials in Civil Engineering*, vol. 20, pp. 552-563, 2008.
- [131] A. Hrennikoff, "Solution of problems of elasticity by the framework method," *Journal of applied mechanics*, vol. 8, pp. A169-A175, 1941.
- [132] P. Cundall, "Lattice method for modeling brittle, jointed rock," in *Proceedings of the 2nd Int'l FLAC/DEM Symposium on Continuum and Distinct Element Numerical Modeling in Geomechanics, Melbourne*, 2011.
- [133] E. Zafati, C. Oliver-Leblond, and F. Ragueneau, "Modeling of quasi-brittle materials cracking using a lattice discrete element approach," in *Computational Modelling of Concrete Structures*, ed: CRC Press, 2018, pp. 661-667.
- [134] E. Schlangen and E. Garboczi, "Fracture simulations of concrete using lattice models: computational aspects," *Engineering fracture mechanics*, vol. 57, pp. 319-332, 1997.
- [135] N. Moës, J. Dolbow, and T. Belytschko, "A finite element method for crack growth without remeshing," *International Journal for Numerical Methods in Engineering*, vol. 46, pp. 131-150, 1999.
- [136] T. Belytschko and T. Black, "Elastic crack growth in finite elements with minimal remeshing," *International Journal for Numerical Methods in Engineering*, vol. 45, pp. 601-620, 1999.
- [137] M. Stolarska, D. L. Chopp, N. Moës, and T. Belytschko, "Modelling crack growth by level sets in the extended finite element method," *International Journal for Numerical Methods in Engineering*, vol. 51, pp. 943-960, 2001.
- [138] S. Osher and J. A. Sethian, "Fronts propagating with curvature-dependent speed: algorithms based on Hamilton-Jacobi formulations," *Journal of computational physics*, vol. 79, pp. 12-49, 1988.
- [139] E. Yamaguchi and W.-F. Chen, "Cracking model for finite element analysis of concrete materials," *Journal of engineering mechanics*, vol. 116, pp. 1242-1260, 1990.
- [140] E. Schlangen and J. Van Mier, "Simple lattice model for numerical simulation of fracture of concrete materials and structures," *Materials and Structures*, vol. 25, pp. 534-542, 1992.
- [141] W. Trawiński, J. Tejchman, and J. Bobiński, "A three-dimensional meso-scale modelling of concrete fracture, based on cohesive elements and X-ray μ CT images," *Engineering fracture mechanics*, 2017.
- [142] G. Lilliu and J. G. van Mier, "3D lattice type fracture model for concrete," *Engineering fracture mechanics*, vol. 70, pp. 927-941, 2003.
- [143] Ł. Skarżyński, M. Nitka, and J. Tejchman, "Modelling of concrete fracture at aggregate level using FEM and DEM based on X-ray μ CT images of internal structure," *Engineering fracture mechanics*, vol. 147, pp. 13-35, 2015.
- [144] P. Cundall, A. Drescher, and O. D. Strack, "Numerical experiments on granular assemblies; measurements and observations," in *Deformation and failure of granular materials. IUTAM symposium, Delft*, Rotterdam, 1982.
- [145] P. A. Cundall, "Formulation of a three-dimensional distinct element model—Part I. A scheme to detect and represent contacts in a system composed of many polyhedral blocks," in *International Journal of Rock Mechanics and Mining Sciences & Geomechanics Abstracts*, 1988, pp. 107-116.
- [146] I. Ishibashi, Y.-C. Chen, and J. Jenkins, "Dynamic shear modulus and fabric: part II, stress reversal," *Geotechnique*, vol. 38, pp. 33-37, 1988.
- [147] C. Thornton and D. Barnes, "Computer simulated deformation of compact granular assemblies," *Acta Mechanica*, vol. 64, pp. 45-61, 1986.
- [148] S. Yu, M. Adams, B. Gururajan, G. Reynolds, R. Roberts, and C.-Y. Wu, "The effects of lubrication on roll compaction, ribbon milling and tableting," *Chemical engineering science*, vol. 86, pp. 9-18, 2013.
- [149] M. Hakuno and K. Meguro, "Simulation of concrete-frame collapse due to dynamic loading," *Journal of engineering mechanics*, vol. 119, pp. 1709-1723, 1993.
- [150] K. MEGURO and M. HAKUNO, "Fracture analyses of concrete structures by the modified distinct element

- method," *Doboku Gakkai Ronbunshu*, vol. 1989, pp. 113-124, 1989.
- [151] S. Takada and N. Hassani, "Analysis of compression failure of reinforced concrete by the modified distinct element method," *Earthquake Resistant Engineering Structures, Computational Mechanics Publications*, vol. 23, pp. 429-438, 1996.
- [152] T. Katsaga, "Geophysical imaging and numerical modelling of fractures in concrete," University of Toronto, 2010.
- [153] N. M. Azevedo and J. Lemos, "Hybrid discrete element/finite element method for fracture analysis," *Computer Methods in Applied Mechanics and Engineering*, vol. 195, pp. 4579-4593, 2006.
- [154] J. Pan, Y. Feng, F. Jin, Y. Xu, Q. Sun, C. Zhang, and D. Owen, "Meso-scale particle modeling of concrete deterioration caused by alkali-aggregate reaction," *International Journal for Numerical and Analytical Methods in Geomechanics*, vol. 37, pp. 2690-2705, 2013.
- [155] M. Nitka and J. Tejchman, "Modelling of concrete behaviour in uniaxial compression and tension with DEM," *Granular Matter*, vol. 17, pp. 145-164, 2015.
- [156] M. S. Diederichs, "Instability of hard rockmasses: the role of tensile damage and relaxation," PhD Thesis, University of Waterloo, Canada, 2000.
- [157] D. O. Potyondy and P. A. Cundall, "A bonded-particle model for rock," *International journal of rock mechanics and mining sciences*, vol. 41, pp. 1329-1364, 2004.
- [158] M. P. Schöpfer, S. Abe, C. Childs, and J. J. Walsh, "The impact of porosity and crack density on the elasticity, strength and friction of cohesive granular materials: insights from DEM modelling," *International journal of rock mechanics and mining sciences*, vol. 46, pp. 250-261, 2009.
- [159] N. a. Cho, C. Martin, and D. Segol, "A clumped particle model for rock," *International journal of rock mechanics and mining sciences*, vol. 44, pp. 997-1010, 2007.
- [160] D. Potyondy and P. Cundall, "A bonded-particle model for rock," *International journal of rock mechanics and mining sciences*, vol. 41, pp. 1329-1364, 2004.
- [161] C. Lian, Y. Zhuge, and S. Beecham, "Numerical simulation of the mechanical behaviour of porous concrete," *Engineering Computations*, vol. 28, pp. 984-1002, 2011.
- [162] S. Zhou, H. Zhu, Z. Yan, J. W. Ju, and L. Zhang, "A micromechanical study of the breakage mechanism of microcapsules in concrete using PFC2D," *Construction and Building Materials*, vol. 115, pp. 452-463, 2016.
- [163] C. Qin and C. Zhang, "Numerical study of dynamic behavior of concrete by mesoscale particle element modeling," in *Seismic Safety Evaluation of Concrete Dams*, ed: Elsevier, 2014, pp. 595-617.
- [164] A. S. K. Elkadi, "Fracture scaling of concrete under multiaxial compression," TU Delft, Delft, Netherlands, 2005.
- [165] N. H. Nguyen, H. H. Bui, G. D. Nguyen, and J. Kodikara, "A cohesive damage-plasticity model for DEM and its application for numerical investigation of soft rock fracture properties," *International Journal of Plasticity*, vol. 98, pp. 175-196, 2017.
- [166] H. Kim, M. P. Wagoner, and W. G. Buttlar, "Numerical fracture analysis on the specimen size dependency of asphalt concrete using a cohesive softening model," *Construction and Building Materials*, vol. 23, pp. 2112-2120, 2009.
- [167] H. Kim, M. P. Wagoner, and W. G. Buttlar, "Micromechanical fracture modeling of asphalt concrete using a single-edge notched beam test," *Materials and Structures*, vol. 42, p. 677, 2009.
- [168] H. Kim and W. G. Buttlar, "Discrete fracture modeling of asphalt concrete," *International Journal of Solids and Structures*, vol. 46, pp. 2593-2604, 2009.
- [169] Y. Ma and H. Huang, "A displacement-softening contact model for discrete element modeling of quasi-brittle materials," *International journal of rock mechanics and mining sciences*, vol. 104, pp. 9-19, 2018.
- [170] Itasca, "Version 5.0," ed: Itasca Consulting Group, Inc., Minneapolis, 2011.

- [171] R. D. Mindlin, "Elastic spheres in contact under varying oblique forces," *J. Applied Mech.*, vol. 20, pp. 327-344, 1953.
- [172] C. O'Sullivan, *Particulate discrete element modelling: a geomechanics perspective*: CRC Press, 2014.
- [173] K. Murali and A. Deb, "Effect of meso-structure on strength and size effect in concrete under tension," *International Journal for Numerical and Analytical Methods in Geomechanics*, pp. 1-27, 2017.
- [174] X.-P. Zhang and L. N. Y. Wong, "Cracking processes in rock-like material containing a single flaw under uniaxial compression: a numerical study based on parallel bonded-particle model approach," *Rock mechanics and rock engineering*, vol. 45, pp. 711-737, 2012.
- [175] J. Saliba, "Apport de l'émission acoustique dans la compréhension et la modélisation du couplage fluage-endommagement du béton," PhD Degree, Institut de Recherche en Génie Civil et Mécanique (GeM), Ecole Centrale de Nantes France, 2012.
- [176] B. Yang, Y. Jiao, and S. Lei, "A study on the effects of microparameters on macroproperties for specimens created by bonded particles," *Engineering Computations*, vol. 23, pp. 607-631, 2006.
- [177] X. Ding, L. Zhang, H. Zhu, and Q. Zhang, "Effect of model scale and particle size distribution on PFC3D simulation results," *Rock mechanics and rock engineering*, vol. 47, pp. 2139-2156, 2014.
- [178] X.-P. Zhang and L. N. Y. Wong, "Loading rate effects on cracking behavior of flaw-contained specimens under uniaxial compression," *International Journal of Fracture*, vol. 180, pp. 93-110, 2013.
- [179] Q. Zhang, H. Zhu, L. Zhang, and X. Ding, "Study of scale effect on intact rock strength using particle flow modeling," *International journal of rock mechanics and mining sciences*, vol. 48, pp. 1320-1328, 2011.
- [180] Y. Cai, H. Zhu, and X. Zhuang, "A continuous/discontinuous deformation analysis (CDDA) method based on deformable blocks for fracture modeling," *Frontiers of Structural and Civil Engineering*, vol. 7, pp. 369-378, 2013.
- [181] K. Levenberg, "A method for the solution of certain non-linear problems in least squares," *Quarterly of applied mathematics*, vol. 2, pp. 164-168, 1944.
- [182] D. W. Marquardt, "An algorithm for least-squares estimation of nonlinear parameters," *Journal of the society for Industrial and Applied Mathematics*, vol. 11, pp. 431-441, 1963.
- [183] X. Ding and L. Zhang, "A new contact model to improve the simulated ratio of unconfined compressive strength to tensile strength in bonded particle models," *International journal of rock mechanics and mining sciences*, vol. 69, pp. 111-119, 2014.
- [184] P. Mondal, S. Shah, and L. Marks, "Nanomechanical properties of interfacial transition zone in concrete," in *Nanotechnology in Construction 3*, ed: Springer, 2009, pp. 315-320.
- [185] J. Chen, T.-Y. Pan, and X.-M. Huang, "Evaluation of styrene-butadiene latex as a vibration damping admixture for concrete: a micromechanical analysis," *Journal of the Chinese Institute of Engineers*, vol. 36, pp. 1008-1016, 2013.
- [186] S. Nakashima, K. Taguchi, A. Moritoshi, N. Shimizu, and T. Funatsu, "Loading conditions in the Brazilian test simulation by DEM," in *47th US Rock Mechanics/Geomechanics Symposium*, 2013.
- [187] X. Xu, S. Wu, Y. Gao, and M. Xu, "Effects of micro-structure and micro-parameters on Brazilian tensile strength using flat-joint model," *Rock mechanics and rock engineering*, vol. 49, pp. 3575-3595, 2016.
- [188] E. McCurdy, *The notebooks of Leonardo da Vinci*. London: G. Braziller, 1958.
- [189] H. Fischer, W. Rentzsch, and R. Marx, "A modified size effect model for brittle nonmetallic materials," *Engineering fracture mechanics*, vol. 69, pp. 781-791, 2002.
- [190] M. R. Van Vliet and J. G. Van Mier, "Experimental investigation of size effect in concrete and sandstone under uniaxial tension," *Engineering fracture mechanics*, vol. 65, pp. 165-188, 2000.
- [191] C. L. Bellego, B. Gérard, and G. Pijaudier-Cabot, "Chemo-mechanical effects in mortar beams subjected to water hydrolysis," *Journal of engineering mechanics*, vol. 126, pp. 266-272, 2000.

- [192] H. F. Gonnerman, "Effect of size and shape of test specimen on compressive strength of concrete," in *ASTM*, 1925, pp. 237-250.
- [193] Z. P. Bažant, "Size effect in blunt fracture: concrete, rock, metal," *Journal of engineering mechanics*, vol. 110, pp. 518-535, 1984.
- [194] W. Weibull, "Basic aspects of fatigue," in *Colloquium on Fatigue*, Stockholm, 1956, pp. 289-298.
- [195] W. Weibull, "The phenomenon of rupture in solids," *Ing Vet Ak Handl*, vol. 151, pp. 5-44, 1939.
- [196] W. Weibull, "A statistical distribution function of wide applicability," *Journal of applied mechanics*, vol. 18, pp. 293-297, 1951.
- [197] W. Weibull, S. Physicist, and S. Physicien, "A statistical representation of fatigue failures in solids," *Trans Royal Inst Technol Stockholm Sweden*, vol. 27, pp. 1-12, 1949.
- [198] A. Carpinteri, B. Chiaia, and G. Ferro, "Multifractal scaling law for the nominal strength variation of concrete structures," in *Japan Concrete Institute International Workshop*, Sendai, Japan, 1994, pp. 193-206.
- [199] A. Carpinteri, "Scaling laws and renormalization groups for strength and toughness of disordered materials," *International Journal of Solids and Structures*, vol. 31, pp. 291-302, 1994.
- [200] A. Carpinteri, "Decrease of apparent tensile and bending strength with specimen size: two different explanations based on fracture mechanics," *International Journal of Solids and Structures*, vol. 25, pp. 407-429, 1989.
- [201] F. T. Peirce, "Tensile tests for cotton yarns: "the weakest link" theorems on the strength of long and of composite specimens," *Journal of the textile institute*, vol. 17, pp. T355-368, 1926.
- [202] L. H. Tippett, "On the extreme individuals and the range of samples taken from a normal population," *Biometrika*, pp. 364-387, 1925.
- [203] A. M. Freudenthal, "Statistical approach to brittle fracture," *Fracture*, pp. 591-619, 1968.
- [204] A. Carpinteri, *Mechanical damage and crack growth in concrete: plastic collapse to brittle fracture* vol. 5: Springer Science & Business Media, 2012.
- [205] Z. Bažant and L. Cedolin, *Stability of structures: Elastic, Inelastic, Fracture and Damage Theories*. New York: Oxford University Press, 1991.
- [206] A. Neville, "Discussion: The influence of size of concrete test cubes on mean strength and standard deviation," *Magazine of Concrete Research*, vol. 9, pp. 52-55, 1957.
- [207] M. Lessard, O. Challal, and P.-C. Aticin, "Testing high-strength concrete compressive strength," *Materials Journal*, vol. 90, pp. 303-307, 1993.
- [208] J. Del Viso, J. Carmona, and G. Ruiz, "Shape and size effects on the compressive strength of high-strength concrete," *Cement and Concrete Research*, vol. 38, pp. 386-395, 2008.
- [209] Z. Bažant and Y. Kwon, "Failure of slender and stocky reinforced concrete columns: Tests of size effect," *Materials and Structures*, vol. 27, p. 79, 1994.
- [210] M. Brocca and Z. P. Bažant, "Size effect in concrete columns: finite-element analysis with microplane model," *Journal of Structural Engineering*, vol. 127, pp. 1382-1390, 2001.
- [211] G. Cusatis and Z. P. Bažant, "Size effect on compression fracture of concrete with or without V-notches: A numerical mesomechanical study," in *Computational modeling of concrete structures, Proc., EURO-C*, 2006, pp. 71-83.
- [212] J.-K. Kim, "Size effect in concrete specimens with dissimilar initial cracks," *Magazine of Concrete Research*, vol. 42, pp. 233-238, 1990.
- [213] Z. P. Bažant and Y. Xiang, "Size effect in compression fracture: splitting crack band propagation," *Journal of engineering mechanics*, vol. 123, pp. 162-172, 1997.
- [214] J.-I. Sim, K.-H. Yang, H.-Y. Kim, and B.-J. Choi, "Size and shape effects on compressive strength of lightweight concrete," *Construction and Building Materials*, vol. 38, pp. 854-864, 2013.

- [215] J.-K. Kim, S.-T. Yi, C.-K. Park, and S.-H. Eo, "Size effect on compressive strength of plain and spirally reinforced concrete cylinders," *ACI Structural Journal*, vol. 96, pp. 88-94, 1999.
- [216] C. Rocco, G. Guinea, J. Planas, and M. Elices, "Review of the splitting-test standards from a fracture mechanics point of view," *Cement and Concrete Research*, vol. 31, pp. 73-82, 2001.
- [217] R. Berenbaum and I. Brodie, "Measurement of the tensile strength of brittle materials," *British Journal of Applied Physics*, vol. 10, p. 281, 1959.
- [218] P. Wright, "Comments on an indirect tensile test on concrete cylinders," *Magazine of Concrete Research*, vol. 7, pp. 87-96, 1955.
- [219] G. M. Sabnis and S. M. Mirza, "Size effect in model concretes," *Journal of the Structural Division*, vol. 105, pp. 1007-1020, 1979.
- [220] Z. P. Bazant, M. T. Kazemi, T. Hasegawa, and J. Mazars, "Size effect in Brazilian split-cylinder tests: measurements and fracture analysis," *ACI Materials Journal*, vol. 88, pp. 325-332, 1991.
- [221] T. Hasegawa, T. Shioya, and T. Okada, "Size effect on splitting tensile strength of concrete," in *Proceedings Japan Concrete Institute 7th Conference*, 1985, pp. 309-312.
- [222] W.-F. Chen and B. Trumbauer, "Double-punch test and tensile strength of concrete," *Journal of Materials*, vol. 7, 1972.
- [223] C. Rocco, G. V. Guinea, J. Planas, and M. Elices, "Size effect and boundary conditions in the Brazilian test: experimental verification," *Materials and Structures*, vol. 32, p. 210, 1999.
- [224] F. Zhou, R. Balendran, and A. Jeary, "Size effect on flexural, splitting tensile, and torsional strengths of high-strength concrete," *Cement and Concrete Research*, vol. 28, pp. 1725-1736, 1998.
- [225] C. Rocco, G. Guinea, J. Planas, and M. Elices, "Size effect and boundary conditions in the Brazilian test: theoretical analysis," *Materials and Structures*, vol. 32, p. 437, 1999.
- [226] S. Mindess, "The effect of specimen size on the fracture energy of concrete," *Cement and Concrete Research*, vol. 14, pp. 431-436, 1984.
- [227] M. Alexander and G. Blight, "A comparative study of fracture parameters in notched concrete beams," *Magazine of Concrete Research*, vol. 40, pp. 50-58, 1988.
- [228] W. Brameshuber and H. Hilsdorf, "Influence of ligament length and stress state on fracture energy of concrete," *Engineering fracture mechanics*, vol. 35, pp. 95-106, 1990.
- [229] H. Linsbauer and A. Šajna, "Size-effect sensitivity-three-point bending test versus wedge splitting test," in *Size-Scale Effects in the Failure Mechanisms of Materials and Structures*, ed London: E & FN Spon, 2002.
- [230] Q. Jueshi and L. Hui, "Size effect on fracture energy of concrete determined by three-point bending," *Cement and Concrete Research*, vol. 27, pp. 1031-1036, 1997.
- [231] J. Mazars, G. Pijaudier-Cabot, and C. Saouridis, "Size effect and continuous damage in cementitious materials," *International Journal of Fracture*, vol. 51, pp. 159-173, 1991.
- [232] Ł. Skarżyński and J. Tejchman, "Calculations of fracture process zones on meso-scale in notched concrete beams subjected to three-point bending," *European Journal of Mechanics-A/Solids*, vol. 29, pp. 746-760, 2010.
- [233] K. Wu, B. Chen, and W. Yao, "Study of the influence of aggregate size distribution on mechanical properties of concrete by acoustic emission technique," *Cement and Concrete Research*, vol. 31, pp. 919-923, 2001.
- [234] A. Yan, K.-R. Wu, D. Zhang, and W. Yao, "Effect of fracture path on the fracture energy of high-strength concrete," *Cement and Concrete Research*, vol. 31, pp. 1601-1606, 2001.
- [235] M. Karamloo, M. Mazloom, and G. Payganeh, "Effects of maximum aggregate size on fracture behaviors of self-compacting lightweight concrete," *Construction and Building Materials*, vol. 123, pp. 508-515, 2016.
- [236] M. H. Beygi, M. T. Kazemi, J. V. Amiri, I. M. Nikbin, S. Rabbanifar, and E. Rahmani, "Evaluation of the effect of maximum aggregate size on fracture behavior of self compacting concrete," *Construction and Building Materials*, vol. 55, pp. 202-211, 2014.

- [237] ASTM and C469, "Standard Test Method for Static Modulus of Elasticity and Poisson's Ratio of Concrete in Compression," in *Annual Book of ASTM Standards*, ed. Philadelphia: American Society of Testing and Materials, 2010, pp. 255-258.
- [238] ASTM and C39, "Standard test method for compressive strength of cylindrical concrete specimens," in *Annual Book of ASTM Standards*, ed. Philadelphia: American Society of Testing and Materials, 2001.
- [239] R. Recommendation, "Fracture Mechanics of Concrete-Test Methods, Size effect method for determining fracture energy and process zone size of concrete," in *Materials and Structures* vol. 23, ed, 1990, pp. 461-465.
- [240] F. Kishinouye, "An experiment on the progression of fracture," *Journal of acoustic emission*, vol. 9, pp. 177-180, 1990.
- [241] J. Kaiser, "Untersuchungen über das Auftreten von Geräuschen beim Zugversuch," Technische Hochschule München, Germany, 1950.
- [242] B. H. Schofield, R. A. Bareiss, and A. A. Kyrala, "Acoustic emission under applied stress," Lessells and Associates, Boston, Massachusetts 1958.
- [243] C. A. Tatro, "Sonic techniques in the detection of crystal slip in metals," *Division of Engineering Research*, vol. 1, pp. 23-28, 1957.
- [244] H. Rüsç, *Physical problems in the testing of concrete*: Cement and Concrete Association, 1960.
- [245] R. G. L'Hermite, "Volume changes of concrete," in *4th International Symposium on the Chemistry of Cement*, Washington, DC, 1960, pp. 659-694.
- [246] G. S. Robinson, "Methods of detecting the formation and propagation of microcracks in concrete," in *International Symposium on the Structure of Concrete*, London, 1968, pp. 131-145.
- [247] D. G. Fertis, "Concrete material response by acoustic spectra analysis," *Journal of the Structural Division*, vol. 102, pp. 387-400, 1976.
- [248] W. M. McCabe, R. M. Koerner, and A. E. Lord, "Acoustic emission behavior of concrete laboratory specimens," *Journal of the American Concrete Institute*, vol. 73, pp. 367-71, 1976.
- [249] K. Haidar, G. Pijaudier-Cabot, J.-F. Dubé, and A. Loukili, "Correlation between the internal length, the fracture process zone and size effect in model materials," *Materials and Structures*, vol. 38, p. 201, 2005.
- [250] E. N. Landis, "Micro-macro fracture relationships and acoustic emissions in concrete," *Construction and Building Materials*, vol. 13, pp. 65-72, 1999.
- [251] D. Grégoire, L. Verdon, V. Lefort, P. Grassl, J. Saliba, J. P. Regoin, A. Loukili, and G. Pijaudier-Cabot, "Mesoscale analysis of failure in quasi-brittle materials: comparison between lattice model and acoustic emission data," *International Journal for Numerical and Analytical Methods in Geomechanics*, vol. 39, pp. 1639-1664, 2015.
- [252] S. Granger, A. Loukili, G. Pijaudier-Cabot, and G. Chanvillard, "Experimental characterization of the self-healing of cracks in an ultra high performance cementitious material: Mechanical tests and acoustic emission analysis," *Cement and Concrete Research*, vol. 37, pp. 519-527, 2007.
- [253] Z. Li and S. P. Shah, "Localization of microcracking in concrete under uniaxial tension," *Materials Journal*, vol. 91, pp. 372-381, 1994.
- [254] M. Ohtsu, "The history and development of acoustic emission in concrete engineering," *Magazine of Concrete Research*, vol. 48, pp. 321-330, 1996.
- [255] K. Ohno and M. Ohtsu, "Crack classification in concrete based on acoustic emission," *Construction and Building Materials*, vol. 24, pp. 2339-2346, 2010.
- [256] C. U. Grosse and F. Finck, "Quantitative evaluation of fracture processes in concrete using signal-based acoustic emission techniques," *Cement and Concrete Composites*, vol. 28, pp. 330-336, 2006.
- [257] A. F. Uddin, K. Numata, J. Shimasaki, M. Shigeishi, and M. Ohtsu, "Mechanisms of crack propagation due to

- corrosion of reinforcement in concrete by AE-SiGMA and BEM," *Construction and Building Materials*, vol. 18, pp. 181-188, 2004.
- [258] C. U. Grosse and M. Ohtsu, *Acoustic emission testing*. Heidelberg, Germany: Springer Science & Business Media, 2008.
- [259] B. Behnia, W. G. Buttlar, H. Reis, and A. K. Apeagye, "Determining the embrittlement temperature of asphalt binders using an acoustic emission approach," in *Structural Materials Technology 2010*, 2010.
- [260] R. K. Miller and P. McIntire, *Acoustic emission testing*. Columbus, Ohio: American Society for Nondestructive Testing, 1987.
- [261] M. Hamstad, "Acoustic emission signals generated by monopole (pencil lead break) versus dipole sources: finite element modeling and experiments," *Journal of acoustic emission*, vol. 25, pp. 92-106, 2007.
- [262] ASTM, "Standard Guide for Determining the Reproducibility of Acoustic Emission Sensor Response," in *ASTM E976-10*, ed. Philadelphia, PA, USA: American Society for Testing and Materials, 2010.
- [263] N. N. Hsu and F. R. Brecknbridge, "Characterization and calibration of acoustic emission sensors," *Materials Evaluation*, vol. 39, pp. 60-68, 1981.
- [264] J. Pujol, "Earthquake location tutorial: graphical approach and approximate epicentral location techniques," *Seismological Research Letters*, vol. 75, pp. 63-74, 2004.
- [265] M. Bath, *Introduction to seismology* vol. 27: Birkhäuser Verlag, Basel, 2013.
- [266] H. Bruck, S. McNeill, M. A. Sutton, and W. Peters, "Digital image correlation using Newton-Raphson method of partial differential correction," *Experimental mechanics*, vol. 29, pp. 261-267, 1989.
- [267] T. Chu, W. Ranson, and M. A. Sutton, "Applications of digital-image-correlation techniques to experimental mechanics," *Experimental mechanics*, vol. 25, pp. 232-244, 1985.
- [268] W. Peters and W. Ranson, "Digital imaging techniques in experimental stress analysis," *Optical engineering*, vol. 21, p. 213427, 1982.
- [269] M. Sutton, W. Wolters, W. Peters, W. Ranson, and S. McNeill, "Determination of displacements using an improved digital correlation method," *Image and vision computing*, vol. 1, pp. 133-139, 1983.
- [270] J. D. Helm, S. R. McNeill, and M. A. Sutton, "Improved three-dimensional image correlation for surface displacement measurement," *Optical engineering*, vol. 35, pp. 1911-1921, 1996.
- [271] P.-F. Luo, Y. J. Chao, and M. A. Sutton, "Application of stereo vision to three-dimensional deformation analyses in fracture experiments," *Optical engineering*, vol. 33, pp. 981-991, 1994.
- [272] P. Luo, Y. Chao, M. Sutton, and W.-H. Peters, "Accurate measurement of three-dimensional deformations in deformable and rigid bodies using computer vision," *Experimental mechanics*, vol. 33, pp. 123-132, 1993.
- [273] B. Pan, Z. Wang, and H. Xie, "Generalized spatial-gradient-based digital image correlation for displacement and shape measurement with subpixel accuracy," *The Journal of Strain Analysis for Engineering Design*, vol. 44, pp. 659-669, 2009.
- [274] B. Pan, A. Asundi, H. Xie, and J. Gao, "Digital image correlation using iterative least squares and pointwise least squares for displacement field and strain field measurements," *Optics and Lasers in Engineering*, vol. 47, pp. 865-874, 2009.
- [275] Y. Altunbasak, R. M. Mersereau, and A. J. Patti, "A fast parametric motion estimation algorithm with illumination and lens distortion correction," *IEEE Transactions on Image Processing*, vol. 12, pp. 395-408, 2003.
- [276] A. Gruen, "Adaptive least squares correlation: a powerful image matching technique," *South African Journal of Photogrammetry, Remote Sensing and Cartography*, vol. 14, pp. 175-187, 1985.
- [277] P. Rastogi, *Digital optical measurement techniques and applications*: Artech House, 2015.
- [278] W. Tong, "An evaluation of digital image correlation criteria for strain mapping applications," *Strain*, vol. 41, pp. 167-175, 2005.
- [279] Z. P. Bažant, "Concrete fracture models: testing and practice," *Engineering fracture mechanics*, vol. 69, pp. 165-

- 205, 2002.
- [280] Z. P. Bažant, "Mechanics of fracture and progressive cracking in concrete structures," in *Fracture mechanics of concrete: Structural application and numerical calculation*, ed Dordrecht: Martinus Nijhoff, 1985, pp. 1-94.
- [281] P. Grassl, D. Grégoire, L. R. Solano, and G. Pijaudier-Cabot, "Meso-scale modelling of the size effect on the fracture process zone of concrete," *International Journal of Solids and Structures*, vol. 49, pp. 1818-1827, 2012.
- [282] S. Y. Alam, "Experimental study and numerical analysis of crack opening in concrete," Ecole Centrale de Nantes, France, 2011.
- [283] W. Dong, Z. Wu, X. Zhou, N. Wang, and G. Kastiukas, "An experimental study on crack propagation at rock-concrete interface using digital image correlation technique," *Engineering fracture mechanics*, vol. 171, pp. 50-63, 2017.
- [284] N. Aissaoui and M. Matallah, "Numerical and analytical investigation of the size-dependency of the FPZ length in concrete," *International Journal of Fracture*, vol. 205, pp. 127-138, 2017.
- [285] Z. P. Bažant, M. T. Kazemi, T. Hasegawa, and J. Mazars, "Size effect in Brazilian split-cylinder tests. Measurements and fracture analysis," *ACI Materials Journal*, vol. 88, pp. 325-332, 1991.
- [286] B. Chen and J.-Y. Liu, "Effect of aggregate on the fracture behavior of high strength concrete," *Construction and Building Materials*, vol. 18, pp. 585-590, 2004.
- [287] P. Nallathambi, B. Karihaloo, and B. Heaton, "Effect of specimen and crack sizes, water/cement ratio and coarse aggregate texture upon fracture toughness of concrete," *Magazine of Concrete Research*, vol. 36, pp. 227-236, 1984.
- [288] P. Strange and A. Bryant, "The role of aggregate in the fracture of concrete," *Journal of Materials Science*, vol. 14, pp. 1863-1868, 1979.
- [289] G. A. Rao and B. R. Prasad, "Fracture energy and softening behavior of high-strength concrete," *Cement and Concrete Research*, vol. 32, pp. 247-252, 2002.
- [290] Y. Jenq and S. Shah, "A fracture toughness criterion for concrete," *Engineering fracture mechanics*, vol. 21, pp. 1055-1069, 1985.
- [291] P. Petersson, "Fracture energy of concrete: practical performance and experimental results," *Cement and Concrete Research*, vol. 10, pp. 91-101, 1980.
- [292] M. H. Beygi, M. T. Kazemi, I. M. Nikbin, J. V. Amiri, S. Rabbanifar, and E. Rahmani, "The influence of coarse aggregate size and volume on the fracture behavior and brittleness of self-compacting concrete," *Cement and Concrete Research*, vol. 66, pp. 75-90, 2014.
- [293] M. Moseley, R. Ojdrovic, and H. Petroski, "Influence of aggregate size on fracture toughness of concrete," *Theoretical and applied fracture mechanics*, vol. 7, pp. 207-210, 1987.
- [294] Z. Bažant, R. Gettu, and M. Kazemi, "Identification of nonlinear fracture properties from size effect tests and structural analysis based on geometry-dependent R-curves," in *International journal of rock mechanics and mining sciences & geomechanics abstracts*, 1991, pp. 43-51.
- [295] L. B. Rojas Solano, "Endommagement non-local, interactions et effets d'échelle," Pau, 2012.
- [296] H. Hertz, "On the contact of elastic solids," *J. Reine Angew Math.*, vol. 92, pp. 156-171, 1881.
- [297] G. Hondros, "The evaluation of Poisson's ratio and the modulus of materials of a low tensile resistance by the Brazilian (indirect tensile) test with particular reference to concrete," *Australian Journal of Applied Science*, vol. 10, pp. 243-268, 1959.
- [298] D. U. Deere and R. Miller, "Engineering classification and index properties for intact rock," Illinois Univ At Urbana Dept Of Civil Engineering 1966.
- [299] M. G. Lay, *Handbook of road technology*: CRC Press, 2014.
- [300] C. Yang, "Effect of the transition zone on the elastic moduli of mortar," *Cement and Concrete Research*, vol. 28,

- pp. 727-736, 1998.
- [301] M. Tasdemir, C. Tasdemir, S. Akyüz, A. Jefferson, F. Lydon, and B. Barr, "Evaluation of strains at peak stresses in concrete: a three-phase composite model approach," *Cement and Concrete Composites*, vol. 20, pp. 301-318, 1998.
- [302] J. G. Van Mier, *Fracture processes of concrete*. Boca Raton, Florida: CRC press, 1997.
- [303] S. Mindess, J. F. Young, and D. Darwin, *Concrete*. Englewood Cliffs, NJ, USA: Prentice Hall, 2003.
- [304] D. Li and L. N. Y. Wong, "The Brazilian disc test for rock mechanics applications: review and new insights," *Rock mechanics and rock engineering*, vol. 46, pp. 269-287, 2013.
- [305] F. Carneiro and A. Barcellos, "Concrete tensile strength," *RILEM Bullet*, vol. 13, pp. 103-107, 1953.
- [306] T. Akazawa, "Tension test method for concrete," *RILEM Bullet*, vol. 16, pp. 13-23, 1953.
- [307] M. Hassanzadeh, "The influence of the type of coarse aggregates on the fracture mechanical properties of high-strength concrete," in *the FRAMCOS-3*, Freiburg, Germany, 1998, pp. 161-170.
- [308] D. Hannant, K. Buckley, and J. Croft, "The effect of aggregate size on the use of the cylinder splitting test as a measure of tensile strength," *Matériaux et Construction*, vol. 6, pp. 15-21, 1973.
- [309] V. Osidze and D. Khoperiya, "Effect of aggregate size on the tensile strength of hydraulic-concrete specimens," *Power Technology and Engineering (formerly Hydrotechnical Construction)*, vol. 13, pp. 239-244, 1979.
- [310] V. Kadleček and S. Modrý, "Size effect of test specimens on tensile splitting strength of concrete: general relation," *Materials and Structures*, vol. 35, p. 28, 2002.
- [311] A. M. Ibragimov, "Effect of the maximum size of coarse aggregate on the main parameters of concrete," *Hydrotechnical Construction*, vol. 23, pp. 141-144, 1989.
- [312] M. T. Uddin, A. H. Mahmood, M. R. I. Kamal, S. Yashin, and Z. U. A. Zihan, "Effects of maximum size of brick aggregate on properties of concrete," *Construction and Building Materials*, vol. 134, pp. 713-726, 2017.
- [313] N. Benkemoun, P. Poullain, H. Al Khazraji, M. Choinska, and A. Khelidj, "Meso-scale investigation of failure in the tensile splitting test: Size effect and fracture energy analysis," *Engineering fracture mechanics*, vol. 168, pp. 242-259, 2016.
- [314] S. Walker and D. L. Bloem, "Effects of aggregate size on properties of concrete," in *Journal Proceedings*, 1960, pp. 283-298.
- [315] J.-I. Sim, K.-H. Yang, E.-T. Lee, and S.-T. Yi, "Effects of aggregate and specimen sizes on lightweight concrete fracture energy," *Journal of Materials in Civil Engineering*, vol. 26, pp. 845-854, 2013.
- [316] W. Kellerman, "Effect of size of specimen, size of aggregate, and method of loading upon the uniformity of flexural strength tests," *Public roads*, vol. 13, p. 177, 1933.
- [317] A. Hillerborg, "Results of three comparative test series for determining the fracture energy G_F of concrete," *Materials and Structures*, vol. 18, pp. 407-413, 1985.
- [318] P. Walsh, "Fracture of plain concrete," *Indian Concrete Journal*, vol. 46, pp. 469-476, 1972.
- [319] P. Nallathambi, B. Karihaloo, and B. Heaton, "Various size effects in fracture of concrete," *Cement and Concrete Research*, vol. 15, pp. 117-126, 1985.
- [320] C. E.-I. d. Béton, "CEB-FIP Model Code," ed. London: Thomas Telford, 1990.
- [321] H. Kleinschrodt and H. Winkler, "The influence of the maximum aggregate size and the size of specimen on fracture mechanics parameters," *Fracture toughness and fracture energy of concrete*, pp. 391-402, 1986.
- [322] S. Wolinski, D. A. Hordijk, H. W. Reinhardt, and H. A. Cornelissen, "Influence of aggregate size on fracture mechanics parameters of concrete," *International Journal of Cement Composites and Lightweight Concrete*, vol. 9, pp. 95-103, 1987.
- [323] B. Barr, E. Hasso, and V. Weiss, "Effect of specimen and aggregate sizes upon the fracture characteristics of concrete," *International Journal of Cement Composites and Lightweight Concrete*, vol. 8, pp. 109-119, 1986.
- [324] P. Regnault and E. Brühwiler, "Holographic interferometry for the determination of fracture process zone in

- concrete," *Engineering fracture mechanics*, vol. 35, pp. 29-38, 1990.
- [325] H. Mihashi and N. Nomura, "Correlation between characteristics of fracture process zone and tension-softening properties of concrete," *Nuclear engineering and design*, vol. 165, pp. 359-376, 1996.
- [326] C. Tasdemir, M. A. Tasdemir, N. Mills, B. I. Barr, and F. D. Lydon, "Combined Effects of Silica Fume, Aggregate Type, and Size on Post-Peak Response of Concrete in Bending," *Materials Journal*, vol. 96, pp. 74-83, 1999.
- [327] Z. P. Bazant and E. Becq-Giraudon, "Statistical prediction of fracture parameters of concrete and implications for choice of testing standard," *Cement and Concrete Research*, vol. 32, pp. 529-556, 2002.
- [328] M. A. Issa, M. A. Issa, M. S. Islam, and A. Chudnovsky, "Size effects in concrete fracture—Part II: Analysis of test results," *International Journal of Fracture*, vol. 102, pp. 25-42, 2000.
- [329] M. A. Issa, M. A. Issa, M. S. Islam, and A. Chudnovsky, "Size effects in concrete fracture: Part I, experimental setup and observations," *International Journal of Fracture*, vol. 102, pp. 1-24, 2000.
- [330] B. Chen and J. Liu, "Effect of aggregate on the fracture behavior of high strength concrete," *Construction and Building Materials*, vol. 18, pp. 585-590, 2004.
- [331] Z. Zhao, S. H. Kwon, and S. P. Shah, "Effect of specimen size on fracture energy and softening curve of concrete: Part I. Experiments and fracture energy," *Cement and Concrete Research*, vol. 38, pp. 1049-1060, 2008.
- [332] B. Chen and J. Liu, "Investigation of effects of aggregate size on the fracture behavior of high performance concrete by acoustic emission," *Construction and Building Materials*, vol. 21, pp. 1696-1701, 2007.
- [333] M. A. Issa, M. A. Issa, M. S. Islam, and A. Chudnovsky, "Fractal dimension—a measure of fracture roughness and toughness of concrete," *Engineering fracture mechanics*, vol. 70, pp. 125-137, 2003.
- [334] Z. P. Bazant and M. T. Kazemi, "Size effect on diagonal shear failure of beams without stirrups," *ACI Structural Journal*, vol. 88, pp. 268-276, 1991.
- [335] A. Carpinteri, B. Chiaia, and G. Ferro, "Size effects on nominal tensile strength of concrete structures: multifractality of material ligaments and dimensional transition from order to disorder," *Materials and Structures*, vol. 28, p. 311, 1995.
- [336] K. Duan, X.-Z. Hu, and F. H. Wittmann, "Thickness effect on fracture energy of cementitious materials," *Cement and Concrete Research*, vol. 33, pp. 499-507, 2003.
- [337] X. Hu and K. Duan, "Influence of fracture process zone height on fracture energy of concrete," *Cement and Concrete Research*, vol. 34, pp. 1321-1330, 2004.
- [338] G. A. Rao and B. R. Prasad, "Fracture process zone in high strength concrete," in *Fourth International Conference on Fracture Mechanics of Concrete and Concrete Structures*, 2001, pp. 327-332.
- [339] H.-Z. Liu, J.-S. Lin, J.-D. He, and H.-Q. Xie, "Discrete elements and size effects," *Engineering fracture mechanics*, vol. 189, pp. 246-272, 2018.
- [340] M. Galouei and A. Fakhimi, "Size effect, material ductility and shape of fracture process zone in quasi-brittle materials," *Computers and Geotechnics*, vol. 65, pp. 126-135, 2015.
- [341] H. W. Reinhardt, H. A. Cornelissen, and D. A. Hordijk, "Tensile tests and failure analysis of concrete," *Journal of Structural Engineering*, vol. 112, pp. 2462-2477, 1986.
- [342] A. A. Griffith and M. Eng, "The phenomena of rupture and flow in solids," *Phil. Trans. R. Soc. Lond. A*, vol. 221, pp. 163-198, 1921.
- [343] G. R. Irwin, "Analysis of stresses and strains near the end of a crack traversing a plate," *J. appl. Mech.*, vol. 24, pp. 361-364, 1957.
- [344] M. Williams, "Stress singularities resulting from various boundary conditions in angular corners of plates in extension," *Journal of applied mechanics*, vol. 19, pp. 526-528, 1952.
- [345] R. C. Bradt, D. Hasselman, D. Munz, M. Sakai, and V. Y. Shevchenko, *Fracture Mechanics of Ceramics: Fatigue, Composites, and High-Temperature Behavior* vol. 12: Springer Science & Business Media, 2012.

- [346] E. M. Wu, "Application of fracture mechanics to anisotropic plates," *Journal of applied mechanics*, vol. 34, pp. 967-974, 1967.
- [347] F. Petri and W. Carlos, *Static and Dynamic Crack Propagation in Brittle Materials with XFEM*: kassel university press GmbH, 2013.
- [348] M. Jirásek and M. Bauer, "Numerical aspects of the crack band approach," *Computers & structures*, vol. 110, pp. 60-78, 2012.
- [349] J. Bobiński and J. Tejchman, "Comparison of continuous and discontinuous constitutive models to simulate concrete behaviour under mixed-mode failure conditions," *International Journal for Numerical and Analytical Methods in Geomechanics*, vol. 40, pp. 406-435, 2016.
- [350] G. Cusatis, Z. P. Bažant, and L. Cedolin, "Confinement-shear lattice model for concrete damage in tension and compression: I. Theory," *Journal of engineering mechanics*, vol. 129, pp. 1439-1448, 2003.
- [351] M. Jiang, J. Konrad, and S. Leroueil, "An efficient technique for generating homogeneous specimens for DEM studies," *Computers and Geotechnics*, vol. 30, pp. 579-597, 2003.
- [352] K. Ha, H. Baek, and K. Park, "Convergence of fracture process zone size in cohesive zone modeling," *Applied Mathematical Modelling*, vol. 39, pp. 5828-5836, 2015.
- [353] M. Wecharatana and S. P. Shah, "Predictions of nonlinear fracture process zone in concrete," *Journal of engineering mechanics*, vol. 109, pp. 1231-1246, 1983.
- [354] K. Duan, X. Hu, and F. Wittmann, "Boundary effect on concrete fracture and non-constant fracture energy distribution," *Engineering fracture mechanics*, vol. 70, pp. 2257-2268, 2003.
- [355] K. Duan and X.-Z. Hu, "Asymptotic analysis of boundary-effect on strength of concrete," *Fracture mechanics of concrete structures, FraMCoS-5*, pp. 12-16, 2004.
- [356] K. Duan, X.-Z. Hu, and F. H. Wittmann, "Size effect on specific fracture energy of concrete," *Engineering fracture mechanics*, vol. 74, pp. 87-96, 2007.
- [357] K. Duan, X. Hu, and F. Wittmann, "Boundary effect on specific fracture energy of concrete," in *Fracture mechanics of concrete structures (Proc FraMCoS-5), Ia-FraMCoS*, 2004, pp. 205-212.

Titre : Effets d'échelle et de la taille des granulats sur la rupture du béton : Étude expérimentale et modélisation par éléments discrets

Mots clés : béton, effet d'échelle, taille de granulats, fissuration, émission acoustique, corrélation d'images, éléments discrets, modèle de contact.

Résumé : Il est de plus en plus admis que l'effet d'échelle doit être pris en compte dans la conception des structures de Génie Civil. Pour le béton, ce problème est complexe car celui-ci ne possède pas d'adoucissement plastique, et sa rupture est due à la fissuration caractérisée par une grande zone de microfissuration (fracture process zone) qui dépend de la taille du granulats d_{\max} . Cette fissuration passe par un adoucissement sous la forme de microfissures et de glissement interparticules.

Expérimentalement, l'effet d'échelle sur le béton est très souvent étudié à l'aide des corps d'épreuves homothétiques entaillés où l'on cherche à relier la résistance nominale (σ_N) estimée à partir de la charge de rupture en flexion à une dimension caractéristique D . Ceci conduit à une diminution du ratio d_{\max}/D avec l'augmentation de la taille de la structure. Parmi les objectifs de cette thèse est d'étudier expérimentalement l'impact de l'hétérogénéité (d_{\max}/D) supposé comme facteur fondamental de l'effet d'échelle. Trois coupures granulaires ont été testées sur trois tailles de poutres différentes en suivant le processus de fissuration par émission acoustique et la technique de corrélation d'images. Celles-ci

permettent de suivre l'ouverture des fissures et identifient assez clairement la FPZ.

Les résultats mettent en évidence une grande influence de la taille du granulats sur le comportement à la rupture du béton. Il existe une relation directe entre les paramètres de l'effet d'échelle obtenus par la loi de Bazant et la taille du granulats (d_{\max}). Le traitement des résultats d'une même taille avec différents granulométries dans le même diagramme conduit à la même loi d'effet d'échelle structurelle classique avec une valeur de transition identique.

La modélisation du comportement mécanique est effectuée par la méthode d'éléments discrets (DEM). Le modèle de contact linéaire ne s'avère pas adéquat pour le mortier et le béton où le rapport compression / traction est très élevé. De ce fait, il a été modifié pour prendre en compte la contribution des moments inter-granulaires. Les paramètres micromécaniques sont déterminés par des essais classiques avec une analyse inverse en utilisant l'algorithme de Levenberg-Marquardt. Les résultats montrent que cette approche est capable de reproduire le comportement à la fissuration locale du béton et de reproduire l'effet d'échelle et celui des granulats. Ensuite, un modèle d'adoucissement est développé afin de mieux reproduire la réponse post pic et le processus de fissuration.

Title : Aggregate Size and Scale effects on concrete fracture : experimental investigation and discrete element modelling

Keywords : concrete, size effect, aggregate size, cracking, acoustic emission, digital image correlation, discrete elements, contact model.

Abstract : It is now commonly understood that in the design of civil engineering structures, size effect must be taken into consideration. For concrete, this problem is complex because it does not exhibit plastic softening. The failure of concrete is generally preceded by propagation of cracks, characterized by a large microcracking zone (fracture process zone or FPZ) which is proportional to the maximum aggregate size (d_{\max}). This fracture process is accompanied by strain-softening in the form of microcracking and fractional slip.

Experimentally, size effect in concrete is commonly studied by using geometrically similar notched beams where the nominal strength (σ_N) obtained from the bending failure load is related to the characteristic dimension (D). This leads to a decrease in the ratio of d_{\max}/D with an increase in the size of the structure. One of the objective of this thesis is to study experimentally the effect of heterogeneity (d_{\max}/D) size. This ratio is recognized as a fundamental factor causing the size effect. Three aggregate grading segments were tested on three different sizes of beams and the cracking process was investigated by acoustic emission and the image correlation

technique. These methods make it possible to trace the crack openings and identify distinctively the FPZ.

The results demonstrate a significant influence of the aggregate size on the fracture behaviour of concrete. There is a direct relationship between the size effect parameters obtained by Bazant's law and maximum aggregate size (d_{\max}). The results obtained from the specimen having the same size but made of concretes with different aggregate sizes produced the same classical size effect with identical transitional between LEM and strength based laws.

The mechanical behaviour is modelled by the Discrete Element Method (DEM). However, the linear contact model inserted in DEM is not suitable to satisfy the materials like mortar and concrete with high unconfined compressive strength to tensile strength ratio. As a result, the model is modified to take into account the contribution of interparticle moments. The micromechanical parameters are determined by conventional tests with inverse analysis using the Levenberg-Marquardt algorithm. The results showed that this approach is able to reproduce the local cracking behaviour of concrete as well as classical size effect and aggregate size effect. Then, a softening model is developed to better reproduce the post-peak response and the cracking process.